
In-Situ Environmental TEM Studies of Electro- and Photo-Electrochemical Systems for Water Splitting

D I S S E R T A T I O N

zur Erlangung des mathematisch-naturwissenschaftlichen Doktorgrades

“Doctor rerum naturalium”

der Georg-August-Universität Göttingen

—

im Promotionsprogramm ProPhys

der Georg-August University School of Science (GAUSS)

vorgelegt von

Emanuel Ronge

aus Kassel

Göttingen, 2021

Betreuungsausschuss:

Prof. Dr. Christian Jooss, Institut für Materialphysik
Prof. Dr. Michael Seibt, IV. Physikalisches Institut

Mitglieder der Prüfungskommission:

Referent: Prof. Dr. Christian Jooss, Institut für Materialphysik
Korreferent: Prof. Dr. Michael Seibt, IV. Physikalisches Institut

weitere Mitglieder der Prüfungskommission:

Prof. Dr. Cynthia Volkert, Institut für Materialphysik
Prof. Dr. Vasily Moshnyaga, I. Physikalisches Institut
Prof. Dr. Wolfram Kollatschny, Institut für Astrophysik
Prof. Dr. Hans Hofsäss, II. Physikalisches Institut

Tag der mündlichen Prüfung: 18.12.2020

Contents

1. Introduction	1
2. Scientific Background	5
2.1 Hydrogen Evolution by MoS _x	5
2.1.1 HER-Relevant Crystal Structures of MoS _x	7
2.1.2 Electrochemical Performance of MoS _x	9
2.2 Oxygen Evolution by Birnessite	11
2.2.1 Crystal Structure of Birnessite	13
2.2.2 Electrochemical Performance of Birnessite	14
2.3 Integrated Water Splitting Device Design	16
2.4 In-situ Electron Microscopy	19
3. Stability and Degradation Mechanism of Si-based Photocathodes	23
3.1 Introduction	24
3.2 Results	25
3.2.1 Pristine State of the Photocathode	25
3.2.2 Performance	26
3.2.3 Post-mortem studies of the photocathode stability	27
3.3 Discussion	30
3.4 Conclusion	31
3.5 Experimental Section	32
3.5.1 Preparation of Si-based Photocathodes solar cells	32
3.5.2 Device Integration	33
3.5.3 Photoelectrochemical Characterization	33
3.5.4 SEM and EDX	34
3.5.5 TEM lamellae preparation and TEM analysis	34
4. Structure of Nanocrystalline, Partially Disordered MoS_{2+δ}	35
4.1 Introduction	36
4.2 Results	38
4.2.1 Electrochemical Characterization of MoS _{2+δ} Electrodes	38
4.2.2 Electron and X-ray Diffraction Analysis of the MoS _{2+δ} Structure	40
4.2.3 HRTEM Analysis of the Microstructure of MoS _{2+δ}	42
4.3 Structure Model	45
4.4 Materials and Methods	48

4.5	Summary	51
5.	Interactions of Birnessite with Phosphate Buffer Anions	53
5.1	Introduction	54
5.2	Experimental Section	56
5.3	Results and Discussion	58
5.3.1	Electrochemistry	58
5.3.2	Investigations of morphology changes and ion-exchange processes of the catalyst layer by SEM, TEM and EDX	60
5.3.3	Ca-Birnessite/electrolyte interactions probed by XPS and NEXAFS	65
5.4	Conclusion	74
6.	Atomic Dynamics of Manganese Oxide in OER like Conditions	77
6.1	Introduction	78
6.2	Experimental Methods	80
6.2.1	Lamella Preparation	80
6.2.2	In Situ ETEM	80
6.2.3	Tracking Atomic Movements in HRTEM	81
6.2.4	Mn L-Edge EELS Analysis	83
6.3	Results	84
6.3.1	HRTEM Analysis of the Pristine State of Birnessite Electrodes	84
6.3.2	Environmental TEM Studies on Surface Dynamics in H ₂ O and O ₂	86
6.3.3	In-situ STEM EELS of the Birnessite Electrodes in H ₂ O and O ₂	88
6.4	Discussion	91
6.5	Conclusion	94
7.	General Discussion and Summary	97
	Bibliography	125
A.	Supporting Information for Chapter 3	127
B.	Supporting Information for Chapter 4	131
B.1	XRD	132
B.1.1	Rietveld refinement	132
B.2	TEM	133
B.3	SEM	139
B.4	EC	141
C.	Supporting Information for Chapter 5	143
C.1	Experimental details	144
C.1.1	Materials	144
C.1.2	Electrocatalysis	144

C.2 Electron Microscopy	146
C.3 Spectroscopy	151
C.4 Theory: Hybridization and Calculation details	159
D. Supporting Information for Chapter 6	161
Author Contributions	175
Acknowledgment	177

List of Figures

1.1	Schematic illustration of a solar hydrogen cycle	2
1.2	Schematic illustration of an integrated device	2
2.1	Crystal Structure of MoS_x and Clusters	8
2.2	Structure models for MoS_x	9
2.3	Comparison of MnO_x structures	12
2.4	Crystal structure of Birnessite	14
2.5	Schematic illustration of different integrated device designs	17
3.1	Configuration of the photo-electrochemical device	26
3.2	Chronopotentiometry measurement of a tandem and triple cell devices	27
3.3	SEM images of the post mortem state of the tandem photocathode	28
3.4	EDX analysis of the Cl inhomogeneity	29
3.5	EDX analysis of a corrosion crater of a tandem photocathode	30
3.6	Schematic illustration of the suggested mechanism	32
4.1	Electrochemical measurements for $\text{MoS}_{2+\delta}$ and MoS_2	39
4.2	Powder XRD diffraction pattern of MoS_2 and $\text{MoS}_{2+\delta}$	41
4.3	Intensity profiles of electron diffraction patterns($\text{MoS}_{2+\delta}$)	42
4.4	HRTEM image of sample $\text{MoS}_{3.4}$ showing the in-plane ordering	43
4.5	HRTEM analysis of nanocrystalline $\text{MoS}_{2+\delta}$	44
4.6	Close up of the HRTEM image of Figure 4.5 B	45
4.7	Schematic illustration of the suggested structure model for $\text{MoS}_{2+\delta}$	47
5.1	Chronoamperometry of Ca-birnessite/FTO electrodes in three different electrolytes	59
5.2	SEM images of Ca-birnessite electrodes	61
5.3	HAADF STEM image and EELS element mapping of birnessite	62
5.4	TEM EDX analysis of birnessite	63
5.5	TEM EDX comparison of phosphate buffer and Imidazole	64
5.6	X-ray photoelectron survey spectra of different Ca-birnessite samples.	66
5.7	Mn L_3 -edge NEXAFS (TEY) spectra of the three different Ca-birnessite samples studied by XAS.	68
5.8	Deconvoluted Ca 2p spectra (data for $E_k = 830 \text{ eV}$) of the three different Ca-birnessite samples studied by XAS	70

5.9	Deconvoluted P 2p XPS spectrum for a Ca-birnessite electrode after electrolysis under OER conditions	73
6.1	Demonstration of the drift correction and image averaging procedure to track atomic motions	82
6.2	HRTEM analysis of differently processed birnessites in HV	85
6.3	In situ HRTEM analysis of the surface dynamics of the pressed birnessite electrode	87
6.4	In situ HRTEM experiment with a printed electrode in 1 hPa O ₂	88
6.5	In situ HRTEM analysis of the dynamic state of the printed electrode in H ₂ O compared to O ₂	89
6.6	Representative in-situ STEM EELS Mn-L Edge spectra of the Birnessite electrodes	90
A.1	Platinum particle size and density from different areas	128
A.2	TEM bright field images of the TiO ₂ layer	128
A.3	Surface with platinum particles	129
A.4	EDX analysis of a hole in a a-Si:H/100xTiO ₂ /Pt photocathode	130
A.5	SEM image of a-Si/a-Si/ μ c-Si/100xTiO ₂ /Pt triple junction	130
B.1	Plot of the Rietveld refinement of MoS ₂	132
B.2	Electron diffraction pattern of MoS _{2.6} , MoS _{3.4} and MoS ₂	133
B.3	HRTEM images of MoS _{2.6} and MoS _{3.4}	136
B.4	HRTEM images of MoS ₂ and their FFTs	137
B.5	Reduced FFT of HRTEM MoS _{3$\pm$$\delta$} image from figure 4.5	138
B.6	SEM images of MoS ₂ , MoS _{2.6} and MoS _{3.4} powder	140
B.7	Cyclic voltammetry of MoS _x and MoS ₂	141
C.1	Cyclic voltammograms of Ca-birnessite-coated FTO-slides	145
C.2	HRTEM-image of a Ca-birnessite electrode coated with a 0.2 μ m thick catalyst layer	146
C.3	Electron diffraction pattern and associated radial intensity profiles of the Ca-birnessite layer	147
C.4	EDX element analysis of birnessite after electrolysis in different electrolytes	149
C.5	EDX linescan of a 4 μ m thick sample after 9 h of electrolysis in phosphate buffered electrolyte	150
C.6	Stability studies for NEXAFS Mn L-edge measurements	151
C.7	X-ray photoelectron survey spectra (XPS, $h\nu = 1486.7$ eV) of different Ca-birnessite samples	152
C.8	X-ray photoelectron spectra for the O 1s region for three Ca-birnessite samples	152
C.9	Mn L ₃ -edge reference spectra and difference spectra	153
C.10	The four component fitting results for studied samples	154

C.11	Ca 2p X-ray photoelectron spectra for three different Ca-Birnessite samples	155
C.12	Ca L ₃ -edge NEXAFS (TEY) spectra of the three different Ca-birnessite samples studied by XAS	155
C.13	Mn L ₃ -edge NEXAFS (TEY) spectra of the three different Ca-birnessite samples studied by XAS	156
C.14	Computed Ca L-edges XA spectra and calculated Ca 2p XP spectra	157
C.15	P 2p X-ray photoelectron spectra for Ca-birnessite electrode after electrolysis	158
C.16	Mn 2p X-ray photoelectron spectra for three different Ca-Birnessite samples	158
D.1	Overview TEM images of pressed and printed birnessite electrodes	162
D.2	Relative gas composition in ETEM experiment in H ₂ O and O ₂ . . .	163
D.3	MLLS Fitting of the Mn L-Edge of the pressed electrode in 1 hPa H ₂ O	163
D.4	STEM-EELS, ADF mapping and HRTEM imaging of the printed electrode in O ₂	164
D.5	FFTs of HRTEM images of the birnessite electrodes	166
D.6	Time dependent HRTEM Analysis of the pressed electrode in HV from movie M8	167
D.7	Pressed electrode in 60,000 e ⁻ /(Å ² s) in 1 hPa H ₂ O	168
D.8	HRTEM analysis of the moving bubbles (printed electrode)	168
D.9	Time resolved surface dynamics of the printed electrode 1 hPa H ₂ O	169
D.10	Strong bubble formation and cracking in the printed electrode . . .	169
D.11	All Mn-L EELS spectra of the pressed electrode	170
D.12	All Mn-L EELS spectra of the printed electrode	171
D.13	EELS O-K edge of the pressed electrode	172
D.14	IV curve with linear fit to determine the resistivity of the printed electrode lamella	172
D.15	Comparison of the dynamics' speed / intensity of the pressed electrode	173
D.16	Single frames from movie M3	174

Introduction

Sustainable energy is a cornerstone of tackling the growing energy demand, the depletion of fossil fuel reserves and the increasing effects of global warming. However, renewable energy sources like wind and solar power have the tendency not to be available all of the time. As a result, most systems with a high share of renewable energy generation will undergo significant fluctuations. Presently these fluctuations are compensated by shutting down the renewable power plants in times of overproduction and turning on fossil fuel power stations, mostly natural gas power plants, in times of undersupply. Both cases are not efficient from a commercial as well as an ecological point of view. Instead, it is desirable to find a convenient way to store the renewable surplus energy.

There are solutions like batteries, pumped hydroelectric or compressed air energy storage on hand, but they are primarily usable for short term load leveling and peak shaving and lack the ability to ensure the base load. Fuel cells are an electrochemical system that transfers the chemical energy of a fuel, often hydrogen, to electrical energy, providing longer periods of back-up power.^[1,2] Hydrogen can be produced with renewable electrical energy by splitting water into hydrogen and oxygen^[3], and can be integrated into the consumption cycle as schematically illustrated in Figure 1.1.

Electrical energy is generated from renewable sources with, e.g., solar panels or wind turbines saturating the existing energy demand. Overproduced power is used by electrolyzers to split water into hydrogen and oxygen. The gases are stored and can be transformed back into power via fuel cells in times of undersupply. However, the efficiency of a full electricity-to-fuel and fuel-to-electricity cycle is not much above 30%^[5] and needs to be further improved.

Aside the utilization of hydrogen as energy storage it also has many other uses. In the iron and steel industry, which is the biggest CO₂ emitter within the industry sector^[6], H₂ can be used as a reduction agent in a furnace instead of coke, reducing the CO₂ emission significantly^[7,8]. The chemical industry needs hydrogen to make ammonia for agricultural fertilizers (the Haber-Bosch process)^[9], and hydrogen is also involved in the production of plastics and pharmaceuticals^[10,11]. Although the paradigm change in the German transportation sector relies heavily on electric mobility, hydrogen based drives are still considered, especially for the heavy goods,

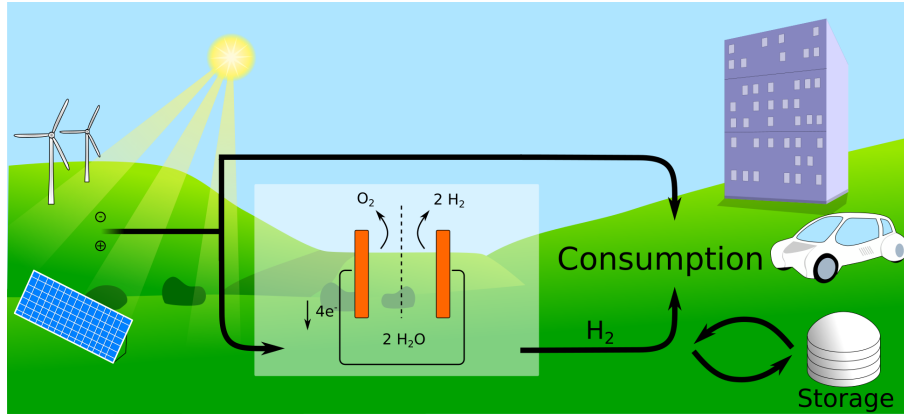


Figure 1.1.: Schematic illustration of a solar hydrogen cycle. Inspired by Ham-bourger et al.^[4].

water and air transport^[12]. The conversion of H_2 and an external source of CO or CO_2 to CH_4 via methanation is another useful application of hydrogen. Methane, which is a substitute for natural gas, can be directly injected into the gas grid and storage, be used in compressed natural gas vehicles or utilized as a raw material in the organic chemistry industry. In addition, also the molecular hydrogen can be added in controlled doses to the gas grid^[13].

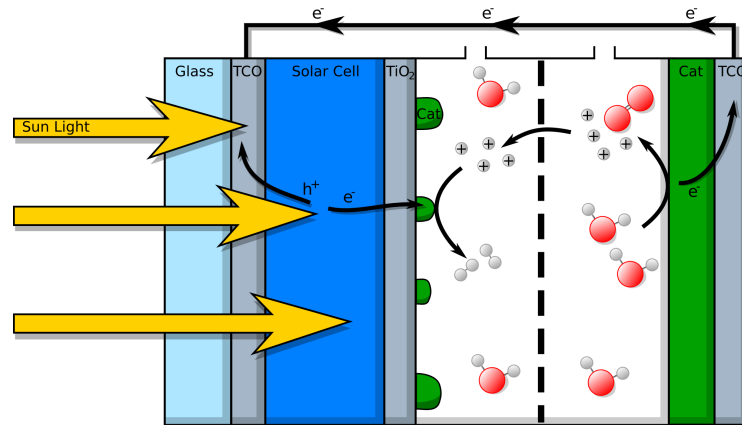


Figure 1.2.: Schematic illustration of an integrated device where a catalyst for the hydrogen evolution is deposited directly onto a solar cell. The anode with catalyst for the oxygen evolution is electrically connected via a cable and is separated with a proton-exchange membrane.

The great range of applications for hydrogen illustrate that the switch to renewable H_2 would reduce the CO_2 emission and enable a reliable sustainable energy supply. However, only about 4% of the hydrogen was produced by electrolysis in the past while the other 96% used fossil fuels as a source^[14]. To meet the demand for renewable hydrogen of the industry and transportation section, a more direct route than illustrated in Figure 1.1 would be desirable. An integrated device, where a

photoabsorber and water splitting catalysts are combined in one device, should be more efficient, due to the reduction of electrical resistance^[15]. The catalyst is directly deposited onto a solar cell reducing the transport distance and number of interfaces significantly. A schematic illustration of such an integrated device is given in Figure 1.2.

Such an integrated device consists essentially of three main components, which are also the focal points of this thesis:

- A** A solar cell with protection layer
- B** The catalyst for the Hydrogen Evolution Reaction (HER)
- C** The catalyst for the Oxygen Evolution Reaction (OER)

For an effective device, the solar cell has to be stable in the electrolyte or be protected with an additional layer. When selecting the materials, costs and environmental concerns, like toxicity and abundance, have also to be taken into consideration.

In the last years a large variety of catalysts have been studied, revealing the high activity of partially disordered chalcogenides for HER and transition metal oxides for OER^[16–23]. Especially for catalysts with a definite active site, e.g. MoS₂, a structural design leading to a higher density of active site is beneficial. The electronic structure can be modulated by defect engineering like amorphization or doping, and nanoscaling can increase the number of active facets^[24,25]. Among the manganese oxides, the partially disordered and often layered oxides are suggested to be particularly well suited for electrochemical water oxidation, where the flexible oxidation states with Mn^{III/IV} play an important role. In addition, beneficial material properties, like high surface areas, which is further enhanced by a porous structure, can often be found together with partially disordered MnO_x^[26].

Therefore, partially disordered materials for the three subsections of the integrated device are utilized in this work. The structural analysis of these materials is challenging due to the local variations and diffraction methods for statistical information about the lattice parameter and orientation of the nanocrystals as well as real space methods to analyze the local variations of the lattice in the nanocrystals are needed. Therefore, the structure is analyzed down to the atomic level by means of electron microscopy. In addition, a new adequate evaluation method for the analysis of dynamics in the TEM in-situ experiments is developed.

The stability of a TiO₂ protection layer on a silicon multi-junction (**A**) is analyzed and a degradation mechanism is suggested, which is published in *Zeitschrift für Physikalische Chemie* (234(6), 1171-1184, 2020)^[27]. To replace the expensive and not-abundant platinum as a HER catalyst (**B**), MoS_{2+δ} electrodes are studied and a structure model is suggested to advance the understanding of possible active sites in this partially disordered system, and to further improve the catalytic activity (*Catalysts*, 10(8):856, 2020)^[28]. And last, for the OER catalyst (**C**), the changes and

dynamics under reactive conditions of the layered calcium manganese oxide Birnesite are analyzed by post-operando (*Preprint on ChemRxiv*, Chemrxiv.13153976.V1, 2020)^[29] and in-situ TEM studies to obtain a better understanding of the stability and the active state of the catalyst (*The Journal of Physical Chemistry C*, 2021 *accepted*)^[30].

Scientific Background

The water splitting reaction at the solid-liquid-gas interface of a solar hydrogen device is given by



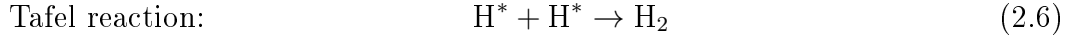
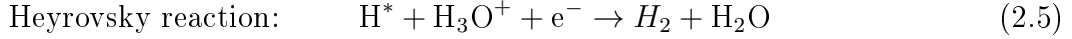
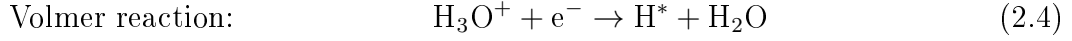
The overall reaction can be divided into two half-cell redox reactions. The hydrogen evolution reaction (HER) takes place at the cathode, while the oxygen evolution reaction (OER) occurs at the anode.^[31] This chapter is composed of several parts, following the structure of an integrated water splitting device. In section 2.1 the HER catalyst MoS_x is discussed while in section 2.2 the OER catalyst Birnessite is introduced. Section 2.3 focuses on the integrated solar hydrogen device design, and in section 2.4 the potential of environmental transmission electron microscopy (ETEM) for studying dynamics of a catalyst under reactive conditions is explored.

2.1. Hydrogen Evolution by MoS_x

Among the water splitting reactions, the HER is relatively simple due to the involvement of only a two-electron transfer compared to the four electrons in the OER:



Generally, the HER in an acidic medium can be described by the following steps. First, an adsorption of the hydrogen intermediate (H*) in the Volmer step, which is followed by a reductive desorption in the Heyrovsky reaction or a H* recombination in the Tafel reaction.^[32]



In alkaline electrolyte, the additional water dissociation to provide protons for the reaction leads to a decrease of the reaction rate compared to acidic solutions.^[32]

Platinum is already known to be a highly active catalyst, which is currently one of, or even, the best catalyst for the hydrogen evolution. In both acid and alkaline conditions, Platinum electrodes show very low overpotentials with high current densities compared to other catalysts (see Table 2.1).^[33] Note that the current densities are normalized to geometric area of the electrode. Thus, the low overpotentials of Molybdenum based catalysts like Ni-Mo are the result of the high electrochemical surface area (ECSA) and not of the higher activity compared to Platinum.

	η at 10 mAcm ⁻² [mV]		RF	Electrolyte
	Acid	Base		
Pt (platinized) ^[33]	-60 ± 10	-60 ± 20	110	1 M H ₂ SO ₄ / 1 M NaOH
Co-Mo ^[33]	-100 ± 10	-100 ± 20	900	1 M H ₂ SO ₄ / 1 M NaOH
Ni-Mo ^[33]	-39 ± 3	-30 ± 10	1000	1 M H ₂ SO ₄ / 1 M NaOH
Ni-Mo-Co ^[33]	-50 ± 10	-90 ± 40	1050	1 M H ₂ SO ₄ / 1 M NaOH
MoS ₂ (step-edged stacks) ^[34]	-104	n/a	2833	0.5 M H ₂ SO ₄
[Mo ₃ S ₁₃] ²⁻ ^[35]	-178	n/a	n/a	0.5 M H ₂ SO ₄
[Mo ₂ S ₁₂] ²⁻ ^[35]	-161	n/a	n/a	0.5 M H ₂ SO ₄
MoS _x ^[33]	-250 ± 30	-480 ± 10	18	1 M H ₂ SO ₄ / 1 M NaOH
MoS _x ^[23]	-160	n/a	n/a	1 M H ₂ SO ₄

Table 2.1.: Benchmarking for selected HER catalysts with the overpotential η at current density of 10 mAcm⁻². The roughness factor (RF) is the ratio of electrochemical surface area (ECSA) determined by the double layer capacitance and the geometric electrode area. Adapted from Mccrory et al.^[33], Hu et al.^[34], Huang et al.^[35] and Morales et al.^[23]. The current densities are normalized to geometric area.

However, the high cost for Platinum of about 25 €/g and also the low abundance of about 0.6 ppb militate against a large scale application^[36]. Thus, other cheaper and more abundant materials are needed. Table 2.2 gives an overview over cost and abundance of the elements for alternative catalysts, which are presented in Table 2.1.

The combination of low cost, high abundance and good catalytic performance makes the Mo based catalysts and especially the Ni-Mo(-Co) catalysts a good al-

ternative to platinum. However, the significant lower cost of Sulfur also promotes the Molybdenum sulfides and several MoS_x catalysts have been studied^[37–40]. Especially the partially disordered MoS_x yield good stability and a low overpotential of -160 mV at 10 mAcm^{-2} ^[23]. The partially disordered MoS_x typically have an S:Mo ratio larger than 2. Several Molybdenum sulfides structures relevant for the HER are discussed in the literature and will be presented in the next section. Knowing the atomic structure of MoS_x is important for a determination of the active sites and further improvement of the catalytic activity.

		Pt	Co	Ni	Mo	S
Cost ¹	€/g	25.08	0.028	0.013	0.014	$4.3 \cdot 10^{-5}$
Abundance ^[36,41]	ppm	$6 \cdot 10^{-4}$	25	75	1.5	260

Table 2.2.: Abundance in the earth crust and cost of elements for active HER catalysts.

2.1.1. HER-Relevant Crystal Structures of MoS_x

Three common polytypes of crystalline Molybdenum disulfide MoS₂ exist, which are shown in Figure 2.1. All of them consist of layered hexagonally packed Molybdenum (Mo⁴⁺) sheets, which are sandwiched between two layers of Sulfur (S²⁻). The van der Waals bound between the layers of MoS₂ leads to a relative large interlayer distance of about 3.49 Å. The 2H and 3R polytypes only differ in the stacking order, while the 1T type consists of Molybdenum Sulfur octahedrons. Neither the 1T nor 3R are thermodynamically stable and convert into the 2H type at about 100 °C.^[22] If not stated differently, MoS₂ will be used for the 2H polytype from here on.

The structure model from Dickinson et al.^[44] and crystal parameters from Wildevanck et al.^[47] for MoS₂ 2H which are used throughout this work are given in Table 2.3.

	space group	a=b ^[47]	c ^[47]	atom position ^[44,48]								
		Å	Å	Mo			S					
MoS ₂ 2H (hexagonal)	P63/mmc	3.1602	12.294	1/3	2/3	1/4	1/3	2/3	0.629	2/3	1/3	0.129
				2/3	1/3	3/4	2/3	1/3	0.371	1/3	2/3	0.871

Table 2.3.: Crystal structure parameters for MoS₂ 2H. The lattice parameter from Wildevanck et al.^[47] and the structure model from Dickinson et al.^[44] is used.²

Next to crystalline MoS₂ there are also molecular Molybdenum sulfides structures which are interesting for HER. Two typical cluster structures $[Mo_2^V S_{12}]^{2-}$ ($= \{Mo_2\}$)

¹<http://www.lme.com> [2020-08-28], <https://www.statista.com/> [2020-09-24]

²Note that Dickinson et al.^[44] give erroneously a wrong value for the z coordinate as stated by Bronsema et al.^[48]. Here, the correct value from Bronsema et al.^[48] is used.

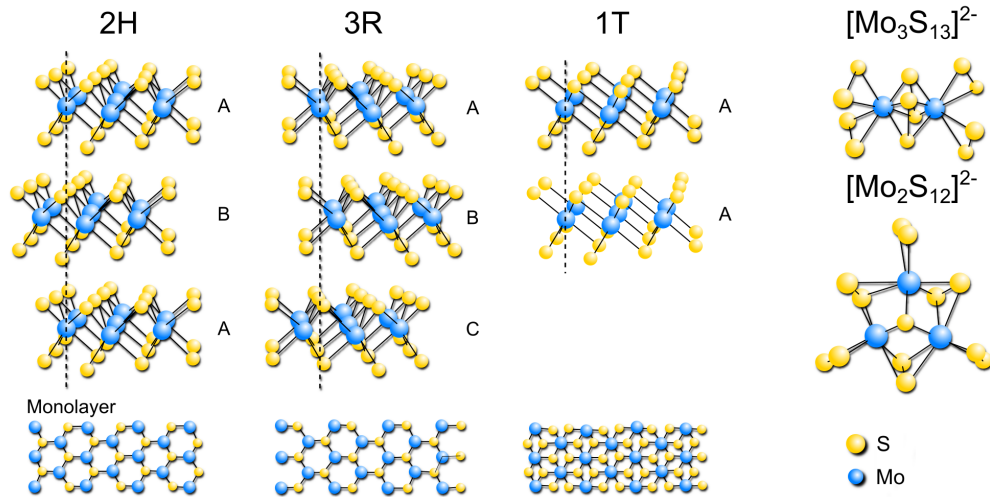


Figure 2.1.: Crystal structure of the common MoS_2 polytypes 2H, 3R, 1T and molecular structures of $[\text{Mo}_2\text{S}_{12}]^{2-}$ and $[\text{Mo}_3\text{S}_{13}]^{2-}$. Crystal structures adapted from Grutza et al.^[22], Takeuchi et al.^[42], Dungey et al.^[43], Dickinson et al.^[44] and Müller et al.^[45,46].

and $[\text{Mo}_3^{\text{IV}}\text{S}_{13}]^{2-}$ ($= \{\text{Mo}_3\}$) are shown in Figure 2.1. $\{\text{Mo}_2\}$ consists of two Mo^{V} ions which are connected via two bridging disulfide ligands. Two terminal disulfides are additionally bonded to each Mo center. The Mo-Mo distance is 2.8 Å.^[22,46] For the $\{\text{Mo}_3\}$, three Mo^{IV} are linked with one bridging disulfide. In the center an apical bridging sulfido ligand ($\eta_3 - \text{S}^{2-}$) is situated. One terminal disulfide is attached to each Mo ion. The Mo-Mo distance here is about 2.722 Å.^[45]

The determination of a structure model for MoS_x is challenging due to a large degree of disorder and diverging preparation methods and Mo:S ratios. In some cases a crystallization of amorphous MoS_x to MoS_2 nanoparticles during HER is reported^[49,50], indicating a structural affinity to MoS_2 . Also nanocrystalline MoS_2 is used for HER^[34,51]. However, for MoS_x with $x > 2$ two different structure models have been suggested. The two model suggestions are based on the molecular clusters and are depicted in Figure 2.2.

In Figure 2.2 **[A]** the cluster based model suggests a network of $\{\text{Mo}_3\}$. The clusters are connected via Mo-S-Mo bonds and the whole structure can be described by $\text{Mo}^{\text{IV}}(\text{S}^{2-})(\text{S}_2^{2-})$. This material has an S:Mo ratio of about 3.1 to 3.2. Extrusion experiments of amorphous $\text{MoS}_{3+\delta}$ indicate that only about 35% of the material exists as $\{\text{Mo}_3\}$.^[22,52] Consequently, in this material also other Mo-S building blocks, which are not included in this model, play an important role. Above 310 °C a decomposition into MoS_2 via reductive elimination of S^{2-} and terminal S_2^{2-} takes place.^[52]

The other cluster based model suggests a polymer like structure as illustrated in Figure 2.2 **[B]**. The chains consist of distorted $[\text{Mo}_2\text{S}_9]$ units. Some covalent Mo-Mo

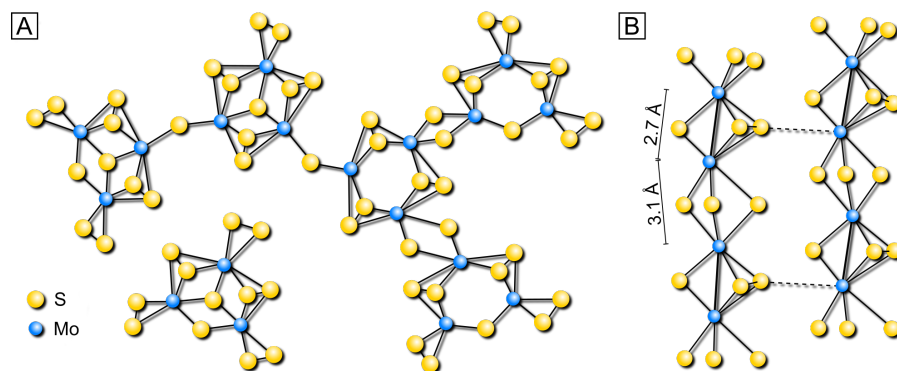


Figure 2.2.: Suggested cluster based structure models for MoS_x. **[A]** : based on $[Mo_3^{IV}S_{13}]^{2-}$ adapted from Weber et al.^[52] and Tran et al.^[53]. **[B]** : based on $[Mo_2^V S_{12}]^{2-}$ adapted from Hunt et al.^[54] and Grutza et al.^[22].

bonds in the chains with a distance of about 2.7 Å exist, but about every second Molybdenum atom is not covalently bonded and has a Mo-Mo distance of 3.1 Å. In addition, some disulfides are also present.^[22,54] Another polymer model is supported by STEM analysis of Tran et al.^[53] and consists of $[Mo_3S_{13}]^{2-}$ building blocks linked by disulfide bonds, similar to the model depicted in Figure 2.2 **[A]**.

2.1.2. Electrochemical Performance of MoS_x

It is well established that the catalytic activity of crystalline MoS₂ 2H is limited to about 5 mAcm⁻² at an overpotential of about -500 mV.^[49] The reason for that is the nature of the active sites which are located at edges of the two-dimensional MoS₂ planes^[55-57]. For the 1T polymorph, also the basal surface might be active leading to a higher HER activity^[57,58]. However, as mentioned before, this system is not stable and thus not suited as a catalyst.

Due to the specific active site of MoS₂, the current densities heavily depend on the morphology of the electrode. As reported by Hu et al.^[34], nanocrystalline step-edged stacks of MoS₂ can actually reach a current density of 10 mAcm⁻² at an overpotential of -104 mV.

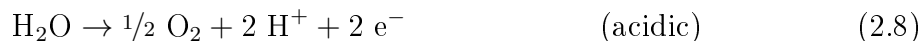
As mentioned before, the structure models for MoS_x are often based on molecular clusters^[22]. The $[Mo_3S_{13}]^{2-}$ cluster exhibits good catalytic HER performance^[35,59] with a current density of 10 mAcm⁻² at an overpotential of about -178 mV^[35]. However, the $\{Mo_3\}$ cluster is even outperformed by $[Mo_2^V S_{12}]^{2-}$ with an overpotential of -161 mV for the same current density^[35].

X-ray photoemission spectroscopy (XPS) studies indicate the presence of unsaturated, terminal, bridging and maybe even apical sulfides and disulfides in partially disordered MoS_x.^[23,39,40,60,61] Together with XPS results, the high activity of the cluster suggests an involvement of units like $\{Mo_2\}$ or $\{Mo_3\}$ in the structure of MoS_x. However, precise high-resolution real space structural information is of significant

importance for the identification of the active site(s) and a better understanding of the high HER activity of partially disordered MoS_x.

2.2. Oxygen Evolution by Birnessite

The oxygen evolution reaction is the bottleneck for water splitting due to the high energy barriers for the mechanistically complicated four-electron process^[62]. At least a potential of 1.23 V vs RHE is thermodynamically needed to drive the reaction.



In Table 2.4 an overview on the top performing OER catalysts in alkaline conditions is given. None of the presented non-noble metal catalysts are stable in 1 M H_2SO_4 ^[33]. This is in accordance with the general thermodynamic instability of many transition metal oxides under strong acid OER conditions as indicated by Pourbaix diagrams^[63,64].

However, in alkaline conditions the presented catalysts in Table 2.4 achieving current densities of 10 mAcm^{-2} at roughly the same overpotentials of $\eta = 252\text{--}380 \text{ mV}$.

	η at 10 mAcm^{-2} mV	RF	Electrolyte
Ru ^[33]	320 ± 20	70	1 M NaOH
Ni-Co ^[33]	350 ± 10	9	1 M NaOH
Co/P ^[33]	380 ± 20	17	1 M NaOH
NiMoFe ^[33]	330 ± 20	9	1 M NaOH
NiOOH-decorated α -FeOOH nanosheet ^[65]	256	56*	1 M KOH
Fe-Co-P ^[66]	252	208**	1 M KOH
δ -MnO ₂ /K _{0.1} MnO _x (Birnessite) ^[67]	330	n/a	1 M KPi-buffer

*For the calculation of RF a specific capacitance of 0.04 mF/cm^2 is used.^[68]

**RF is calculated from the specific surface area $104.1 \text{ m}^2/\text{g}$ determined by BET.

Table 2.4.: Benchmarking for selected OER catalysts with the overpotential η at current density of 10 mAcm^{-2} in alkaline conditions. The roughness factor (RF) is the ratio of the electrochemical surface area (ECSA) determined by the double layer capacitance and the geometric electrode area. Adapted from Mccrory et al.^[33], Zhang et al.^[65], Liu et al.^[66] and Melder et al.^[67]. The current densities are normalized to geometric area.

The reported capability of some of the Mn, Co and Ni based catalysts for self-healing in a phosphate or borate buffer is noteworthy^[21,69,70]. This was first observed for the CoPi catalyst^[21,71,72]. The corrosion of these catalysts due to leaching of metal ions and dissolution of the oxide is overcome to a large degree by constantly self-assembling a new catalyst layer on the electrode at applied potentials less than needed for OER.^[72]

Concerning the abundance and cost, which are presented in Table 2.5, the manganese based catalysts stand out, which makes MnO_x a promising OER catalyst candidate for large scale applications.

		Ir	Ru	Co	Ni	Mn
Cost ³	€/g	49.3	8.25	0.028	0.013	$1.3 \cdot 10^{-6}$
Abundance ^[36,41]	ppm	$2.2 \cdot 10^{-5}$	$3.00 \cdot 10^{-5}$	25	75	950

Table 2.5.: Abundance in the earth crust and cost of elements for active OER catalysts from Table 2.4.

Inspired by the CaMn_4O_5 cluster in the oxygen-evolving complex in the photosystem II and the high abundance of manganese, a research focus was placed on the manganese oxides (MnO_x).^[73-79] A large number of MnO_x structures with varying composition and ordering are known. A selected overview of common manganese oxides is given in Figure 2.3.

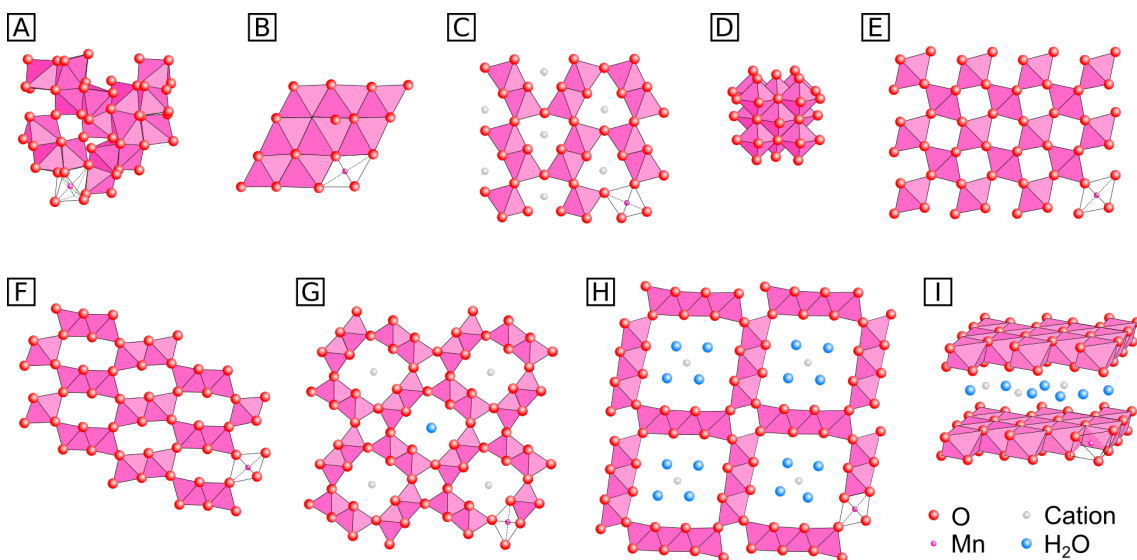


Figure 2.3.: Structures of different manganese oxides. **A** : Bixbyite; **B** : spinel-type Hausmannite (Mn_3O_4); **C** : Marokite (CaMn_2O_4); **D** : Manganosite (MnO). Tunneled structures: **E** : Pyrolusite, (MnO_2); **F** : Ramsdellite; **G** : Hollandite-group; **H** : Todorokite. Layered structure: **I** : Birnessite. Structures adapted from Frey et al.^[80], Lopano et al.^[81] and Smyth & Bish^[82].

All structures are based on $[\text{MnO}_6]$ octahedral blocks and can be categorized into three different groups^[80]:

Group 1 A crystalline 3D network of $\text{Mn}^{2+/3+/4+}$ and O^{2-} ions. Figure 2.3 **A** -**D** : e.g. Bixbyite, Hausmannite, Marokite and Manganosite.

³pmm.umicore.com [2020-09-02], lme.com [2020-08-28] and price.metal.com [2020-09-02]

Group 2 Tunnels formed by $[\text{MnO}_6]$ octahedrons. Depending on the tunnel size, ions and/or waters of crystallization are incorporated within the tunnels. The typical Mn oxidation state is between 3+ and 4+. Figure 2.3 **E** -**H** : e.g. Pyrolusite, Ramsdellite, Hollandite, Cryptomelane and Todorokite.

Group 3 Layered oxides with interlayer distances of 7–10 Å and a typical manganese valence of +3.5 to +4. Similar to the second group, waters of crystallization and cations are intercalated in between the layers. Figure 2.3 **I** : e.g. Birnessite and Vernadite.

Especially for the layered MnO_x (Birnessite), good stability ($>24\text{ h}$ ^[67]) and OER rates have been found^[17,80,83–85]. The different catalytic behavior of the groups suggests an influence of the crystal structure and five structural related factors have been proposed to improve the catalytic activity^[80]:

- 1) A flexible structure to allow substrate binding and valence changes
- 2) A high surface area for good accessibility of the catalytic centers
- 3) An average Mn valence greater than +3.5 to drive OER
- 4) The presence of secondary cations to assist oxidation by activation of H_2O
- 5) A good conductivity to support the four electron process

These points are not in a specific order and some may affect each other. But they demonstrate the importance of the structural analysis to understand the catalytic activity of the MnO_x catalyst. For the following research Birnessite was selected due to its high activity and stability among the MnO_x family.

2.2.1. Crystal Structure of Birnessite

Birnessite, also known as $\delta\text{-MnO}_2$, consists of layered MnO_6 octahedrons with an interlayer distance of about 7 Å. Cations and waters of crystallization are intercalated in between these layers. Above 500°C the crystal water is completely removed from the oxide structure and between 800°C and 1000°C Birnessite decomposes into a mixture of Marokite (CaMn_2O_4) and Hausmannite (Mn_3O_4).^[17] A schematic illustration of the ordered crystalline structure is shown in Figure 2.4.

Birnessite typically consists of a mixture of Mn^{III} and Mn^{IV} with an average valency between +3.3 and +4.0^[17,18,84,86]. Also, the presence of a small amount of Mn^{II} , probably bonded to the MnO_6 layer, is proposed^[84]. It is suggested that the cation charges are balanced by Mn^{III} and/or Mn vacancies in the Mn octahedral layer^[87]. The resistivity of Birnessite⁴ of $5.2 \cdot 10^5 \text{ } \Omega\text{cm}$ is relatively high and has to be

⁴Measured for a K-Birnessite.

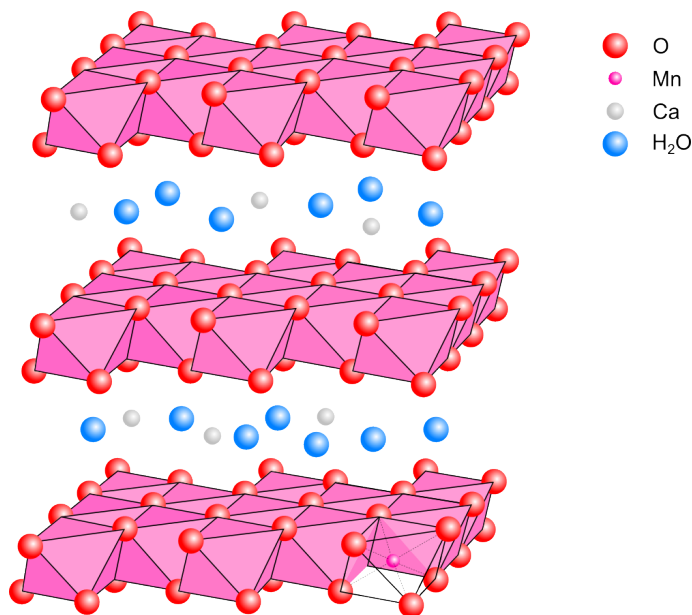


Figure 2.4.: Illustration of the ordered crystal structure of Birnessite. The structure model from Lopano et al.^[81] is used.

taken into account regarding the layer thickness when preparing the electrodes^[88]. Preparation parameters like the temperature or the Ca:Mn ratio influence the crystal structure, since a higher temperature and a low Ca:Mn ratio result in a higher order. However, a high degree of order leads to a reduced catalytic activity^[17]. As a result, typical Birnessite electrodes are partially disordered, as indicated by the absence of strong long range order features in the extended X-ray absorption fine structure (EXAFS) and very weak and broad, or even absent, reflections in X-ray diffraction (XRD)^[84,86,89].

2.2.2. Electrochemical Performance of Birnessite

The catalytic rate of Birnessite is influenced by the cation species and concentration. The highest rates are typically achieved with Ca^{2+} cations with a Ca:Mn ratio of ≈ 0.21 ^[17,84]. However, recently Melder et al.^[67] also achieved a good activity with Na-Birnessites, where 10 mAcm^{-2} were reached at an overpotential of 330 mV. In this case the Na-Birnessite was deposited by a redox reaction of potassium permanganate and carbon on graphitized carbon fiber paper^[67]. In addition, Birnessite displays good stability under OER conditions^[67,83,89], which is also suggested by the Pourbaix diagram of MnO_x where Birnessite is the only stable structure under OER condition from pH 2 to 14 amongst the compared structures^{5 [90]}.

Some studies indicated an activity not only at the outer surface of the electrode, but also within the mesoporous material. However, this volume effect has a limiting

⁵ MnO_2 , Mn_2O_3 , Mn_3O_4 and $\text{Mn}(\text{OH})_2$ were considered.

thickness, probably due to the low electric conductivity of Birnessite.^[67,89]

In alkaline conditions, the OER catalyst typically operates at potentials of about 300 mV and 10 mA cm^{-2} (see Table 2.4), potentially suggesting a common mechanistic limitation^[33,68]. For the oxide based OER catalysts, a mechanism is typically proposed which includes a surface hydroxide OH^* intermediate formation and a further oxidation to OOH^* ^[91-94]. DFT calculations indicate no significant difference in binding energies for OOH^* and OH^* at the surface regardless of the metal oxide, due to thermodynamics suggesting a minimum “thermodynamic overpotential” at planar metal-oxide surfaces^[33,68,94].

2.3. Integrated Water Splitting Device Design

Renewable generation of hydrogen requires the implementation of the HER and OER catalysts discussed in the previous sections as well as an energy source. In photo-electrochemical devices for water splitting, the energy is provided by a photoabsorber, and in an integrated device, the catalysts are directly deposited on the photoabsorber. These devices are developed with the objective to gain higher efficiencies than modular photovoltaic and electrolysis systems^[15], thanks to reduced systems costs and contact losses. Due to the overpotentials of OER and HER, the photoabsorber needs to provide a voltage of 1.6–2.4 V^[15]. However, most of the interesting absorber materials are not electrochemically stable in aqueous electrolytes^[95]. Thus, an electrically conducting anticorrosion layer covering the semiconductor absorber is generally required^[96]. In principal, a closed and stable catalyst layer could also fulfill this task. However, this makes the catalyst choice difficult and might also reduce the achievable efficiency. Thus, a separate protection layer will be used in this work and the additional interface has to be a trade-off. The stability of the integrated device typically improves with increasing layer thickness. However, the series resistance rises, too, and thus the photoelectric current density drops. Consequently, ultra-thin conducting protecting layers are highly desirable but require a perfect layer deposition and a fundamental understanding of the defects and their role in corrosion.

In this work multi-junction silicon solar cells are utilized due to their abundance, high conversion efficiencies and capability to provide enough potential for water splitting. In addition, a TiO₂ protection layer is used which is well established for water splitting devices in various thicknesses^[97–104]. TiO₂ is stable for >500 h in alkaline conditions^[98], it possesses a relatively good electric conductivity and the growth of ultra-thin layers by atomic layer deposition (ALD) is well established^[98,99,105].

Efficiency and Device Design

The solar-to-hydrogen efficiency (STH) is the ratio of the energy which is put into the system in form of the total incident solar irradiance S and the stored energy of the water splitting reaction ($\Delta E=1.23$ V):^[106]

$$STH(\%) = J \cdot \Delta E / S \cdot 100\%. \quad (2.9)$$

J is the current density at the photoelectrode. The STH efficiency can also be expressed as a product of the efficiency of the solar conversion of the photovoltaic (PV) cell $\varphi(PV)$ and the water splitting efficiency $\varphi(WS)$:

$$STH(\%) = \varphi(PV) \cdot \varphi(WS). \quad (2.10)$$

This distinction is helpful to determine which part of the device is the bottle-

neck for overall efficiency. In principal, there are three different ways to design an integrated device which are illustrated in Figure 2.5.

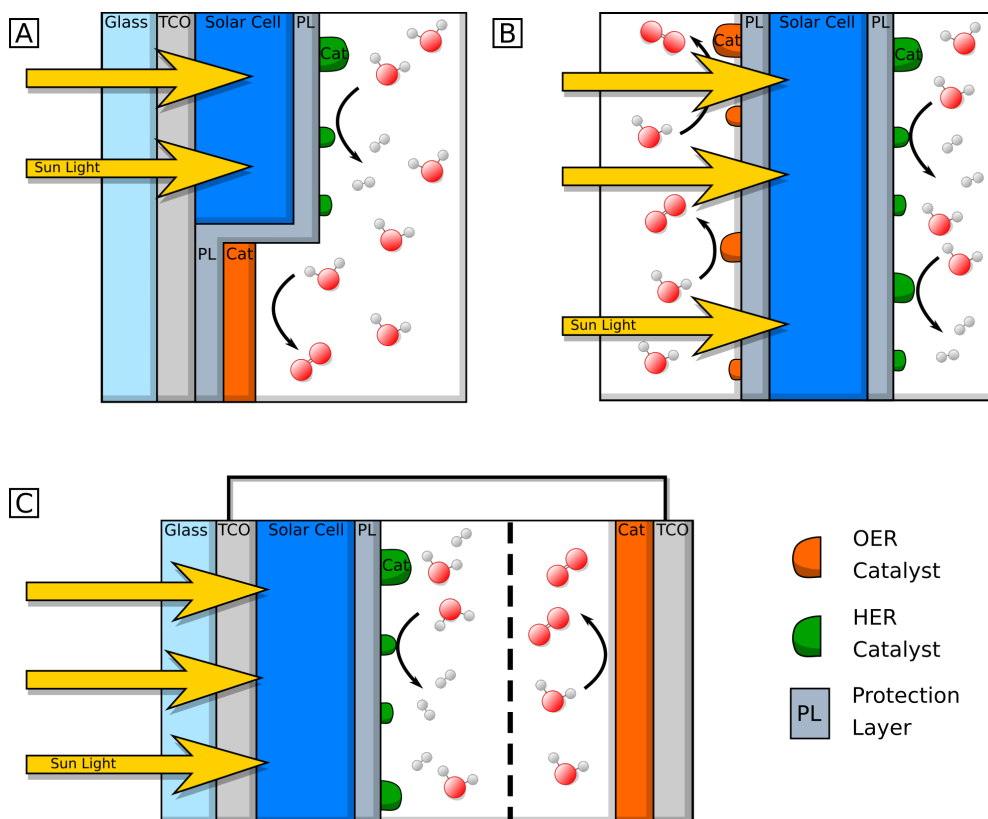


Figure 2.5.: Schematic illustration of different integrated device designs.

Design **A** consists of two separated stacks on a transparent conduction oxide (TCO) substrate. One stack consists of a solar cell with a protection layer where the HER catalyst is directly deposited on top. The other stack is the OER catalyst. Depending on the preparation method of the device, the protection layer is also in between the OER catalyst and the TCO. This device is illuminated through the glass substrate and TCO. The TCO acts as the electric contact between the solar cell and the OER catalyst. Only the backside of the device is immersed into the electrolyte.^[107] The downside of this design is the inefficient use of area since the OER and HER catalyst are directly next to each other. Another problem is the separation of the reaction products (O_2 & H_2). Due to the design, an implementation of the H_2/O_2 separation membrane is impractical so that a subsequent separation is necessary. With a AlGaAs/Si solar cell and a RuO_2 and Pt catalyst, a STH efficiency⁶ of 18.3% has been achieved^[107].

To overcome the insufficient area usage, in design **B** the solar cell is covered with a protection layer on both sides, and the OER and HER catalyst are deposited separately on different sides. The whole device is then immersed into and illuminated

⁶Note that the geometric electrolysis area is larger than the illuminated area by a factor 5

through the electrolyte.^[106,108,109] Here a separation of the reaction products can be realized with a membrane. But there is a trade-off between the efficiency $\varphi(WS)$ of the catalysts and the efficiency $\varphi(PV)$ of the solar cell. On the one hand, a higher coverage of the catalyst increases the product yield, but on the other hand, it increases the shadowing of the solar cell and thus reduces the charge carrier separation. In addition, a much a higher surface area is exposed to the electrolyte which increases the risk of degradation. Also, a lower water splitting efficiency $\varphi(WS)$ is expected for this configuration since protons that are generated at the front side have to move around the device to the backside where they are reduced to H_2 . The long distance for ion transport induces ohmic losses which result in a lower $\varphi(WS)$.^[106] In addition, the solar irradiance is reduced by the electrolyte which cuts down on $\varphi(PV)$.

Design **C** simplifies the idea of **B** by removing the OER catalyst from the front. The OER catalyst can operate in the dark, electrically connected by wiring. As a result, only one side of the solar cell is in contact with the electrolyte, here a protection layer and the HER catalyst are deposited. In this way, the semiconductor is cathodically protected.^[110] This decreases the risk of degradation, maximizes the illuminated area and prevents shadowing which results in high PV efficiency $\varphi(PV)$. However, the device is not fully integrated since the OER catalyst is connected via wires. With the implementation of a membrane, similar to design **B**, the separation of O_2 and H_2 can be realized. The ion transport can be improved by reducing the anode-cathode distance, which will improve the water splitting efficiency $\varphi(WS)$. A triple junction of amorphous Si with a Cobalt OER catalyst and NiMoZn for HER can reach a STH efficiency of 4.7% (design **C**)^[106]. With the same materials but the configuration of design **B**, an STH efficiency of only 2.5% is reported^[106], indicating the mentioned flaws in design **B**. Here an operation in 0.1 M KOH was not possible due to degradation within less than 2h. With a GaAs photocathode and a Pt catalyst (design **C**) an STH efficiency of 17% was reported by Kang et al.^[111] However, without a protection layer, this device is not stable and with the implementation of a protection layer the efficiency decreases to 12.7%. In a tandem setup of two devices, with one for OER and one for HER, similar to design **A**, an efficiency of 13.1% can be achieved.^[111]

Motivated by the promising results, design **C** was selected to be used in this work. However, regardless of the device design, a stable and electronic conducting protection layer for the solar cell is needed and the corrosion pathways have to be carefully analyzed.

2.4. In-situ Electron Microscopy

During catalysis the structure of the catalyst can change in complex ways. For the investigation of the correlation of structure and catalytic performance, structural information on the atomic- or nanoscale under reaction conditions is needed. Environmental transmission electron microscopy (ETEM) is, next to electrochemical scanning tunneling microscopy (EC STM), one of the few methods with high real space spatial resolution which can analyze the catalyst surfaces in-situ^[112]. In general, a TEM needs a high vacuum throughout the microscope to avoid interactions of the beam with gas molecules, to avoid contamination of the specimen and to protect the electron gun^[113]. Consequently, the gas system in an ETEM must provide a high pressure in the sample region while maintaining a high vacuum in the rest of the TEM. This can be achieved by differential pumping or the application of thin transparent windows^[112].

Window Method

The so-called window method uses a thin electron transparent membrane (e.g. Si_3N_4 or graphene) as a window to separate the high pressure area around the sample from the high vacuum in the rest of the microscope. Typically, the membranes are used in sample holders which also contain a gas inlet and outlet. With this technique pressures up to 4 bar are possible. A thin electron transparent window ($\approx 18 \text{ nm}$ ^[114]) within the membrane allows a reasonable resolution of 0.18 nm at 1 bar^[112,115]. In principal, electrolytes instead of gases can be used, however, this increases the bulging of the membranes, which decreases the resolution due to enlargement of the electrolyte thickness. In addition, non laminar flow and disturbances due to bubble formation can occur between the two membranes.

The advantages of the window method are the high pressures and the use of electrolytes. Due to the high pressures the conditions in the TEM can be quite similar to ex-situ studies. However, the window method comes with the downside of less spatial resolution and challenges with EELS and EDX. Remarkably, the small reaction chamber enables the detection of reaction products with a residual gas analyzer (RGA). For example, Vendelbo et al.^[114] investigated the CO oxidation of Pt nanoparticles and were able to detect anti-cyclic oscillations of the reactant and product gases with the RGA. These oscillations could then be correlated with structural changes of the nanoparticles^[114].

Differential Pumping

Alternative to the membrane a differential pumping system can be used to maintain a pressure of environmental gases around the sample and a high vacuum in the rest of the TEM. This is achieved by differential pump apertures and additional pumps along the TEM column. The first pair of apertures is placed close to the sample

within the objective lens pole pieces. A turbo molecular pump is pumping out most of the leaking gas. This system is repeated several times along the column.^[116]

The main advantages of the differential pumping is the maintenance of high resolution as well as possible use of analytical TEM since the electron beam is not influenced by a membrane. However, with higher gas pressures the resolution will also decrease due to scattering at gas molecules. Another benefit is the possibility to use a wide range of specialized specimen holders for in-situ experiments with, e.g., scanning tunneling microscope (STM) tips, heating/cooling, mechanical stress, electrical and optical measurements. However, the pressure is limited depending on the gas type to about 10 to 20 mbar due to the differential pumping.^[112] In addition, the RGA employment is challenging due to the significantly larger volume compared to the surface area of the lamella. Measuring the catalytic products from a TEM lamella is highly challenging. However, the fabrication of pellets which fit into the TEM stage enables the detection with the RGA.^[117]

Visualizing Dynamics at the Catalyst Surface with Transmission Electron Microscopy

Aberration-corrected in-situ environmental transmission electron microscopy has reached a level where it provides atomic resolution real space information about the surface under ambient conditions^[118–120]. In addition, an electron beam induced or applied electric potential allows for in-situ studies of the surface in OER like conditions^[78,121]. In the following sections, the capability of visualizing dynamics on the catalyst surface with TEM is displayed on the basis of the work of Lole et al.^[122] and Yuan et al.^[123].

Visualizing absorbed molecules on the surface in the ETEM is a great challenge due to a lack of sufficient contrast. Yuan et al.^[123] solved this problem by using the highly ordered active row of protrusions of TiO₂. The ordered protrusions are a (1x4) reconstruction at the (001) surface and are formed in-situ in the ETEM at 700°C and 10⁻³ mbar O₂. When introducing 1 mbar H₂O in the TEM twin protrusions become visible, indicating absorbed water species. The absorption is analyzed with fourier-transform infrared spectroscopy (FTIR). And with the help of density-functional theory (DFT), the features in the spectra can be assigned to a symmetric protrusion with each a OH-H₂O group.

TiO₂ is catalyzing the H₂O + CO → H₂+CO₂ reaction at elevated temperatures, which is studied in a 5 mbar 1:1 mixture of H₂O and CO with the ETEM. Here the twin protrusion becomes unstable which is visible by contrast changes. DFT suggests a reaction pathway where adsorbed H₂O species are consumed and then replenished from the water vapor. The dissociation of the H₂O molecule which forms the twin or single protrusion has the largest energy barrier, indicating a relative stable structure. Hence, the blurring of contrast could be an interference of the two structures which occasionally clears when one structure is the majority of the protrusion row.

With these experiments Yuan et al.^[123] could show that the ETEM can visualize reacting H₂O molecules and hence be used to study catalytic processes at highly ordered surfaces.

While Yuan et al.^[123] visualized adsorbed and reacting molecules on an ordered surface, Lole et al.^[122] focused on the dynamics of Mn adatoms on the top of the OER catalysts La_{0.6}Sr_{0.4}MnO₃ (LSMO) and Pr_{0.33}Ca_{0.67}MnO₃ (PCMO).

LSMO yields a stable current density of 1.03 mA/cm² at 1.75 V vers. RHE, and, in the presence of water vapor, a hopping of Mn adatoms can be visualized by ETEM. The detection limit of Mn adatoms is determined to triple or higher occupancy of the column by comparing the experimental signal to noise ratio of a 4.2 nm thick lamella to image simulations. The dynamic adatom contrast mainly appears at interstitial surface positions with a minimal hopping rate of $\geq 4\text{s}^{-1}$. The determination of the hopping rate is limited by the frame rate. A surface step can affect the dynamics due to an Erich-Schwöbel barrier which is visible by the increased Mn adatom contrast in the vicinity of atomic step edge at the surface. This is also represented by the reduced hopping rate of 0.7s^{-1} . The dynamic hopping of Mn adatoms is unique for H₂O since in O₂ and HV the hopping rate is significantly reduced to 0.25s^{-1} (HV) and 0.2s^{-1} (O₂). In addition, the Mn valence is quite stable as well as the stoichiometry.

In comparison to LSMO, PCMO shows a redox couple in rotating ring disk electrode (RRDE) cyclic voltammetry (CV) which is related to the reversible formation and annihilation of oxygen vacancies. In addition, post-mortem analysis reveals an increase in surface roughness and a depletion of Mn in the first 2–3 nm of the surface. In accordance with the prior results, PCMO displays irreversible Mn adatom dynamics in the ETEM experiments in the presence of H₂O. The detection of the hopping rate $r \geq 4\text{s}^{-1}$ is again limited by the frame rate. After a full ordering/recrystallization of the surface in O₂, highly mobile and disordered Mn adatoms are visible on the surface in H₂O, while no movement of the Pr/Ca is observed. In addition, an increase in contrast dynamics of Mn at the subsurface is detectable. After about 11 min the effect of Mn leaching becomes visible by the newly formed 3–4 monolayer thick Pr rich surface layer. HRTEM and post mortem EELS analysis reveal a cubic PrO_x ($x \approx 2$) structure and, thus, a Mn depletion which is accompanied by a Mn oxidation state reduction.

According to literature^[124–126] 2–4 monolayers of adsorbed H₂O can be expected on the catalysts surface in the pressure range of 0.01–5 Pa. Together with the appearance of the surface dynamics solely in H₂O this indicates a correlation with the adsorbed water layer. Beam induced hopping of the Mn adatoms can be ruled out by comparing the experimental hopping rates with calculated rates for beam induced hopping. Instead, the reduction of the effective surface barrier in the presence of H₂O due to a partially solvation of Mn is more likely to be the reason for the increased dynamics.

The same trends in the ETEM experiments and electrolysis are remarkable and suggest that maintaining a high Mn oxidation state of the surface is essential for preventing irreversible dynamics. The different behavior of LSMO and PCMO can

be explained by the different covalence and charge localization. The formation of delocalized large polarons in LSMO prevents a change in the Mn oxidation state at the surface, while in PCMO the localized *Zener Polaron* leads to the formation of an O^- species. At anodic potentials this can lead to a oxygen vacancy formation and, thus, a reduction of Mn. The reaction can be irreversible due to the higher solubility and leaching of Mn^{2+} .

The consequences of the dynamics could be a modification of the adsorption energies, coordination and electric properties of the active site. A more flexible coordination of Mn with OH_2 and OH, compared to a static surface and hence new configurations of O-O formation, is possible. The hopping and electron transfer rate is in the same order of magnitude indicating that Mn can move across several sites during a full O_2 evolution cycle.

The presented work from Lole et al.^[122] and Yuan et al.^[123] demonstrate the capability of in-situ ETEM studies to reveal surface dynamics of highly ordered active catalysts. These dynamics have to be taken into account for further catalyst research and the discussion of the reaction mechanism. However, the visualization of the surface dynamics in the presented research was possible due to the highly ordered catalysts. This work meets the challenge of the structural analysis and the visualization of dynamics in more disordered materials in the following chapters.

Stability and Degradation Mechanism of Si-based Photocathodes

This whole chapter is a complete reproduction of the original publication^[27]:

Stability and Degradation Mechanism of Si-based Photocathodes for Water Splitting with Ultrathin TiO₂ Protection Layer

*E. Ronge, T. Cottre, K. Welter, V. Smirnov, N. Ottinger, F. Finger, B. Kaiser,
W. Jaegermann and C. Jooss*

Republished with permission of de Gruyter, from “*Stability and Degradation Mechanism of Si-based Photocathodes for Water Splitting with Ultrathin TiO₂ Protection Layer*”, Ronge, T. Cottre, K. Welter, V. Smirnov, N. Ottinger, F. Finger, B. Kaiser, W. Jaegermann and C. Jooss, *Zeitschrift für Physikalische Chemie* 234(6), 1171-1184, 2020;^[27] permission conveyed through Copyright Clearance Center, Inc. References, labels and arrangement of figures have been modified to suit this thesis.

***Corresponding author:** Christian Jooss, Institute of Materials Physics,
University of Goettingen, 37077 Goettingen, Germany, e-mail: cjooss@gwdg.de

Emanuel Ronge and Natalie Jacqueline Ottinger: Institute of Materials
Physics, University of Goettingen, 37077 Goettingen, Germany

Thorsten Cottre, Bernhard Kaiser and Wolfram Jaegermann: Institut für
Materialwissenschaft, Technische Universität Darmstadt, 64287 Darmstadt,
Germany

Katharina Welter, Vladimir Smirnov and Friedhelm Finger: Institut für
Energie- und Klimaforschung (IEK-5), Forschungszentrum Jülich GmbH, 52425
Jülich, Germany

Abstract

Using transmission and scanning electron microscopy, we study mechanisms which determine the stability of Silicon photocathodes for solar driven water splitting. Such tandem or triple devices can show a promising stability as photocathodes if the semiconductor surface is protected by an ultrathin TiO_2 protection layer. Using atomic layer deposition (ALD) with Cl-precursors, 4-7 nm thick TiO_2 layers can be grown with high structural perfection. The layer can be electrochemically covered by Pt nanoparticles serving as electro-catalysts. However, Cl-remnants which are typically present in such layers due to incomplete oxidation, are the origin of an electrochemical degradation process. After 1 hour AM1.5G illumination in alkaline media, circular shaped corrosion craters appear in the topmost Si layer, although the TiO_2 layer is intact in most parts of the crater. The crater development is stopped at local inhomogeneities with a higher Pt coverage. The observations suggests that reduced Titanium species due to $\text{Cl}^-/\text{O}^{2-}$ substitution are nucleation sites of the initial corrosion steps due to enhanced solubility of reduced Ti in the electrolyte. This process is followed by electrochemical dissolution of Si, after direct contact between the electrolyte and the top Si layer surface. To increase the stability of TiO_2 protected photocathodes, formation of reduced Ti species must be avoided.

3.1. Introduction

High efficiency photo-electrochemical devices for solar-driven hydrogen generation require the integration of different materials, which show optimal performance for the specific functions. Such integrated devices are developed with the goal to establish a higher efficiency in water splitting than modular photovoltaic and electrolysis systems, due to reduced contacts losses.^[15] Silicon solar cells are well suited for efficient absorption of the solar spectrum with resulting high conversion efficiencies but require a multi-junction or series connection set-up to provide sufficient voltage for water splitting. However Si and also most other interesting absorbers are not electrochemically stable in aqueous electrolytes.^[95] Since most earth abundant efficient oxygen evolution catalysts operate only stable in alkaline conditions, the hydrogen evolution has to be preferably carried out in alkaline electrolyte media, too. Thus, the photocathodes and anodes would be in contact with aqueous alkaline electrolytes so an electrically conducting anticorrosion layer covering the semiconductor absorber in addition to a suitable catalyst is generally needed. Several metal and oxide protection layers have been explored including Pd, Ni, SiO_x , NiO_x and TiO_2 .^[97,127-130] For TiO_2 a durability of >500 h in alkaline conditions has been achieved.^[98] Furthermore, it possesses a relatively good electric conductivity and methods for the growth of ultra-thin layers, such as atomic layer deposition (ALD), are established.^[98,99,105] ALD offers the opportunity of deposition of high quality thin films by a layer by layer growth mode, which is required to obtain a fully covered ultrathin film. TiO_2 protection layers of various thicknesses are well

established for water splitting devices^[97-104], including the combination of a TiO₂ layer with nanostructured TiO₂ for obtaining high surface areas.^[100] Generally, there are competing performance requirements on the protection layer. Stability typically improves with increasing layer thickness, however, the photoelectric current density drops because of the higher series resistance. Consequently, ultra-thin conducting layers are highly desirable due to their good charge transport properties, but posing the challenges for layer perfection and thus require a fundamental understanding of the role of defects for corrosion. In this work we analyze the influence of growth-induced defects and impurities in ultrathin TiO₂ protection layers on the stability and efficiency of a photocathode device. The 4-6 nm thick amorphous TiO₂ protection layer is deposited by ALD on silicon based tandem and triple junctions. The devices are operated for 1 h under AM1.5G in alkaline media (0.1 M KOH) to analyze their stability and processes initiating corrosion. After operation the devices are studied by scanning (SEM) and transmission electron microscopy (TEM). Our results suggest that impurity-induced reduced TiO₂ sites are the origin of an accelerated electrochemical corrosion process.

3.2. Results

3.2.1. Pristine State of the Photocathode

The pristine photocathodes with Si-based tandem/triple cell, covered with 100x cycles of ALD grown TiO₂ and electrochemically deposited Pt nanoparticles were analysed by SEM and TEM. The TiO₂ and Pt particle features described in the following, do not depend on the Si cell configuration. Exemplarily, the results are summarized in figure 3.1 for the tandem cell configuration.

Although areas with higher and lower Pt coverage are found (figure 3.1 C and D, respectively), the TiO₂ film appears in SEM as a homogeneous and smooth layer without any growth features such as e.g. pinholes. This indicates a full TiO₂ coverage in the pristine state. TEM cross-section lamellas are prepared at different photocathodes and different locations. The bright field image (figure 3.1 B) reveals the expected structure of the photocathode, where even the a-Si/a-Si interface is visible. The junction between the Si sub-cells consists of a thin doped microcrystalline silicon or doped microcrystalline silicon oxide layer, depending on the junction configuration, which is visible in bright field (figure 3.1 B). The TiO₂ layer is visible in the TEM overview image only at positions without overlap to Pt particles. The bright field image at higher magnification in figure 3.1 E shows the typical morphology of TiO₂ layer. The film thickness varies between different photocathode samples and is in the range between 4 to 7 nm, fluctuating across the layer by ± 1 nm. The amorphous structure of the TiO₂ layer is confirmed by HRTEM and electron diffraction.

The inhomogeneous coverage of the photocathode by Pt nanoparticles in the pristine state seems to be correlated to the TiO₂ layer thickness. Areas with high Pt density

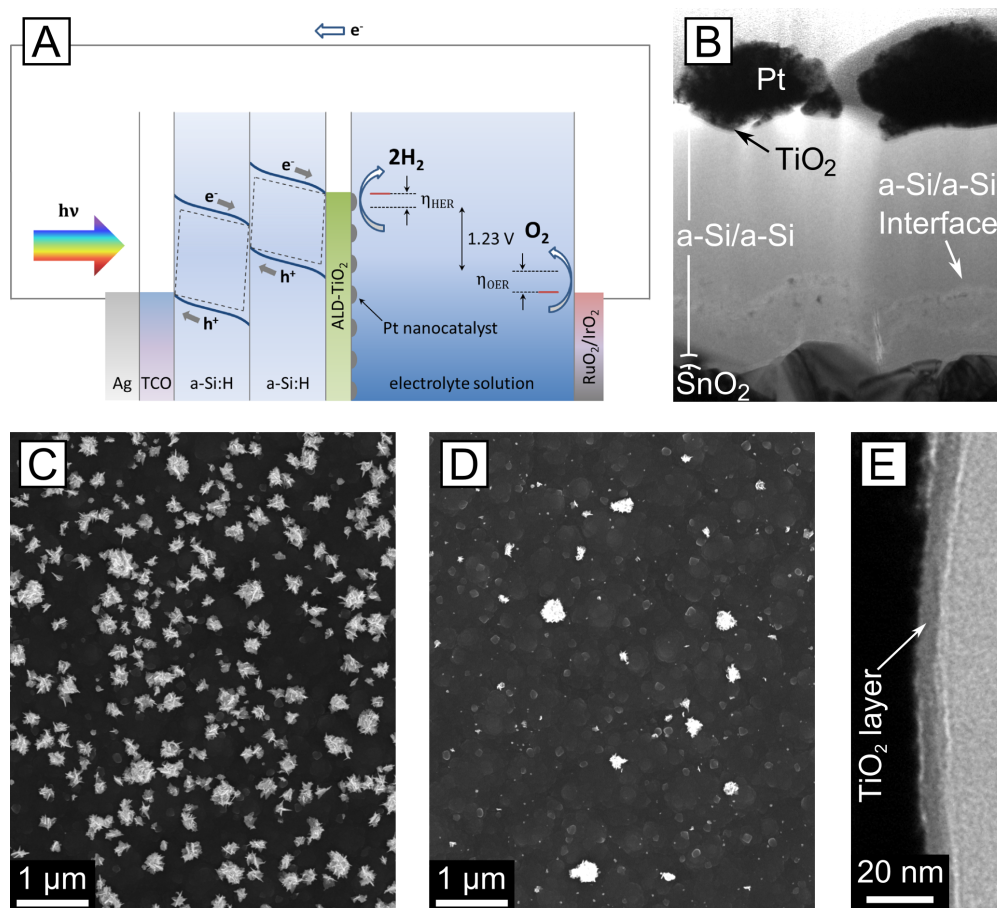


Figure 3.1.: Configuration of the photo-electrochemical device: A: Scheme of the device; B: TEM bright field image in cross section of a tandem cell photocathode; C: representative SEM image of a photocathode surface at an area with high Pt coverage; D: area with low Pt coverage; E: Cross-section TEM bright field image of the TiO₂ layer from an area with high Pt coverage.

(H.Pt) occur at thicker TiO₂ regions and areas with low Pt density (L.Pt) occur at thinner TiO₂ regions, respectively. Within the sample series the absolute values for Pt density and particle size varies slightly (see Figure A.2) but Pt rich and reduced areas are observed for all studied surfaces.

3.2.2. Performance

The photoelectrochemical performances of the tandem and triple cell devices were tested in 0.1M KOH under AM1.5G illumination by using chronopotentiometry with a constant current density of -2 mAcm^{-2} for 1 h. The corresponding results are depicted in figure 3.2.

Both devices show a constant potential at the beginning with initial values of

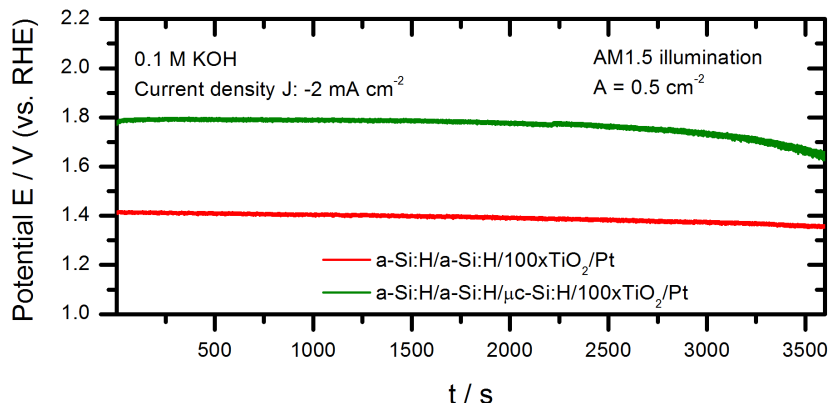


Figure 3.2.: Chronopotentiometry measurement of a tandem and triple cell devices under AM1.5G illumination with a constant current density of -2 mA cm^{-2} for 1 h.

1.4 V vs RHE for the tandem cell and 1.8 V vs RHE for the triple cell. In previous studies, operating times of 12 h could be achieved for similar systems.^[131] However, in these studies a titanium dioxide layer thickness of 30.5 nm was used, which is much higher than in the systems reported here. Figure 3.2 shows that both the tandem as well as the triple junction photocathodes experience a decrease of the potential, which is most pronounced for the triple cell device at the end of the measurement. From this observation, an early onset of a continuous device degradation can be concluded, which later turns into a rapid corrosion. The degradation mechanism including the influence of the Pt particle distribution, impurities as well as the passivation layer thickness will be discussed below.

3.2.3. Post-mortem studies of the photocathode stability

Change in Surface Morphology by SEM

The SEM studies address two topics: (i) The stability of the coverage, shape and size of the Pt nanoparticles and (ii) of the TiO_2 protection layer after 2 h, 4 h, and 6 h of AM1.5G illumination in 0.1 M KOH at -2 mA cm^{-2} . For the Pt particle coverage, size distribution and morphology, no significant changes could be observed even after 6 h of hydrogen evolution (Figure A.1 & A.3). However, in areas with low Pt coverage the formation of circular holes in the TiO_2 layer and the underlying Si film is visible in figure 3.3. These circular holes are already present at the surface of the photocathode after 1 h of electrolysis in 0.1 M KOH. In contrast to the hole formation in areas with low Pt coverage, no hole formation can be observed in areas with high Pt density. Remarkably, the lateral hole growth even stops at areas with high Pt coverage (figure 3.3A).

The circular shape of the craters indicates, that the hole growth is nucleated

at very local point like nucleation centers in the TiO_2 layer and then grows in a concentric manner. The dependence of the crater formation on the Pt nanoparticle coverage provides strong evidence for an electrochemical degradation process of the TiO_2 layer nucleating at defects and a subsequent electrochemical dissolution process of the Si material below the TiO_2 layer. Clearly, hole growth is stopped after reaching an area with high Pt coverage. Consequently a high Pt coverage prevents or at least slows down the electrochemical degradation of the TiO_2 layer and underlying Si. As revealed by the TEM studies of corrosion craters (see e.g. figure 3.5), the TiO_2 layer is preserved in most parts of the crater, even at locations where the Si has been dissolved. This supports that the TiO_2 layer is stable under operation conditions and electrochemical corrosion of Si is nucleated at small inhomogeneities and propagates in a concentric manner in low Pt regions.

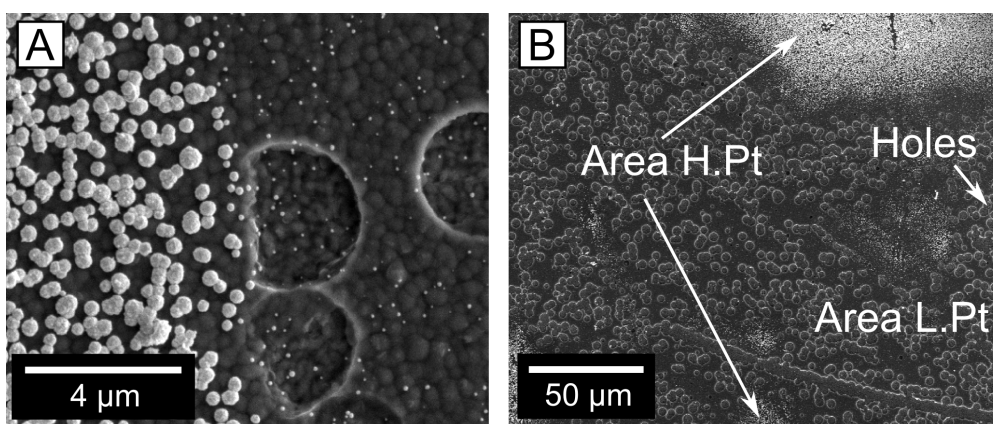


Figure 3.3.: SEM images of the post mortem state of the tandem photocathode after 1 h of operation. A: detailed view of the corrosion craters at the interface of high and low Pt coverage; B: Overview of the different areas of high and low Pt coverage. The round shapes in the L.Pt areas are corrosion craters.

Post Mortem Studies of Chemical Inhomogeneities

In order to further investigate the role of chemical inhomogeneity for the device stability, EDX measurements were carried out. Several EDX spectra were taken in areas with high and low Pt density. These spectra then were summed up accordingly, the background was removed and the signal normalized to the $\text{K}\alpha_1$ Si Reflex. The result in figure 3.4 indicates that Cl is present in some areas of the TiO_2 layer. In general, the Cl concentration is the highest in the holes and also in areas with low Pt density compared to the high Pt density areas.

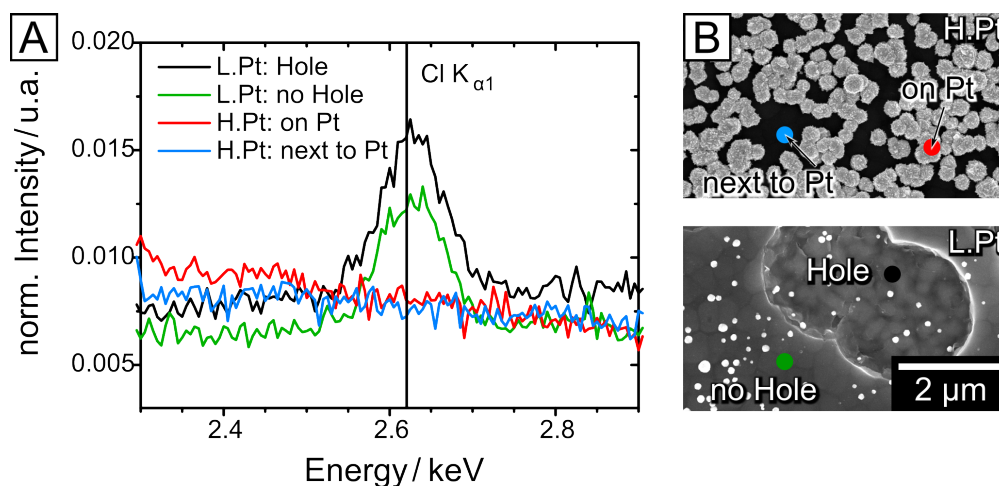


Figure 3.4.: EDX analysis of the Cl inhomogeneity in corroded and non-corroded areas of a tandem device after 1 h of operation. A: Overview on EDX spectra at the Cl $K\alpha_1$ line for different areas; B: SEM images of areas of high (H:Pt) and low (L:Pt) coverage, where coloured circles exemplify areas where the spectra in A were taken.

Post Mortem TEM Studies of the TiO_2 Layer and Corrosion Craters

The cross-section HAADF scanning transmission electron microscopy (STEM) image in figure 3.5 displays the edge of a corrosion crater. Within the crater (right side) the Si is only partially removed. The dissolution has stopped at the a-Si/a-Si interface of the solar cell. The EDX maps in figure 3.5 B and C reveal a partially intact TiO_2 layer within large areas of the holes. This is supported by EDX measurements carried out at a SEM (Figure A.2). These findings support the electrochemical nature of the Si dissolution. Even the Si beneath a preserved TiO_2 layer goes into solution via a lateral process involving neighbouring pin holes. The remaining TiO_2 layers within the craters then just shift down during the Si dissolution, demonstrating the stability of such a protective layer. Post mortem TEM studies of cross-section lamellas outside the crater regions confirm the results obtained at the pristine devices: Depending on the area, the thickness of the TiO_2 layer varies by a few nanometres (Figure A.2). The thickness of the specific photocathode studied has an average value of (7.4 ± 1.2) nm in the area with high Pt coverage and (5.4 ± 0.8) nm in the low Pt density area. Together with the previous results this points toward a correlation between stability, TiO_2 layer thickness, Pt coverage and Cl content. The photocathodes preferably degrade in areas with low Pt coverage, a thinner TiO_2 layer thickness and a higher Cl concentration.

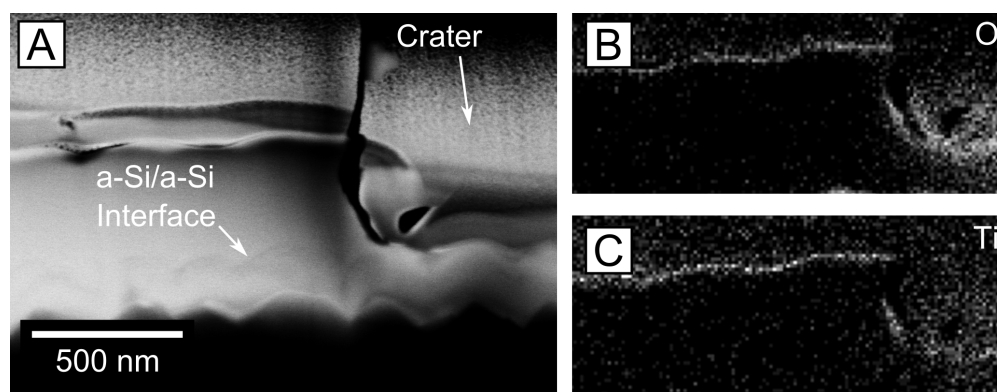
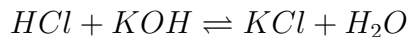


Figure 3.5.: EDX analysis of a corrosion crater of a tandem photocathode after 1 h of operation in cross plane view; A: HAADF cross-section image of the edge of the corrosion crater. EDX element maps: B: Oxygen; C: Titanium.

3.3. Discussion

In the preparation of the TiO_2 protection layer of the photocathode by the ALD process, Ti-tetrachloride is used as the Ti precursor. In addition, K_2PtCl_4 is used for the electrochemical deposition of Pt nanoparticles. The EDX data point toward the ALD process as the origin of the correlation between Cl species and corrosion craters, since no increase in Cl can be detected at or near the Pt particles. Thus, there are Cl impurities stemming from a non ideal ALD process, where Cl-doped $\text{TiO}_{2-x}\text{Cl}_x$ is formed in an incomplete reaction. Such Cl-remnants are typically observed in TiO_2 layer formation by Cl-containing precursors.^[132,133] The calculated Pourbaix diagram as well as cyclovoltammetry studies reveal that TiO_2 is stable at potentials close to HER in alkaline conditions.^[63,134] However, reduced TiO_{2-x} such as the Magneli phase shows a redox peak at -0.1 V vs Hg/HgO .^[135] Hence, Ti^{3+} exists in the Magneli phase which is redox active in CV under alkaline conditions. In Cl-doped TiO_2 , Cl is an electron donor, suggesting that Ti^{4+} is reduced due to replacement of O^{2-} by Cl^- . In addition oxygen is more electronegative than Cl, facilitating the formation of reduced Ti^{3+} species in the $\text{TiO}_{2-x}\text{Cl}_x$ layers. The hypothesis that Cl-doping leads to Ti^{3+} formation is additionally supported by the electronic bandstructure calculations of Yang et al, which reveal a shift in the TiO_2 conduction band to lower values due to Cl doping.^[136] If Ti^{3+} is already present due to the chemical impurity, it can be even further reduced to Ti^{2+} in the cathodic current branch of the CV. The Pourbaix diagram^[63] suggests that Ti^{3+} and Ti^{2+} is only soluble in the acidic pH regime and TiO_2 transforms into other solid Ti-O phase at potentials negative of the E_0 (HER). However, this applies only in electrochemical equilibrium with an electrolyte containing dissolved Ti species. In our case the Ti concentration in the electrolyte is basically zero. In non-equilibrium dissolution of Ti^{3+} and Ti^{2+} can set in even in alkaline conditions. The leaching of $\text{Ti}^{3+/2+}$ is consequently facilitated in locally Cl^- enriched areas, leading to the formation

of small pinholes in the TiO_2 , which can in turn act as nucleation centres for the electrochemical crater formation in Si. An alternative scenario is the local change of the pH value due to the formation of HCl at the interface of the electrolyte to Cl-doped TiO_2 . This is unlikely because at pH 13 (0.1 M KOH) HCl would immediately react to KCl:



The chemical cathodic etching of Si in alkaline solution is an intensively studied subject due to its importance in Si technology (see e.g. Ref^[137-139]). After extensive studies, the model of a coupled chemical/electrochemical mechanism has been developed which is a combination of an $\text{H}_2\text{O}/\text{OH}^-$ attack of Si-Si or Si-H bonds with the formation of soluble $\text{Si}(\text{OH})_4$ species and anodic currents due to electron injection. Cathodic currents lead to the formation of activated H and Si- H_x bonds which may also form reactive and soluble SiH_x species.^[140,141]

The suggested mechanism of crater nucleation by electrochemical dissolution of $\text{Ti}^{3+}/\text{Ti}^{2+}$ at Cl-doped TiO_2 areas and subsequent dissolution of Si (illustrated in figure 3.6) is consistent with the following observations: (i) the crater formation depend on the TiO_2 layer thickness. (ii) The crater formation is centred at areas of locally enhanced Cl concentration within the TiO_2 protection layer. (iii) The crater formation preferentially takes place at locations of lower Pt particle coverage, where large overpotentials can develop. In addition to Cl-induced preformed Ti^{3+} defect states, a locally increased overpotential can drive Ti^{4+} reduction. The equilibrium potential for Ti^{4+} reduction is -1.38 V compared to -0.82 V for proton reduction in alkaline conditions pH=14.^[142] (iv) The observation of an intact TiO_2 layer in large areas inside the dissolution craters strongly supports that the TiO_2 can endure HER under alkaline conditions and only the Cl impurities lead to the degradation of the TiO_2 layer. (v) The stop of the vertical degradation of Si at the a-Si/a-Si interface is consistent with the suggested electrochemical degradation mechanism for Si. The removal of one PIN subcell of tandem junction reduces the photovoltage that drives the Si dissolution. (vi) A high Pt coverage can reduce the dissolution of TiO_2 and Si, probably due to a locally reduced overpotential.

3.4. Conclusion

The degradation of chemical passivation layers on Si photocathodes has been analyzed using TEM and SEM studies. It is evident that the desired HER is competing to other unwanted electron transfer reactions (electron induced Si decomposition). The latter can be suppressed by an ultrathin electrically conductive protection layer which stability is influenced by the layer morphology and stoichiometry. In the case of TiO_2 layers a non-ideal ALD process for the growth of ultrathin TiO_2 layers based on Cl-containing precursors can lead to a Cl doping of the TiO_2 protection layer. As a result locations of partially reduced Titanium represent nucleation centers for the onset of the corrosion. Ti^{3+} dispenses or is further reduced to Ti^{2+} , which can then also dissolve in the electrolyte. To increase the stability of TiO_2 protected

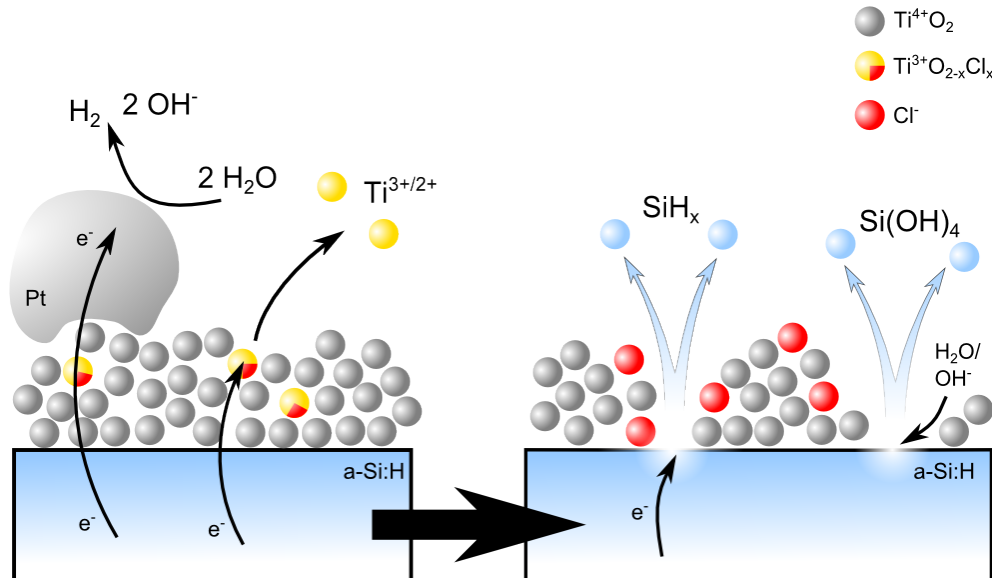


Figure 3.6.: Schematic illustration of the suggested mechanism of pinhole formation in TiO_2 and the subsequent Si dissolution mechanism.

photocathodes, defects such as chemical impurities, maybe also oxygen vacancies that give rise to reduced Ti species, must be avoided. The effect of degradation can be reduced by a homogenous coverage of Pt as a co-catalyst. In summary, the chemical composition (impurities) as well as the morphology of the electrochemically involved surface, including the electronically conduction protection layer as well as the catalyst must be well-chosen, for obtaining stable devices.

3.5. Experimental Section

3.5.1. Preparation of Si-based Photocathodes solar cells

Thin-film silicon solar cells were deposited in a p-i-n sequence (superstrate configuration) by a Plasma Enhanced Chemical Vapor Deposition (PECVD) technique in a multi-chamber system. All solar cell (a-Si:H/a-Si:H tandem and a-Si:H/a-Si:H/ $\mu\text{c-Si:H}$ triple) were deposited on 100 cm^2 fluorine-doped tin dioxide ($\text{SnO}_2\text{:F}$) coated glass substrates (Asahi U type) at substrate temperatures below 185°C . For the intrinsic absorber layers (i-layers) a mixture of silane (SiH_4) and hydrogen (H_2) gases was used. For the doped p- and n-type layers, trimethylborane (TMB), methane (CH_4), phosphine (PH_3), and carbon dioxide (CO_2) gases were added to the silane-hydrogen mixture. For $\mu\text{c-Si:H}$ intrinsic and p-type layer depositions an excitation frequency of 94.7 MHz was used. For all a-Si:H layers an excitation frequency of 13.56 MHz was used. Additional details on the solar cell preparation can be found in refs. ^[130,143]

3.5.2. Device Integration

The prepared silicon solar cells were coated with thin films of amorphous TiO_2 for surface passivation and corrosion protection by using a custom-built thermal ALD reactor. Titanium tetrachloride (99.995 %, Sigma-Aldrich) and Milli-Q water were used as precursors at a growth temperature of 160°C with high purity nitrogen (99.999 %) as a purging gas. Detailed information about the ALD setup are given in Cottre et al.^[131] Prior to the TiO_2 deposition etching procedures were used for the surface preparation. The a-Si:H/a-Si:H tandem cells were etched with ammonium fluoride (40 %, semiconductor grade VLSI PURANAL, Sigma-Aldrich) for 5 min while the a-Si:H/a-Si:H/ μc -Si:H triple cells were cleaned by using a piranha bath with sulfuric acid (96 %, VLSI Selectipur, BASF) and hydrogen peroxide (31 %, VLSIn Selectipur, BASF) in a defined ratio ($\text{H}_2\text{SO}_4 : \text{H}_2\text{O}_2 = 3 : 1$) for 5 min. The next step of the device integration is the preparation of the Pt electrocatalyst particles for the hydrogen evolution reaction by galvanostatic electrodeposition. Unless otherwise stated 2 mM K_2PtCl_4 (99 %, Carbolution Chemicals GmbH) in 0.5 M H_2SO_4 ($\pm 0.2\%$, Carl Roth GmbH) solution was used. The Pt deposition was carried out with a current density of -0.5 mA cm^{-2} for 120 s in a three-electrode setup under AM1.5G illumination with a silver/silverchloride (3 M NaCl) reference electrode and a platinum wire as a counter electrode.

3.5.3. Photoelectrochemical Characterization

The photoelectrochemical characterization of the integrated systems was performed in a three electrode setup in 0.1 M KOH ($\pm 0.2\%$, Carl Roth GmbH) under AM1.5G illumination. The formation of an ohmic contact to the TCO was achieved by scratching the silicon solar cells and using colloidal silver paste (Ted Pella Inc). The photoelectrochemical measurements were performed in a Zahner PECC-2 cell with a Gamry potentiostat (Interface 1000). The reference electrode was a silver/silverchloride electrode (3 M NaCl) while a platinum wire was used as a counter electrode. The spectral light incidence (AM1.5G) was created by a full spectrum solar simulator equipped with a 150 W Xe short arc lamp (LS0108, LOT-QuantumDesign GmbH). The integrated devices were also tested in a two electrode setup under AM1.5G illumination in a modified Zahner PECC-2 cell combined with a commercial ruthenium-iridium oxide counter electrode (Metakem GmbH) for the oxygen evolution reaction. Here various electrolyte solutions were used (0.1 M and 1 M KOH ($\pm 0.2\%$, Carl Roth GmbH) and 0.1 M and 1 M H_2SO_4 ($\pm 0.2\%$, Carl Roth GmbH)) to study the performance of the systems in dependence of the pH value. The respective photoelectrochemical measurements of the two electrode setup can be found in Cottre et al.^[131]

3.5.4. SEM and EDX

The SEM analysis was carried out with a Nova NanoSem 650 in-situ SEM from FEI. An Everhart-Thornley (ET) detector was used to take overview images while the more detailed images were taken with a *through the lens* (TTL) detector. In every case an acceleration voltage of 10 kV was used. For energy-dispersive X-ray spectroscopy (EDX) an acceleration voltage of 20 kV was used and an Oxford Instrument X-Max detector was employed. The livetime for each spectrum was 120 s and a minimum of 10 spectra per specific area was used for the analysis. In the case of the cross-section lamella EDX analysis in Fig. 3.5 the SEM was operated in scanning transmission electron microscopy (STEM) mode where for imaging a High Angle Annular Dark Field (HAADF) detector was deployed.

3.5.5. TEM lamellae preparation and TEM analysis

Cross-section TEM lamellas were cut using a Nova Nanolab 600 focused ion beam (FIB) system from FEI with an ion acceleration voltage of 30 kV. First a protective layer of FIB-Platinum was deposited via electron beam induced deposition. Then a thicker layer was fabricated by ion beam induced deposition. After rough cuts with 7 nA and 3 nA currents a transfer to a copper grid was performed and cleaning cuts with down to 29 pA at 5 kV were carried out. The TEM investigations were performed with a Phillips CM12 at 120 kV (overview image in Fig. 3.1 B). The TiO₂ layer thickness was measured with a Phillips CM 30 at 300 kV (Fig. 3.1 E and Fig A.2).

Acknowledgements

Funding from the Deutsche Forschungsgemeinschaft in the priority program SPP 1316 is gratefully acknowledged.

Structure of Nanocrystalline, Partially Disordered $\text{MoS}_{2+\delta}$

This whole chapter is a complete reproduction of the original publication^[28]

Structure of nanocrystalline, partially disordered $\text{MoS}_{2+\delta}$ derived from HRTEM - an abundant material for efficient HER catalysis

Emanuel Ronge, Sonja Hildebrandt, Marie-Luise Grutza, Helmut Klein, Philipp Kurz and Christian Jooss

originally published in *Catalysts* 2020, 10(8), 856^[28] under the terms and conditions of the CC BY license. doi:10.3390/catal10080856

References, labels and arrangement of figures have been modified to suit this thesis.

¹ Institute of Materials Physics, University of Göttingen, Friedrich-Hund-Platz 1, 37077 Göttingen, Germany; emanuel.ronge@phys.uni-goettingen.de (E.R.); s.hildebrandt01@stud.uni-goettingen.de (S.H.)

² Institute for Inorganic and Analytical Chemistry and Freiburg Material Research Center (FMF), University of Freiburg, Albertstraße 21, 79104 Freiburg, Germany; marie-luise.grutza@ac.uni-freiburg.de

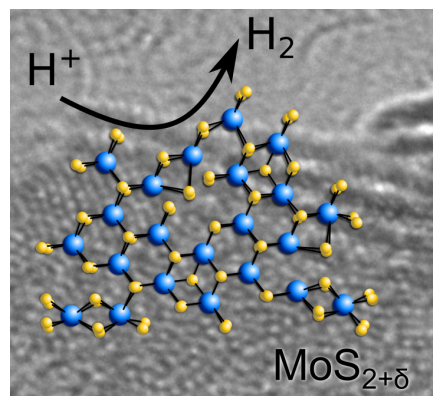
³ GZG Crystallography University of Göttingen, Goldschmidtstr. 1, 37077 Göttingen, Germany; hklein@uni-goettingen.de

⁴ International Center for Advanced Studies of Energy Conversion (ICASEC), University of Göttingen, D-37077 Göttingen, Germany

* Correspondence: philipp.kurz@ac.uni-freiburg.de (P.K.); cjooss@gwdg.de (C.J.); Tel.: +49-0761-203-6127 (P.K.); +49-551-39-25303 (C.J.)

Abstract

Molybdenum sulfides (MoS_x , $x > 2$) are promising catalysts for the hydrogen evolution reaction (HER) that show high hydrogen evolution rates and potentially represent an abundant alternative to platinum. However, a complete understanding of the structure of the most active variants is still lacking. Nanocrystalline $\text{MoS}_{2+\delta}$ was prepared by a solvothermal method and immobilized on graphene. The obtained electrodes exhibit stable HER current densities of 3 mA cm^{-2} at an overpotential of 200 mV for at least 7 h. A structural analysis of the material by high-resolution transmission electron microscopy (HRTEM) show partially disordered nanocrystals of a size between 5-10 nm. Both X-ray and electron diffraction reveal large fluctuations in lattice spacing, where the average *c*-axis stacking is increased and the in-plane lattice parameter is locally reduced in comparison to the layered structure of crystalline MoS_2 . A three-dimensional structural model of $\text{MoS}_{2+\delta}$ is derived from the experiments, in which $[\text{Mo}_2\text{S}_{12}]^{2-}$ and $[\text{Mo}_3\text{S}_{13}]^{2-}$ clusters as well as disclinations represent the typical defects in the ideal MoS_2 structure. It is suggested that defect-rich coordinatively modified Mo edges with lower Mo-Mo distances contain the active sites for HER catalysis and that these structural features are more important than the S:Mo ratio for the activity.



4.1. Introduction

The production of hydrogen from renewable energy sources by the splitting of water is a clean alternative to fossil fuels.^[144-146] For a large scale application of water-splitting electrolyzers, abundant, stable and efficient electrocatalysts for the hydrogen evolution reaction (HER) are needed. However, the best known materials for this purpose in acidic condition are noble metals, such as e.g. platinum. Because of the low abundance of noble metals and their resulting high price, the search for more affordable alternatives is of high interest.^[23,37] Due to their relatively low overpotentials and the good availability of Mo, molybdenum sulfides have gained increasing attention in HER catalyst research during the past few decades.^[37] However, it is by now accepted that the catalytic activity of crystalline MoS_2 in its most common 2H modification is limited to about -5 mA cm^{-2} at an overpotential $\eta \approx 500 \text{ mV}$ ^[49] because of the special nature of the HER active sites, which are mainly present at the edges of the two-dimensional MoS_2 planes.^[55-57] In contrast, for the 1T polymorph which has a higher HER activity, the crystalline basal planes might be active sites.^[57,58] However, this system is not stable. In order to improve catalytic activity,

sulfur-rich “MoS_x” materials (with $x > 2$) have been synthesized and this approach has yielded very promising results.^[23,39,40] Some MoS_x electrodes can deliver current densities of 10 mAcm⁻² at $\eta \approx 170$ mV in 0.5 M H₂SO₄. In special applications, e.g. acidic industrial wastewaters, these catalysts also show a much better longterm stability than Pt.^[38] MoS_x materials can be synthesized by solvothermal synthesis^[40,60], wet chemical synthesis^[37,61], electrodeposition^[23,53], thermal decomposition^[147] or chemical oxidation^[53]. Typical precursors include ammonium tetrathiomolybdate ((NH₄)₂[MoS₄]) as a solid^[40,53,60], aqueous solutions containing [MoS₄]²⁻^[23,53] or ammonium heptamolybdate ((NH₄)₆[Mo₇O₂₄])^[37] or MoO₃ reacting with NaS₂^[61]. These different synthesis routes for MoS_x generally lead to stoichiometries with $2 < x < 4$ and highly disordered, X-ray amorphous structures.^[22,23,39,60] X-ray photoemission spectroscopy (XPS) indicates the presence of a variety of different sulfur species in the form of unsaturated, terminal, bridging and maybe even apical sulfides and disulfides.^[23,39,40,60,61] As a result from these studies, two quite different structure models for MoS_x have been proposed. One model suggests a polymer like structure with chains of [Mo₂S₉]-^[22,39,52,54,148] or [Mo₃S₁₃]-units.^[22,53] Other models feature a disordered arrangement of [Mo₃S₁₃]-clusters.^[22,39,40,52,149,150] Sometimes, crystallization of the amorphous phase to MoS₂ nanoparticles during HER is reported,^[37,50] indicating a structural affinity to MoS₂. The polymer model is supported by a publication of Tran et al.^[53] using real space scanning transmission electron microscopy (STEM) imaging of a MoS_x sample with a relatively large S/Mo ratio of about 4. However, the structural analyses of other MoS_x with lower sulfur contents ($2 < x < 4$) were mostly based on X-ray diffraction (XRD) which does not provide precise structural information for partially disordered systems. Thus, precise high-resolution real space information about MoS_x structures is of crucial importance for a better understanding of the HER activity and the identification of active site(s). The nature of the active sites for disordered MoS_x with $x > 2$ (MoS_{2+ δ}) is controversially discussed in the literature. Depending on the suggested structural model, different hypotheses exist. If a MoS₂-like nanostructure arises during HER, there is evidence that terminal disulfides (S₂²⁻) at the edges of the nanocrystals act as active centers.^[37,50] However, no crystalline edges are present in amorphous MoS_{2+ δ} , but here coordinatively unsaturated molybdenum or sulfur sites are considered to act as HER active sites.^[23] Moreover, density functional theory indicate a higher activity of bridging S₂²⁻ which would explain the excellent performance of [Mo₃S₁₃]²⁻ clusters.^[39,151] That S₂²⁻ may be an active site for MoS_{2+ δ} is also supported by XPS studies.^[40] Consequently, a better understanding of the actual HER mechanism of disordered MoS_x requires a comprehensive structure model. Herein, we report on a detailed structural analysis of two solvothermally synthesized MoS_{2+ δ} samples and their hydrogen evolution activity compared to MoS₂, using different electrochemical measurements (CV, CP and Tafel analysis), high-resolution transmission electron microscopy (HRTEM), as well as electron- and X-ray diffraction. HRTEM shows that the “X-ray amorphous” structure is in fact nanocrystalline and features a pronounced disorder within the individual nanocrystals. The detected fluctuations of in-plane and out of plane lattice parameters measured by XRD, electron diffraction

and HRTEM agree very well. These observations serve as the basis for the development of a three-dimensional structural model for MoS_{2+δ}, which is qualitatively consistent with spectroscopic and structural information about MoS_x for 2 < x < 4 from literature.

4.2. Results

4.2.1. Electrochemical Characterization of MoS_{2+δ} Electrodes

Electrodes were prepared by immobilizing synthetic MoS_x (with x=2.6 and 3.4, respectively) and commercially available 2H- MoS₂ on graphene. Cyclic voltammograms (CVs), Tafel plots and chronopotentiometric measurements (CPs) in a strongly acidic electrolyte (0.5 M sulfuric acid, pH 0.3) were used as descriptors for the electrocatalytic performance (Figure 4.1). In cyclic voltammograms, the onset potentials for HER at 450 mV were with a value of -190 mV similar for both synthetic MoS_x materials, while MoS₂ showed a significantly higher onset potential (-365 mV) and therefore lower catalytic activity.

Another common descriptor for the HER activity is the overpotential (*eta*) needed to reach current densities of 10 mAcm⁻² in the CVs (Table 4.1). MoS_{2.6} showed the best performance with an overpotential of $\eta = 235$ mV, followed by MoS_{3.4} with $\eta = 245$ mV and MoS₂ with $\eta \approx 450$ mV. This is in agreement with the literature^[23,49], where it is also described that disordered MoS_x are far more active HER catalysts than crystalline MoS₂. For all of these values, one has to keep in mind that the current densities are derived for the geometric area of the electrodes. However, the difference in activity between the prepared samples could also lie in their different stoichiometric compositions. Assuming a molybdenum-based proton reduction mechanism as postulated e.g. by Tran et al.^[53], defective structures and molybdenum-rich materials would be in favor of high proton reduction activity. Indeed, when the detected currents are normalized to the amount of molybdenum on the electrodes, MoS_{2.6} and MoS_{3.4} show nearly identical overpotentials of $\eta = 250$ and 255 mV at 10 mAcm⁻², while MoS₂ is not able to reach this current (see Figure B.7). Concluding from these results, a high sulfur content seems to be much less important for the HER catalysis rate than the existence of a disordered structure for 2 < x < 3.5. In addition, the particle sizes of the synthesized materials differ with (0.18 ± 0.06) μm significantly from the commercial MoS₂ with particle sizes of (0.8 ± 0.9) μm showing a much broader dispersity of the particles (see Figure B.6). Hence, the prepared MoS_x both contain more accessible active sites than MoS₂ where the active sites are believed to be the structural sulfur-rich edges^[55]. However, the different particle sizes and shapes result in an increase of the MoS_{2+δ} surface by a factor of only about 1.9 compared to MoS₂ (see ESI for details). Assuming the same degree of porosity, this indicates that the higher activity of the MoS_{2+δ} electrodes compared to the MoS₂ electrode cannot be explained by morphology effects alone. Tafel slopes were calculated from chronoamperometric “staircase measurements” (see materials

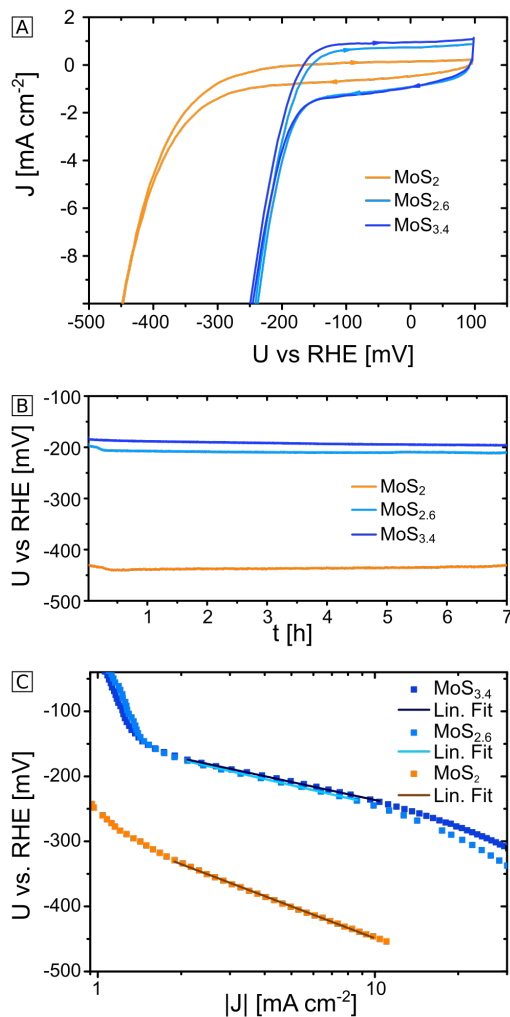


Figure 4.1.: Electrochemical measurements for $\text{MoS}_{2+\delta}$ and MoS_2 (immobilized on graphite) in sulfuric acid (0.5 M, pH 0.3). A: Cyclic voltammetry; B: Chronopotentiometry at a current density of 3 mA cm^{-2} , the first 2 min are cut off; C: Tafel analysis.

and methods) and values of 100 mVdec^{-1} for $\text{MoS}_{2.6}$, 90 mVdec^{-1} for $\text{MoS}_{3.4}$ and 160 mVdec^{-1} for MoS_2 were obtained for the same catalyst loadings. According to these values, the rate limiting step for MoS_2 might be the adsorption of an H atom (the Volmer reaction, while the results for $\text{MoS}_{2.6}$ and $\text{MoS}_{3.4}$ do not give clear evidence on the rate limiting step as the values lie between the boundary values of 40 mVdec^{-1} for the Heyrovsky reaction (reductive desorption) and the Volmer reaction ($>120 \text{ mVdec}^{-1}$)^[38]. All of the measured values for overpotentials and Tafel slopes of the MoS_x studied here cannot compete with the best MoS_x that are known today (Table 4.1), which is hardly surprising given the fact that both material synthesis and electrode fabrication were not optimized. However - and most important for the following detailed structural characterization - both

MoS_x samples show very respectable electrocatalytic HER activity while the MoS₂ reference does not.

	Tafel slope [mV dec ⁻¹]	η @ 10 mAcm ⁻² [mV]	η @ 10 mAμmol(Mo) ⁻¹ [mV]
MoS _{2.6}	100	235	250
MoS _{3.4}	90	245	255
MoS ₂	160	450	-
MoS ₂ ^[152]	160	-	-
MoS ₂ (step- edged stacks) ^[34]	59	104	-
1T MoS ₂ (porous) ^[153]	43	153	-
MoS _{2+x} ^[23]	40	160	-
MoS _{3.5} ^[37]	≈60	≈200	-

Table 4.1.: Tafel slopes and overpotentials at 10 mAcm⁻² of MoS_{2+δ} and MoS₂.

The long-term stability of the electrodes was tested in CP measurements (Figure 4.1 B). Herein, both MoS_x materials clearly outperformed crystalline molybdenum disulphide over a period of 7 h. For a set current density of 3 mAcm⁻², at the end of the experiments MoS_{2.6} and MoS_{3.4} showed overpotentials of ≈210 mV and ≈195 mV, respectively, in comparison to ≈430 mV for MoS₂. In these measurements, both synthetic MoS_x showed extremely stable performances with negligible increases of the overpotentials. The difference in the catalytic activity of MoS_x might be due to some MoS₂ particles as the powder diffractogram shows a sharp peak at (002) for MoS_{2.6}. Over time, MoS₂ showed a slight increase of the HER overpotential, which might be due to a reduced electric resistivity of the catalyst layer related to a shrinking thickness and/or structural rearrangements of the surface leading to a higher amount of active sites.

4.2.2. Electron and X-ray Diffraction Analysis of the MoS_{2+δ} Structure

For the determination of the structure of MoS_{2+δ}, XRD measurements were carried out. The powder diffractograms for the two MoS_{2+δ} samples (MoS_{2.6} & MoS_{3.4}) from different batches are given in Figure 4.2. For comparison, a powder XRD of the crystalline MoS₂ sample was measured as well. A Rietveld refinement of the MoS₂ data was conducted, which yielded results in good agreement with the structural model of Wildervanck et al.^[47] The results are shown in the ESI in Figure B.2 and Table B.2 and B.3. In contrast to MoS₂, the XRD reflexes of MoS_{2+δ} are strongly broadened. Both samples show a very wide peak at about 8 Å which deviates about 1-2 Å from the literature value for MoS₂. Besides this difference, the centers of the other reflexes of the MoS_{2+δ} XRD pattern fit the positions of the MoS₂ data (see Table B.1). The main difference among the MoS_{2+δ} samples

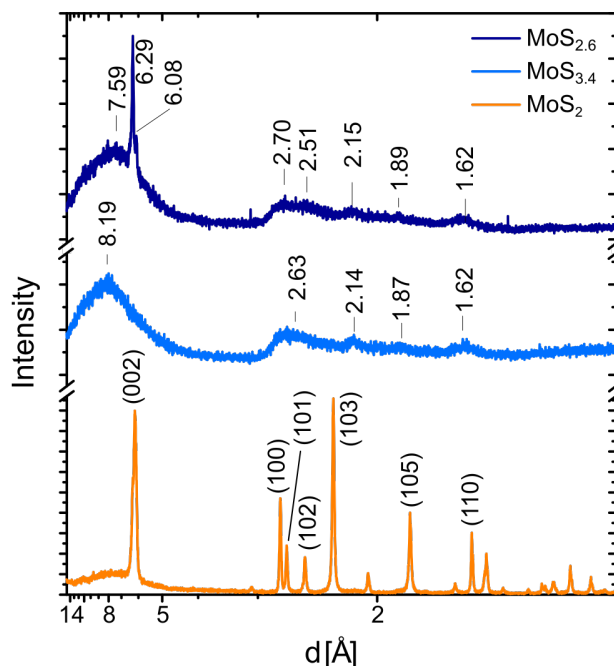


Figure 4.2.: Powder XRD diffraction pattern of MoS_2 and the nanocrystalline, partially disordered samples $\text{MoS}_{2.6}$ and $\text{MoS}_{3.4}$. The indicated diffraction maxima are determined by fitting of a gaussian function.

themselves is the sharp double peak of sample $\text{MoS}_{2.6}$, which reflects the presence of some larger more MoS_2 -like grains. This might indicate a convergence of the $\text{MoS}_{2+\delta}$ structure towards MoS_2 for decreasing S:Mo ratios. The presence of only one sharp MoS_2 reflex (002) in $\text{MoS}_{2.6}$ can be explained by a preferred orientation of MoS_2 -like crystals due to their plate like morphology (see Figure B.6 A).

In addition to the XRD analysis, selected area electron diffraction (SAD) was carried out. The electron diffraction patterns of the two samples $\text{MoS}_{2.6}$ and $\text{MoS}_{3.4}$ are shown in Figure B.2 and consist of only of rings, while no spots are visible. By circular integration of the intensities, the profiles shown in Figure 4.3 were obtained. Three very broad reflexes are visible in the intensity profiles of both samples while the values for $\text{MoS}_{2.6}$ are shifted to slightly lower values. Nevertheless, both are consistent with the MoS_2 structure within the measurement accuracy. A detailed discussion of the peak positions of $\text{MoS}_{2+\delta}$ compared to MoS_2 can be found in the supplement (see Table B.4).

The results of the X-ray and electron diffraction experiments indicate that the structure of the $\text{MoS}_{2+\delta}$ samples is comparable and compatible with a disordered MoS_2 structure independent of the S:Mo ratio. The shift of the first peak of the $\text{MoS}_{2+\delta}$ samples compared to the (002) reflex of MoS_2 towards lower angles and the variation of the peak center reflects an enlargement and fluctuations of the lattice parameter in [001] direction.

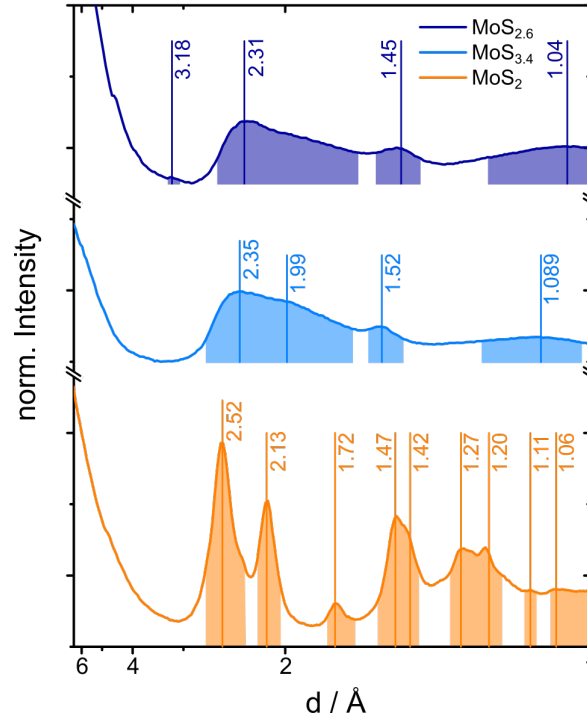


Figure 4.3.: Intensity profiles of the representative electron diffraction patterns of the two $\text{MoS}_{2+\delta}$ batches investigated in this study ($\text{MoS}_{2.6}$ in dark blue & $\text{MoS}_{3.4}$ in light blue). Vertical lines indicate the positions of diffraction maxima and the marked areas indicate the width of the reflexes.

4.2.3. HRTEM Analysis of the Microstructure of $\text{MoS}_{2+\delta}$

To gain a deeper insight into the structure, HRTEM analysis was performed. During the HRTEM analysis, no significant changes to the crystal structure was observed over time at a beam dose rate of 10000 to $64,700 \text{ e}^{-}(\text{\AA}^2\text{s})^{-2}$. Thus we find that $\text{MoS}_{2+\delta}$ is stable under the electron beam which is a requirement for a reliable HRTEM analysis. The HRTEM images of $\text{MoS}_{2+\delta}$ reveal a bended and partially disordered crystal layer stacking. Coherence length of ordered stacking along the (001) direction is about 5 nm and ordering within the planes is reaching up to 10 nm. The in-plane ordering can also be observed along [001] zone axis: A HRTEM image of such a crystal plate is presented in Figure 4.4.

Fast Fourier Transformation (FFT) shows the typical hexagonal symmetry of the (100) lattice planes of MoS_2 . The discovery of this ordering with a hexagonal lattice symmetry of atomic positions within the layers as well as an ordering of the layers along the (001) direction support our conclusion that $\text{MoS}_{2+\delta}$ and MoS_2 show a close structural affinity. The correlation length along (001) is $\xi_c \approx 5 \text{ nm}$, while from the in-plane ordering an in-plane correlation length of $\xi_{ab} \approx 4 \text{ nm}$ can be determined. The reason for the deviation from the prior determined length of $\text{MoS}_{2+\delta}$ planes

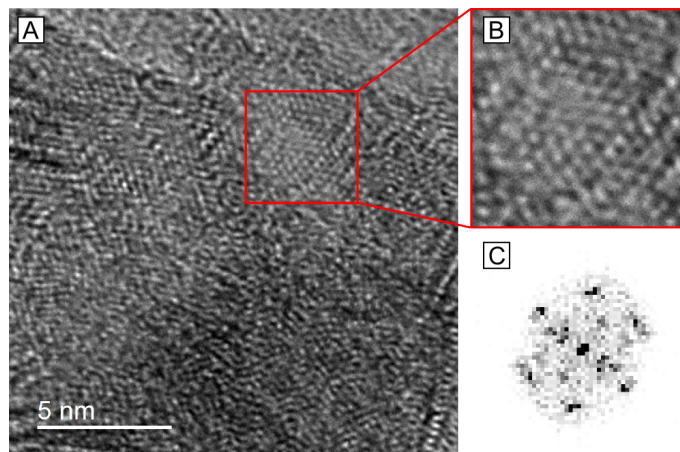


Figure 4.4.: HRTEM image of sample MoS-2 showing the in-plane ordering. A: Overview of the edge of a particle; B: zoom in the area marked with a red square in A; C: FFT of the area shown in B.

of 10 nm is the bending of the crystal planes which disturbs the phase contrast in the top down view. Such a correlation length in the order of 1-5 nm is also called medium range order and can be found in nanocrystalline^[154] as well as in amorphous systems^[155]. From the XRD measurements, a correlation length of 1.22 ± 0.10 nm can be calculated with the Scherrer-Formula. It is well known that the Scherrer-Formula underestimates the grain size for partially disordered nanoparticles, since it measures the coherence length of the lattice^[156].

A more detailed analysis of the HRTEM images for $\text{MoS}_{2+\delta}$ was carried out using FFT and its results are exemplified in Figure 4.5 C. The lattice distance $d_{(100)}$ exhibits a general trend of being locally reduced compared to the literature values of MoS_2 ($d_{(100)} = 2.7368 \text{ \AA}$ ^[47]) with an average value of $d_{(100)} = (2.69 \pm 0.21) \text{ \AA}$ and local variations from 2.45 \AA to 2.79 \AA (see also Table B.5 in the ESI for a summary). Within the measurement accuracy and statistics no significant difference between the two S:Mo ratios can be observed. Both samples ($\text{MoS}_{2.6}$ & $\text{MoS}_{3.4}$) show similar reduction and local variations in the Mo-Mo distance.

A close up of a cross section image of the crystal layers is shown in Figure 4.6 A. The layers are not perfectly flat and parallel which leads to a variation in layer distances. On average, the lattice stacking distance $d_{(001)}$ of $\text{MoS}_{2+\delta}$ varies from 11.15 \AA to 15.93 \AA . The overview in Table B.5 indicates that $d_{(001)}$ is generally enlarged when compared to the literature value of MoS_2 ($d_{(001)} = 12.294 \text{ \AA}$)^[47] for both S:Mo ratios, which is in good agreement with XRD analysis. Next to dislocations also disclinations are visible in Figure 4.6 B (see also Figure B.4 B). This is quite unusual for solid state materials, but e.g. has been observed in fullerene-like variants of MoS_2 by Srolovitz et al.^[157].

In order to provide accurate calibration of the HRTEM images, all images were calibrated by measurements of gold particles. In addition, the crystalline MoS_2 sample was also analyzed by HRTEM as shown in Figure B.4. Both average lattice

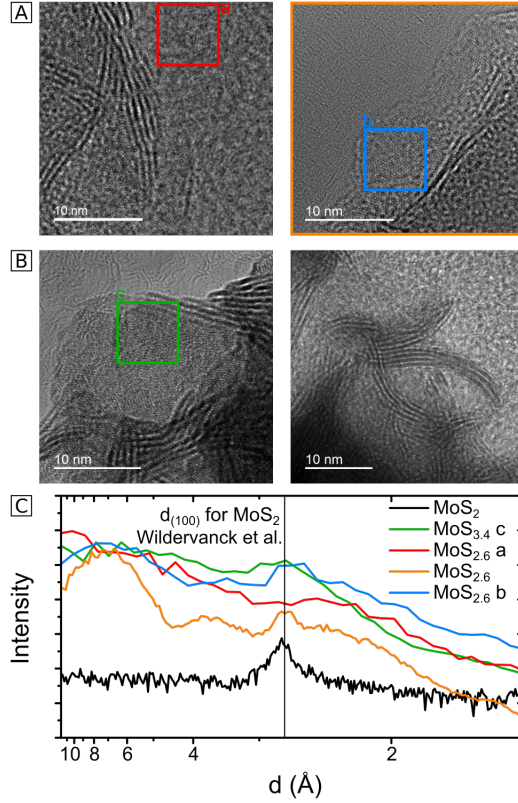


Figure 4.5.: HRTEM analysis of nanocrystalline $\text{MoS}_{2+\delta}$. A: HRTEM images of $\text{MoS}_{2.6}$; B: HRTEM images of $\text{MoS}_{3.4}$; C: representative FFT intensity profiles. The FFT of MoS_2 is taken from Figure B.3 A, and the other underlying FFTs can be found in Figure B.4; The in-plane lattice spacing of MoS_2 $d_{(100)} = 2.737 \text{ \AA}$ (Wildervanck et al.^[47]) is indicated. The region of interest of the FFT plots is marked with a rectangular in subfigure A and B with the corresponding color.

parameters $d_{(100)}$ and $d_{(001)}$ are in agreement to the literature values^[47] within the accuracy (see experimental) as well as to our XRD data. In some cases, a recrystallization of amorphous MoS_x under the electron beam was observed^[158,159]. In addition Xi et al.^[159] report on the transformation of amorphous MoS_x after 2 h of HER to a nanocrystalline material which is stable under the electron beam. The crystal diameter is comparable to the ones shown in Figure 4.4 and 4.5. However, they observe a lower degree of stacking of crystal planes compared to Figure 4.6, indicating a higher degree of order in our system. The transformation of the amorphous to nanocrystalline MoS_x in Xi et al.^[159] was also accompanied by an increase in hydrogen production indicating that the nanocrystalline phase is the more active and stable configuration. Together with our results this suggests that our two $\text{MoS}_{2+\delta}$ samples both represent a thermodynamic stable and active form of MoS_x .

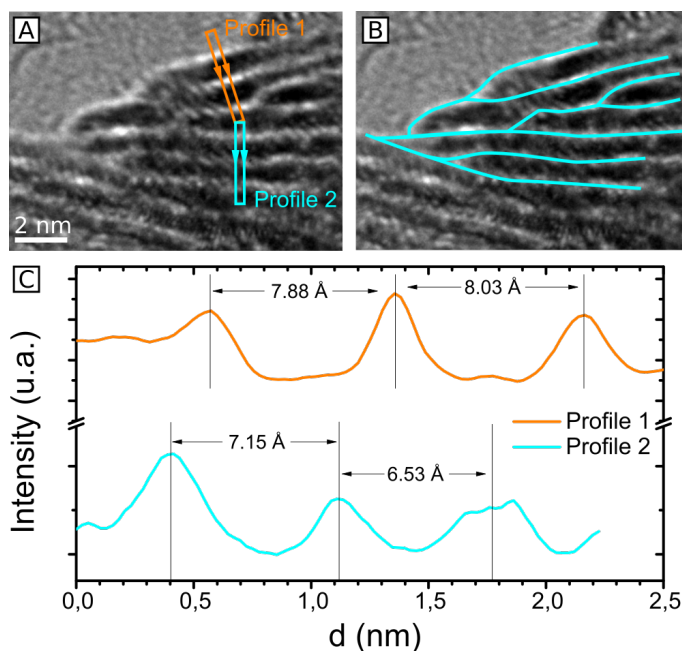


Figure 4.6.: Close up of the HRTEM image from the left side of Figure 4.5 B, showing the $\text{MoS}_{3.4}$ lattice planes in cross section view. A: Position of the intensity profile with a width of 10 px and, direction marked by arrows. B: Disclinations formed by merging MoS_x layers are highlighted by cyan lines. C: Intensity profiles indicated in A and exemplary variations in lattice distance. For the full analysis see Table B.2 and B.5

4.3. Structure Model

The combined application of electron and X-ray probes reveal that $\text{MoS}_{2+\delta}$ exhibits a nanocrystalline, partially disordered MoS_2 -like structure with a locally reduced lattice parameter a and an enlarged mean parameter c , with both showing strong fluctuations. This follows from the observed hexagonal in-plane symmetry of the crystallites, the c -axis stacking of planes and the measured fluctuations of the lattice distances revealed by HRTEM as well as diffraction techniques. A suggested structural model for $\text{MoS}_{2+\delta}$ consistent with these results is depicted in Figure 4.7. Table 4.2 compares the measured mean lattice spacing in $[001]$ and $[100]$ directions as well as their fluctuations with the literature values for MoS_2 . The results for d_{100} from TEM are in good agreement with the X-ray diffraction analysis. In addition to the small grain sizes of a few nm, the strong disorder within the nanocrystals is consistent with the broad reflexes in XRD and SAD.

In agreement with the stoichiometry of $\text{MoS}_{2+\delta}$, the excess sulfur must be present in the form of unsaturated, terminal, bridging and possibly apical sulfides and disulfides, as visible by XPS.^[23,39,40,60,61] This modification results in structural changes relative to the 2H- MoS_2 structure. Our model suggests that some parts of the struc-

	Literature ^[47]	HRTEM MoS _{2+δ}			XRD
	MoS ₂	Mean	Min.	Max	
d ₍₁₀₀₎ [Å]	2.7368	2.69 ± 0.21	2.45 ± 0.18	2.79 ± 0.03	2.69 ^{+0.16} _{-0.39}
d ₍₀₀₁₎ [Å]	12.294	12.9 ± 0.8	11.15 ± 0.19	15.93 ± 0.61	15 ⁺¹⁰ ₋₄

Table 4.2.: Comparison of the (100) and (001) lattice distances of MoS_{2+δ} found by TEM and XRD with literature values for MoS₂.^[47] The XRD uncertainty is determined by the full width half maximum (FWHM).

ture show similarities to the atomic arrangements found in [Mo₂S₁₂]²⁻ and [Mo₃S₁₃]²⁻ clusters. Like MoS_{2+δ} these clusters have also a reduced Mo-Mo distance compared to MoS₂ (see Table 4.3). The disorder in the in-plane lattice distance of MoS_{2+δ} thus reflects local sulfur-rich disorder in the form of cluster like structural units which are incorporated into the MoS₂ nanocrystals.

	MoS _{2+δ}			MoS ₂	[Mo ₂ S ₁₂] ²⁻	[Mo ₃ S ₁₃] ²⁻
	Mean	Min	Max	^[47]	^[22]	^[22]
d _{Mo-Mo} [Å]	3.11 ± 0.24	2.83 ± 0.21	3.22 ± 0.04	3.16	≈2.8	≈2.7

Table 4.3.: Mo-Mo distance of MoS_{2+δ} compared with MoS₂^[47] and the cluster anions [Mo₂S₁₂]²⁻ and [Mo₃S₁₃]²⁻.^[22]

Compared to the [100] direction, the variations in lattice spacings in the [001] direction are larger and the XRD analysis indicates an overall increased distance between the MoS₂ layers, which are only bound to each other by weak Van der Waals interactions. The previously described in-plane variations and cluster-like disorder also can lead to local alternations in out of plane sulfur positions which might affect the Van der Waals bonding distance and thus induce a varying layer spacing. In particular, the alternation of the layer spacing at the nanocrystallite edges as well as at the disclinations is very large. In addition, external stress from boundaries to other neighboring crystals can induce further lattice spacing modulations.

Our suggested model is in qualitative agreement with literature results for disordered MoS_x with 2 < x < 4. MoS_{2+δ} is generally highly disordered. The in-plane structure of the detected nanocrystals partially features a hexagonal symmetry like MoS₂. The local defect structures show similarities to [Mo₂S₁₂]²⁻ and [Mo₃S₁₃]²⁻ clusters, which correlates well with the increased sulfur content compared to MoS₂.

Hinnemann et al.^[55] studied MoS₂ nanoparticles with approximately 4 nm in diameter and 1 nm in apparent height on graphite and stated that only the edges of MoS₂ are interesting in the context of HER, as the basal plane of MoS₂ is catalytically inactive. Our structure model for MoS_{2+δ} strongly features frayed edges similar to nanocrystalline MoS₂ and due to the high defect concentration, coordinatively modified Mo sites these also appear within the basal planes. Consequently we expect that some of the active sites are similar to the report of Hinnemann et al.^[55]. But in addition, cluster like structures appear within the lattice planes as

well as at their edges and in the disclinations. These planar structures exhibit a partial stacking and ordering along the c-axis, also establishing a similarity to the MoS_2 crystal, however, with increased lattice parameters c due to small crystal sizes as well as disorder in the in-plane structure. Typically, XPS for MoS_x with $2 < x < 4$ indicates bridging and terminal disulfides as well as unsaturated molybdenum and sulfur ions.^[23,39,40,60,61] The structure observed here featuring disordered nanocrystals with a size of a few nanometers can thus explain a high density of catalytically active sites which are present at the defective nanocrystal planes as well as at their edges. This, in consequence, could very well explain the much higher HER activity of $\text{MoS}_{2+\delta}$ compared to MoS_2 .

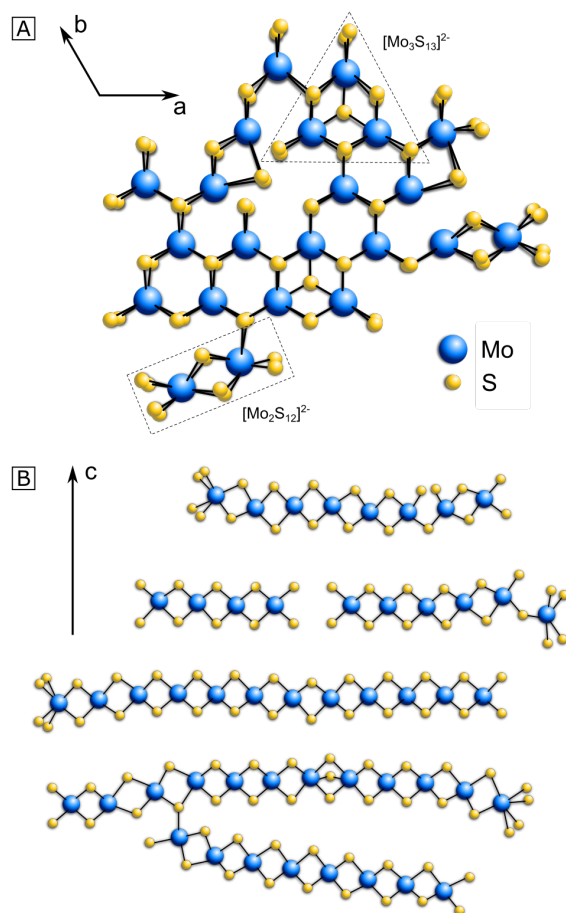


Figure 4.7.: Schematic illustration of the suggested structure model for $\text{MoS}_{2+\delta}$. The indicated a-, b- and c-axis represent the unit cell and lattice parameters of MoS_2 . A: plane view; B: out of plane view.

Wu et al.^[25] also report a reduced Mo-Mo distance of 2.778 Å for their amorphous MoS_x , which is in good agreement with this work (smallest Mo-Mo distance (2.83±0.21) Å) and suggest it as a key feature for the higher activity as the electronic structure gets even more similar to the clusters. In addition, no influence of the sulfur dimer content on the activity was observed by Wu et al.^[25]. This is in good agreement with this work, where the catalytic activity tends to correlate with Mo content. Considering also the high catalytic activity of disordered nanocrystalline MoS_x with $x < 2$ reported by Xi et al.^[159] this might indicate the larger impact of the presence of coordinately modified Mo sites and reduced lattice parameter rather than the S:Mo ratio. In addition, Ying et al.^[153] reports on the improved catalytic activity by increasing the concentration of sulfur vacancies. This supports to allocate the active site to the Mo edges. In addition, the structure model for nanocrystalline, partially disordered $\text{MoS}_{2+\delta}$ is based on stoichiometry compensating defects that change the Mo coordination and Mo-Mo bonding distance. Thus both the S:Mo ratio and the processing induced microstructure influence the crystal structure.

4.4. Materials and Methods

All chemicals were purchased commercially and, if not stated otherwise, used without further purification. Deionized water ($R = 18.2 \text{ M}\Omega$) from an Elga Veolia PURE-LAB flex 4 water purification system was used for all experiments. Crystalline MoS_2 was purchased from Sigma-Aldrich.

Synthesis of $\text{MoS}_{2+\delta}$

Ammonium tetrathiomolybdate $(\text{NH}_4)_2[\text{MoS}_4]$ was prepared following a literature procedure by McDonald et al.^[160]. The very high purity of the $(\text{NH}_4)_2[\text{MoS}_4]$ was confirmed by mass and Raman spectroscopy as well as XRD. To obtain amorphous molybdenum sulfide, a slightly modified method from the route of Li et al.^[51] was used: $(\text{NH}_4)_2[\text{MoS}_4]$ (100 mg) was dissolved in water and hydrazine ($\text{N}_2\text{H}_4 \cdot \text{H}_2\text{O}$, 0.3 mL) was added. The mixture was transferred into a steel autoclave with a Teflon inlet (45 mL), heated up to 200°C for 12 h and then allowed to cool down to room temperature. The reaction mixture was centrifuged (10 min @ 75,000 rpm), washed with THF (3 x 25 mL) as well as water (2 x 30 mL) and freeze-dried. As comparably high amounts of MoS_x were required for the XRD and TEM analyses, two batches of the product ($\text{MoS}_{2.6}$ and $\text{MoS}_{3.4}$) were synthesized due to the rather small volume of the available steel autoclave. Both MoS_x batches were obtained as black powders in a yield of ≈ 60 mg each.

Stoichiometry Determination

An Analytik Jena novAA 350 flame atomic absorption spectrometer (F-AAS) (Analytik Jena, Jena, Germany) was used in order to determine S:Mo ratios. The

calibration was performed using an ammonium heptamolybdate solution diluted by 0.03% v/v aqua regia. Prior to analysis, the samples (5 mg) were completely dissolved in aqua regia (5 ml) to oxidize molybdenum to Mo(VI). This solution was diluted to 200 ml and used without further dilution. The measurements were conducted five times for each sample and the mean value taken. The S:Mo ratios 2.6 ± 0.13 and 3.4 ± 0.17 were calculated from the initial sample weight and the F-AAS results presuming the absence of any other elements than molybdenum and sulfur. Another reason for the divergent composition could lie in the synthesis process. The addition of the reductant hydrazine is not performed in a controlled manner; neither is the solution stirred during the synthesis. This and the fact that the reaction mixture possibly contains high amounts of different sulfur species like sulfides, disulfides as well as hydrazine, ammonia and water in variable proportions could explain the differing S:Mo ratios.

X-ray fluorescence (XRF) (M4 Tornado from Bruker Corporation, Billerica, Massachusetts, USA) measurements calibrated with MoS₂ resulted in a similar S:Mo ratio of about 3. However, due to a strong peak overlap between molybdenum and sulfur, the resulting S:Mo ratio uncertainties are quite high when using XRF, energy-dispersive X-ray spectroscopy (EDS) (INCA detector from Oxford Instruments, Abingdon, England) or wavelength-dispersive X-ray spectroscopy (WDS) (JXA-8900 RL from JEOL, Akishima, Tokyo, Japan) which makes AAS the most reliable method in this case.

Electrochemistry

For the electrochemical measurements a PRINCETON Applied Research Versa Stat 4 potentiostat (AMETEK Princeton Applied Research, Oak Ridge, TN, USA) was used. All measurements were performed in a three-electrodes setup using MoS₂ resp. MoS_{2+ δ} on graphite sheets as working electrodes (WE), platinum as counter electrode (CE) in a separate compartment with a glass frit and an Ag/AgCl electrode as counter electrode (3M KCl, RE). Sulfuric acid (0.5 M, pH 0.3) served as electrolyte.

Cyclic voltammograms (CV) were recorded in a range of 0.1-(-0.5) VRHE with a sweep rate of 20 mVs⁻¹. Tafel slopes were determined from the sixth cycle (first half) of the CV. All electrochemical measurements were iR-corrected at 85%.

Electrode Preparation

To eliminate impurities from the graphite sheet, the blank electrodes were cleaned with water, isopropanol and ethanol. The electrodes were prepared following procedures published by Cui et al.^[161] 3 mg of the catalyst and 6 L of Nafion solution (5 wt %) were dispersed in 0.6 mL water/ethanol (49:50, v:v) and treated with ultrasound for 30 min 48 μ L of the ink was dropcasted onto an area of 1 cm x 1 cm of graphite sheet and dried under air at 60°C for 1 h (catalyst loading ≈ 0.24 mgcm⁻²).

XRD Analysis

For the powder diffraction measurements a Philips PW 1720 (Philips Analytical Technology GmbH) with a copper anode ($\lambda = 1.541 \text{ \AA}$) and a 5 x 0.1 mm line focus was used. The sample was placed in a pan made of brass. For data collection frames were measured for the duration of 10 s per step in 0.02° intervals of 2Θ among 5° and 91°. The data were collected with by using a graphite secondary monochromator and a proportional counter.

TEM Lamella Preparation and TEM Analysis

For the TEM analysis 5 mg of powder (MoS_{2+δ} / MoS₂) were dissolved in 1 ml of THF and then a 30 min long ultra-sonic treatment applied. One drop of this solution was then put on a carbon TEM Grid. The electron diffraction TEM investigations were performed with a Phillips CM12 (Philips Electron Optics GmbH) at 120 kV. For the high resolution TEM analysis a FEI Titan (FEI, Hillsboro, Oregon, USA) aberration corrected electron microscope with 300 keV was employed. For this microscope the information limit in high vacuum is about 0.08 nm.

Accuracy of Lattice Spacing Measurement in TEM

The TEM was calibrated using a gold reference sample to get a reliable accuracy. The dependence of the precision $\Delta d/d$ on defocus induced changes of diffuseness of the FFT reflections is much smaller than the effect of a small diffraction vector length.^[162] For each magnification, area of the FFT and measured d value, the precision $\Delta d/d$ is calculated as a function of diffraction vector length and presented in table B.5. For the average values in table 4.2, the weighted average of each lattice spacing d_{hkl} is calculated from individual measurements, taking into account the error of the individual values. The total error is the statistical deviation from the weighted average plus the highest systematic error of the single measurements. The TEM calibration was verified by using MoS₂ nanoparticles. The resulting values for MoS₂ are $d_{(100)} = (2.80 \pm 0.06) \text{ \AA}$ and $d_{(001)} = (12.8 \pm 0.7) \text{ \AA}$. They are matching our XRD data and deviate from the literature values of $d_{(100)} = 2.737 \text{ \AA}$ and $d_{(001)} = 12.294 \text{ \AA}$ obtained by x-ray diffraction in Wildervanck et al.^[47] by $\delta_{(100)} = 2.3\%$ and $\delta_{(001)} = 4.2\%$. Within error, the determined MoS₂ lattice parameters are in agreement to these XRD results. Based on the calibration, the measurement of the locally reduced $d_{(100)}$ value of MoS_{2+δ} in this work is significant.

4.5. Summary

MoS_{2+δ} was prepared by solvothermal synthesis, immobilized on electrodes and electrochemically analyzed by cyclic voltammetry and chronopotentiometry. A comparison with MoS₂ confirmed the much higher activity of MoS_{2+δ}. Hence the analyzed samples show the typical characteristics of MoS_{2+δ} which are reported in literature.^[22,23,39,60] However, by means of HRTEM, XRD and electron diffraction, the structure of MoS_{2+δ} is assigned to a highly disordered variant of MoS₂ with very small nanocrystal size and cluster like local defects. The in-plane lattice parameter shows strong local variations and is reduced locally, whereas c-axis is increased in average. Due to the nanocrystalline structure, a high concentration of edges with changed Mo coordination and Mo-Mo distance is present. Furthermore, our HRTEM observations suggest that disorder within the MoS₂ planes represent [Mo₃S₁₃]²⁻ cluster like defects. Such structural features are also involved in the formation of disclinations. Altogether, this increases the ratio of coordinatively modified Mo and is in accordance to the scaling of electrochemical activity with Mo. Our results imply that S:Mo ratios > 2 are mainly important for the HER activity due to the processing induced nano- and defect structure.

Supplementary Materials:¹ The following are available online at <http://www.mdpi.com/2073-4344/10/8/856/s1>, Figure S1: Rietveld refinement of MoS₂, Figure S2: Electron diffraction pattern of MoS_{2.6} and MoS_{3.4}, Figure S3: HRTEM images of MoS_{2+δ} used for the lattice parameter analysis in Table S5, Figure S4: HRTEM images of MoS₂ and their FFTs, Figure S5: Reduced FFT of HRTEM image from Figure 5 A & B, Figure S6: SEM images of MoS₂ and MoS_{3.4} powder, Figure S7: Cyclic voltammetry of the two MoS_x samples and MoS₂, Table S1: Comparison of d_{hkl} from XRD and SAD from Figures 2 and 3 for MoS_{2+δ} with MoS₂, Table S2: Goodness parameters and correction factor for the texture, Table S3: Refined lattice parameters and atom positions of MoS₂, Table S4: Overview of the most intense lattice planes in electron diffraction of MoS₂, Table S5: Result from the FFT analysis of HRTEM images of MoS_{2+δ}.

Author Contributions: Conceptualization, E.R., S.H., Ph.K. and C.J.; investigation, E.R., M.L.G., H.K., Ph.K., C.J.; data curation, E.R., S.H., M.L.G.; writing-original draft preparation, E.R., S.H., M.L.G. and C.J.; writing-review and editing, E.R., M.L.G., Ph.K., C.J.; supervision, H.K., Ph.K. and C.J.; All authors have read and agreed to the published version of the manuscript.

Funding: This research was funded by Deutsche Forschungsgemeinschaft (DFG), within the national priority program SPP 1613 “Fuels Produced Regeneratively Through Light-Driven Water Splitting”.

¹The figure numbers refer to the original publication. The supplementary material is also available in section B.

Acknowledgments: The authors would like to thank Max Baumung for his contribution to the TEM sample preparation and Vladimir Roddatis for practical advices in TEM work.

Conflicts of Interest: The authors declare no conflict of interest.

Interactions of Birnessite with Phosphate Buffer Anions

This whole section is a complete reproduction of the original publication^[29]

Operation of Calcium-Birnessite Water-Oxidation Anodes: Interactions of the Catalyst with Phosphate Buffer Anions

Emanuel Ronge^a, Jonas Ohms^b, Vladimir Roddatis^a, Travis Jones^d, Frederic Sulzmann^d, Axel Knop-Gericke^d, Robert Schlögl^{d,e}, Christian Jooss^{,a,c}, Philipp Kurz^{*,b}, and Katarzyna Skorupska^{*,d,e}*

originally published as a preprint in *Chemrxiv* (2020)^[29] under the terms and conditions of the CC BY-NC-ND 4.0 license. doi:10.26434/chemrxiv.13153976.v1
References, labels and arrangement of figures have been modified to suit this thesis.

^a Institut für Materialphysik, Georg-August-Universität Göttingen, Friedrich-Hund-Platz 1, 37077 Göttingen, Germany.

^b Institut für Anorganische und Analytische Chemie and Freiburger Materialforschungszentrum (FMF), Albert-Ludwigs-Universität Freiburg, Albertstraße 21, 79104 Freiburg, Germany

^c International Center for Advanced Energy Studies, Georg-August-Universität Göttingen, Tammannstr. 4, 37077 Göttingen, Germany.

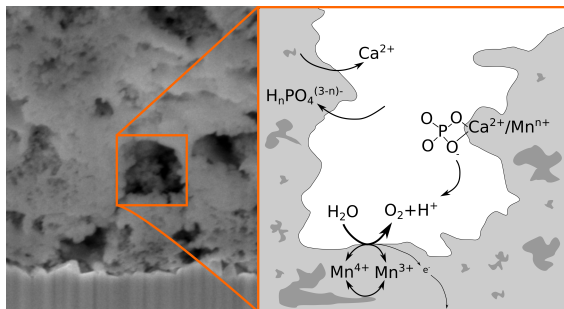
^d Max-Planck-Institut für Chemische Energiekonversion, Stiftstraße 34-36, 45470 Mülheim an der Ruhr, Germany.

^e Fritz-Haber-Institut der Max-Planck-Gesellschaft, Faradayweg 4-6, 14195 Berlin, Germany.

KEYWORDS. oxygen evolution reaction, manganese oxides, phosphates, ion exchange, electrocatalysis.

Abstract

Investigating the interfaces between electrolytes and electrocatalysts during electrochemical water oxidation is of tremendous importance for an understanding of the factors influencing catalytic activity and stability. Here, the interaction of a well-established, nanocrystalline and mesoporous Ca-birnessite catalyst material (initial composition $\text{K}_{0.2}\text{Ca}_{0.21}\text{MnO}_{2.21}\cdot 1.4\text{H}_2\text{O}$, initial Mn-Oxidation state $\sim +3.8$) with an aqueous potassium phosphate buffer electrolyte at pH 7 was studied by using various electron microscopy and spectroscopy techniques. In comparison to electrolyte solutions not containing phosphate, Ca-birnessite electrodes show especially high and stable oxygen evolution activity in phosphate buffer. During electrolysis, partial ion substitutions of Ca^{2+} by K^+ and $\text{OH}^- / \text{O}^{2-}$ by $\text{H}_n\text{PO}_4^{(3-n)-}$ were observed, leading to the formation of a stable, partially disordered Ca-K-Mn- $\text{H}_n\text{PO}_4\text{-H}_2\text{O}$ layer on the outer and the pore surfaces of the electrocatalyst. In this surface layer, Mn(III) ions are stabilized, which are often assumed to be of key importance for oxygen evolution catalysis. Further-more, evidence for the formation of $[\text{Ca}/\text{PO}_4/\text{H}_2\text{O}]$ -complexes located between the $[\text{MnO}_6]$ layers of the birnessite was found using Ca 2p and Ca L-edge the soft X-ray synchrotron-based spectroscopy. A possible way to interpret the obviously very favorable, “special relationship” between (hydrogen)phosphates and Ca-birnessites in electrocatalytic water oxidation would be that $\text{H}_n\text{PO}_4^{(3-n)-}$ anions are incorporated into the catalyst material where they act as stabilizing units for Mn^{3+} centers and also as “internal bases” for the protons released during the reaction.



5.1. Introduction

One major bottleneck for the production of hydrogen by electrochemical water splitting is the sluggish kinetics of the oxygen evolution reaction (OER).^[163,164] Here, the rational design of better electrocatalysts requires a better understanding of the mechanisms controlling OER activity and stability.

Inspired by the oxygen-evolving complex (OEC) of photosystem II - a Mn_4CaO_5 cluster which constitutes the OER active site in biological photosynthesis - a large variety of manganese oxide (MnO_x) catalysts has been studied as potential synthetic OER catalyst materials.^[26,73,75-79,165,166] Beside some crystalline binary or ternary manganese oxides, disordered MnO_x materials with a low degree of long-range order often show a high intrinsic catalytic activity.^[18,26,74,84,86,167-170] For some crystalline systems, the formation of catalytically much more active nanocrystals or disordered

surface layers during the OER process has been observed.^[75,76,171–173]

Among the different less-ordered manganese oxides, birnessites have been identified as especially promising OER catalysts showing both high activity and stability.^[80,84,168] The birnessite structure is built up from edge-sharing $[\text{MnO}_6]$ -octahedra forming extended layers. The stacking of the layers in *c*-direction depends on the amount of incorporated water and the type of additional cations and typically results in an interlayer distance of is about 7 Å.^[84,168,174] Many different cations can be present in birnessite-type materials (*s*-block metal cations are most common) and these lead to different degrees of crystalline order as well as different ion exchange properties in contact with aqueous solutions.^[175,176]

Previous studies have shown that the OER activity of birnessites is influenced by various parameter such as their crystallinity, type and concentration of additional cations and synthesis parameters (especially sintering temperatures). For cation incorporation into the birnessite structure, an upper concentration limit is usually observed, which is e.g. $\text{Ca} : \text{Mn} \sim 0.6$ for Ca^{2+} .^[17]

In previous investigations on birnessite-catalyzed OER by some of us, a synthetic birnessite with an approximate composition of $\text{K}_{0.20}\text{Ca}_{0.21}\text{MnO}_{2.21} \cdot 1.4 \text{H}_2\text{O}$ emerged as especially active catalyst material in both chemical (Ce^{4+} oxidation) and electrochemical OER screenings.^[17,80] When immobilized onto FTO substrates, stable current densities of $\sim 1 \text{mA} \cdot \text{cm}^{-2}$ could be reached in neutral, phosphate buffered electrolytes at overpotentials of $\eta \sim 500 \text{mV}$.^[89]

Detailed X-ray diffraction and X-ray absorption spectroscopy investigations of this and closely related synthetic Ca-birnessites indicated little long-range, in-plane order and also irregular stackings of the $[\text{MnO}_6]$ -layers.^[84,86,168] N_2 sorption experiments revealed a mesoporous structure with quite high surface areas of SBET $\sim 50\text{-}250 \text{m}^2 \cdot \text{g}^{-1}$ (mainly depending on the reaction temperatures used during post-synthetic sintering) and average Mn oxidation states were found to be in the range between +3.3 and +4.0.^[17,84,86,168] The latter observation indicates, that the Mn valence state within the birnessite structure can be reversibly changed - a material property which might be of general, crucial importance for OER catalysis by transition metal oxides.^[20,26,86,177–180]

Additionally, manganese oxides with oxidation states close to +3.0 exhibit labile Mn-O bonds due to the typical Jahn-Teller distortions of the octahedral coordination spheres of Mn^{3+} cations (*hs-d⁴*), which might promote OER catalysis.^[73] Indeed, oxides rich in Mn^{3+} often show much higher OER activities than Mn(IV) materials.^[18] On the other hand, the higher charge of Mn^{4+} seems to inhibit the decomposition of Mn(IV) compounds, as e.g. exemplified by the OEC of photosystem II.^[180]

Concerning MnO_x corrosion in aqueous media, the Pourbaix diagram for Mn suggests dissolution via solvation of Mn^{2+} for acidic pH, whereas dissolution of Mn via the formation of permanganate MnO_4^- at high anodic potentials is expected for neutral to alkaline pH.^[90] Both corrosion routes would result in Mn depleted surface layers, and these have indeed been found experimentally.^[83] On the other hand, such corrosion processes might be compensated by repair steps, as e.g. found by

Najafpour et al. for reactions of a $K_{0.25}$ -birnessite with Ce^{4+} . Here, the corrosion products MnO_4^- and Mn^{2+} were found to react back to a stable, layered $(K,Ce)MnO_x$ compound, which catalyzed the OER for 15 days without degradation or leaching of manganese.^[83,181] Finally, it has been proposed that redox inert ions like Ca^{2+} can stabilize MnO_x and / or facilitate the formation of modified and open structures for water oxidation.^[181,182]

Overall the literature data discussed so far hints at a general importance of additional cations for the OER performances of birnes-sites, not only by influencing the Mn valence state but also by increasing the stability of these MnO_x -based (electro)catalysts. Consequently, the composition of the electrolyte should be carefully chosen in order to control possible cation exchange processes.

In this study, Ca-birnessite coated electrodes were prepared by screen printing the previously mentioned, optimized OER catalyst material $K_{0.20}Ca_{0.21}MnO_{2.21} \cdot 1.4 H_2O$ on fluorine-doped tin oxide (FTO) as conductive support material following an established and already optimized method.^[89] In order to study the influence of ion exchange reactions on the electrochemical OER activity and stability as well as the material's microstructure, the Ca-birnessite anodes were operated in three different, near neutral aqueous electrolyte solutions: a potassium phosphate buffer (pH 7), solutions of imidazolium sulphate (pH 7.4) and potassium sulphate (pH 7). Structural analyses of the electrodes' surfaces and bulk material were performed using transmission and scanning electron micro-copy (TEM/SEM). To gain further insights into the interaction of the electrolyte with the MnO_x catalyst, we investigated the chemical compositions, Mn valence states and coordination environments by electron energy-loss spectroscopy (EELS) element mapping, energy-dispersive X-ray spectroscopy (EDX), X-ray photoelectron spectroscopy (XPS) and near edge X-ray absorption fine structure (NEXAFS) at the Ca and Mn L-edges. The results hint at a special, favorable interaction between birnes-sites and phosphate-containing electrolytes, explaining why phosphate buffers might be the medium of choice for birnessite-catalyzed OER at near-neutral pH.

5.2. Experimental Section

Please consult previous publications and the supplementary in-formation for details of the synthesis of the Ca-birnessite catalyst material, the preparation of MnO_x -coated electrodes by screen-printing, the exact compositions of the electrolytes as well as the electrochemical measurements.^[80,89]

SEM, EDX and cross-section imaging. SEM analysis was carried out with a Nova NanoSem 650 in-situ SEM from FEI. A “through the lens” (TTL) detector was used to take images at an acceleration voltage of 10 kV. For energy-dispersive X-ray spectroscopy (EDX), an Oxford Instruments X-Max detector was employed. The quantification of the Ca/Mn and P/Mn ratios was performed with line-scans of a minimum of 10 points and 100s of acquisition time per point over a range of $\sim 60 \mu\text{m}$. The EDX acceleration voltage was 20 kV. Cross-section samples used for SEM imaging were cut using a Nova Nanolab 600 focused ion beam (FIB) system from FEI (ion acceleration voltage 30 kV). For the pristine sample, a protective layer of platinum was first deposited via electron beam induced deposition, followed by a thicker Pt layer fabricated by ion beam induced deposition. After rough cuts with 3 nA currents, cleaning cuts of the cross sections with 0.3 nA were carried out. The images of the cross sections were taken at an acceleration voltage of 5 kV and an angle of 52° using the TTL detector.

TEM lamellae preparation and (S)TEM analysis. Electron-transparent cross-section lamellae of $\sim 4 \mu\text{m}$ thick electrodes before and after electrolysis were prepared by means of the FIB system described above. In order to avoid an overlap of the P and Pt signals, no protective Pt layer was applied in this case. For the 200 nm thin electrodes, the lamellas were prepared by conventional cutting, dragging and ion milling using a Gatan Model 691 precision ion polishing system (PIPS). The TEM investigations including imaging, electron energy loss spectroscopy (EELS) and EDX-measurements were performed using an aberration corrected FEI Titan electron microscope with 300 keV electrons. For this microscope, the information limit in high vacuum is about 0.08 nm. High angle annular dark field (HAADF) imaging was performed in scanning transmission electron microscopy mode (STEM). The STEM capability combined with EELS gives access to the local chemical composition with a spatial resolution of $\sim 0.2 \text{ nm}$ and an energy resolution of $\sim 1.3 \text{ eV}$. The following energy edges were used for the EELS-Mapping: Ca - L-edge, Mn - L-edge, O - K-edge, P - K-edge. The TEM EDX analyses were carried out with an Oxford Instruments X-Max detector and electron diffraction patterns were collected with a Phillips CM12 at 120 kV.

X-ray spectroscopy. Near-ambient pressure X-ray photoelectron spectroscopy (NAP-XPS) measurements were carried out using a setup located at the Innovative Station for In Situ Spectroscopy (ISISS) beamline at the BESSY II synchrotron of the Helmholtz-Zentrum Berlin.^[183] For the as-prepared oxide, $\sim 20 \text{ mg}$ of Ca-birnessite powder was pressed into a pellet ($\emptyset \sim 2 \text{ mm}$) by applying a force of 1 ton for 1 min. Ca-birnessite-coated FTO slides were directly used for measurements as prepared or after electrochemical operation. In each case, the samples were mounted on a sapphire sample holder and positioned $\sim 1 \text{ mm}$ in front of the first aperture of the differentially pumped electrostatic lens system. Measurements were conducted using an incident X-ray beam spot of roughly $100 \times 300 \mu\text{m}$ at a pressure of 10^{-4} mbar . A pass energy of 20 eV was used for XPS measurements and the inelastic

mean free path (IMFP) of the photoelectrons was calculated using the model of Tanuma et al.^[184]. The binding energies of measured XPS spectra were calibrated using an O 1s second order peak with a theoretical photon energy of 730 eV. The X-ray photoelectron spectra were recorded at different excitation energies in order to obtain IMFPs of 0.7 nm (for $E_k = 200$ eV) or 1.7 nm ($E_k = 830$ eV), respectively. The deconvolution of the XP spectra was performed using the software CasaXPS after subtraction of the Shirley background.

To perform NEXAFS measurements, the photon energy was scanned while the total electron (TEY) and Auger electron (AEY) yields were counted. Ca L-edges spectra were recorded for photon energies between 342 and 362 eV, while the photon energy was scanned between 625 and 660 eV to cover the Mn L₃- and L₂-edges. For clarity, only the data for the Mn L₃-edge is presented. To assess possible beam damage, which is a well-known problem for NEXAFS of manganese oxides,^[185] stability tests were performed. Figure 5.6 presents three Mn L-edge scans recorded successively on the same spot of three studied samples. The deviations between subsequent scans indicate that Mn ions in the samples are reduced by the beam, but also that the observed spectral changes are small enough so that a meaningful analysis of the spectra is well possible.

5.3. Results and Discussion

5.3.1. Electrochemistry

The number of possible electrolytes for OER experiments is generally limited as it is of particular importance in OER electrocatalysis that the electrolyte species are themselves redox-inert at strongly oxidizing conditions in water. Among others, the study presented here tries to provide answers to the following two questions concerning OER electrocatalysis by MnO_x in near-neutral conditions: 1) why is the use of a buffering electrolyte generally beneficial and 2) why are phosphate containing media apparently especially well-suited?^[26] Given the general constraint of redox-inertness presented above, we chose the following three electrolytes in order to be able to address these questions experimentally: 1) potassium (di)hydrogen phosphate as a typical phosphate-buffered electrolyte; 2) imidazolium sulfate as a buffering, but phosphate-free medium and 3) potassium sulfate as a solution which is both phosphate-free and not possessing any buffer qualities at pH = 7.

In Figure 5.1, chronoamperometry traces for the three different electrolyte systems are presented. In each case, identically prepared Ca-birnessite / FTO - anodes were immersed in the respective media and an overpotential of $\eta \sim 500$ mV was applied for a time of 1 h, while the OER current density was recorded. For details concerning these measurements, please consult ref.^[17].

Interestingly, we find very different j vs. t -traces for the three investigated solutions, despite their virtually identical pH-values and the fact that the applied oxidation potentials were iR-compensated to correct for conductivity differences. In

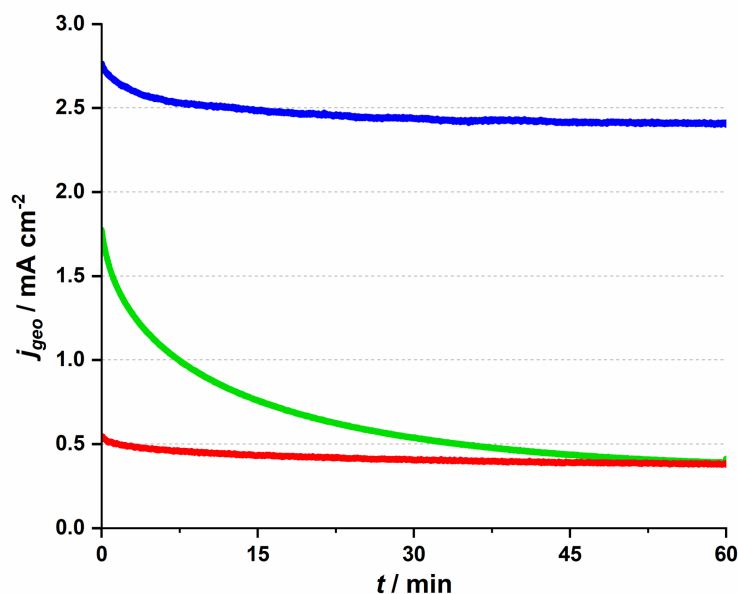


Figure 5.1.: Chronoamperometry of Ca-birnessite/FTO electrodes at 1.71 V vs. RHE ($\eta = 490$ mV) in three different, near neutral electrolytes (all 70 mM): phosphate buffer (pH 7, blue trace), imidazolium sulfate buffer (pH 7.4, green trace) and potassium sulfate solution (pH 7, red trace). CV can be found in Figure C.1.

all three cases we find that current densities are significantly higher for the first ~ 2 min of the experiment, but already here the j observed during the very first phase for phosphate ($\sim 2.7 \text{ mA} \cdot \text{cm}^{-2}$) is about 50% higher than the value for imidazolium ($\sim 1.8 \text{ mA} \cdot \text{cm}^{-2}$), while the current for potassium sulfate is very low ($\sim 0.2 \text{ mA} \cdot \text{cm}^{-2}$). As already observed in other studies, we again find the current density in phosphate reaches a rather stable value after ~ 1 h of operation (here with a current of $\sim 2.5 \text{ mA} \cdot \text{cm}^{-2}$).^[17] The higher currents found during the first phase of OER electrocatalysis were previously explained by Mn-centered oxidation events occurring “on top” of the OER current, an explanation e.g. supported by XAS data for the Mn K-edge where a Mn oxidation from an average state of $\sim +3.3$ to $\sim +3.7$ was detected for the Ca-birnessite under electrocatalytic conditions.^[89]

For imidazolium, such a steady-state is reached after ~ 1 h as well, but here the decrease in current over the first phase is dramatic, leaving a remaining current density of only $\sim 0.5 \text{ mA} \cdot \text{cm}^{-2}$ after 1 h - and thus less than a third of the starting value. This low current density is the same as observed for the non-buffering potassium sulfate electrolyte during the entire chronoamperometry experiment.

The OER electrocatalysis traces shown in Figure 5.1 thus clearly demonstrate that 1) a buffering electrolyte solution seems to be generally necessary if significant OER currents are to be reached over significant electrolysis times (phosphate / imidazolium buffers vs. potassium sulfate) and that 2) a phosphate buffer is apparently an exceptionally good choice for OER electrocatalysis by MnO_x at pH 7,

as the also buffering, but phosphate-free imidazolium system both fails to reach the initial current densities found for phosphate by far and also lacks long-term stability.

Next, we were of course eager to identify possible reasons for the profound differences in the electrolysis experiments. For this, we first turned to electron microscopy and X-ray spectroscopy in order to identify differences in morphology and / or elemental composition of the catalytic Ca-birnessite layer after continuous electrocatalysis in the three different solutions.

5.3.2. Investigations of morphology changes and ion-exchange processes of the catalyst layer by SEM, TEM and EDX

Four different types of samples were investigated by electron microscopy: 1) reference samples of pristine Ca-birnessite electrodes; 2) electrodes after use as water oxidation anodes for different electrolysis times in 70 mM phosphate or 3) 70 mM imidazolium sulfate buffer and 4) samples which had been immersed in a 70 mM phosphate buffer without applying an electrochemical potential. To facilitate the electron microscopy measurements, we prepared Ca-birnessite electrodes with a reduced catalyst layer thickness of $\sim 0.2 \mu\text{m}$ for some of the measurements.

The scanning electron microscopy (SEM) images of Figures 5.2 A-D show representative parts of the surface as well as cross-sections of the electrode layer. Clearly visible are agglomerations of particles with a size of a few hundred nanometers forming a rough surface structure. In addition, there are surface cracks which are most likely a result of gaseous H_2O and CO_2 (the latter from carbon-oxidations, see XPS section below) leaving the electrode during the annealing procedure. These observations confirm that the already known mesoporosity and large surface area of the Ca-birnessite powder²⁷ are not greatly affected by the fabrication process. The pore morphology is e.g. well illustrated by the SEM cross-sections, where small pores of diameters between 10 and 300 nm as well as large crack-like openings with a width of several micrometers are visible (Fig. 5.2 C and 5.2 D), supporting a previous characterization of the Ca-birnessite as a mesoporous material with a large surface area.^[80]

High-resolution transmission electron microscopy (HRTEM) images show the presence of nanocrystals for both the freshly prepared electrodes and also the electrodes after electrolysis for which a birnessite phase could be assigned by the analysis of the electron diffraction data (see ESI, Figs. C.2 and C.3).

Post-operando measurements using electron diffraction, XRD and SEM show that neither 9 h of electrochemical water-oxidation electrolysis nor extended immersion of the electrode into a phosphate-containing electrolyte lead to significant changes of the Ca-birnessite layer, therefore confirming previous Raman and XAS results that the birnessite oxide phase and the overall morphology of the catalyst layer is retained during OER.²⁸ An important exception to this is the morphology of the electrode surface, where a thin new surface layer is formed during electrolysis which

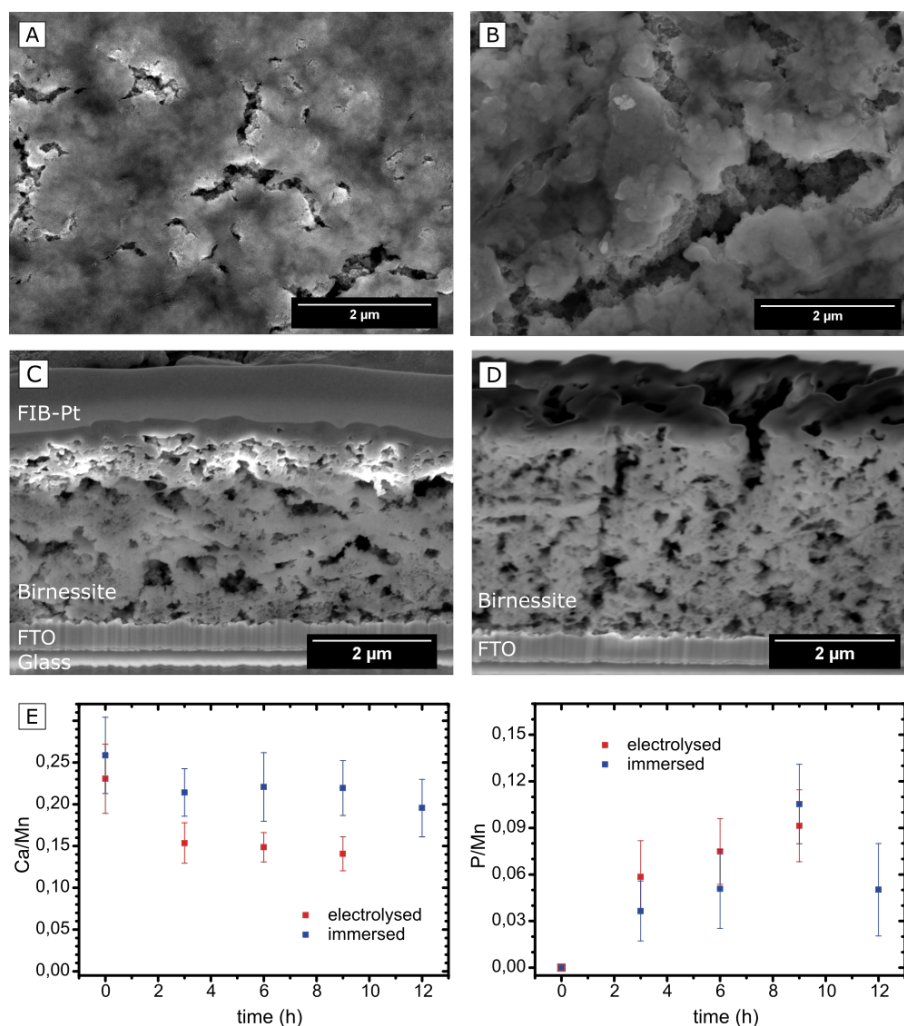


Figure 5.2.: SEM images of Ca-birnessite electrodes. Top views of (A) a pristine electrode; (B) an electrode after 9 h of electrolysis in 0.07 M phosphate buffer (pH 7, $\eta = 530$ mV); cross-sections of a pristine sample with a protective layer of platinum (C) and a sample after electrolysis (D) without protection layer; (E) EDX-SEM measurements of changes of the Ca/Mn and P/Mn ratios over time for electrodes subjected to electrolysis in phosphate buffer (red data points) in comparison to samples immersed in phosphate buffer without applying an electrochemical potential (black data points).

is visible in the TEM images (Fig. 5.3 and ESI, Fig. C.2).

Despite the apparently unchanged MnO_x -structure, SEM-EDX indicates that the electrocatalytic process induced significant changes of the average elemental composition for the entire volume of the oxide layer. The calcium concentration decreased markedly, especially during the first 2 h of electrolysis from an initial Ca : Mn ratio of 0.24 : 1 to ~ 0.14 : 1 (Fig. 5.2 E). This value seems to represent a new equilib-

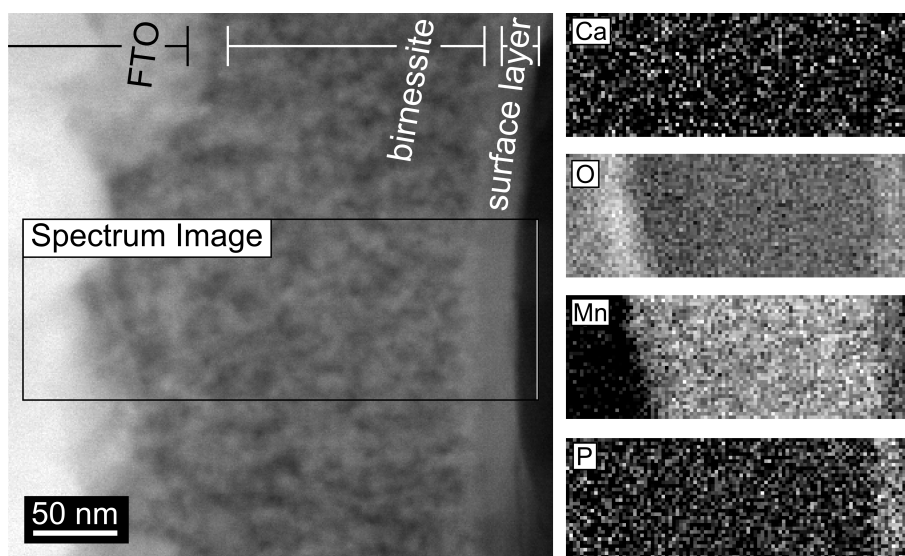


Figure 5.3.: HAADF STEM image (left) and EELS element mapping (right) of a 200 nm thick birnessite layer used during 12 h for electrolysis. The FTO substrate is on the far left, the exposed anode surface on the far right part of the images.

rium concentration as it then remains constant after ~ 6 h for the following hours of the electrolysis. In contrast, the Ca : Mn ratio of samples which are just immersed in phosphate buffer does not change significantly within the error margin of the detection method. From this we conclude that calcium is not simply dissolved out of the material but rather actively exchanged during the electro-catalytic process.

Given the importance of the electrolyte composition to reach high catalytic current densities (see Fig. 5.1), a closer look at the distribution of the elements within the material is required. Thus, high-angle annular dark field (HAADF) STEM images and EELS map-pings of a 200 nm thick electrode after 12 h of electrolysis at $\eta = 530$ mV were recorded (Fig. 5.3). EELS confirmed the formation of a ~ 25 nm thick, phosphorous-rich surface layer (far right part of the images in Fig. 5.3). This surface layer also contains manganese, oxygen and (very little) calcium. Based on the EELS mapping, we however cannot make a statement about the presence of phosphorous in the entire volume of the catalyst layer, because the phosphorous K edge at 2146 eV is too weak to detect phosphorous concentrations below ~ 5 atom%. On the other hand, we were able to detect P in the entire birnessite-layer using TEM-EDX, as EDX is much more sensitive for P but unfortunately does not offer space resolution. For a sample with a thickness of $\sim 4 \mu\text{m}$ that had been operated as OER anode for 9 h, the average P : Mn ratio for bulk birnessite was determined by TEM-EDX as $\sim 0.15 : 1$ (Fig. 5.4) and thus as very similar to the ratio reported above as the final state of the exchange equilibrium after 9 h of operation (Fig. 5.2 E). However, despite of the good agreement of the average values, the fluctuations of the local P : Mn ratios are in the order of $\sim 65\%$. As can be seen in Figure 5.4 A, there is a

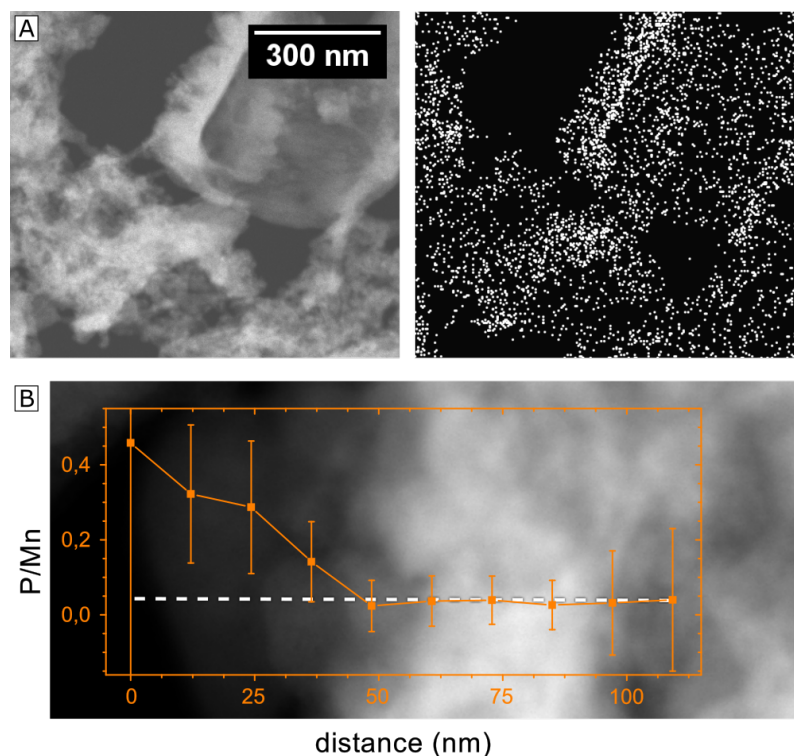


Figure 5.4.: (A) EDX element mapping for a $\sim 4 \mu\text{m}$ thick birnessite electrode after 9 h of electrolysis ($\eta = 530 \text{ mV}$). left: HAADF STEM image of the mesoporous oxide structure; right: EDX map of phosphorus for the same part of the oxide layer (EDX sum-spectra in Fig. C.4 A). The color levels of the phosphorus map were adjusted for better visibility; (B) EDX line scan from a pore surface into a nanocrystalline dense area of the same lamella as shown in B. Foreground: EDX line scan of the P : Mn ratio; Background: (HAADF) STEM image of the area of the line scan. The dashed line shows the location of the scan.

correlation between the phosphorous signal in the EDX map and the contrast of the STEM-image (which is a measure of the local lamella thickness).

Altogether, the element mapping data offers strong evidence for the presence of phosphorous in the entire birnessite volume. The detected variations of the phosphorous concentration can partially be explained by variations of the sample thickness, but also reflect real fluctuations within the nanocrystalline material. A further explanation can be found by a closer look at Figure 5.4 B. Here, an EDX line scan over a distance of only 100 nm indicates a much higher P : Mn ratio close to the surface of an inner pore of the birnessite film in comparison to the denser bulk of the material. This observation might also represent an early stage of the formation of a phosphorous-rich surface layer similar to the feature at the outer electrode surface shown in Figure 5.3. Additional EDX line scans at high spatial resolution were recorded and these are also in agreement with the general conclusion that phospho-

rous is mainly located on the surfaces of the birnessite nanocrystals (see ESI, Fig. C.5).

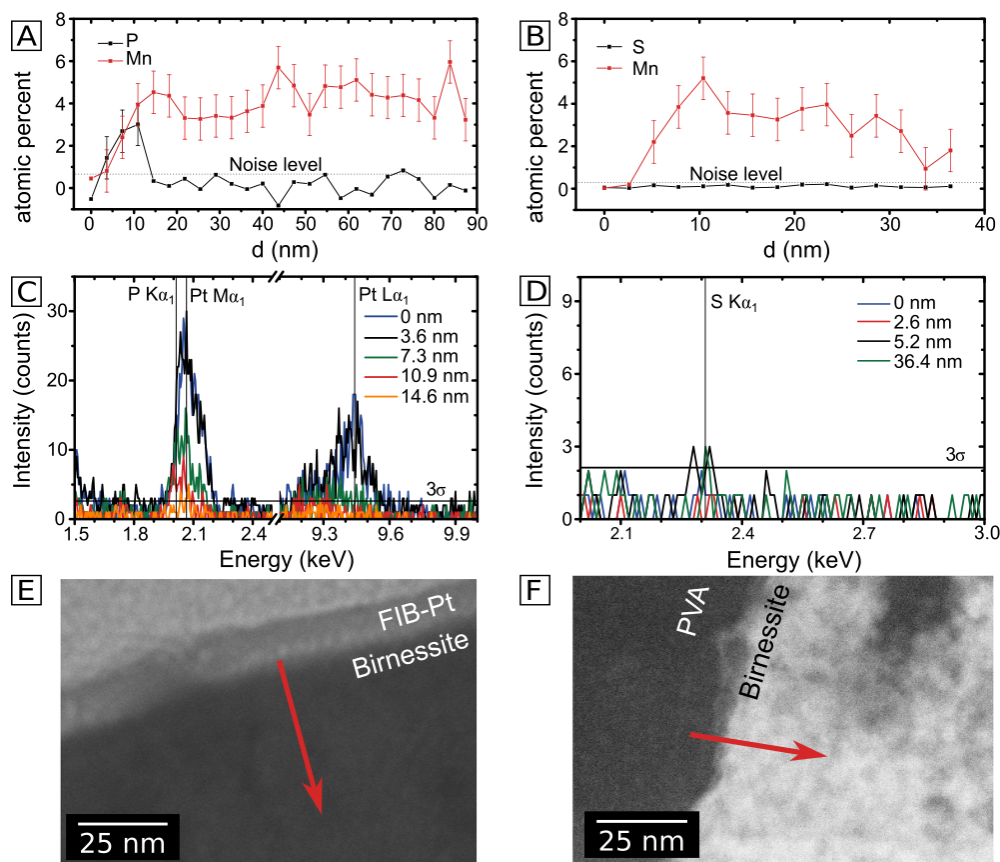


Figure 5.5.: Comparison of 200 nm thick birnessite electrodes after 12 h of electrolysis in 70 mM phosphate buffer (left column) and imidazolium sulfate (right column). (A-B): EDX line scans taken at cross sections of the electrode surface, where the surface position is set to 0 nm, the dotted line indicates the noise level of the EDX measurement; (C-D): corresponding EDX spectra taken at different positions, the horizontal line represents the 3σ level of the noise; (E-F): HAADF image of the position of the line scans.

In order to investigate whether the anion-exchange-processes during electrolysis are unique for the P / Mn couple, we compared the observations for the phosphate buffer to the buffering, but phosphate free imidazolium electrolyte. Here, the ion exchange processes were analyzed by transmission electron microscopy for 200 nm thick Ca-birnessite layers after 12 h of electrolysis. In Figures 5.5 A, C and E, EDX line scans of the electrode after an electrolysis in the phosphate buffer are shown. Similar to Figure 5.4, a significantly higher P : Mn ratio can be observed. Despite the overlap off the Pt and P peaks in den EDX spectra, the data indicates a significant P concentration in the subsurface region down to 10 nm. In contrast, Figures 5.5 B,

D and F show the same dataset for a sample after electrolysis in the imidazolium sulfate electrolyte. Interestingly, here the sulfur signals (which would indicate sulfate binding) are barely above the noise level. We conclude that, unlike for phosphate, no sulfate containing surface layer is apparently formed during OER electrocatalysis in the imidazolium sulfate electrolyte. This interpretation is also supported by SEM-EDX measurements for a 4 μm thick sample after 9 h of electrolysis in imidazolium sulfate, where no sulfur signal was detected (see ESI, Fig. C.4 B). For the Ca / Mn ratio, a value of 0.11 ± 0.06 could be calculated from the SEM-EDX data, indicating partial removal of calcium from the material to a very similar degree as found before for phosphate.

In summary, the presented electron microscopy results confirm that the mesoporous calcium-manganese oxide used here as electrocatalyst retains its nanocrystalline, birnessite-like structure during the electrolysis process, even as at least one third of the initially present Ca^{2+} ions are lost and / or replaced during electrocatalysis. For the phosphate buffered electrolyte, P enters the entire volume of the birnessite material. In addition, a P-rich oxide layer with a thickness of 15 - 20 nm forms at the outer surface of the electrode. After extended electrolysis, phosphorous can finally be found all over the sample, but its distribution appears to be inhomogeneous as the inner surfaces of the pores and the surfaces of the nanocrystals show much higher P-concentrations than the dense, nanocrystalline parts of the Ca-birnessite. The observed high and stable catalytic activity might thus be correlated to the formation of a P-containing, calcium-manganese oxide surface layer acting as “true” OER electrocatalyst.

5.3.3. Ca-Birnessite/electrolyte interactions probed by XPS and NEXAFS

The results from the previous sections indicate that different ion exchange processes take place when the Ca-birnessite material is used as OER electrocatalyst in phosphate buffer: Ca ions are partially exchanged and phosphate ions enter the material. In contrast, no sulfur incorporation was detectable after electrolysis in imidazolium sulfate. These different ion interactions, the accompanying changes of the Mn oxidation states and the role of calcium were now studied in more detail using X-ray spectroscopy methods.

X-ray photoelectron spectroscopy (XPS) and near edge X-ray absorption fine structure spectroscopy (NEXAFS) were performed with the aim to gain insights into both the elemental composition and the chemical bonding situation. Such measurements typically probe the material close to the electrode surface (the penetration depth of a few nanometers) and thus have to be seen as complimentary e.g. to the previously carried out XAS measurements at the Mn K-edge,³⁰ as well as the EDX and SEM experiments described above, all of which provide information about the entire μm -thick oxide layer. Similar to the previous section, XPS and NEXAFS spectra were recorded for four different types of samples: 1) the synthetic

Ca-birnessite powder, 2) pristine Ca-birnessite electrodes, 3) electrodes after 16 h of operation at +1.77 V vs. RHE ($\eta = 540$ mV) in 70 mM phosphate buffer and for comparison 4) in 70 mM imidazolium sulfate buffer.

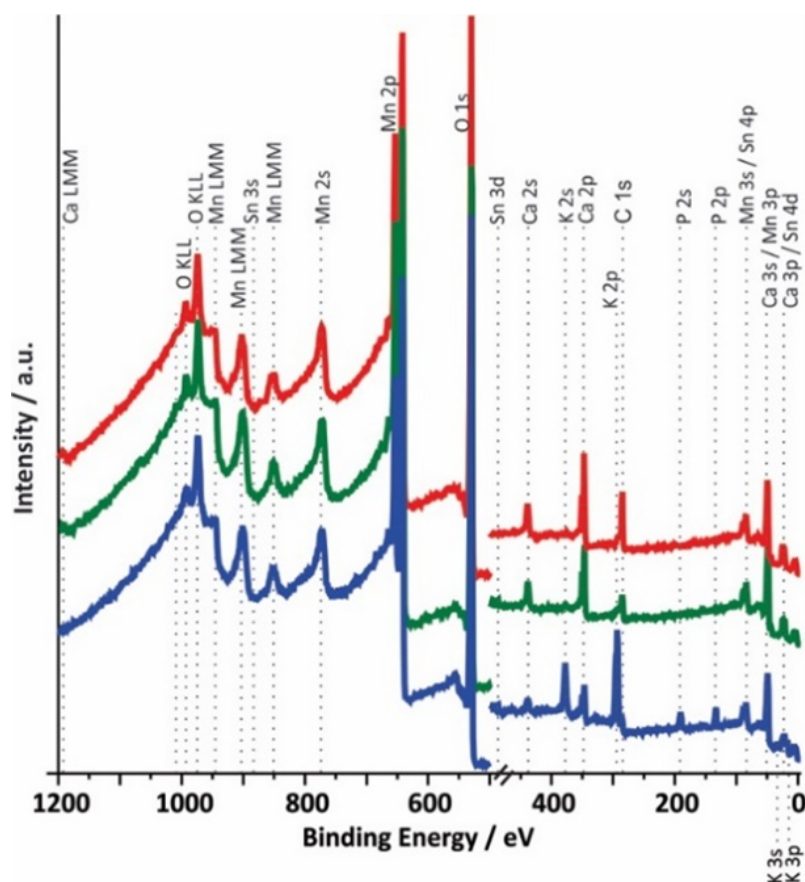


Figure 5.6.: X-ray photoelectron survey spectra (XPS, $h\nu = 1486.7$ eV) of different Ca-birnessite samples. red: synthetic Ca-birnessite powder, green: screen printed, 10 μ m thick Ca-birnessite layer on FTO substrate after annealing at 450°C and blue: XPS of an electrode after 16 h of OER electrocatalysis in 0.1 M phosphate buffer ($\eta = 540$ mV).

XPS survey spectra for samples 1 to 3 between 0 and 1200 eV are shown in Figure 5.6. As expected for a calcium containing manganese oxide, the most intense signals in all spectra are observed for the O 1s and the Mn 2p electrons and calcium lines can also be found in all cases. The presence of weak tin signals from the underlying FTO substrate confirms the already detected cracks and/or the porosity of the catalyst layers, which allows some photons to reach the underlying SnO₂:F support material. In addition, freshly prepared electrodes contain a significant amount of carbon, which must originate from the binder substances used during the printing process as carbon is not visible in the spectrum of the synthetic oxide on its own.

The most obvious differences between the spectra recorded for Ca-birnessite electrodes before and after 16 h of OER electrocatalysis in phosphate buffer are the

appearances of additional signals for potassium and phosphorous in the spectral region between 100 and 400 eV (Fig. 5.6, blue trace), which coincide with a marked decrease of the Ca peak intensity. On the other hand, the fact that the XPS spectra of Figure C.6 are overall very similar again confirms that the electrocatalyst layer retains the characteristics of a layered calcium manganese oxide even after extended electrolysis time. However - and in full agreement with the results from the previous section - we also observe significant changes of the chemical composition caused by the electrocatalytic process (this time for the zone close to the surface accessible to XPS): most of the carbon and some calcium leave the MnO_x -layer, while potassium and phosphate from the electrolyte enter the material. In case of the imidazolium sulfate electrolyte, no S 1s line was found and additionally the Ca signals in the survey spectrum are not detectable any more after electrochemistry (see ESI, Fig. C.7). Thus XPS confirms that very different ion exchange processes are at play when these two buffer systems interact with the Ca-birnessite catalyst during OER. In order to obtain more detailed information about the chemical environment of the different elements, we also analyzed the Mn and Ca L-edge spectra in combination with the XPS data for Mn 2p, O 1s, P 2p and Ca 2p.^[89,186–189] The spectra were measured at kinetic electron energies of 200 eV or 830 eV which relate to inelastic mean free paths (IMFP) for the electrons of ~ 1 or ~ 2 nm, respectively. The NEXAFS spectra were taken both in the detection modes total electron yield (TEY, probing depth 3 - 10 nm) as well as Auger electron yield (AEY, probing depth < 1 nm). The same spectral features were found in both modes and thus only the TEY spectra are shown in Figures 5.7 and 5.8 (see also ESI, Fig. C.6).

The O 1s XP spectra show contributions from water, Mn-bound hydroxide and bridging μ -oxido ligands between two Mn centers (see ESI, Fig C.8). A comparison of the data for the different electron energies indicates (as expected) a higher concentration of hydroxide groups and water at the surface of the samples compared to the underlying oxide volume. Furthermore, the spectral differences between the three samples show that the hydroxide concentration of the precursor powder is higher than that of the annealed electrode, but smaller than in the used electrodes. This is also expected, as the calcination step at 450°C used for the electrode preparation should result in the elimination of OH^- and/or H_2O from the material, while the exposure to the aqueous medium during electrolysis will result in a renewed binding of these species. The shoulder appearing at 530.8 eV for the sample after electrochemistry can be connected to phosphates originating from the electrolyte.^[190,191] As can be seen in Figure C.8, the surface of the electrode ($E_b = 200$ eV) shows a more pronounced signal related to the phosphate electrolyte residuals.

To gain insights into the oxidation states of the manganese species located on the surface of the electrode, NEXAFS spectra were taken at the Mn L-edges and the recorded Mn L3-edge spectra are shown in Figure 5.7. The Mn 2p spectra for all the samples were also measured (ESI, Fig. C.16). Due to significant multiplet splitting of the three oxidation states of manganese (II, III, IV), and the overlapping binding energy for these multiplet splitting structures we decided to focus on the Mn L-edge (NEXAFS) analysis. From comparisons of reference data^[192] with the

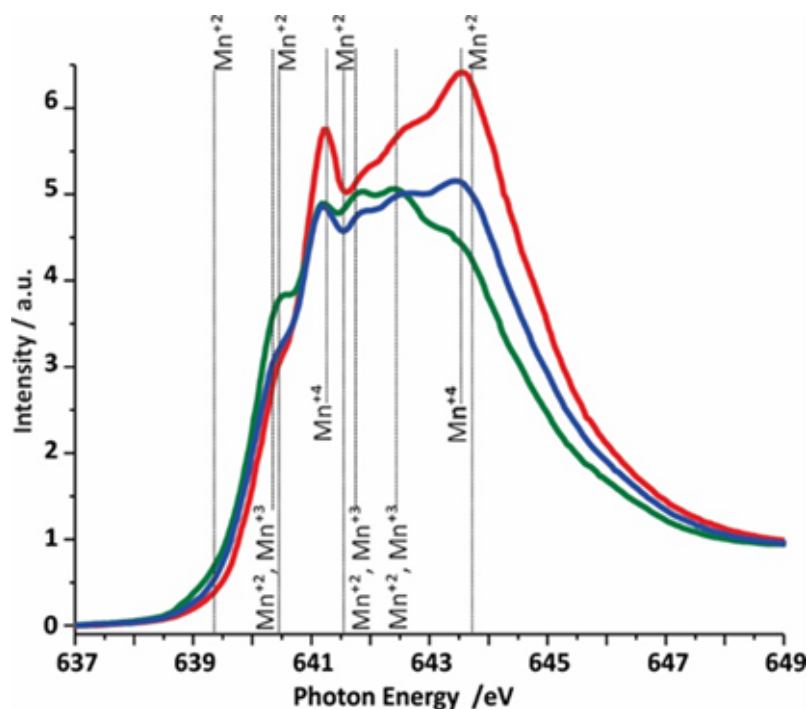


Figure 5.7.: Mn L_3 -edge NEXAFS (TEY) spectra of the three different Ca-birnessite samples studied by XAS. Color code and sample descriptions are identical to Figure 5.6.

spectra measured for reference oxides and used for the difference spectra analysis (Fig. C.9) and also for linear combination analysis (LCA) (Fig. C.10), we conclude that the as-prepared Ca-birnessite powder mainly contains Mn in the form of Mn^{4+} ions, giving rise to two pronounced NEXAFS peaks at 641.3 and 643.5 eV, respectively (59% Mn^{4+} vs. 41% Mn^{3+} from LCA). During electrode preparation, manganese is partially reduced (most likely by the organic components of the ink, see XPS results for carbon) to an oxide material containing Mn predominantly in its Mn^{3+} oxidation state (LCA here: 7% Mn^{2+} , 6% Mn^{2+}/Mn^{3+} , 65% Mn^{3+} and 22% Mn^{4+}). This is manifested by two additional NEXAFS signals at 641.8 and 642.4 eV, while the feature at 643.5 eV almost disappears from the spectrum. Electrolysis at OER conditions results in a re-oxidation of manganese and the Mn^{4+} -peak at 643.5 eV reappears. However, the peaks assigned to Mn^{4+} do not reach the same intensities after electrolysis as initially found for the powder sample, which suggests that a certain concentration of Mn^{3+} is still present on the material surface even after extended electrolysis at OER potentials (LCA after electrolysis: 2% Mn^{2+} , 5% Mn^{2+}/Mn^{3+} , 45% Mn^{3+} and 48% Mn^{4+}). This observation differs from the behavior of birnessites containing only potassium as additional cation^[193,194] and it is thus feasible that the Ca^{2+} ions have a stabilizing effect on the Mn^{2+} and Mn^{3+} oxidation states. When an oxidizing potential was applied to the electrode in buffered electrolyte solutions, we detected electrochemical “pre-waves” in the CVs (see ESI,

Fig. C.1) and also some reorganization of the material at its surface by electron microscopy. Both processes most likely involve complex Mn-centered redox reactions.^[89] In the light of the changes observed in the Mn NEXAFS spectra, we can now identify electrochemical oxidations of Mn^{3+} and possibly also Mn^{2+} , (see Fig. C.6 in the ESI) centers to Mn^{4+} occurring for $E > 1\text{ V}$ to be responsible for these events.

Next, the XPS and NEXAFS data for calcium was analyzed (Fig. 5.8 and ESI, Fig. C.11). The Ca 2p spectra were measured at kinetic energies of $E_k = 200\text{ eV}$ and $E_k = 830\text{ eV}$, respectively. A quantitative analysis of the Ca 2p spectra shows that the calcium ions are eliminated from the structure resulting in a decrease of the Ca : Mn ratio from 0.3 : 1 for the powder sample and 0.18 : 1 for the freshly prepared electrode to 0.11 : 1 for the electrode after electrochemical performance in phosphate buffer. These numbers are in very good agreement with EDX-SEM measurements described above.

Deconvolutions of the Ca 2p lines yielded a main doublet at 346.4 eV for all samples (Fig. 5.8). From the literature, this is typical for calcium manganese oxides like CaMnO_3 or CaMn_2O_4 , where Ca^{2+} interacts with neighboring $\text{Mn}^{3+/4+}$ cations via μ -oxido bridges.^[195] After electrolysis in phosphate buffer, both the Ca 2p (XPS) and the Ca L-edges (NEXAFS) spectra show additional contributions when compared to those of the powder sample or the pristine electrode, indicating that some of the Ca^{2+} ions enter a new chemical environment during electrochemical OER in phosphate buffer. In the XPS, after electrolysis an additional peak is found in the Ca 2p spectrum at a higher binding energy of 353.5 eV. Furthermore, NEXAFS shows an additional resonance at a lower excitation energy. This effect was observed only when phosphate buffer was used as electrolyte, while in the case of imidazolium sulfate no additional Ca L-edge feature was observed (see ESI, Fig. C.12)

The calcium ions in the interlayer space of birnessite-type oxides are expected to show strong Coulomb interactions with the oxido anions of the $[\text{MnO}_6]$ layers and neighboring water molecules. On the other hand, we found that most of the Ca^{2+} is removed from the birnessite material during OER in imidazolium sulfate (see ESI, Fig. C.7). In this case, the Mn L3-edge spectrum is also dominated by Mn^{4+} (Fig. S12) and an analysis of the data shows that there is ca. 20% less Mn^{3+} present in comparison to the sample obtained after electrolysis in phosphate buffer (LCA here: 6% Mn^{2+} , 7% $\text{Mn}^{2+}/\text{Mn}^{3+}$, 21% Mn^{3+} and 66% Mn^{4+} ; see ESI, Fig. C.10). To us, it seems that all these observations might be explainable by the following interwoven effects: 1) Ca^{2+} - phosphate interactions obviously stabilize Ca^{2+} within the birnessite, 2) it is known that secondary cations like Ca^{2+} influence the energetics of the conversion of Mn^{4+} to Mn^{3+} ,^[196] so that in consequence 3) the presence of phosphate, mediated via the Ca^{2+} ions in the material, stabilize lower oxidation states of manganese in the Ca-birnessite catalyst and thus make it more active in OER catalysis.

To test this assertion, we noticed that all XP spectra of Figure 5.8 feature a Ca 2p satellite peak at about 355 eV. At $\sim 10\text{ eV}$ of energy above the main line, these signals could well be exciton satellites associated with Ca^{2+} .^[197,198] However, the

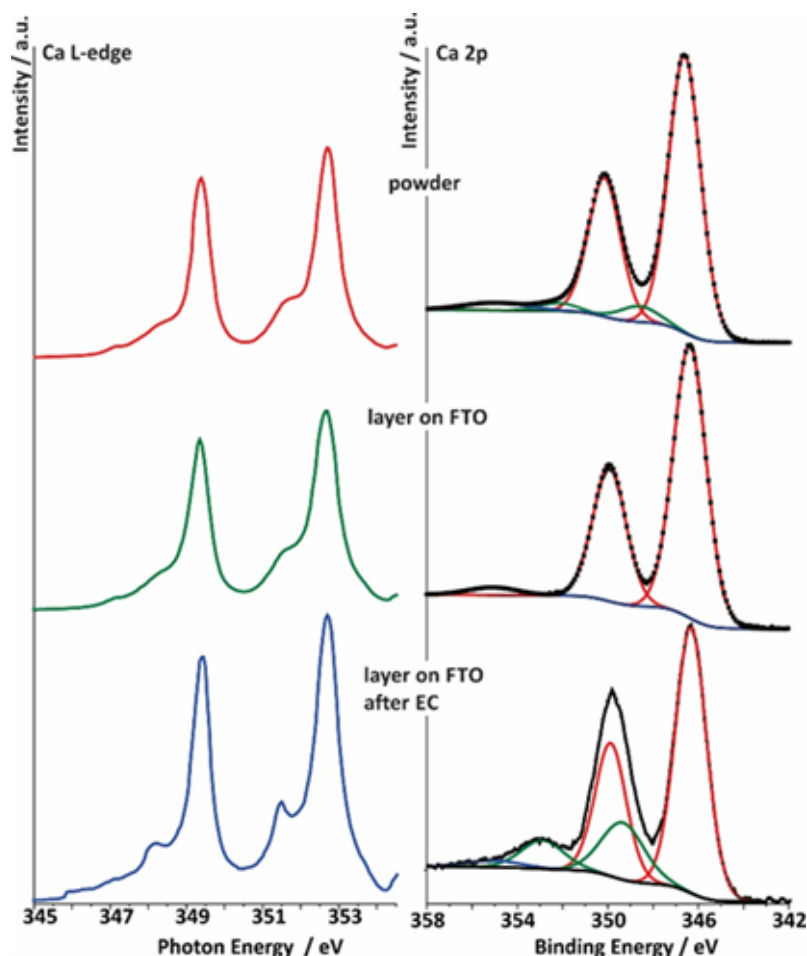


Figure 5.8.: right: deconvoluted Ca 2p spectra (data for $E_k = 830$ eV) of the three different Ca-birnessite samples studied by XAS: powder (top), printed Ca-birnessite layer on FTO before (middle) and after electrolysis in phosphate buffer (bottom). left: Ca L-edge NEXAFS spectra of Ca-birnessite samples in total electron yield (TEY) mode. Color code and sample descriptions are identical to Figures 5.8 and 5.9.

spectra for the Ca-birnessite powder and post-operando spectrum from the phosphate electrolyte additionally contain a satellite just 3 eV above the main line. It is accepted that such additional high energy features in XPS are charge transfer satellites resulting from the hybridization between valence orbitals of cations and anions, in our case Ca^{2+} and O^{2-} (for more details see ESI, 4th text paragraph and Fig. C.14b).^[197-199]

This hybridization can effectively be described by charge transfer from the ligand to the metal, resulting in a $d^1\bar{L}$ configuration, where \bar{L} denotes a ligand hole and d^1 indicates an additional d electron on the metal. The energy separation between these satellites and the main Ca 2p line is indicative of the degree of hybridization. For the powder birnessite sample, the energy separation between the primary peak

and the charge transfer satellite is 2 eV (Fig. 5.8, right). After electrochemistry the separation between the satellite and the main line increases to 2.7 eV, which indicates that the d1L final state has a lower energy than in the powder, meaning that the Ca^{2+} remaining after electrochemistry is bound through a highly covalent metal-ligand interaction.

Turning now to the oxide material obtained after printing onto the FTO substrate, we see that the charge transfer satellite seen initially in the powder sample is lost (Fig. 5.8). Unlike the partially covalent ground state found after electrochemistry, the ground state after printing on FTO is then dominated by the ionic d^0 configuration. The origin of this change in covalency can be seen on the basis of hybrid density functional theory calculations which show an increase in both band gap and Ca-O distance in the presence of a high concentration of Mn^{3+} ions due to the Jahn-Teller distortion of these centres.^[200] Thus, the appearance of a high concentration of Mn^{3+} may lead to a loss of the charge transfer satellite in the Ca 2p XPS and a decrease in covalency of the Ca oxygen bonds. To test if this is the case, we turned to the Mn L-edge measurements (Figure 5.7), from these spectra it seems that the existence of the Ca 2p charge transfer satellite may be connected with the presence of Mn^{4+} . After printing, the sample is composed primarily of Mn^{3+} and there is no charge transfer satellite in the Ca 2p XP spectrum. However, when Mn^{4+} dominates the Mn L-edge spectra as in the powder sample and the sample after electrochemistry, the charge transfer satellite is seen in the Ca 2p XP spectrum. In the latter case, a slightly more covalent character of the metal - ligand interaction was found and the Mn L-edge spectrum also shows a contribution of Mn^{3+} .

The analysis of the Ca L-edge spectra shows that the spectrum recorded for the electrode after OER electrocatalysis in phosphate buffer shows an additional feature similar to what was found for the XPS Ca 2p lines. The main spin-orbit related peaks L3 ($2p_{3/2}$) and L2 ($2p_{1/2}$) at 349.4 eV and 252.7 eV, respectively, are present in all three spectra. The position of these main absorptions is nearly the same for all three samples. For the sample treated electrochemically in phosphate buffer, peaks appear at 348.2 eV and 351.47 eV, while spectra of the two others samples show only small shoulders at these photon energies.

The Ca L-edge spectra is known to be dominated by transitions into localized Ca 3d states meaning that $p \rightarrow s$ transitions can be ignored to first approximation.^[201] Thus, for Ca^{2+} without hybridization, the final state in NEXAFS is $|cd^1\rangle$. In spherical symmetry this would lead to two primary lines associated with the $p_{3/2}$ and $p_{1/2}$ initial states, while in an octahedral field the d orbitals are no longer degenerate and two final states become available for each initial state. If we furthermore include the hybridization approach we used to explain the Ca 2p XP spectra, additional NEXAFS features can appear due to the increase in multiplet lines.^[202]

It is difficult to know a priori how these additional states modify the Ca L-edge spectrum. Thus, we calculated the spectra using a multiplet Hamiltonian that includes hybridization with the same parameters as for the XPS calculations described above. These calculations reproduce the L-edge spectrum expected for both

the Ca^{2+} ion of spherical symmetry and Ca^{2+} in an octahedral environment of O^{2-} counter-ions ($10 D_q = 0.75 \text{ eV}$) (see ESI, Fig. C.14a). They also reveal additional small leading edge peaks due to multipole interactions of the core hole with the valence electron.⁵⁷ A comparison of these calculated L-edge spectra with the experimental results shows that Ca^{2+} interacts weakly with its surroundings in the as prepared birnessite powder, with a value of only $10 D_q = 0.75 \text{ eV}$ required to model the shoulders at 348.2 eV and 351.5 eV. For comparison, $10 D_q$ is 1.2 eV in CaO .^[202] When hybridization is introduced, it leads to the growth of two peaks, consistent with what is observed in the measured Ca L-edge spectrum after electrochemistry in phosphate buffer (see Fig. 5.8, left, blue curve).

The agreement between the theoretical description of the NEXAFS and XPS spectra allows us to conclude that the additional peaks in the Ca L-edge spectra recorded for the electrode sample after OER electrocatalysis in phosphate buffer can be assigned to a partial change in environment of the calcium ions. This indicates the formation of a new Ca^{2+} -containing phase, in which the Ca-ligand interaction becomes highly covalent, and therefore resistant to dissolution into the electrolyte. For the sample obtained from the imidazolium sulfate electrolyte, such additional features at 348.2 eV and 351.47 eV are not observed, suggesting that hybridization between Ca^{2+} and O^{2-} is not taking place in this case and might thus be phosphate-dependent (see ESI, Fig. C.12).

The survey XP spectrum of the sample after electrochemistry in phosphate buffer also revealed the presence of a P 2p signal, which must originate from phosphate ions incorporated into the oxide (Fig. 5.6). At this stage it is unclear whether this signal might also originate from calcium phosphates ($E_b = 347 - 348 \text{ eV}$) as possible products from the reaction between Ca^{2+} from the Ca-birnessite and $(\text{H})\text{PO}_4^{2/3-}$ anions from the electrolyte.^[203] Taking into account the well-studied chemistry of calcium phosphates and the TEM-EDX data presented above (where phosphorous was found close to the surfaces of the Ca-birnessite nanocrystals), the formation of some kind of calcium phosphate moieties seems plausible. Unfortunately, in our case calcium phosphate species cannot be identified by their Ca 2p XP spectra as the binding energies for calcium manganese oxides and calcium phosphates are separated by less than 1 eV.^[196]

Nevertheless, in order to be able to detect possible contribution from calcium phosphates next to calcium manganese oxides, a P 2p XPS for the electrode after electrolysis was measured using two kinetic energies ($E_k = 200 \text{ eV}$ and 830 eV, see ESI, Fig. C.4). The two spectra differ by a greater bulk contribution ($E_k = 820 \text{ eV}$ vs. $E_k = 200 \text{ eV}$) of a phase appearing at higher binding energy ($\sim 136 \text{ eV}$). After deconvolution of the 830 eV spectrum, three doublets were found (Fig. 5.9). A comparison with literature data combined with theoretical calculations allows an analysis of the contributions to this P 2p peak: the first doublet located at 132.8 eV (red line) can be assigned to HPO_4^{2-} and H_2PO_4^- , the buffer anions present in the electrolyte.^[203] The second (133.7 eV) (blue line) and third (135.75 eV) (green line) doublet are related to each other. The energetic position of the second doublet is

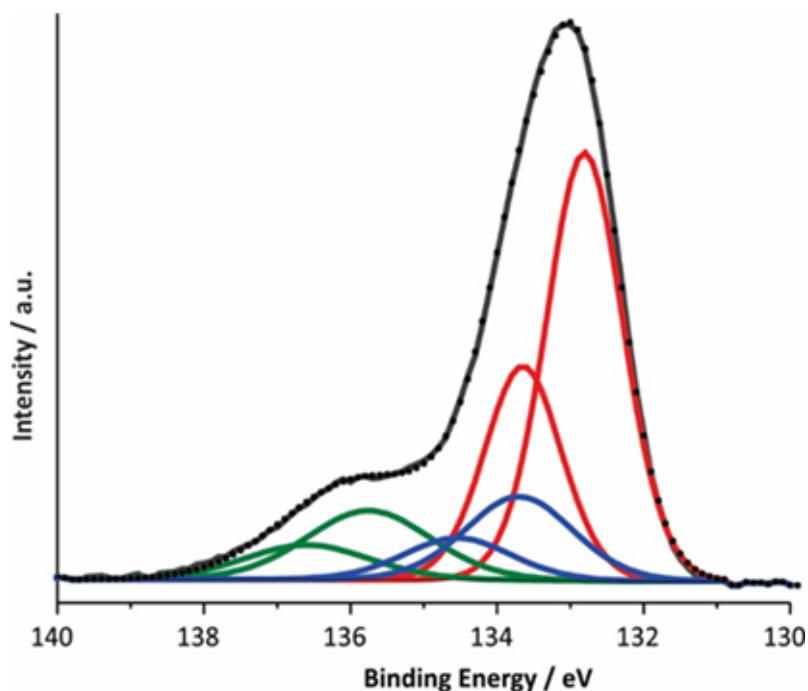


Figure 5.9.: Deconvoluted P 2p XPS spectrum for a Ca-birnessite electrode after electrolysis under OER conditions (16 h in 0.1 M phosphate buffer at $\eta = 540$ mV).

in very good agreement with the literature data for calcium phosphates and the formation of such compounds from the reaction between phosphate from the electrolyte and calcium ions located within the birnessite structure appears to us very plausible. The spectral contribution located at the highest binding energy was assigned to calcium phosphates containing H_2O and/or OH^- and its observation is in agreement with our findings for the Ca 2p line and the Ca L-edge spectra described above. Here, the formation of clusters like $\text{CaH}(\text{PO}_4)$ associated with water molecules is possible which are known from the minerals brushite ($\text{CaH}(\text{PO}_4) \cdot 2 \text{H}_2\text{O}$) or octacalcium phosphate ($\text{Ca}_8\text{H}_2(\text{PO}_4)_6 \cdot 5 \text{H}_2\text{O}$). Another possible reaction at pH 7 is the formation of hydroxyapatite ($\text{Ca}_5(\text{PO}_4)_3(\text{OH})$).

The most obvious explanation for the appearance of the contributions of the P 2p line is the reaction of phosphate ions with the surface of the manganese oxide layer, where oxygen point-defects could react especially well with phosphate units.^[204] For this, different phosphate binding motifs are possible: direct binding of phosphate to the $[\text{MnO}_6]_n$ -layer could occur via a single oxygen vacancy or a phosphate bonded via two oxygen atoms to two neighboring O-defects. Another possibility is the reaction of phosphate with calcium ions located between the $[\text{MnO}_6]$ -layers, which are separated by a rather large 7 Å interlayer space for birnessites. This is supported by the reduced Ca^{2+} concentration in phosphate enriched areas.

In conclusion, the XPS results can be interpreted by equilibria involving dynamic exchanges of Ca^{2+} , K^+ , PO_4^{3-} and HPO_4^{2-} ions bound to the surfaces, within the

pores and probably even between the $[\text{MnO}_6]_n$ layers of the birnessite material (see graphical abstract). Among the anions, phosphate species seem to have an especially high affinity for birnessites, leading to a substantial incorporation of phosphate into the birnessites' surface layers where catalytic water oxidation most likely occurs. The combination of XPS, NEXAFS and theoretical approaches indicates that the binding of phosphate can either occur directly via O-vacancies in the $[\text{MnO}_6]$ -layers or also by the formation of $[\text{Ca}/\text{PO}_4/\text{H}_2\text{O}]$ - complexes within the layers. The latter appear to be of significant importance because close calcium-manganese and calcium-phosphate interactions are indicated by the detailed analyses not only of the P 2p but also the Ca 2p and Ca, Mn L-edges signals. Finally, we would like to add that the described incorporation of phosphate is to a large extent reversible: if an anode "loaded" with phosphate by OER electrocatalysis is placed in deionised water for 12h, no XPS peaks for P can be detected any more.

5.4. Conclusion

While few studies on water-oxidation catalysis by manganese oxides emphasize the critical role of the electrolyte for effective water oxidation catalysis, our results clearly show the potential benefits of a rational, concerted development of catalyst and electrolyte in parallel. For Ca-birnessite, we find that the use of buffering electrolytes is generally beneficial and that phosphate-based systems seem to be particularly advantageous for the operation of birnessite-anodes at near-neutral conditions.

Our detailed investigation of the interactions between the Ca-birnessite material and (hydrogen) phosphate electrolytes during electrocatalysis provided proof for very dynamic, complicated ion exchange equilibria between the solution and the heterogeneous water-oxidation catalyst. Using a broad set of investigation methods (electron microscopy, EDX, XPS and NEXAFS), we could show that the elements carbon and calcium, which are part of the catalyst layer as a result of the preparation method, are fully (C) or to a large degree (Ca) eliminated from the material after some hours of operation as OER electrocatalyst. Further analysis of the XPS and NEXAFS spectra acquired after OER reveals that a large fraction of the remaining calcium-oxygen interactions is likely of covalent nature, preventing the complete dissolution of calcium from the material. It seems that phosphate plays a role in accruing this phenomenon as no hybridization was observed in the case of the imidazolium sulfate electrolyte, and much more Ca^{2+} ions left the structure. This in turn leads to a destabilization of the Mn^{3+} state resulting in a decrease of OER activity.

For the neutral potassium phosphate electrolyte, our data suggests that both K^+ and $\text{HnPO}_4^{(3-n)-}$, enter the mesoporous birnessite layer. After some time, these ions can be found in the entire volume of the catalyst, with especially high concentrations at the top of the catalyst layer (where a new, probably re-precipitated material is formed) and on the inner surfaces of the pores.

The interpretation of XPS and NEXAFS data for a nanocrystalline, partially disordered manganese oxide like birnessite is complex and far from routine. However, our analysis is in agreement with previous investigations which indicated that the redox equilibrium $\text{Mn}^{3+} \rightleftharpoons \text{Mn}^{4+}$ is of central importance for OER catalysis by birnessites. A significant concentration of Mn^{3+} ions at the surface of the oxide might be key for the material to be catalytically active. Mediated by bridging oxygen atoms, Mn cations interact with both calcium (which seems to influence its oxidation state) and phosphorous during electrocatalysis and furthermore Ca^{2+} and $\text{HnPO}_4^{(3-n)-}$ additionally seem to form some kind of aggregates within the material as detected by XPS.

Overall, the operation of Ca-birnessite as water-oxidation catalyst in phosphate electrolytes significantly alters the manganese oxide material. Especially striking is the incorporation of (hydro-gen)phosphate anions into the catalyst, where they stabilize Ca^{2+} in the structure and might additionally act as “internal bases” to shuttle protons released from the OER reaction at catalytic sites into the bulk of the solution. These special effects of the interaction of $\text{HnPO}_4^{(3-n)-}$ with the catalyst might explain the markedly better OER-performance of the Ca-birnessites catalyst material in phosphate solutions in comparison to other buffering electrolytes. We would like to add that the processes described here might be closely related to the incorporation of phosphate ions into the much-studied “CoPi”-catalyst films generated by the electrodeposition of cobalt from phosphate-containing solutions.^[71] Thus amorphous CoO_x - and nanocrystalline, layered MnO_x - electrocatalysts for water-oxidation show an important similarity: in addition to the atomic structure and morphology of the catalyst material, the interaction of the oxides with the ionic components of the electrolyte is of central importance for the catalytic process.

ASSOCIATED CONTENT

Supporting Information. Additional TEM analysis and spectroscopic information can be found in the supplemental information.¹

AUTHOR INFORMATION

Corresponding Authors

*E-mail: skorupska@fhi-berlin.mpg.de

*E-mail: cjooss@gwdg.de

*E-mail: philipp.kurz@ac.uni-freiburg.de

Author Contributions

The manuscript was written through contributions of all authors.

¹See section C

ACKNOWLEDGMENT

This project was made possible by the generous financial support by the Federal Ministry of Education and Research (BMBF cluster project MANGAN), the German Research Foundation (DFG) priority program SPP1613, grants KU2885/2-2 and JO348/11-1 and SFB 1073, project C02, funded by DFG. T. E. J. acknowledges the Alexander-von-Humboldt Foundation for financial support.

Atomic Dynamics of Manganese Oxide in OER like Conditions

This whole section is a complete reproduction of the original publication^[30]

Atom Surface Dynamics of Manganese Oxide under Oxygen Evolution-Like Conditions Studied by In-Situ Environmental Transmission Electron Microscopy

Emanuel Ronge¹, Jonas Lindner¹, Jens Melder², Jonas Ohms², Vladimir Roddatis^{1,†}, Philipp Kurz², Christian Jooss^{1,}*

accepted by *The Journal of Physical Chemistry C* (2021)

References, labels and arrangement of figures have been modified to suit this thesis.

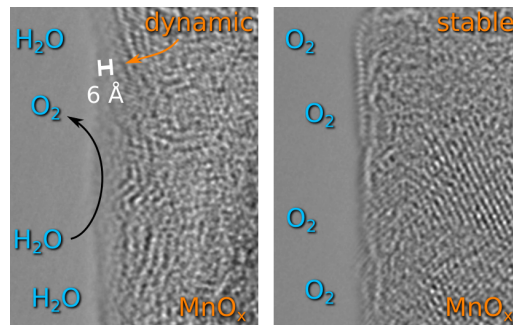
¹ Institut für Materialphysik, Georg-August-Universität Göttingen, Friedrich-Hund-Platz 1, 37077 Göttingen, Germany.

² Institut für Anorganische und Analytische Chemie and Freiburger Materialforschungszentrum (FMF), Albert-Ludwigs-Universität Freiburg, Albertstraße 21, 79104 Freiburg, Germany

KEYWORDS. oxygen evolution reaction, manganese oxides, in-situ microscopy, surface dynamics

Abstract

Hydrogen production by electrochemical water splitting is limited by the sluggish oxygen evolution reaction (OER). In order to improve our understanding of the underlying mechanisms, information about the atomic surface structure of the active state of the electrode is necessary. Here, we present environmental transmission electron microscopy studies of Ca-birnessite ($\text{K}_{0.20}\text{Ca}_{0.21}\text{MnO}_{2.21} \cdot 1.4\text{H}_2\text{O}$) electrodes under conditions close to those of the OER. Remarkably, in H_2O vapor, a highly dynamic state of the surface and subsurface develops with a thickness of the dynamic layer of up to 0.6 nm, which is absent in O_2 and inert gases. Electron beam induced effects are carefully studied, showing high stability of the material against radiation damage in high vacuum until dose rates of $42.000 \text{ e}^-/(\text{\AA}^2 \text{ s})$. In contrast, in H_2O the dynamic surface layer develops and forms a stationary state even at low dose rates down to $5.000 \text{ e}^-/(\text{\AA}^2 \text{ s})$. Electron energy-loss spectroscopy reveals an increase in the Mn oxidation state in H_2O and in O_2 ambient. Our results are interpreted as the formation of a few-angstrom-thick, dynamic, and hydrated surface layer of birnessite in H_2O , with an increased Mn valence state. Such a dynamic surface layer with a flexible Mn coordination and valence state might be optimal for oxygen evolution due to the higher effective interaction volume beyond the surface area and a flexible bond coordination of partially hydrated Mn species.



Remarkably, in H_2O vapor, a highly dynamic state of the surface and subsurface develops with a thickness of the dynamic layer of up to 0.6 nm, which is absent in O_2 and inert gases. Electron beam induced effects are carefully studied, showing high stability of the material against radiation damage in high vacuum until dose rates of $42.000 \text{ e}^-/(\text{\AA}^2 \text{ s})$. In contrast, in H_2O the dynamic surface layer develops and forms a stationary state even at low dose rates down to $5.000 \text{ e}^-/(\text{\AA}^2 \text{ s})$. Electron energy-loss spectroscopy reveals an increase in the Mn oxidation state in H_2O and in O_2 ambient. Our results are interpreted as the formation of a few-angstrom-thick, dynamic, and hydrated surface layer of birnessite in H_2O , with an increased Mn valence state. Such a dynamic surface layer with a flexible Mn coordination and valence state might be optimal for oxygen evolution due to the higher effective interaction volume beyond the surface area and a flexible bond coordination of partially hydrated Mn species.

6.1. Introduction

The oxygen evolution reaction (OER) is one of the main bottlenecks for the production of hydrogen by electrochemical water splitting using renewable energy.^[164] A better understanding of the mechanisms affecting the activity and stability of OER electrocatalysts is thus required. Inspired by the highly efficient oxygen-evolving complex of photosystem II, which features an active site with stoichiometry of CaMn_4O_x , significant research activity on finding efficient systems for OER has focused on various manganese oxides (MnO_x).^[73,75-79,165,166] From the many known MnO_x structures with varying composition and ordering, layered birnessite-type MnO_x compounds show especially good stability and OER activity^[17,80,83-85]. Birnessites consist of a layered arrangement of MnO_6 octahedra with an interlayer distance of 7-10 \AA . Between these layers, water and cations can be intercalated in variable concentrations in a fashion similar to clay minerals. Doping by different cations can modify the degree of the crystalline order as well as the ion exchange properties of the materials when in contact with aqueous solutions.^[175,176] In ad-

dition, the presence of redox-inert intercalated ions like Ca^{2+} might stabilize or even support the formation of modified and more flexible structural moieties within MnO_x , which is most likely favorable for OER catalysis.^[181,182] Previous studies have shown the influence of the birnessite crystallinity on the OER activity, where a lower degree of order leads to a higher activity. Detailed X-ray diffraction and X-ray absorption structure analysis of active Ca-birnessite catalysts confirmed a low long-range order within the $[\text{MnO}_6]$ -layers as well as irregular stacking of the layers.^[84,86,168] Such birnessite electrodes yield stable current densities of $\approx 1 \text{ mA cm}^{-2}$ at overpotentials η of $\approx 500 \text{ mV}$ in neutral, phosphate buffered electrolytes.^[89] Manganese species with oxidation states close to +3 display Jahn-Teller distortions of the octahedral coordination spheres of Mn^{3+} cations and the resulting metastable Mn-O bond length might enhance OER activity.^[73] Compared to Mn^{4+} -rich oxides, Mn^{3+} -rich oxides often show much higher OER activities.^[18] However, Mn^{4+} might also stabilize manganese complexes against decomposition, as observed for the oxygen-evolving complex of photosystem II.^[174] For birnessites Mn oxidation states are in the range between 3.3 and 4.0,^[17,84,86,168] indicating a flexible Mn valence state that can be reversibly modified during OER which might be a key characteristic for OER catalysis by manganese oxides.^[26,86,174,179] In previous studies^[29,205], the formation of an amorphous surface layer in correlation to the ion exchange of Ca^{2+} with $\text{HnPO}_4^{(3-n)-}$ has been observed during OER, hinting to a pronounced atom dynamics at the electrolyte birnessite interface. In-situ transmission electron microscopy (TEM) experiments enable the study of the evolution of the catalyst surface under reactive conditions in real space in order to gain insights into the surface dynamics of the MnO_x material, however, high resolution experiments in H_2O vapor with a condensed H_2O surface layer are presently restricted to pure H_2O without addition of foreign ions, typical for real electrolytes^[122].

In this work, we analyze two different types of Ca-birnessite ($\text{K}_{0.20}\text{Ca}_{0.21}\text{MnO}_{2.21}\cdot 1.4\text{H}_2\text{O}$) electrodes. The first is a pressed birnessite powder, which thus represents a chemically pure binder-free electrode. The second type of electrodes is a typical screen-printed electrode, containing the same birnessite powder that is immobilized by an ink containing organic (and therefore carbon-containing) compound. It is used as a reference to verify the observed dynamics at an electrode which is used in the electrochemical setup. Results for the printed electrode are mostly in the Supporting Information. In order to study the birnessite surface under OER conditions, an environmental transmission electron microscope (ETEM) was deployed. With a 1 hPa H_2O water pressure and a beam induced local positive electric potential, conditions can be reached that allow OER in the ETEM.^[78] The initial structure of the electrode was revealed with high-resolution transmission electron microscopy (HRTEM) and electron energy-loss spectroscopy (EELS), showing a rather high stability under electron beam irradiation. Under beam-induced reactive conditions in H_2O , pronounced surface dynamics emerges, which were analyzed with time sequences of HRTEM as a function of the dose rate. To gain further insights into the electronic structure of the electrode, the change in the oxidation state under OER conditions was investigated by EELS of the Mn

L-edge and fitting of reference spectra. Our results demonstrate the formation of a few-angstrom-thick dynamic surface layer of birnessite in H₂O, with an increased Mn valence state.

6.2. Experimental Methods

Typically birnessite electrodes for electrochemical experiments are fabricated by using an ink to immobilize the Ca-birnessite powder on the conductive support. This improves the stability and leads to a reduced electric resistance. However, printed electrodes contain a certain amount of carbon which can contribute to undesired TEM lamella contamination in in-situ TEM experiments. Consequently, we performed a comparative analysis of pressed birnessite powder and printed electrodes fabricated from the same source powder, that allows us to differentiate the effects of birnessite and carbon in in-situ experiments. The results on the printed electrode are used as a reference and are mostly shown in the Supporting Information. Please consult previous publications concerning the synthesis of the birnessite powder and the screen printing of the electrodes.^[17,89]

6.2.1. Lamella Preparation

For pressed electrodes, the birnessite powder was moistened with isopropanol and pressed into a cylinder 1 cm in diameter at 50 bar for 30 min. Electron-transparent lamella were then prepared from the pressed pellet by the conventional thinning method; that is, cracked pieces were polished down to 150 μm and then ion milled with Ar ions at an acceleration voltage of 5 kV, which is stepwise decreased to 0.5 kV. The printed electrode lamellas were cut with a focused ion beam (FIB). To protect the electrode from beam damage during preparation, a PVA protection layer was used. After thinning the remaining PVA was removed with PIPS and plasma cleaning. Figure D.1 shows overview TEM images of the lamellas of a pressed and a printed electrode.

6.2.2. In Situ ETEM

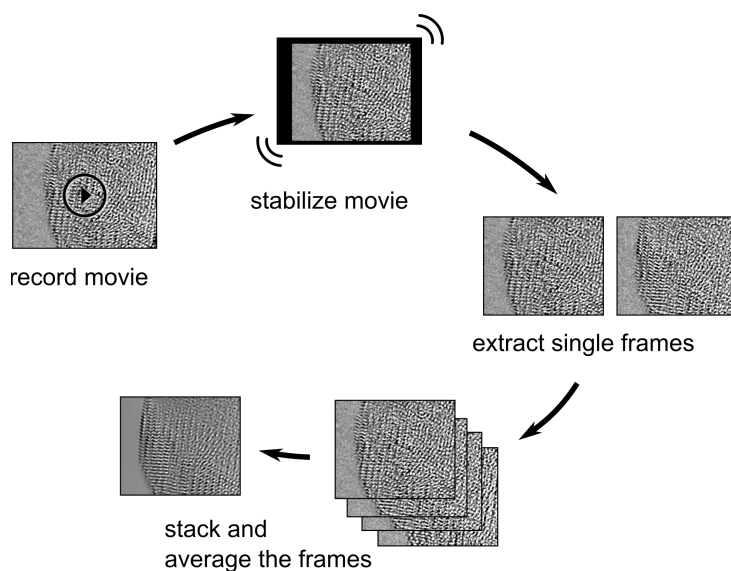
TEM analysis was performed at an FEI Titan ETEM with an acceleration voltage of 300 kV. The Titan ETEM is equipped with an image CEOS C_s corrector, enabling a point resolution of better than 0.1 nm. Furthermore, it is equipped with an FEI X-FEG module and a Quantum 965ER Gatan Image Filter (GIF). In a high vacuum (HV) operation, a gas pressure of 10⁻⁷ hPa is maintained by using a cold trap. Without a cold trap, typically 10⁻⁶ hPa is reached. In ETEM experiments, the gas pressure can be adjusted from $\approx 10^{-4}$ hPa to ≈ 5 hPa, depending on the type of the gas. The residual gas analyzer (RGA) measurements shown in Figure D.2 indicate a purity of the gas system better by 95%, when 1 mbar H₂O or O₂ is used. The beam intensity is adjusted with the available monochromator focus in the unfiltered mode.

To determine the dose rate (D), the calibrated electron count from the camera is divided by the area of the image and the acquisition time. For the recorded movies, the acquisition time is 0.1 s per frame.

In STEM an ADF detector is used with a camera length of 68 mm. The resulting collection angle of greater than 55 mrad gives predominant contributions of incoherent scattering, leading to Z-dependence of the contrast.^[206]

6.2.3. Tracking Atomic Movements in HRTEM

The analysis of atomic surface dynamics of a partially disordered system is challenging due to two reasons: (i) image drift has to be separated from the contrast change due to displacement of atomic columns. Here, usual drift correction procedures based on autocorrelation have serious limitations. They correlate entire frames, which is unsuitable due to the rather homogeneous, featureless contrast of the entire TEM image. Furthermore, if autocorrelations are restricted to an area close to the region of interest, that is, the interface to H_2O , the small number of image pixels limits a reliable drift determination. Thus, a video software package is required which is capable of tracking objects in real space. (ii) Movement of atoms in a partially disordered material cannot be tracked by analysis of the coherent shift of entire atomic columns; hence, the application of image averaging procedures after drift correction enables distinguishing of regions of pronounced atom dynamics from the rather static areas. In the following, we describe the drift correction / image averaging procedure based on tracking with the professional and freely available video editing application Davinci Resolve 16.1.^[207]



Scheme 6.1: Illustration of the analysis method for the in-situ HRTEM movies.

Within Davinci, the so called “Fusion” tool is used to remove drift via stabilizing the movie with the planar tracker. This tool allows the tracking of multiple points

close to the surface area due to their intensity. This method results in the highest degree of stabilization. After rendering the stabilized movie, the single frames are extracted, stacked and averaged (see Scheme 6.1). We denote the averaged frame number \bar{N} and the total time for averaged frames T .

Figure 6.1 shows three frames (A-C) from the stabilized movie and the averaged image (subfigure D). To demonstrate that Davinci Resolve (Fusion) can track individual atomic rows, six positions of atoms were marked in the first frame. The position relative to the frame was copied to the other images after drift correction. The inset in each image confirms that single atom rows can indeed be tracked (see also Movie S1).

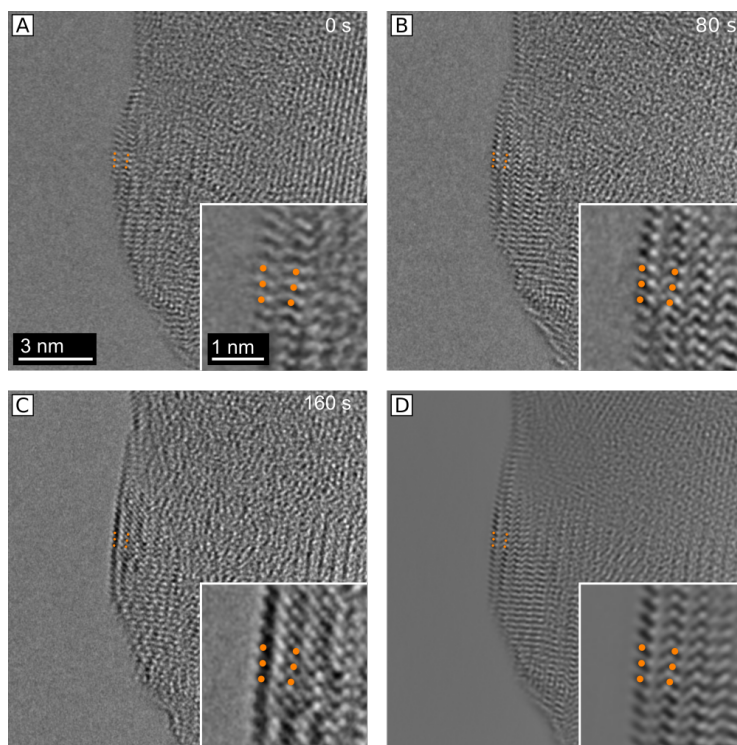


Figure 6.1.: Demonstration of the drift correction and image averaging procedure to track atomic motions for the example of a pressed electrode in 1 hPa O_2 ($D=22,600 e^-/(\text{\AA}^2 s)$). Images are taken at negative defocus, i.e. dark spots mark the position of atomic columns. The superimposed orange dots mark the same position in all the images; (A) $t=0 s$; (B) $t=80 s$; (C) $t=160 s$; and (D) averaged image ($\bar{N}=998$, $T=181 s$). Frames are taken from movie M1.

If the involved atom columns do not change their relative position over time, atomic column contrast will remain sharp in the averaged image. Relative motions of atoms will blur the contrast of atomic columns that may even entirely disappear, depending on the atomic displacement rate and duration of the frame sequence. This allows analysis of the involved area of surface dynamics based on the averaged

frames as well as on the movies. The lower accuracy limit of this analysis method is given by the accuracy of the drift correction that would induce a blurring of the entire time averaged image for static structures. This effect is used for accuracy determination and excludes the fact that blurred surface areas are generated due to errors in the drift correction. The spatial resolution of this method is thus limited by the quality of the tracking and not by the HRTEM resolution. From Figure 6.1 the lower limit can be determined to be 0.1 nm. A drift of the sample height has a similar impact on the tracking as the in-plane-drift. To sustain good track quality the time duration of the tracked video is kept a few 100's of seconds.

6.2.4. Mn L-Edge EELS Analysis

The Mn L-edge is recorded via the dual EELS method with the zero-loss peak (ZLP) in the low loss and the Mn-L and O-K edge in the high loss region. Energy calibration is conducted by fitting the ZLP by a Voigt profile and subtracting the center. The background is fitted with a power law and subtracted. For the normalization, the spectra are divided by the averaged background value right above the L2 white line peak. The Hartree-Slater function is adjusted to the L3 and L2 position and then shifted by 3 eV before being subtracted from the normalized spectra, in order to account for the ionization cross-sections of the continuum. By numerical integration of the L3 and L2 peaks of several spectra the average L3/L2 ratio is determined. Comparing different TEM lamella of the pressed electrode indicates that lamella preparation by FIB, followed by PIPS and plasma cleaning slightly reduces the lamella surface. Once the lamella is studied in ambient O₂ and H₂O, no difference in the Mn valence state of different lamellas is detectable. Since the pristine Mn valence state of the lamella might be affected by the ion milling, we selected the data with the lowest Mn reduction as the reference state in HV.

The Mn valence is determined by multiple linear least squares (MLLS) fitting of the reference spectra of Garvie et al.^[208], where manganosite (Mn²⁺), norrishite (Mn³⁺) and ramsdellite (Mn⁴⁺) were used to calibrate the three relevant oxidation states of Mn. The fit parameters ξ_i are then used to determine the Mn valence:

$$Valence(Mn) = \frac{2 \cdot \xi_{(2+)} + 3 \cdot \xi_{(3+)} + 4 \cdot \xi_{(4+)}}{\xi_{(2+)} + \xi_{(3+)} + \xi_{(4+)}} \quad (6.1)$$

An exemplary fit together with the reference spectra is given in Figure D.3. Several spectra per sample were analyzed and averaged for the results shown in Table 6.2.

Since the MLLS fitting is sensitive to the energy position of the Mn-L edge, the energy calibration of the spectrometer is of importance. However, the energy positions of the Mn-L edge in the reference spectra can differ up to 1.5 eV (compare Garvie et al.^[208] vs Tan et al.^[209]) for the same material. As a test for consistency of energy calibration, the trends in the oxygen K edge position, compared to the L3/L2 ratio, are also included in the analysis. The energy calibration for the TEM session, is adjusted for each session leading to an accuracy of ≤ 0.6 eV. The energy

position of the O K edge was determined by fitting the maximum of the first main peak via a Gaussian function. In order to evaluate the consistency of the Mn valence obtained by MLLS fitting, it is compared to the valence trend obtained from the L3/L2 ratio that is independent of the energy calibration as well as of the reference spectra choice. The signal to noise ratio of the Mn L-edge was not sufficient for the determination of the surface valence state.

6.3. Results

6.3.1. HRTEM Analysis of the Pristine State of Birnessite Electrodes

Two different kinds of electrodes were analyzed in this work: a printed and a pressed electrode. The printed electrode represents an electrode type which has already been used in electrochemical oxygen evolution studies^[89], while the pressed electrode acts as a pure birnessite reference material and is used to reduce the effects of carbon redeposition in TEM. Overview TEM images for both electrodes are presented in Figure S1. Scanning transmission electron microscopy (STEM) images and EELS of the printed electrode, showing the composite structure of the birnessite and carbon binder, are shown in Figure D.4.

In order to analyze the crystal structure of the birnessite electrodes, HRTEM images were taken (Figure 6.2). The particles have an irregular shape with a typical size of ≈ 600 nm and contain nanocrystals with a diameter of (5 ± 2) nm. In HRTEM images the visibility of partially overlapping crystals depends on the diameter and lamella thickness^[210]. Hence the areas which appear disordered in Figure 6.2 are not necessarily amorphous and could also be due to small overlapping grains out of the zone axis. For the pressed and printed electrodes, the coherent domain size measured by HRTEM, indicative of the crystal diameter, is the same within the error margin (Table 6.1). An analysis of the lattice spacings is provided in Figure 6.2 E. Here the intensity profiles of the FFTs from the different samples are compared, see Figure D.5. An overview over the found lattice distances is given in Table D.2. No change in lattice parameters between the powder and fabricated electrodes is observed. The broad peak of the powder at ≈ 4.5 Å is due to a moiré pattern stemming from the edges of the birnessite particles. This confirms that electrode fabrication does not change the crystal structure, for example, due to a change in the crystal water concentration.

d [nm]		
powder	pressed	printed
5.1 ± 2.0	3.9 ± 1.7	3.6 ± 1.3

Table 6.1.: Crystal size of birnessite powder, printed and pressed electrode.

The absence of the visibility of (001) planes in the HRTEM images can be ex-

plained by disorder of the lattice spacing in c -direction. This was also observed by Zhang et al.^[211]. Our HRTEM analysis thus reveals that printed and pressed electrodes display a nanostructure consisting of plate like nanocrystals with a diameter of ≈ 4 nm. In HV the powder, printed, and pressed electrodes show no sign of morphology changes or electron beam induced sputtering and, thus, are stable up to an electron dose rate of at least $42.000 \text{ e}^- / (\text{\AA}^2 \text{ s})$ (see Movie S8 and Figure D.6).

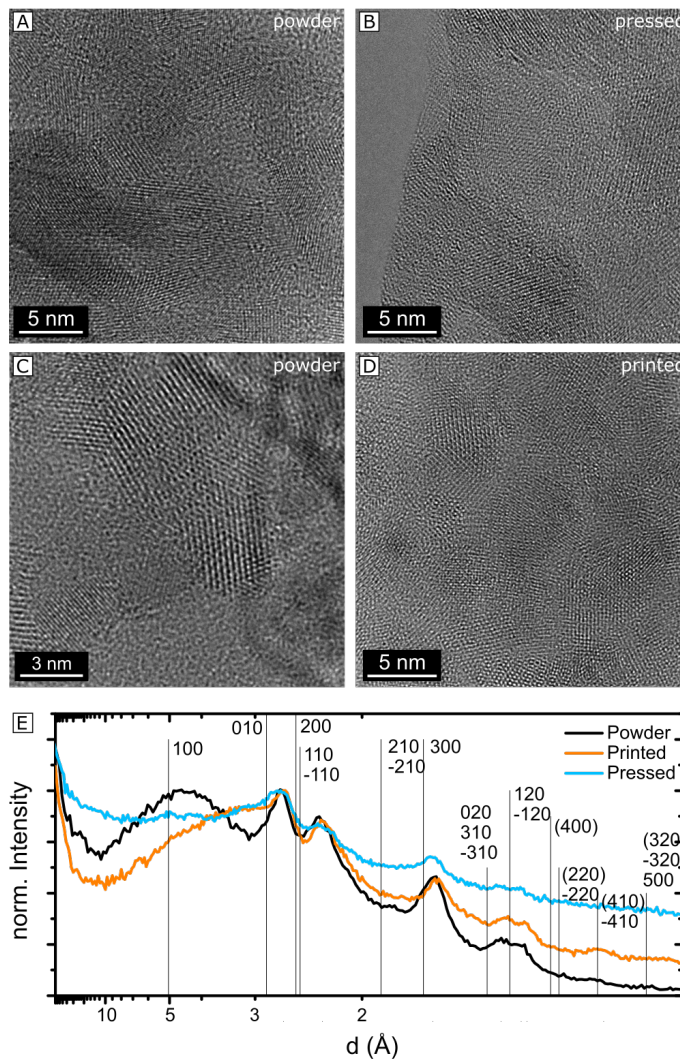


Figure 6.2.: HRTEM analysis of differently processed birnessites in HV. (A,C) powder; (B) pressed electrode; (D) printed electrode; (E) representative intensity FFT profiles of HRTEM images of powder, printed, and pressed electrodes (for representative FFTs, see Figure D.5). A detailed overview over the lattice parameters is given in Table D.2.

6.3.2. Environmental TEM Studies on Surface Dynamics in H₂O and O₂

Carbon Free Pressed Electrodes

We have systematically studied the pressed birnessite electrodes at dose rates between $2000 \text{ e}^-/(\text{\AA}^2 \text{ s})$ and $60,000 \text{ e}^-/(\text{\AA}^2 \text{ s})$ in HV, O₂ and H₂O in the HRTEM mode to analyze the changes of the electrode surface structure in dependence of the gas type and dose rate (see Figure 6.3). The pressed electrodes are remarkably stable over several minutes and show no signs of amorphization, crystallization or surface sputtering in HV (10^{-7} hPa), 1 hPa H₂O and in 1 hPa O₂ up to extreme electron dose rates of about $60,000 \text{ e}^-/(\text{\AA}^2 \text{ s})$. Only in H₂O and then only at the surface, an intense dynamic movement of atoms can be observed above an electron dose rate of $4000 \text{ e}^-/(\text{\AA}^2 \text{ s})$ (see Figure 6.3A and Movie S3).

The level of dynamics is stationary over at least several minutes, and no degradation of the surface is visible. In comparison, no significant surface dynamics were detected in 1 hPa O₂ or in HV (Figure 6.3B,C and Movie S4). Thus, the dynamics of the atoms at the surface is restricted to the presence of water vapor. For a quantitative approach, the thickness of the dynamic layer was measured in dependence of the electron dose rate (Figure 6.3C). In the range of $<5000 \text{ e}^-/(\text{\AA}^2 \text{ s})$, a correlation of the dynamic surface layer thickness with the dose rate may exist. However, above $5000 \text{ e}^-/(\text{\AA}^2 \text{ s})$, its thickness saturates at a value of about 0.6 nm. Furthermore, decreasing the H₂O pressure from 1 to 0.5 hPa does not change the dynamics. Above $60,000 \text{ e}^-/(\text{\AA}^2 \text{ s})$, bubble formation within the electrode appears (see Figure D.7 and Movie S2), and the electrode degrades.

The independence of the dynamic layer thickness on the electron dose rate above $5000 \text{ e}^-/(\text{\AA}^2 \text{ s})$ excludes an effect driven purely by the impact of the primary electrons. This statement is further supported by the observation that the dynamic surface layer is only present in H₂O.

Printed Electrodes with particle Embedded in Carbon

The printed electrodes consist of birnessite nanocrystals embedded in an amorphous carbon containing matrix, as indicated by STEM combined with EELS in the Supporting Information (see Figure 6.4). After introducing O₂ to the printed electrode lamella, different kinds of dynamics can be observed (Figure 6.4, and Figure 6.5A). Remarkably, some surfaces show no dynamics (Figure 6.4B and Figure 6.5A), while, at the same time, the less ordered carbon-rich areas in the bulk show pronounced structure dynamics (Figure 6.4B indicated by the circle). In addition, the formation and movement of bubbles can be observed even at a moderate dose rate ($7400 \text{ e}^-/(\text{\AA}^2 \text{ s})$, Figure 6.4C,D). This reveals an additional contribution to the structure dynamics in printed electrodes due to the presence of carbon, that is absent in pressed electrodes.

In H₂O vapor, the structure dynamics of the printed electrode intensifies by show-

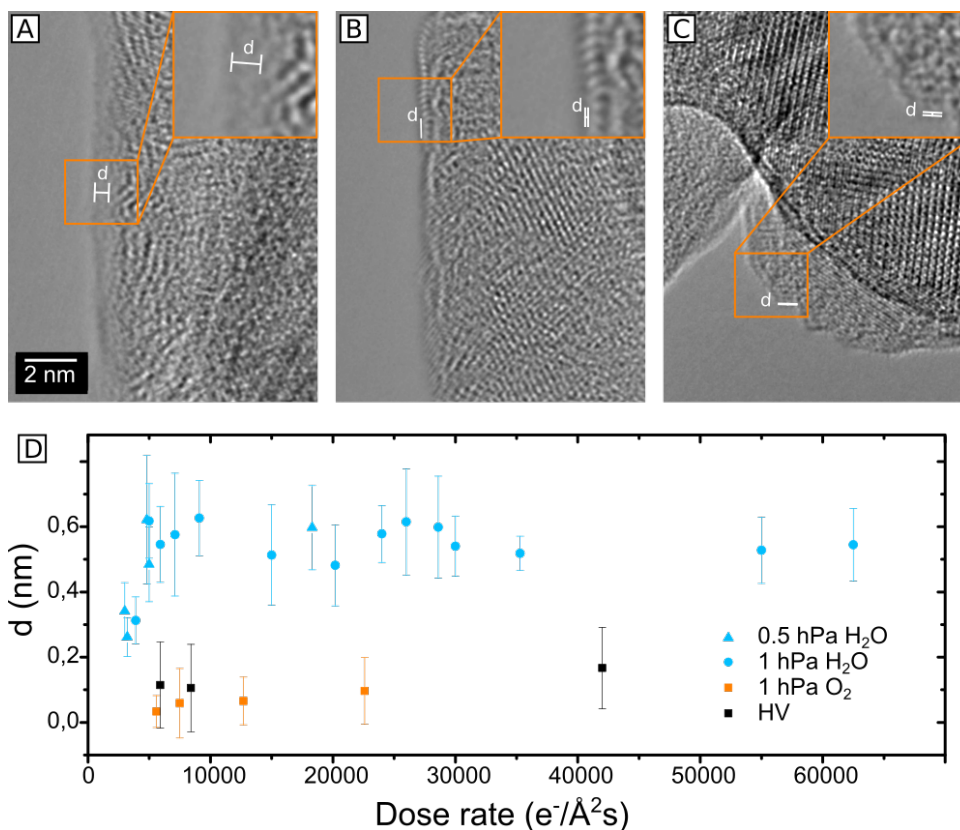


Figure 6.3.: In situ HRTEM analysis of the surface dynamics of the pressed birnessite electrode in HV, H₂O and O₂. (A) Averaged image in 1 hPa H₂O ($\bar{N}=258$, $T=44.4$ s, $D=7100$ $e^{-}/(\text{\AA}^2\text{s})$, Movie S3); (B) averaged image in 1 hPa O₂ ($\bar{N}=375$, $T=67.9$ s, $D=7500$ $e^{-}/(\text{\AA}^2\text{s})$, Movie S4); (C) averaged image in HV ($\bar{N}=52$, $T=13.5$ s, $D=8400$ $e^{-}/(\text{\AA}^2\text{s})$); and (D) measured thickness of the dynamic surface layer in dependence of the dose rate, pressure, and gas type (H₂O, O₂, and HV).

ing strong bulk dynamics (Figure 6.5C,D) and bubble formation (Figure D.8). An agglomeration of these bubbles is possible if they meet. The analysis of the FFT yields a constant distance of the rings/spots from the center of the FFT, confirming the preservation of the crystal structure of the birnessite nanocrystals (see also Movies S5 and S6). Some of the visible spots are moving on a circular path of constant lattice spacing, consistent with the orientation changes of entire nanocrystals. Such a movement of the nanocrystals may be induced by the bulk dynamics of the disordered carbon-rich areas and the bubble formation.

The bulk dynamics in carbon-rich areas in water vapor can be quite intense, as shown in Figure 6.5B-D. If such a dynamical area is close to the surface, the whole surface is moving (Figure 6.5C,D and D.9). Remarkably, even under these conditions, the nanocrystals are quite stable.

The threshold for the bubble formation in H₂O depends mainly on the dose rate.

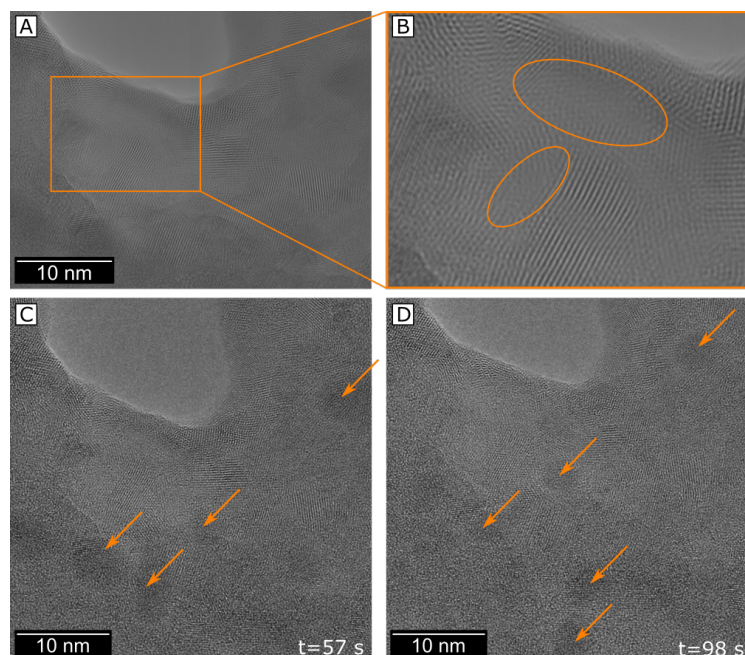


Figure 6.4.: In situ HRTEM experiment with a printed electrode in 1 hPa O_2 and $D=7400 e^-/(\text{\AA}^2 s)$ (A) average image ($\bar{N}=640$, $T=103.9 s$, Movie S5); (B) magnification of area in (A); and (C-D): time series [(C) $t=57 s$; (D) $t=98 s$]. Arrows indicate positions of bubbles.

At a dose rate of $\approx 5000 e^-/(\text{\AA}^2 s)$, the movement of crystals due to bubble formation sets in. The size of the bubbles increases with a higher electron dose rate. In addition, the mobility and agglomeration rate are also increased, leading to the formation of very large voids (Figure D.10 / Movie S7). Such intense bubbling that is absent in the pressed electrodes gives rise to degradation of the materials due to fracturing. It is most likely due to the oxidation of carbon-rich domains. The inner surface area of formed holes is amorphous and does not display any dynamic surface layer.

In addition to bubble formation, the formation of a dynamic surface can also be observed at birnessite crystals of the printed electrode in H_2O (inset Figure 6.5B and Figure D.9). This confirms that the dynamic surface layer is a characteristic feature in both the printed and the pressed electrodes. However, the analysis of this surface dynamics is restricted due to overlap with bulk dynamics.

6.3.3. In-situ STEM EELS of the Birnessite Electrodes in H_2O and O_2

Figure 6.6 shows the STEM EELS Mn L-edge spectra of the pressed and printed electrodes in H_2O , O_2 and HV. The O-K edge is dominated by losses in the H_2O/O_2 vapor in the TEM column and thus cannot provide spectroscopic information about

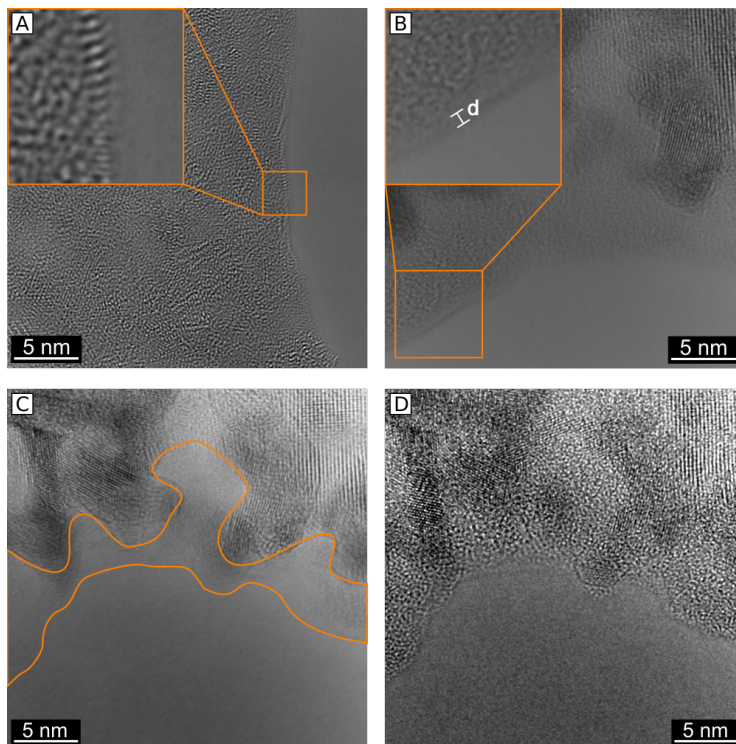


Figure 6.5.: In situ HRTEM analysis of the dynamic state of the printed electrode in 1 hPa H₂O compared to 1 hPa O₂. (A) Averaged image in O₂ ($\bar{N}=187$, $T=30$ s, $D=10,400$ e⁻/(Å²s)); (B) averaged image in 1 hPa H₂O ($\bar{N}=516$, $T=88$ s, $D=22,200$ e⁻/(Å² s), time resolved frames in Figure D.9); (C) averaged image in 1 hPa H₂O ($\bar{N}=478$, $T=63$ s, $D=40,300$ e⁻/(Å² s) the orange marked area indicates the area with the strongest blurring; and (D) single frame of (C).

the sample (see Figure D.12). In contrast, the L3/L2 intensity ratio of the Mn L-edge reveals information about the oxidation state of manganese. The accuracy of the method for valence state determination is limited by statistical scattering connected to the required fitting, background subtraction and assessment of multiple scattering effects.^[212] In addition, the absolute valence determination is limited due to variations of L3/L2 ratio in the reference spectra of typical manganese oxides and birnessites.^[208,209,213–216] We thus use the L3/L2 ratio to indicate relative oxidation trends of Mn species in the birnessite.

In Table 6.2 L3/L2 ratios for the pressed and printed electrodes are given. In HV, both electrodes present the same oxidation state. By adding 1 hPa O₂, the L3/L2 ratio decreases, thus indicating oxidation. The presence of 1 hPa H₂O further oxidizes the samples. Therefore, for both the electrodes the manganese valence is the highest in H₂O (H₂O > O₂ > HV).

Note that the printed electrode shows a higher oxidation state in H₂O and O₂ compared to the pressed electrode. This indicates that the presence of carbon in-

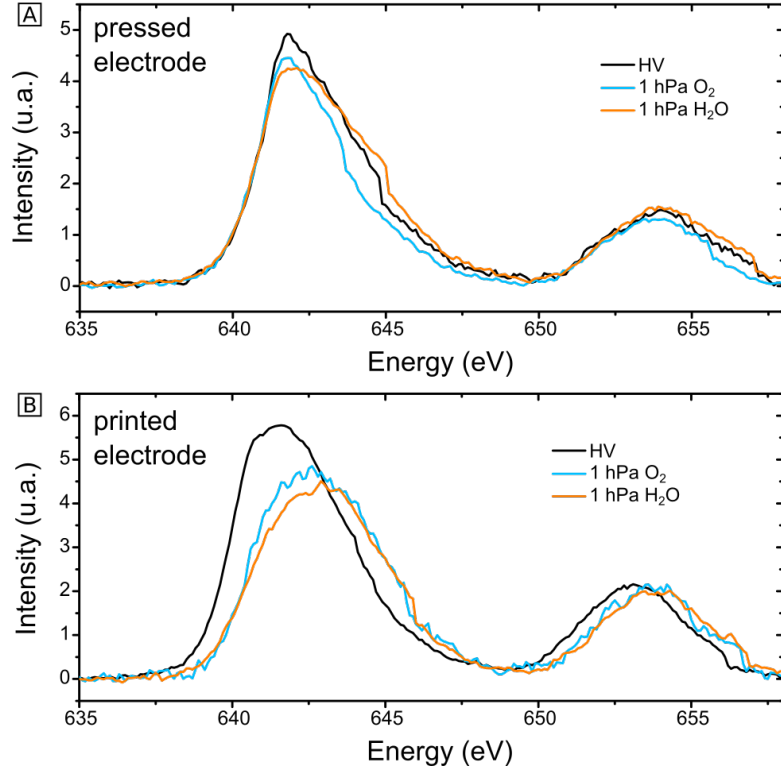


Figure 6.6.: Representative in-situ STEM EELS Mn-L Edge spectra in 1 hPa H₂O, 1 hPa O₂ and HV of (A) pressed electrode and (B) printed electrodes. More spectra from different areas can be found in Figure D.11 and D.12.

		HV	1 hPa O ₂	1 hPa H ₂ O
printed electrode	L3/L2 ratio	3.1 ± 0.2	2.5 ± 0.2	2.3 ± 0.3
	valence	3.3 ± 0.1	3.7 ± 0.1	3.9 ± 0.2
pressed electrode	L3/L2 ratio	3.3 ± 0.3	3.1 ± 0.1	2.9 ± 0.3
	valence	3.1 ± 0.1	3.3 ± 0.1	3.6 ± 0.3

Table 6.2.: Overview of the EELS L3/L2 intensity ratio of the pressed and printed birnessite electrodes in H₂O, O₂ and HV. In addition, Mn valence is determined by MLLS fitting. The accuracy is given by statistical deviations. All spectra used in the EELS analysis can be found in Figure D.11 and D.12.

creases the surface of the electrode which is exposed to H₂O/O₂ and, therefore, facilitates raising the average oxidation state of the lamella.

In order to determine the absolute manganese valence from the EELS Mn spectra, MLLS fitting was used. Inspired by a previous, successful MLLS-fit used for the correct determination of the Mn valence state of birnessite,^[214] the same method was applied here for the reference spectra^[208] of manganosite (Mn²⁺), norrishite

(Mn^{3+}) and ramsdellite (Mn^{4+}). The MLLS fit is exemplified in Figure D.3, and the resulting Mn valences are given in Table 6.2. In HV, the MLLS fit yields a valence of 3.3 ± 0.1 for the printed and 3.1 ± 0.1 for the pressed electrode. This is in very good agreement with the results from XANES measurements, where the manganese valence for similar printed birnessite electrodes was determined to be 3.226. MLLS fitting is quite sensitive to energy calibration and thus, a slight difference in the spectrometer calibration can cause significant deviations. However, the accordance with the XANES analysis^[29] indicates that our spectrometer energy calibration matches that of the used reference spectra. This was additionally confirmed by O-K edge spectroscopy in HV, whereas in $\text{H}_2\text{O}/\text{O}_2$ vapor it is dominated by the gas spectra (see Figure D.13).

Similar to the L3/L2 ratio, MLLS fitting shows oxidation of both samples in O_2 and H_2O , where the printed electrode become oxidized more strongly than the pressed one. For the printed electrode, the valence reaches 3.9 ± 0.2 in H_2O compared to 3.6 ± 0.3 of the pressed electrodes. An increase of the Mn oxidation state from 3.2 to 3.5 after electrochemical operation is also established in post-operando XANES analysis.^[29] This value is slightly reduced compared to this work.

6.4. Discussion

The Relevance of Beam Effects

In general, there are four different types of beam effects which could influence the sample and influence the in-situ experiments.

First, elastic scattering with a high incident beam energy and large scattering angles can lead to knock-on damage via displacement of atoms. This effect depends on the displacement energy of the material and can only be avoided if the acceleration voltage of the transmission electron microscopy is below the displacement threshold.^[217] In the HV TEM analysis of the pressed electrode at a dose rate of $8400 \text{ e}^-/(\text{\AA}^2 \text{ s})$ and an accumulated dose of $336.000 \text{ e}^-/\text{\AA}^2$, no dynamics or beam damage is observed (see Figure 6.3C). With a higher dose rate of $42.000 \text{ e}^-/(\text{\AA}^2 \text{ s})$ and an accumulated dose of $2.209,200 \text{ e}^-/\text{\AA}^2$ slight movements of the surface ($< 0.17 \text{ nm}$) at some areas occur (see Movie S8). Since in HV operation, no cold trap was used in the octagon, the presence of a small H_2O background concentration must be taken into consideration. Based on Roddatis et al.,^[218] we estimate 1% of H_2O , i.e. a partial pressure of 10-9 hPa in HV. However, in the averaged image in Figure D.6, atomic ordering up to the surface is still visible and the distance from a grain boundary to the surface is not changing with time. In addition, the O_2 analysis of the pressed electrode at a dose rate of $22.600 \text{ e}^-/(\text{\AA}^2 \text{ s})$ and an accumulated dose of $4.082,400 \text{ e}^-/\text{\AA}^2$ indicates no dynamics or beam damage (see Figure 6.1 and Movie S1). The orange markers in the figure and movie show explicitly that the surface is stable and that no atoms are removed. The same applies to electron beam sputtering which describes the removal of surface atoms. Due to the reduced number of

bonds at the surface, the threshold energy for atomic displacements is also reduced. However, no sputtering of the birnessite surface is observed in HV or O₂ (see Movie S1) on time scales of minutes, demonstrating that the energy threshold for electron beam sputtering is not exceeded at the surfaces.

Secondly, inelastic electron-electron scattering can transfer energy to the specimen. The temperature rise is proportional to the beam current and typically in the order of 1 K.^[217,219] The analysis in HV and 1 hPa O₂ yields no dependency of the surface dynamic layer thickness on the dose rate/beam current, and thus, thermal heating is neglectable.

Thirdly, the breaking of chemical bonds (radiolysis) originating from inelastic scattering of electrons must be considered. In the cases of insulators and some semiconductors, incident electrons can create holes in the valence band or inner shell, which can diffuse and break chemical bonds permanently.^[219] In addition, for transition metals, creation of the inner-shell holes on the metal site followed by a Auger decay from the oxygen results in the ejection of the O atom, which finally leads to a metal-rich surface.^[217] In HV, no breakage of bonds (reduction of crystallinity) was observed under our conditions. Moreover, this effect should depend on the dose rate, similar to the possible beam-heating described above, unlike the observed surface dynamics.

Finally, electrostatic effects can lead to beam induced electric potentials due to the emission of secondary electrons.^[121] The value of the beam induced electric potential depends on the dose rate and resistance of the TEM lamella. The series resistance of the used birnessite lamella is estimated in a STM contact experiment to $R \approx 5 \cdot 10^{11} \Omega$ (see Figure D.14), which lies within the expected values from the literature^[88,220]. Following Mildner et al.^[121] we calculate an induced potential of 1-SI6.5V for a variation of the beam current between 1 and 25 nA with equation (7) in this reference. For a typical in-situ experiment in H₂O with a dynamic surface layer, we used a dose rate of $8000 \text{ e}^- / (\text{\AA}^2 \text{ s})$ with a beam current of 4 nA, which corresponds to a beam induced potential of 2.6 V. Thus, OER-like conditions for the birnessite lamella in the ETEM can indeed be established in the presence of water vapor and the electron beam. The drop of the dynamic surface layer thickness below a dose rate of $5000 \text{ e}^- / (\text{\AA}^2 \text{ s})$, as shown in Figure 6.3, may be interpreted as being due to the reduction in the beam-induced potential from 2 V for a dose rate of $5000 \text{ e}^- / (\text{\AA}^2 \text{ s})$ to 1 V for $2000 \text{ e}^- / (\text{\AA}^2 \text{ s})$. Although the thickness of the dynamic layer does not increase with the beam-induced potential, there is indication for an increase of speed/intensity of the dynamics. This can be visualized by a stronger surface blurring for a higher induced potential in frames averaged over a short time (1 s) than that for a smaller beam induced potential (see Figure D.15).

About the Nature of the Dynamic Layer

One important structural feature of birnessites is the intercalation of cations and water molecules between MnO₆-layers. The cations balance charge inhomogeneities within the layer due to different manganese oxidation states or vacancies.^[84,221] A

similar structure can be found in clays, which are capable of swelling due to a change in the water content.^[222] Hensen and Smit.^[223] suggest the presence of one water layer in the interlayer in low humidity and the location of the cations at the edge of the water layer forming an inner-sphere surface complex, which is bonded via hydrogen-bonds to the clay surface. With increasing humidity, the water layer expands but the inner-sphere complex is preserved. At high relative humidity, the cations are partially to fully hydrated and located in the center of the interlayer.^[223] The cation-clay interaction depends on the structure and charge distribution of the clay layer and determines the bond strength of the inner-sphere complex. An increase in the bond strength can prevent the swelling of the clay.^[223]

In birnessites, the interlayer distance also depends on the type of the cation so that, for example, with the incorporation of Mg^{2+} , a buserite with a largely expanded layer can be formed.^[215] X-ray diffraction analysis of Appelo and Postma^[224] indicated a swelling of Ca-birnessite in 100% relative humidity, resulting in an increase of the interlayer distance from ≈ 7 to ≈ 10 Å. The formation of a dynamic and disordered birnessite surface layer with a thickness of the order of 6 Å in the presence of H_2O suggests a hydration process at the near-surface area of the electrode. Due to the relatively low water partial pressure in the ETEM experiments between 0.5 and 1 hPa, which is clearly below the equilibrium vapor pressure of liquid water at room temperature, a liquid water layer can only be formed on the surface for a large adsorption energy of H_2O on surfaces. In the literature, the existence of a few monolayers of H_2O on oxide surfaces is suggested, because of the large negative adsorption energy of the order of -160 kJ/mol.^[122,124-126] Some experiments indicate that the thickness of the H_2O surface layer does not significantly change over a pressure range of 10^{-7} to 10^{-2} hPa.^[126] This might explain the H_2O pressure independence of the dynamic surface layer thickness in Figure 6.3.

In the case of a hydrated surface layer in contact with H_2O , the bond strength may be reduced compared to that of crystalline birnessite in HV. Thus, the energy threshold for beam-induced atom displacements is also reduced. However, if the pronounced surface dynamics were caused by electron beam-induced atom displacement or diffusion, this should also lead to a sputtering of the dynamic surface since the energy thresholds for sputtering and displacement along the surface are comparable.^[219,225] Despite the lower cross-section of sputtering than that of surface diffusion,^[225] sputtering should be visible after several minutes due to the intense surface layer dynamics. However, no distance change between the stable bulk features and the dynamic surface develops, and hence, sputtering can be excluded within the accuracy limit of our experiments (e.g., see Figure D.16 and Movie S3). This suggests that the dynamics of the surface layer is not predominantly caused by the electron beam induced atom displacement.

A partial or full hydration of the Ca^{2+} and $\text{Mn}^{3+/4+}$ ions of the surface layer could facilitate the dynamics of the ions, that would then form a disordered, liquid-like state. The high stability of this layer in ETEM experiments also suggests a high stability in electrochemical OER conditions. Our HRTEM analysis furthermore indicates defect- and vacancy-rich birnessite layers, as already reported by Wiechen

et al.^[84]. In the presence of a surface water layer, hydration of the rough birnessite surface layers might occur where H₂O molecules are arranged around the Ca²⁺ and Mn^{3+/4+} ions, while still bonded to the MnO_x surface. However, it cannot be clarified whether the dynamics is caused by OER or a similar reactions. In previous research,^[29,205] an interaction of Ca²⁺ with phosphorus ions from a phosphate buffer and the formation of a phosphorous rich-amorphous surface layer were observed only after OER. The in-situ study of the dynamic surface layer presented here can well explain the formation of such an amorphous surface layer.

The detected oxidation of birnessites in O₂ and H₂O supports the presence of a flexible manganese valence in birnessites, which depends on the ambient and electric potential and might be a key characteristic for an efficient OER catalyst. Since the oxidation of the material via incorporation of oxygen species from the environment takes place via the accessible surface, the manganese ions with increased oxidation states may be mainly located in regions close to the surface, including the dynamic surface layer. The higher oxidation state of Mn in H₂O under reactive conditions might also be the reason for the good stability of birnessites at OER conditions, where the formation of Mn²⁺ would give rise to Mn leaching and, thus, electrode corrosion.^[90]

Altogether, we suggest that the formed dynamic surface layer of the birnessite in H₂O at a positive electric potential represents a partially hydrated state, where Mn assumes a higher oxidation state due to the incooperation of additional OH⁻ anions. Although there are several differences between an in-situ ETEM experiment in H₂O and an OER in a liquid electrolyte, some of the features are comparable: the presence of a condensed H₂O layer on the birnessite surface as a prerequisite for hydration and the beam-induced positive electric potential. This suggests that a dynamic surface layer might represent the active state of birnessite and facilitate oxygen evolution due to the increased reaction volume that also involves subsurface regions. This might facilitate a simple charge transfer, flexible bond coordination, and bond formation and breaking.

6.5. Conclusion

We analyzed printed and pressed birnessite electrodes under OER-like conditions in the ETEM, that is, in H₂O that forms a condensed surface layer under anodic stimulation. Both types of electrodes show significant surface dynamics in 1 hPa H₂O.

In contrast to Han et al.,^[226] who detected the formation of oxygen bubbles in Ba_{0.5}Sr_{0.5}Co_{0.8}Fe_{0.2}O₃ (BSCF) under OER conditions in an ETEM at low dose rates of $1 \text{ e}^- / (\text{\AA}^2 \text{ s})$, we observe bubble formation at moderate dose rates only in carbon-containing printed birnessite electrodes. For carbon-free pressed electrodes, bubble formation is clearly related to radiation damage. Indeed, BSCF particles are not stable and become amorphous under OER conditions.^[227,228] This is different compared to birnessites which are stable OER catalysts^[205].

The second main observation is the emergence of an atomic surface dynamics at birnessite in contact with H₂O, which is absent in O₂, inert gases, or vacuum. We give evidence that this indicates an H₂O intercalation into a region close to the surface of the birnessite and the beam-induced potential as the probable origin of the dynamic surface. The dynamic layer thickness above 5000 e⁻/(Å²s) is independent of the electron dose rate. Together with the stability in HV and O₂ and under OER-like conditions, this indicates that such atomic surface dynamics is involved in the active state of the birnessite electrode. A comparison with the literature suggests hydration of the surface birnessite layer. The EELS analysis shows an oxidation of birnessite in H₂O and O₂, revealing the higher oxidation state of the manganese in the dynamic surface layer. This emphasizes the flexible Mn valence and stability of the catalyst, which might be a key characteristic for an efficient OER. In addition, the dynamic surface layer might be optimal for oxygen evolution due to the high surface area, flexible Mn coordination, and the resulting simpler bond formation and breaking.

Associated Content

Supporting Information

The following files are available free of charge at <https://pubs.acs.org/doi/10.1021/acs.jpcc.0c09806>.

HRTEM movies of the birnessite electrodes in different environments (HV, O₂ and H₂O), dose rates and speeds.

Movie S1: Pressed electrode in 1 hPa O₂ with 22600 e⁻/(Å²s) and 8.6x speed (MP4)

Movie S2: Pressed electrode in 1 hPa H₂O with 60000 e⁻/(Å²s) and 6.2x speed (MP4)

Movie S3: Pressed electrode in 1 hPa H₂O with 7100 e⁻/(Å²s) and 4.1x speed (MP4)

Movie S4: Pressed electrode in 1 hPa O₂ with 7500 e⁻/(Å²s) and 8.6x speed (MP4)

Movie S5: Printed electrode in 1 hPa O₂ with 7400 e⁻/(Å²s) and 4.1x speed (MP4)

Movie: S6: Printed electrode in 0.1 hPa H₂O with 5000 e⁻/(Å²s) and 22.3x speed (MP4)

Movie: S7: Printed electrode in 1 hPa H₂O with 7700 e⁻/(Å²s) and 11.2x speed (MP4)

Movie S8: Pressed electrode in HV (no cold trap) with 42000 e⁻/(Å²s) and 6.2x speed (MP4)

TEM data including FFT analysis, single frames from the movies, and IV curve of a lamella, representative illustration of MLLS fitting, additional EELS spectra of the carbon and O-K edge and EELS Mn-L edge spectra used for valence analysis

(PDF).

Author Information

Corresponding Author

*E-mail: cjooss@gwdg.de

Present Addresses

†Helmholtz-Zentrum Potsdam Deutsches GeoForschungsZentrum GFZ, Telegrafenberg, 14473 Potsdam, Germany

Author Contributions

The manuscript was written through contributions of all authors. All authors have given approval to the final version of the manuscript.

Acknowledgment

This project was made possible by the generous financial support by the German Research Foundation (DFG) priority program SPP1613, grants KU2885/2-2 and JO348/11-1, and SFB 1073, project C02, funded by the DFG. The Authors would like to thank Kerstin Born for her contribution to the preparation of the pressed birnessite samples.

Abbreviations

dose rate (D), averaged frame number (\bar{N}), total time for averaged frames (T)

General Discussion and Summary

In this work three partially disordered material systems for use in a water splitting integrated device were studied by means of electron microscopy. Following the three main components of an integrated device, this work has been subdivided into the OER, HER and the protection of a photoabsorber. With Birnessite ($\delta\text{-MnO}_2$) and $\text{MoS}_{2+\delta}$ two catalysts with a high abundance and low cost, but high performance, were investigated as possible substitutes for expensive and non-abundant precious metal catalysts. The analysis of partially disordered systems is challenging due to the importance of inhomogeneities down to the atomic level. Thus, a structural analysis by XRD is often not sufficient, especially for amorphous materials, and HRTEM is recommendable.

To protect the Si solar cells from corrosion in an integrated device, an amorphous TiO_2 layer was utilized in chapter 3. However, after 1 h of operation in 1 M KOH, the potential drops and the formation of pinholes in the device is visible. In general, the ultra-thin TiO_2 layer of only 4-7 nm is stable under reactive conditions, but Cl impurities were revealed to start the corrosion process. A reduction of Ti^{4+} to Ti^{3+} is suggested due to the replacement of O with Cl which consequently leads to a leaching of $\text{Ti}^{2+/3+}$. The pinhole formation can be delayed by increasing the thickness of the TiO_2 layer^[131], which is in accordance with our corrosion model, but not desirable due to an increase in electric resistivity.

One reasonable solution for this problem is the optimization of the ALD process. The TiO_2 layer thickness and also the Cl content is inhomogeneous, i.e., the thicker layers contain less Cl, have a higher Pt catalyst coverage and are more stable. A higher Pt coverage is also suggested to reduce the dissolution of TiO_2 and Si (see chapter 3). A second solution would be the replacement of the Cl containing precursor for the ALD process.

For an efficient integrated water splitting device, a HER catalyst on the photocathode is required. With $\text{MoS}_{2+\delta}$, an abundant, highly active and partially disordered HER catalyst was analyzed in chapter 4 as an alternative to the non-abundant and expensive platinum. However, the structure of MoS_x is controversially discussed in literature^[22,53,54]. Especially for the partially disordered Molybdenum sulfides, the structure determination is essential for a rational catalyst design.

The structure of $\text{MoS}_{2+\delta}$ was determined to be a partially disordered nanocrystalline variant of MoS_2 with a very small grain size. In addition, $[\text{Mo}_3\text{S}_{13}]^{2-}$ cluster like defects and disclinations are formed. Due to disorder, the Mo-Mo distance is locally reduced and the c-axis is increased in average. As a result, the number of coordinatively modified Mo is increased which is also supported by the scaling of the activity with Mo. For crystalline MoS_2 the active sites are located at the edges^[55-57] which makes a partially disordered system with a high number of edges beneficial, and in-plane defects also make the basal plane basically active. In addition, cluster-like structures, which are known for their high activity^[35,59], appear within the lattice planes as well as at their edges. In accordance with our structure model, XPS typically indicates bridging and terminal disulfides as well as unsaturated Molybdenum and Sulfur ions for MoS_x with $2 < x < 4$ ^[23,39,40,60,61]. The observed structural changes thus explain the high density of catalytic active sites which are present at the defective nanocrystalline planes as well as at their edges and, in consequence, could very well explain the much higher HER activity of $\text{MoS}_{2+\delta}$ compared to MoS_2 .

MoS_x can be prepared via different routes, e.g. by solvothermal synthesis or electrodeposition, and also different precursors can be used, resulting in a varying S:Mo ratio and maybe even different crystal structures. Sulfur-rich materials with a S:Mo ratio larger than 4 could comprise a higher amount of cluster features as suggested by Tran et al.^[53]. A ratio closer to 2 might result in a more MoS_2 -like structure as indicated by our XRD analysis. Thus, the suggested structure model applies only for MoS_x with $2 < x < 4$. However, the observed crystallization of amorphous MoS_x to MoS_2 ^[49,50] indicates the thermodynamic stability of MoS_2 related structures, like the structure of our suggested model, under HER conditions. It also emphasizes the importance of future HRTEM analysis of structural changes of MoS_x during electrolysis.

Besides the HER catalyst, an OER catalyst is also needed in an integrated water splitting device. The emphasis in this work is on the manganese oxide OER catalyst Birnessite ($\delta\text{-MnO}_2$). In chapter 5 and 6 the active state and the changes during OER of Birnessite are analyzed. For the Ca-Birnessite the operation in phosphate-based electrolytes seems to be particularly advantageous. A post-mortem analysis of the electrolyzed sample in a phosphate buffer revealed a leaching of Calcium and the formation of an amorphous and Phosphor rich surface layer. The incorporated Phosphor in the surface is proposed to act as an "acceptor base"^[229] for the deprotonation step, and thus it might explain the higher activity of Birnessite in a phosphate buffer.

In principal two ways the surface layer was formed are possible: 1) An amorphization of the nanocrystalline Birnessite surface, leaching of Ca and incorporation of P into the amorphous layer. 2) First, a leaching of Ca and Mn into the electrolyte and then redeposition of P, Ca and Mn under reactive conditions. The formation of an amorphous MnO_x layer under oxidizing conditions is in accordance with reports from literature^[76,171,230,231]. However, the type of formation mechanism could not be identified by the post-mortem experiments.

More insights are gained with in-situ ETEM studies from chapter 6. Here, the formation of a dynamic disordered surface layer was observed under OER-like conditions which fits in with the amorphous P-rich surface layer from the post-mortem experiments. We suggest an interaction of Birnessite with the water vapor and the beam induced positive electric potential as the origin and interpret the observation as a hydrated disordered and highly dynamic Birnessite surface layer under OER-like conditions. Although redeposition is not possible in the ETEM experiment in H₂O water vapor, the dynamic surface layer indicates that mechanism 1), the amorphization of the surface, plays a role in the formation of the surface layer in electrolytes. However, the in-situ identified dynamic layer thickness of ≈ 6 Å is significantly smaller compared to the P rich surface layer of ≈ 25 nm after electrolysis in phosphate buffer. The thickness of the dynamic surface layer might be limited by the water layer in ETEM on top of the lamella surface and would be thicker with a real electrolyte. However, no formation of a significantly thick¹ amorphous surface layer is observed with imidazolium sulphate, indicating that the formation of the thick amorphous surface layer is associated with the electrolyte selection. Hence, the relevance of mechanism 2), the redeposition of an amorphous MnO_x material, might depend on the electrolyte.

In a phosphate buffer, when mechanism 2) might be relevant, the redeposition could represent an electrolyte dependent self-healing process. Huynh et al.^[70] suggested the ability of MnO_x electrodes to maintain self-healing for electrolytes with pH greater than 0. The lack of long-term stability of the Birnessite electrodes in imidazolium sulphate together with the absence of the thick amorphous surface layer under these conditions supports this assumption.

Typically, the Birnessite electrodes are highly porous, so an increase of the current density² with increasing layer thickness is expected. Due to a competition of the proton-electron/hole transport with the consumption of holes in catalytic reactions, an optimal thickness exists^[70]. However, a volume activity going beyond the activity on the pore surfaces is suggested by Lee et al.^[89] and Melder et al.^[67]. In this context, the dynamic surface layer as observed in the ETEM experiments could also be interpreted as a catalytic activity in the dynamic subsurface (< 6 Å). In addition to the porous structure, the oxidation of the carbon and the bubble formation in the printed electrode lamella also suggests the presence of fine pathways into the electrode for H₂O and O₂, which might have not been detected by the determination of the active surface area dependent on the deployed method.

By means of in-situ EELS, the oxidation of Mn at the surface from +3.3 in HV to +3.9 in OER-like conditions was observed which is also supported by the post-mortem XANES analysis. A flexible mixture of Mn³⁺ and Mn⁴⁺ is suggested to be a key characteristic for efficient OER by manganese oxides^[26,86,179,180]. For Birnessite the Mn valence and Ca:Mn ratio is correlated with the structure. Hence, the struc-

¹Significantly thick in the sense of larger than 0.6 nm. The detection of the formation of an 0.6 nm thick amorphous surface layer on a partially disordered material after electrolysis is challenging but could be possible with identical location TEM (IL-TEM) or a suitable liquid cell holder.

²Current density normalized to the geometric area.

ture also has a large impact on the activity which is exemplified by the inactive, regularly assembled and layered Birnessite with an oxidation state of 4+ reported by Zaharieva et al.^[18]. A high disorder leads to a heterogeneous ligand environment of coordinatively unsaturated μ -oxo bridges and terminal coordination sites for water binding which is suggested to increase OER rates^[18]. This is supported by the structure model of Mattioli et al.^[167] where the active MnO_x catalysts are formed by interconnection of small planar Mn-oxido sheets with introduced disorder by out of plane linked Mn atoms. Undercoordinated Mn^{3+} at the edge of the network might act as hole traps and facilitate the OER^[167]. The activity of the Birnessite catalyst from chapter 5 and 6 with its small and partially disordered crystal plates fits in well. Furthermore, the dynamic surface layer could offer the suggested ideal conditions for OER with

- a flexible structure consisting of a heterogeneous ligand environment, coordinatively unsaturated μ -oxo bridges and terminal coordination sites for water binding,
- an average Mn valance state greater than +3.5 which can dynamically change due to the flexible structure,
- a good accessibility of the catalytic centers,
- the presence of secondary cations to assist oxidation by activating of H_2O ,

and thus explain the high activity of Birnessite.

Here, a similarity to the partially disordered MoS_x in respect to the modified coordination stands out. In the case of $\text{MoS}_{2+\delta}$ the disorder also leads to a coordinatively modified Mo network and changes in the Mo-Mo distance. In both cases the disorder leads to a change of the coordination and the creation of a heterogeneous ligand environment which is suggested to improve the activity of the OER/HER catalyst.

This work demonstrates the potential of partially disordered systems for the use in integrated water splitting devices and the capability and necessity of detailed TEM studies on partially disordered systems for water splitting. The determination and analysis of the catalyst's active state and its dynamics are crucial for a rational catalyst design, and thus a real space visualization is highly desirable. The visualization by in-situ ETEM and the analysis of the dynamic surface layer of Birnessite in this work is an important step towards an understanding of the dynamics in the active state of partially disordered systems during OER. It further emphasizes the importance of a detailed real space structural analysis, especially for catalysts under reactive conditions, and thus motivates further developments of in-situ ETEM methods.

Bibliography

- [1] Sam Koochi-Kamali, V. V. Tyagi, N. A. Rahim, N. L. Panwar, and H. Mokhlis. Emergence of Energy Storage Technologies as the Solution for Reliable Operation of Smart Power Systems: A Review. *Renewable and Sustainable Energy Reviews*, 25:135–165, September 2013.
- [2] W. Smith. Role of Fuel Cells in Energy Storage. *Journal of Power Sources*, 86(1):74–83, March 2000.
- [3] Frano Barbir. PEM Electrolysis for Production of Hydrogen from Renewable Energy Sources. *Solar Energy*, 78(5):661–669, May 2005.
- [4] Michael Hambourger and Thomas A Moore. Nailing Down Nickel for Electrocatalysis. *Science (New York, N.Y.)*, 326(5958):1355–6, 2009.
- [5] Sean B. Walker, Ushnik Mukherjee, Michael Fowler, and Ali Elkamel. Benchmarking and selection of power-to-gas utilizing electrolytic hydrogen as an energy storage alternative. *International Journal of Hydrogen Energy*, 41:7717–7731, May 2016.
- [6] Markus Lorenz, Martin Lüers, Max Ludwig, Simon Rees, Hartmut Rauen, Matthias Zelinger, and Robert Stiller. Grüne Technologien für grünes Geschäft. Technical report, Boston Consulting Group, Verband Deutscher Maschinen- und Anlagenbau, 2020.
- [7] M. Sastri, R. Viswanath, and B. Viswanathan. Studies on the Reduction of Iron Oxide with Hydrogen. *International Journal of Hydrogen Energy*, 7(12):951–955, January 1982.
- [8] Hsin-Yu Lin, Yu-Wen Chen, and Chiuping Li. The Mechanism of Reduction of Iron Oxide by Hydrogen. *Thermochimica Acta*, 400(1-2):61–67, April 2003.
- [9] Jayant M. Modak. Haber Process for Ammonia Synthesis. *Resonance*, 16(12):1159–1167, December 2011.
- [10] James G. Speight. Petroleum Refinery Processes. In *Kirk-Othmer Encyclopedia of Chemical Technology*. John Wiley & Sons, Inc., Hoboken, NJ, USA, August 2005.

- [11] Mariette M Pereira and Mário J F Calvete, editors. *Sustainable Synthesis of Pharmaceuticals*. Green Chemistry Series. Royal Society of Chemistry, Cambridge, March 2018.
- [12] Bundesministerium für Wirtschaft und Energie. Die Nationale Wasserstoffstrategie. Technical report, Bundesministerium für Wirtschaft und Energie (BMWi), 2020.
- [13] Manuel Götz, Jonathan Lefebvre, Friedemann Mörs, Amy McDaniel Koch, Frank Graf, Siegfried Bajohr, Rainer Reimert, and Thomas Kolb. Renewable Power-to-Gas: A Technological and Economic Review. *Renewable Energy*, 85:1371–1390, January 2016.
- [14] Alfredo Ursua, Luis M. Gandia, and Pablo Sanchis. Hydrogen Production From Water Electrolysis: Current Status and Future Trends. *Proceedings of the IEEE*, 100(2):410–426, February 2012.
- [15] Michael G. Walter, Emily L. Warren, James R. McKone, Shannon W. Boettcher, Qixi Mi, Elizabeth A. Santori, and Nathan S. Lewis. Solar Water Splitting Cells. *Chemical Reviews*, 110(11):6446–6473, November 2010.
- [16] Michael Huynh, Chenyang Shi, Simon J.L. Billinge, and Daniel G. Nocera. Nature of Activated Manganese Oxide for Oxygen Evolution. *Journal of the American Chemical Society*, 137(47):14887–14904, November 2015.
- [17] Carolin E. Frey, Mathias Wiechen, and Philipp Kurz. Water-Oxidation Catalysis by Synthetic Manganese Oxide-Systematic Variations of the Calcium Birnessite Theme. *Dalton Transactions*, 43(11):4370–4379, 2014.
- [18] Ivelina Zaharieva, Petko Chernev, Marcel Risch, Katharina Klingan, Mike Kohlhoff, Anna Fischer, and Holger Dau. Electrosynthesis, Functional, and Structural Characterization of a Water-Oxidizing Manganese Oxide. *Energy & Environmental Science*, 5(5):7081–7089, 2012.
- [19] Yang Yang, Huilong Fei, Gedeng Ruan, Changsheng Xiang, and James M. Tour. Efficient Electrocatalytic Oxygen Evolution on Amorphous Nickel-Cobalt Binary Oxide Nanoporous Layers. *ACS Nano*, 8(9):9518–9523, September 2014.
- [20] Katharina Klingan, Franziska Ringleb, Ivelina Zaharieva, Jonathan Heidkamp, Petko Chernev, Diego Gonzalez-Flores, Marcel Risch, Anna Fischer, and Holger Dau. Water Oxidation by Amorphous Cobalt-Based Oxides: Volume Activity and Proton Transfer to Electrolyte Bases. *ChemSusChem*, 7(5):1301–1310, 2014.
- [21] Matthew W. Kanan and Daniel G. Nocera. In Situ Formation of an Oxygen-Evolving Catalyst in Neutral Water Containing Phosphate and Co^{2+} . *Science*, 321(5892):1072–1075, August 2008.

- [22] Marie-Luise Grutza, Ashwene Rajagopal, Carsten Streb, and Philipp Kurz. Hydrogen Evolution Catalysis by Molybdenum Sulfides (MoS_x): are Thiomolybdate Clusters like $[\text{Mo}_3\text{S}_{13}]^{2-}$ - Suitable Active Site Models? *Sustainable Energy & Fuels*, 2(9):1893–1904, August 2018.
- [23] Carlos G. Morales-Guio and Xile Hu. Amorphous Molybdenum Sulfides as Hydrogen Evolution Catalysts. *Accounts of Chemical Research*, 47(8):2671–2681, August 2014.
- [24] Junfeng Xie and Yi Xie. Structural Engineering of Electrocatalysts for the Hydrogen Evolution Reaction: Order or Disorder? *ChemCatChem*, 7(17):2568–2580, September 2015.
- [25] Longfei Wu, Alessandro Longo, Nelson Y. Dzade, Akhil Sharma, Marco M. R. M. Hendrix, Ageeth A. Bol, Nora H. Leeuw, Emiel J. M. Hensen, and Jan P. Hofmann. The Origin of High Activity of Amorphous MoS_2 in the Hydrogen Evolution Reaction. *ChemSusChem*, 12(19):4383–4389, October 2019.
- [26] Jens Melder, Peter Bogdanoff, Ivelina Zaharieva, Sebastian Fiechter, Holger Dau, and Philipp Kurz. Water-Oxidation Electrocatalysis by Manganese Oxides: Syntheses, Electrode Preparations, Electrolytes and Two Fundamental Questions. *Zeitschrift für Physikalische Chemie*, 234(5):925–978, May 2020.
- [27] Emanuel Ronge, Thorsten Cottre, Katharina Welter, Vladimir Smirnov, Natalie Jacqueline Ottinger, Friedhelm Finger, Bernhard Kaiser, Wolfram Jaegermann, and Christian Jooss. Stability and Degradation Mechanism of Si-based Photocathodes for Water Splitting with Ultrathin TiO_2 Protection Layer. *Zeitschrift für Physikalische Chemie*, 234(6):1171–1184, June 2020.
- [28] Emanuel Ronge, Sonja Hildebrandt, Marie-Luise Grutza, Helmut Klein, Philipp Kurz, and Christian Jooss. Structure of Nanocrystalline, Partially Disordered $\text{MoS}_{2+\delta}$ Derived from HRTEM—An Abundant Material for Efficient HER Catalysis. *Catalysts*, 10(8):856, August 2020.
- [29] Emanuel Ronge, Jonas Ohms, Vladimir Roddatis, Travis Jones, Frederic Sulzmann, Axel Knop-Gericke, Robert Schlögl, Philipp Kurz, Christian Jooss, and Katarzyna Skorupska. Operation of Calcium-Birnessite Water-Oxidation Anodes: Interactions of the Catalyst with Phosphate Buffer Anions. *ChemRxiv.13153976.V1*, <https://doi.org/10.26434/chemrxiv.13153976.v1>, October 2020.
- [30] Emanuel Ronge, Jonas Lindner, Jens Melder, Jonas Ohms, Vladimir Roddatis, Philipp Kurz, and Christian Jooss. Atom Surface Dynamics of Manganese Oxide in OER like Conditions revealed by in-situ Environmental TEM. *The Journal of Physical Chemistry C (accepted)*, 2021.

- [31] P. Millet. Membrane Electrolysers for Hydrogen (H₂) Production. In *Advanced Membrane Science and Technology for Sustainable Energy and Environmental Applications*, chapter 18, pages 568–609. Woodhead Publishing, January 2011.
- [32] Jumeng Wei, Min Zhou, Anchun Long, Yanming Xue, Hanbin Liao, Chao Wei, and Zhichuan J. Xu. Heterostructured Electrocatalysts for Hydrogen Evolution Reaction Under Alkaline Conditions, October 2018.
- [33] Charles C. L. McCrory, Suho Jung, Ivonne M Ferrer, Shawn M Chatman, Jonas C. Peters, and Thomas F. Jaramillo. Benchmarking Hydrogen Evolving Reaction and Oxygen Evolving Reaction Electrocatalysts for Solar Water Splitting Devices. *Journal of the American Chemical Society*, 137(13):4347–4357, 2015.
- [34] Jue Hu, Bolong Huang, Chengxu Zhang, Zilong Wang, Yiming An, Dan Zhou, He Lin, Michael K.H. Leung, and Shihe Yang. Engineering Stepped Edge Surface Structures of MoS₂ Sheet Stacks to Accelerate the Hydrogen Evolution Reaction. *Energy and Environmental Science*, 10(2):593–603, February 2017.
- [35] Zhongjie Huang, Wenjia Luo, Lu Ma, Mingzhe Yu, Xiaodi Ren, Mingfu He, Shane Polen, Kevin Click, Benjamin Garrett, Jun Lu, Khalil Amine, Christopher Hadad, Weilin Chen, Aravind Asthagiri, and Yiyang Wu. Dimeric [Mo₂S₁₂]²⁻ Cluster: A Molecular Analogue of MoS₂ Edges for Superior Hydrogen-Evolution Electrocatalysis. *Angewandte Chemie - International Edition*, 54(50):15181–15185, December 2015.
- [36] Jung Woo Park, Zhaochu Hu, Shan Gao, Ian H. Campbell, and Hujun Gong. Platinum Group Element Abundances in the Upper Continental Crust Revisited - New Constraints from Analyses of Chinese Loess. *Geochimica et Cosmochimica Acta*, 93:63–76, September 2012.
- [37] Jesse D. Benck, Zhebo Chen, Leah Y. Kuritzky, Arnold J. Forman, and Thomas F. Jaramillo. Amorphous Molybdenum Sulfide Catalysts for Electrochemical Hydrogen Production: Insights into the Origin of their Catalytic Activity. *ACS Catalysis*, 2(9):1916–1923, September 2012.
- [38] M. Kokko, F. Bayerköhler, J. Erben, R. Zengerle, Ph. Kurz, and S. Kerzenmacher. Molybdenum Sulphides on Carbon Supports as Electrocatalysts for Hydrogen Evolution in Acidic Industrial Wastewater. *Applied Energy*, 190:1221–1233, March 2017.
- [39] Louisa Rui Lin Ting, Yilin Deng, Liang Ma, Yin-Jia Zhang, Andrew A. Peterson, and Boon Siang Yeo. Catalytic Activities of Sulfur Atoms in Amorphous Molybdenum Sulfide for the Electrochemical Hydrogen Evolution Reaction. *ACS Catalysis*, 6(2):861–867, February 2016.

- [40] Chang Lung Hsu, Yung Huang Chang, Tzu Yin Chen, Chien Chih Tseng, Kung Hwa Wei, and Lain Jong Li. Enhancing the Electrocatalytic Water Splitting Efficiency for Amorphous MoS_x . *International Journal of Hydrogen Energy*, 39(10):4788–4793, March 2014.
- [41] S.R. Taylor. Abundance of Chemical Elements in the Continental Crust: a New Table. *Geochimica et Cosmochimica Acta*, 28:1273–1285, 1964.
- [42] Y. Takeuchi and W. Nowacki. Detailed Crystal Structure of Rhombohedral MoS_2 and Systematic Deduction of Possible Polytypes of Molybdenite. *Schweizer Mineralogische und Petrographische Mitteilungen*, 44(1):105–120, 1964.
- [43] Keenan E. Dungey, M. David Curtis, and James E. Penner-Hahn. Structural Characterization and Thermal Stability of MoS_2 Intercalation Compounds. *Chemistry of Materials*, 10(8):2152–2161, 1998.
- [44] Roscoe G. Dickinson and Linus Pauling. The Crystal Structure of Molybdenite. *ACS Publications*, 45:1466–1471, 1923.
- [45] A. Müller, R. Jostes, W. Jaegermann, and R. Bhattacharyya. Spectroscopic Investigation on the Molecular and Electronic Structure of $[\text{Mo}_3\text{S}_{13}]^{2-}$, a Discrete Binary Transition Metal Sulfur Cluster. *Inorganica Chimica Acta*, 41(C):259–263, January 1980.
- [46] A. Müller, W. Jaegermann, and John H. Enemark. Disulfur Complexes. *Coordination Chemistry Reviews*, 46(C):245–280, October 1982.
- [47] J. C. Wildervanck and F. Jellinek. Preparation and Crystallinity of Molybdenum and Tungsten Sulfides. *Zeitschrift für anorganische und allgemeine Chemie*, 328(5-6):309–318, April 1964.
- [48] K. D. Bronsema, J. L. De Boer, and F. Jellinek. On the Structure of Molybdenum Diselenide and Disulfide. *Zeitschrift für anorganische und allgemeine Chemie*, 540(9-10):15–17, September 1986.
- [49] Sijia Liu, Xin Zhang, Jie Zhang, Zhigang Lei, Xin Liang, and Biaohua Chen. MoS_2 with Tunable Surface Structure Directed by Thiophene Adsorption Toward HDS and HER. *Science China Materials*, 59(12):1051–1061, December 2016.
- [50] Yanpeng Li, Yifei Yu, Yufeng Huang, Robert A. Nielsen, William A. Goddard, Yao Li, and Linyou Cao. Engineering the Composition and Crystallinity of Molybdenum Sulfide for High-Performance Electrocatalytic Hydrogen Evolution. *ACS Catalysis*, 5(1):448–455, January 2015.

- [51] Yanguang Li, Hailiang Wang, Liming Xie, Yongye Liang, Guosong Hong, and Hongjie Dai. MoS₂ Nanoparticles Grown on Graphene: an Advanced Catalyst for the Hydrogen Evolution Reaction. *Journal of the American Chemical Society*, 133(19):7296–7299, May 2011.
- [52] Th. Weber, J. C. Muijsers, and J. W. Niemantsverdriet. Structure of Amorphous MoS₃. *The Journal of Physical Chemistry*, 99(22):9194–9200, June 1995.
- [53] Phong D. Tran, Thu V. Tran, Maylis Orío, Stephane Torelli, Quang Duc Truong, Keiichiro Nayuki, Yoshikazu Sasaki, Sing Yang Chiam, Ren Yi, Itaru Honma, James Barber, and Vincent Artero. Coordination Polymer Structure and Revisited Hydrogen Evolution Catalytic Mechanism for Amorphous Molybdenum Sulfide. *Nature Materials*, 15(6):640–646, June 2016.
- [54] Deborah R. Huntley, T. G. Parham, R. P. Merrill, and M. J. Sienko. An EXAFS Study of the Thermal Decomposition of Molybdenum Trisulfide. *Inorganic Chemistry*, 22(26):4144–4146, December 1983.
- [55] Berit Hinnemann, Poul Georg Moses, Jacob Bonde, Kristina P Jørgensen, Jane H Nielsen, Sebastian Horch, Ib Chorkendorff, and Jens K Nørskov. Biomimetic Hydrogen Evolution: MoS₂ Nanoparticles as Catalyst for Hydrogen Evolution. *Journal of the American Chemical Society*, 127(15):5308–5309, 2005.
- [56] Thomas F. Jaramillo, Kristina P. Jørgensen, Jacob Bonde, Jane H. Nielsen, Sebastian Horch, and Ib Chorkendorff. Identification of Active Edge Sites for Electrochemical H₂ Evolution from MoS₂ Nanocatalysts. *Science*, 317(5834):100–102, July 2007.
- [57] Bora Seo and Sang Hoon Joo. Recent Advances in Unveiling Active Sites in Molybdenum Sulfide-Based Electrocatalysts for the Hydrogen Evolution Reaction. *Nano Convergence*, 4(1):19, December 2017.
- [58] Damien Voiry, Maryam Salehi, Rafael Silva, Takeshi Fujita, Mingwei Chen, Tewodros Asefa, Vivek B. Shenoy, Goki Eda, and Manish Chhowalla. Conducting MoS₂ Nanosheets as Catalysts for Hydrogen Evolution Reaction. *Nano Letters*, 13(12):6222–6227, December 2013.
- [59] Jakob Kibsgaard, Thomas F Jaramillo, and Flemming Besenbacher. Building an Appropriate Active-Site Motif into a Hydrogen-Evolution Catalyst with Thiomolybdate [Mo₃S₁₃]²⁻ Clusters. *Nature Chemistry*, 6(3):248–253, March 2014.
- [60] Ya Yan, Xiaoming Ge, Zhaolin Liu, Jing Yuan Wang, Jong Min Lee, and Xin Wang. Facile Synthesis of Low Crystalline MoS₂ Nanosheet-Coated CNTs for

- Enhanced Hydrogen Evolution Reaction. *Nanoscale*, 5(17):7768–7771, August 2013.
- [61] Heron Vrubel, Daniel Merki, and Xile Hu. Hydrogen Evolution Catalyzed by MoS₃ and MoS₂ Particles. *Energy & Environmental Science*, 5(3):6136, March 2012.
- [62] Jens Melder, Wai Ling Kwong, Dmitriy Shevela, Johannes Messinger, and Philipp Kurz. Electrocatalytic Water Oxidation by MnO_x/C: In Situ Catalyst Formation, Carbon Substrate Variations, and Direct O₂/CO₂ Monitoring by Membrane-Inlet Mass Spectrometry. *ChemSusChem*, 10(22):4491–4502, November 2017.
- [63] Marcel Pourbaix. *Atlas of Electrochemical Equilibria in Aqueous Solutions*. Pergamon Press, Oxford; New York, 1966.
- [64] Alessandro Minguzzi, Fu Ren F. Fan, Alberto Vertova, Sandra Rondinini, and Allen J. Bard. Dynamic Potential-pH Diagrams Application to Electrocatalysts for Water Oxidation. *Chemical Science*, 3(1):217–229, January 2012.
- [65] Dongbin Zhang, Xianggui Kong, Meihong Jiang, Deqiang Lei, and Xiaodong Lei. NiOOH-Decorated α -FeOOH Nanosheet Array on Stainless Steel for Applications in Oxygen Evolution Reactions and Supercapacitors. *ACS Sustainable Chemistry and Engineering*, 7(4):4420–4428, February 2019.
- [66] Kewei Liu, Changlin Zhang, Yuandong Sun, Guanghui Zhang, Xiaochen Shen, Feng Zou, Haichang Zhang, Zhenwei Wu, Evan C. Wegener, Clinton J. Taubert, Jeffrey T. Miller, Zhenmeng Peng, and Yu Zhu. High-Performance Transition Metal Phosphide Alloy Catalyst for Oxygen Evolution Reaction. *ACS Nano*, 12(1):158–167, January 2018.
- [67] Jens Melder, Stefan Mebs, Philipp A. Heizmann, Rebekka Lang, Holger Dau, and Philipp Kurz. Carbon Fibre Paper Coated by a Layered Manganese Oxide: a Nano-Structured Electrocatalyst for Water-Oxidation with High Activity Over a Very Wide pH Range. *Journal of Materials Chemistry A*, 7(44):25333–25346, 2019.
- [68] Charles C. L. McCrory, Suho Jung, Jonas C. Peters, and Thomas F. Jaramillo. Benchmarking Heterogeneous Electrocatalysts for the Oxygen Evolution Reaction. *Journal of the American Chemical Society*, 135(45):16977–16987, 2013.
- [69] D. Kwabena Bediako, Benedikt Lassalle-Kaiser, Yogesh Surendranath, Junko Yano, Vittal K. Yachandra, and Daniel G. Nocera. Structure-Activity Correlations in a Nickel-Borate Oxygen Evolution Catalyst. *Journal of the American Chemical Society*, 134(15):6801–6809, April 2012.

- [70] Michael Huynh, D. Kwabena Bediako, and Daniel G. Nocera. A Functionally Stable Manganese Oxide Oxygen Evolution Catalyst in Acid. *Journal of the American Chemical Society*, 136(16):6002–6010, April 2014.
- [71] Daniel A. Lutterman, Yogesh Surendranath, and Daniel G. Nocera. A Self-Healing Oxygen-Evolving Catalyst. *Journal of the American Chemical Society*, 131(11):3838–3839, 2009.
- [72] Cyrille Costentin and Daniel G. Nocera. Self-Healing Catalysis in Water. *Proceedings of the National Academy of Sciences of the United States of America*, 114(51):13380–13384, December 2017.
- [73] David M. Robinson, Yong Bok Go, Michelle Mui, Graeme Gardner, Zhijuan Zhang, Daniel Mastrogiovanni, Eric Garfunkel, Jing Li, Martha Greenblatt, and G. Charles Dismukes. Photochemical Water Oxidation by Crystalline Polymorphs of Manganese Oxides: Structural Requirements for Catalysis. *Journal of the American Chemical Society*, 135(9):3494–3501, March 2013.
- [74] Feng Jiao and Heinz Frei. Nanostructured Manganese Oxide Clusters Supported on Mesoporous Silica as Efficient Oxygen-Evolving Catalysts. *Chemical Communications*, 46(17):2920, 2010.
- [75] Prashanth W. Menezes, Arindam Indra, Patrick Littlewood, Michael Schwarze, Caren Göbel, Reinhard Schomäcker, and Matthias Driess. Nanostructured Manganese Oxides as Highly Active Water Oxidation Catalysts: A Boost from Manganese Precursor Chemistry. *ChemSusChem*, 7(8):2202–2211, August 2014.
- [76] Alejandra Ramírez, Philipp Hillebrand, Diana Stellmach, Matthias M. May, Peter Bogdanoff, and Sebastian Fiechter. Evaluation of MnO_x , Mn_2O_3 , and Mn_3O_4 Electrodeposited Films for the Oxygen Evolution Reaction of Water. *The Journal of Physical Chemistry C*, 118(26):14073–14081, July 2014.
- [77] Paul F. Smith, Benjamin J. Deibert, Shivam Kaushik, Graeme Gardner, Shin-jae Hwang, Hao Wang, Jafar F. Al-Sharab, Eric Garfunkel, Laura Fabris, Jing Li, and G. Charles Dismukes. Coordination Geometry and Oxidation State Requirements of Corner-Sharing MnO_6 Octahedra for Water Oxidation Catalysis: An Investigation of Manganite (γ - MnOOH). *ACS Catalysis*, 6(3):2089–2099, March 2016.
- [78] Stephanie Raabe, Daniel Mierwaldt, Jim Ciston, Matthé Uijtewaal, Helge Stein, Jörg Hoffmann, Yimei Zhu, Peter Blöchl, and Christian Jooss. In situ electrochemical electron microscopy study of oxygen evolution activity of doped manganite perovskites. *Advanced Functional Materials*, 22(16):3378–3388, August 2012.

- [79] Julius Scholz, Marcel Risch, Kelsey A. Stoerzinger, Garlef Wartner, Yang Shao-Horn, and Christian Jooss. Rotating Ring-Disk Electrode Study of Oxygen Evolution at a Perovskite Surface: Correlating Activity to Manganese Concentration. *Journal of Physical Chemistry C*, 120(49):27746–27756, December 2016.
- [80] Carolin E. Frey and Philipp Kurz. Water Oxidation Catalysis by Synthetic Manganese Oxides with Different Structural Motifs: A Comparative Study. *Chemistry - A European Journal*, 21(42):14958–14968, October 2015.
- [81] Christina L. Lopano, Peter J. Heaney, Jeffrey E. Post, Jonathan Hanson, and Sridhar Komarneni. Time-Resolved Structural Analysis of K- and Ba-Exchange Reactions with Synthetic Na-Birnessite Using Synchrotron X-Ray Diffraction. *American Mineralogist*, 92(2-3):380–387, 2007.
- [82] Joseph R. Smyth and David L. Bish. *Crystal Structures and Cation Sites of the Rock-Forming Minerals*. ALLEN & UNWIN, 1988.
- [83] Mohammad Mahdi Najafpour and Davood Jafarian Sedigh. Water Oxidation by Manganese Oxides, a New Step Towards a Complete Picture: Simplicity is the Ultimate Sophistication. *Dalton Transactions*, 42(34):12173–12178, 2013.
- [84] Mathias Wiechen, Ivelina Zaharieva, Holger Dau, and Philipp Kurz. Layered Manganese Oxide for Water-Oxidation: Alkaline Earth Cations Influence Catalytic Activity in a Photosystem II-Like Fashion. *Chemical Science*, 3(7):2330–2339, 2012.
- [85] Aparna Iyer, Joselyn Del-Pilar, Cecil K. King'ondou, Edward Kissel, Hector F. Garces, Hui Huang, Abdelhamid M. El-Sawy, Prabir K. Dutta, and Steven L. Suib. Water Oxidation Catalysis using Amorphous Manganese Oxides, Octahedral Molecular Sieves (OMS-2), and Octahedral Layered (OL-1) Manganese Oxide Structures. *The Journal of Physical Chemistry C*, 116(10):6474–6483, March 2012.
- [86] I. Zaharieva, D. González-Flores, B. Asfari, C. Pasquini, M. R. Mohammadi, K. Klingan, I. Zizak, S. Loos, P. Chernev, and H. Dau. Water Oxidation Catalysis - Role of Redox and Structural Dynamics in Biological Photosynthesis and Inorganic Manganese Oxides. *Energy & Environmental Science*, 9(7):2433–2443, 2016.
- [87] Jeffrey E. Post and David R. Veblen. Crystal Structure Determinations of Synthetic Sodium, Magnesium, and Potassium Birnessite Using TEM and the Rietveld Method. *American Mineralogist*, 75(5-6):477–489, 1990.
- [88] Roberto N. De Guzman, Amir Awaluddin, Yan-Fei Shen, Zheng Rong Tian, Steven L. Suib, Stanton Ching, and Chi-Lin O'Young. Electrical Resistivity Measurements on Manganese Oxides with Layer and Tunnel Structures:

- Birnessites, Todorokites, and Cryptomelananes. *Chem. Mater.*, 7(7):1286–1292, 1995.
- [89] Seung Y. Lee, Diego González-Flores, Jonas Ohms, Tim Trost, Holger Dau, Ivelina Zaharieva, and Philipp Kurz. Screen-Printed Calcium-Birnessite Electrodes for Water-Oxidation at Neutral pH and an “Electrochemical Harriman Series”. *ChemSusChem*, 7:3442–3451, 2014.
- [90] Alex Izgorodin, Orawan Winther-Jensen, and Douglas R. MacFarlane. On the Stability of Water Oxidation Catalysts: Challenges and Prospects. *Australian Journal of Chemistry*, 65(6):638–642, July 2012.
- [91] Isabela C. Man, Hai Yan Su, Federico Calle-Vallejo, Heine A. Hansen, José I. Martínez, Nilay G. Inoglu, John Kitchin, Thomas F. Jaramillo, Jens K. Nørskov, and Jan Rossmeisl. Universality in Oxygen Evolution Electrocatalysis on Oxide Surfaces. *ChemCatChem*, 3(7):1159–1165, July 2011.
- [92] J. Rossmeisl, A. Logadottir, and J. K. Nørskov. Electrolysis of Water on (Oxidized) Metal Surfaces. *Chemical Physics*, 319(1-3):178–184, December 2005.
- [93] J. Rossmeisl, Z. W. Qu, H. Zhu, G. J. Kroes, and J. K. Nørskov. Electrolysis of Water on Oxide Surfaces. *Journal of Electroanalytical Chemistry*, 607(1-2):83–89, September 2007.
- [94] Marc T.M. Koper. Thermodynamic Theory of Multi-Electron Transfer Reactions: Implications for Electrocatalysis. *Journal of Electroanalytical Chemistry*, 660(2):254–260, September 2011.
- [95] Shiyou Chen and Lin Wang Wang. Thermodynamic Oxidation and Reduction Potentials of Photocatalytic Semiconductors in Aqueous Solution. *Chemistry of Materials*, 24(18):3659–3666, September 2012.
- [96] Dowon Bae, Brian Seger, Peter C.K. Vesborg, Ole Hansen, and Ib Chorkendorff. Strategies for Stable Water Splitting: Via Protected Photoelectrodes. *Chemical Society Reviews*, 46(7):1933–1954, April 2017.
- [97] Yongjing Lin, Corsin Battaglia, Mathieu Boccard, Mark Hettick, Zhibin Yu, Christophe Ballif, Joel W. Ager, and Ali Javey. Amorphous Si Thin Film Based Photocathodes with High Photovoltage for Efficient Hydrogen Production. *Nano Letters*, 13(11):5615–5618, November 2013.
- [98] Jianyun Zheng, Yanhong Lyu, Ruilun Wang, Chao Xie, Huaijuan Zhou, San Ping Jiang, and Shuangyin Wang. Crystalline TiO₂ Protective Layer with Graded Oxygen Defects for Efficient and Stable Silicon-Based Photocathode. *Nature Communications*, 9(1):3572, December 2018.

- [99] Matthew G. Kast, Lisa J. Enman, Nicholas J. Gurnon, Athavan Nadarajah, and Shannon W. Boettcher. Solution-Deposited F:SnO₂/TiO₂ as a Base-Stable Protective Layer and Antireflective Coating for Microtextured Buried-Junction H₂-evolving Si Photocathodes. *ACS Applied Materials & Interfaces*, 6(24):22830–22837, December 2014.
- [100] Dong Heon Nam, Jenny Z. Zhang, Virgil Andrei, Nikolay Kornienko, Nina Heidary, Andreas Wagner, Kenichi Nakanishi, Katarzyna P. Sokol, Barnaby Slater, Ingo Zebger, Stephan Hofmann, Juan C. Fontecilla-Camps, Chan Beum Park, and Erwin Reisner. Solar Water Splitting with a Hydrogenase Integrated in Photoelectrochemical Tandem Cells. *Angewandte Chemie - International Edition*, 57(33):10595–10599, August 2018.
- [101] Chong Liu, Jinyao Tang, Hao Ming Chen, Bin Liu, and Peidong Yang. A Fully Integrated Nanosystem of Semiconductor Nanowires for Direct Solar Water Splitting. *Nano Letters*, 13(6):2989–2992, June 2013.
- [102] Erik Verlage, Shu Hu, Rui Liu, Ryan J.R. Jones, Ke Sun, Chengxiang Xiang, Nathan S. Lewis, and Harry A. Atwater. A Monolithically Integrated, Intrinsically Safe, 10% Efficient, Solar-Driven Water-Splitting System Based on Active, Stable Earth-Abundant Electrocatalysts in Conjunction with Tandem III-V Light Absorbers Protected by Amorphous TiO₂ Films. *Energy and Environmental Science*, 8(11):3166–3172, October 2015.
- [103] Gaowei Wu, Chengxi Zhang, Shuirong Li, Zhiqi Huang, Suli Yan, Shengping Wang, Xinbin Ma, and Jinlong Gong. Sorption Enhanced Steam Reforming of Ethanol on Ni-CaO-Al₂O₃ Multifunctional Catalysts Derived from Hydrotalcite-Like Compounds. *Energy & Environmental Science*, 5(10):8942–8949, 2012.
- [104] Shu Hu, Matthew R. Shaner, Joseph A. Beardslee, Michael Lichterman, Bruce S. Brunschwig, and Nathan S. Lewis. Amorphous TiO₂ Coatings Stabilize Si, GaAs, and GaP Photoanodes for Efficient Water Oxidation. *Science (New York, N.Y.)*, 344(6187):1005–1009, May 2014.
- [105] Gabriela C. Correa, Bo Bao, and Nicholas C. Strandwitz. Chemical Stability of Titania and Alumina Thin Films Formed by Atomic Layer Deposition. *ACS Applied Materials & Interfaces*, 7(27):14816–14821, July 2015.
- [106] Steven Y. Reece, Jonathan A. Hamel, Kimberly Sung, Thomas D. Jarvi, Arthur J. Esswein, Joep J.H. Pijpers, and Daniel G. Nocera. Wireless Solar Water Splitting Using Silicon-Based Semiconductors and Earth-Abundant Catalysts. *Science*, 334(6056):645–648, November 2011.
- [107] S. Licht, B. Wang, S. Mukerji, T. Soga, M. Umeno, and H. Tributsch. Efficient Solar Water Splitting, Exemplified by RuO₂-Catalyzed AlGaAs/Si Photoelec-

- trolysis. *The Journal of Physical Chemistry B*, 104(38):8920–8924, September 2000.
- [108] Richard E. Rocheleau, Eric L. Miller, and Anupam Misra. High-Efficiency Photoelectrochemical Hydrogen Production Using Multijunction Amorphous Silicon Photoelectrodes. *Energy & Fuels*, 12(1):3–10, January 1998.
- [109] G. H. Lin, M. Kapur, R. C. Kainthla, and J. O.M. Bockris. One Step Method to Produce Hydrogen by a Triple Stack Amorphous Silicon Solar Cell. *Applied Physics Letters*, 55(4):386–387, July 1989.
- [110] Oscar Khaselev. A Monolithic Photovoltaic-Photoelectrochemical Device for Hydrogen Production via Water Splitting. *Science*, 280(5362):425–427, April 1998.
- [111] Dongseok Kang, James L. Young, Haneol Lim, Walter E. Klein, Huandong Chen, Yuzhou Xi, Boju Gai, Todd G. Deutsch, and Jongseung Yoon. Printed Assemblies of GaAs Photoelectrodes with Decoupled Optical and Reactive Interfaces for Unassisted Solar Water Splitting. *Nature Energy*, 2(5):1–5, March 2017.
- [112] Peter A. Crozier and Thomas W. Hansen. In Situ and Operando Transmission Electron Microscopy of Catalytic Materials. *MRS Bulletin*, 40(1):38–45, January 2015.
- [113] Jürgen Thomas and Thomas Gemming. Was wir über Elektronenoptik und den Aufbau eines Elektronenmikroskops wissen sollten. In *Analytische Transmissionselektronenmikroskopie*, pages 19–48. Springer Vienna, Vienna, 2013.
- [114] S. B. Vendelbo, C. F. Elkjær, H. Falsig, I. Puspitasari, P. Dona, L. Mele, B. Morana, B. J. Nelissen, R. van Rijn, J. F. Creemer, P. J. Kooyman, and S. Helveg. Visualization of Oscillatory Behaviour of Pt Nanoparticles Catalysing CO Oxidation. *Nature Materials*, 13(9):884–890, September 2014.
- [115] J.F. Creemer, S. Helveg, G.H. Hovelings, S. Ullmann, P.J. Kooyman, A.M. Molenbroek, H.W. Zandbergen, and P.M. Sarro. MEMS Nanoreactor for Atomic-Resolution Microscopy of Nanomaterials in their Working State. In *2009 IEEE 22nd International Conference on Micro Electro Mechanical Systems*, pages 76–79. IEEE, January 2009.
- [116] Ai Leen Koh, Sang Chul Lee, and Robert Sinclair. A Brief History of Controlled Atmosphere Transmission Electron Microscopy. In *Controlled Atmosphere Transmission Electron Microscopy*, pages 3–43. Springer International Publishing, Cham, 2016.
- [117] Benjamin K. Miller and Peter A. Crozier. Analysis of Catalytic Gas Products Using Electron Energy-Loss Spectroscopy and Residual Gas Analysis for

- Operando Transmission Electron Microscopy. *Microscopy and Microanalysis*, 20(3):815–824, June 2014.
- [118] Hideto Yoshida, Yasufumi Kuwauchi, Joerg R. Jinschek, Keju Sun, Shingo Tanaka, Masanori Kohyama, Satoshi Shimada, Masatake Haruta, and Seiji Takeda. Visualizing Gas Molecules Interacting with Supported Nanoparticulate Catalysts at Reaction Conditions. *Science*, 335(6066):317–319, January 2012.
- [119] Yuyuan Lin, Zili Wu, Jianguo Wen, Kenneth R. Poeppelmeier, and Laurence D. Marks. Imaging the Atomic Surface Structures of CeO₂ Nanoparticles. *Nano Letters*, 14(1):191–196, January 2014.
- [120] M. Bugnet, S. H. Overbury, Z. L. Wu, and T. Epicier. Direct Visualization and Control of Atomic Mobility at {100} Surfaces of Ceria in the Environmental Transmission Electron Microscope. *Nano Letters*, 17(12):7652–7658, December 2017.
- [121] Stephanie Mildner, Marco Beleggia, Daniel Mierwaldt, Thomas W. Hansen, Jakob B. Wagner, Sadegh Yazdi, Takeshi Kasama, Jim Ciston, Yimei Zhu, and Christian Jooss. Environmental TEM Study of Electron Beam Induced Electrochemistry of Pr_{0.64}Ca_{0.36}MnO₃ Catalysts for Oxygen Evolution. *Journal of Physical Chemistry C*, 119(10):5301–5310, March 2015.
- [122] G. Lole, V. Roddatis, M. Risch, J. Geppert, G. Wartner, D. Busse, and C. Jooss. Dynamic Observation of Mn-Adatom Mobility at Perovskite Oxide Catalyst Interfaces to Water. *Communications Materials*, 1(1):68, September 2020.
- [123] Wentao Yuan, Beien Zhu, Xiao-Yan Li, Thomas W. Hansen, Yang Ou, Ke Fang, Hangsheng Yang, Ze Zhang, Jakob B. Wagner, Yi Gao, and Yong Wang. Visualizing H₂O Molecules Reacting at TiO₂ Active Sites with Transmission Electron Microscopy. *Science*, 367(6476):428–430, January 2020.
- [124] John W. Drazin and Ricardo H. R. Castro. Water Adsorption Microcalorimetry Model: Deciphering Surface Energies and Water Chemical Potentials of Nanocrystalline Oxides. *The Journal of Physical Chemistry C*, 118(19):10131–10142, May 2014.
- [125] Sriram Goverapet Srinivasan, Radha Shivaramaiah, Paul R. C. Kent, Andrew G. Stack, Alexandra Navrotsky, Richard Riman, Andre Anderko, and Vyacheslav S. Bryantsev. Crystal Structures, Surface Stability, and Water Adsorption Energies of La-Bastnäsite via Density Functional Theory and Experimental Studies. *The Journal of Physical Chemistry C*, 120(30):16767–16781, August 2016.

- [126] A. Opitz, M. Scherge, S. I.U. Ahmed, and J. A. Schaefer. A Comparative Investigation of Thickness Measurements of Ultra-Thin Water Films by Scanning Probe Techniques. *Journal of Applied Physics*, 101(6):064310, March 2007.
- [127] Yoshihiro Nakato, Toshihiro Ohnishi, and Hiroshi Tsubomura. Photoelectrochemical behaviors of semiconductor electrodes coated with thin metal films. *Chemistry Letters*, 4(8):883–886, August 1975.
- [128] Michael J. Kenney, Ming Gong, Yanguang Li, Justin Z. Wu, Ju Feng, Mario Lanza, and Hongjie Dai. High-Performance Silicon Photoanodes Passivated with Ultrathin Nickel Films for Water Oxidation. *Science (New York, N.Y.)*, 342(6160):836–40, November 2013.
- [129] Xinghao Zhou, Rui Liu, Ke Sun, Dennis Friedrich, Matthew T. McDowell, Fan Yang, Stefan T. Omelchenko, Fadl H. Saadi, Adam C. Nielander, Sisir Yalamanchili, Kimberly M. Papadantonakis, Bruce S. Brunshwig, and Nathan S. Lewis. Interface Engineering of the Photoelectrochemical Performance of Ni-Oxide-Coated n-Si Photoanodes by Atomic-Layer Deposition of Ultrathin Films of Cobalt Oxide. *Energy and Environmental Science*, 8(9):2644–2649, August 2015.
- [130] F. Urbain, V. Smirnov, J. P. Becker, U. Rau, J. Ziegler, F. Yang, B. Kaiser, W. Jaegermann, S. Hoch, M. Blug, and F. Finger. Solar Water Splitting with Earth-Abundant Materials using Amorphous Silicon Photocathodes and Al/Ni Contacts as Hydrogen Evolution Catalyst. *Chemical Physics Letters*, 638:25–30, October 2015.
- [131] Thorsten Cottre, Katharina Welter, Emanuel Ronge, Vladimir Smirnov, and Friedhelm Finger. Integrated Devices for Photoelectrochemical Water Splitting Using Adapted Silicon Based Multi-junction Cells Protected by ALD TiO₂ Coatings. *Zeitschrift für Physikalische Chemie*, February 2020.
- [132] Jina Leem, Inhye Park, Yinshi Li, Wenhao Zhou, Zhenyu Jin, Seokhee Shin, and Yo Sep Min. Role of HCl in Atomic Layer Deposition of TiO₂ Thin Films from Titanium Tetrachloride and Water. *Bulletin of the Korean Chemical Society*, 35(4):1195–1201, April 2014.
- [133] Sébastien Moitzheim, Joan Elisabeth Balder, Paul Poodt, Sandeep Unnikrishnan, Stefan De Gendt, and Philippe M. Vereecken. Chlorine Doping of Amorphous TiO₂ for Increased Capacity and Faster Li⁺-Ion Storage. *Chemistry of Materials*, 29(23):10007–10018, December 2017.
- [134] Francisco Fabregat-Santiago, Ivan Mora-Seró, Germà Garcia-Belmonte, and Juan Bisquert. Cyclic Voltammetry Studies of Nanoporous Semiconductors. Capacitive and Reactive Properties of Nanocrystalline TiO₂ Electrodes in

- Aqueous Electrolyte. *The Journal of Physical Chemistry B*, 107(3):758–768, 2002.
- [135] Xiaoxia Li, Aaron Li Zhu, Wei Qu, Haijiang Wang, Rob Hui, Lei Zhang, and Jiujun Zhang. Magneli Phase Ti_4O_7 Electrode for Oxygen Reduction Reaction and its Implication for Zinc-Air Rechargeable Batteries. *Electrochimica Acta*, 55(20):5891–5898, August 2010.
- [136] Kesong Yang, Ying Dai, Baibiao Huang, and Myung Hwan Whangbo. Density Functional Characterization of the Band Edges, the Band Gap States, and the Preferred Doping Sites of Halogen-Doped TiO_2 . *Chemistry of Materials*, 20(20):6528–6534, October 2008.
- [137] P. Allongue, V. Costa-Kieling, and H. Gerischer. Etching of Silicon in NaOH Solutions. *Journal of The Electrochemical Society*, 140(4):1018, April 1993.
- [138] Orest J. Glembocki, Robert E. Stahlbush, and Micha Tomkiewicz. Bias-Dependent Etching of Silicon in Aqueous KOH. *Journal of The Electrochemical Society*, 132(1):145, January 1985.
- [139] Xinghua Xia, Colin M. A. Ashruf, Patrick J. French, Joerg Rappich, and John J. Kelly. Etching and Passivation of Silicon in Alkaline Solution: A Coupled Chemical/Electrochemical System. *The Journal of Physical Chemistry B*, 105(24):5722–5729, 2001.
- [140] Takahiro Yamada, Hiromasa Ohmi, Hiroaki Kakiuchi, and Kiyoshi Yasutake. Effect of H_2 Flow Rate on High-Rate Etching of Si by Narrow-Gap Microwave Hydrogen Plasma. *Plasma Chemistry and Plasma Processing*, 33(4):797–806, August 2013.
- [141] Stan Veprek, Chunlin Wang, and Maritza G. J. Veprek-Heijman. Role of Oxygen Impurities in Etching of Silicon by Atomic Hydrogen. *Journal of Vacuum Science & Technology A: Vacuum, Surfaces, and Films*, 26(3):313–320, May 2008.
- [142] Allen J. Bard, Roger Parsons, and Joseph Jordan. *Standard Potentials in Aqueous Solution*. CRC Press, New York, 1 edition, 1985.
- [143] Félix Urbain, Vladimir Smirnov, Jan Philipp Becker, Andreas Lambertz, Florent Yang, Jürgen Ziegler, Bernhard Kaiser, Wolfram Jaegermann, Uwe Rau, and Friedhelm Finger. Multijunction Si Photocathodes with Tunable Photovoltages from 2.0 V to 2.8 V for Light Induced Water Splitting. *Energy and Environmental Science*, 9(1):145–154, January 2016.
- [144] Matthew A. Pellow, Christopher J. M. Emmott, Charles J. Barnhart, and Sally M. Benson. Hydrogen or Batteries for Grid Storage? A Net Energy Analysis. *Energy & Environmental Science*, 8(7):1938–1952, July 2015.

- [145] Steven G. Chalk and James F. Miller. Key Challenges and Recent Progress in Batteries, Fuel Cells, and Hydrogen Storage for Clean Energy Systems. *Journal of Power Sources*, 159(1):73–80, September 2006.
- [146] P. P. Edwards, V. L. Kuznetsov, W. I F David, and N. P. Brandon. Hydrogen and Fuel Cells: Towards a Sustainable Energy Future. *Energy Policy*, 36(12):4356–4362, December 2008.
- [147] Zhifeng Ye, Jia Yang, Bo Li, Lei Shi, Hengxing Ji, Li Song, and Hangxun Xu. Amorphous Molybdenum Sulfide/Carbon Nanotubes Hybrid Nanospheres Prepared by Ultrasonic Spray Pyrolysis for Electrocatalytic Hydrogen Evolution. *Small*, 13(21):1700111, June 2017.
- [148] Simon J. Hibble and Glenn B. Wood. Modeling the Structure of Amorphous MoS₃: A Neutron Diffraction and Reverse Monte Carlo Study. *Journal of the American Chemical Society*, 126(3):959–965, 2004.
- [149] Achim Müller, Vladimir Fedin, Kaspar Hegetschweiler, and Walter Amrein. Characterization of Amorphous Substances by Studying Isotopically Labelled Compounds with FAB-MS: Evidence for Extrusion of Triangular Mo₃^{IV} Clusters from a Mixture of ⁹²MoS₃ and ¹⁰⁰MoS₃. *J. Chem. Soc., Chem. Commun.*, 0(24):1795–1796, January 1992.
- [150] Simon J. Hibble, Mark R. Feavioir, and Matthew J. Almond. Chemical Excision from Amorphous MoS₃; a Quantitative EXAFS Study. *Journal of the Chemical Society, Dalton Transactions*, 0(6):935–940, January 2001.
- [151] M. Dave, A. Rajagopal, M. Damm-Ruttensperger, B. Schwarz, F. Nägele, L. Daccache, D. Fantauzzi, T. Jacob, and C. Streb. Understanding Homogeneous Hydrogen Evolution Reactivity and Deactivation Pathways of Molecular Molybdenum Sulfide Catalysts. *Sustainable Energy and Fuels*, 2(5):1020–1026, 2018.
- [152] Zhaoyan Luo, Yixin Ouyang, Hao Zhang, Meiling Xiao, Junjie Ge, Zheng Jiang, Jinlan Wang, Daiming Tang, Xinzhong Cao, Changpeng Liu, and Wei Xing. Chemically Activating MoS₂ via Spontaneous Atomic Palladium Interfacial Doping Towards Efficient Hydrogen Evolution. *Nature Communications*, 9(1):2120, December 2018.
- [153] Ying Yin, Jiecai Han, Yumin Zhang, Xinghong Zhang, Ping Xu, Quan Yuan, Leith Samad, Xianjie Wang, Yi Wang, Zhihua Zhang, Peng Zhang, Xingzhong Cao, Bo Song, and Song Jin. Contributions of Phase, Sulfur Vacancies, and Edges to the Hydrogen Evolution Reaction Catalytic Activity of Porous Molybdenum Disulfide Nanosheets. *Journal of the American Chemical Society*, 138(25):7965–7972, June 2016.

- [154] F. M. Michel, S. M. Antao, P. J. Chupas, P. L. Lee, J. B. Parise, and M. A. A. Schoonen. Short- To Medium-Range Atomic Order and Crystallite Size of the Initial FeS Precipitate from Pair Distribution Function Analysis. *Chemistry of Materials*, 17(25):6246–6255, 2005.
- [155] Badri Shyam, Kevin H. Stone, Riccardo Bassiri, Martin M. Fejer, Michael F. Toney, and Apurva Mehta. Measurement and Modeling of Short and Medium Range Order in Amorphous Ta₂O₅ Thin Films. *Scientific Reports*, 6(1):32170, October 2016.
- [156] B. D. Hall, D. Zanchet, and D. Ugarte. Estimating nanoparticle size from diffraction measurements. *Journal of Applied Crystallography*, 33(6):1335–1341, December 2000.
- [157] D. J. Srolovitz, S. A. Safran, M. Homyonfer, and R. Tenne. Morphology of Nested Fullerenes. *Physical Review Letters*, 74(10):1779–1782, March 1995.
- [158] Duc N. Nguyen, Linh N. Nguyen, Phuc D. Nguyen, Tran Viet Thu, Anh D. Nguyen, and Phong D. Tran. Crystallization of Amorphous Molybdenum Sulfide Induced by Electron or Laser Beam and Its Effect on H₂ -Evolving Activities. *The Journal of Physical Chemistry C*, 120(50):28789–28794, December 2016.
- [159] Fanxing Xi, Peter Bogdanoff, Karsten Harbauer, Paul Plate, Christian Höhn, Jörg Rappich, Bin Wang, Xiaoyu Han, Roel van de Krol, and Sebastian Fiechter. Structural Transformation Identification of Sputtered Amorphous MoS_x as an Efficient Hydrogen-Evolving Catalyst during Electrochemical Activation. *ACS Catalysis*, 9(3):2368–2380, March 2019.
- [160] John W. McDonald, G. Delbert Friesen, Laurence D. Rosenhein, and William E. Newton. Syntheses and Characterization of Ammonium and Tetraalkylammonium Thiomolybdates and Thiotungstates. *Inorganica Chimica Acta*, 72:205–210, January 1983.
- [161] Wei Cui, Qian Liu, Zhicai Xing, Abdullah M. Asiri, Khalid A. Alamry, and Xuping Sun. MoP Nanosheets Supported on Biomass-Derived Carbon Flake: One-Step Facile Preparation and Application as a Novel High-Active Electrocatalyst Toward Hydrogen Evolution Reaction. *Applied Catalysis B: Environmental*, 164:144–150, March 2015.
- [162] Johannes Biskupek. Practical Considerations on the Determination of the Accuracy of the Lattice Parameters Measurements from Digital Recorded Diffractograms. *Journal of Electron Microscopy*, 53(6):601–610, December 2004.
- [163] Nathan S. Lewis and Daniel G. Nocera. Powering the Planet: Chemical Challenges in Solar Energy Utilization. *Proceedings of the National Academy of Sciences*, 103(43):15729–15735, October 2006.

- [164] Ioannis Katsounaros, Serhiy Cherevko, Aleksandar R. Zeradjanin, and Karl J. J. Mayrhofer. Oxygen Electrochemistry as a Cornerstone for Sustainable Energy Conversion. *Angewandte Chemie International Edition*, 53(1):102–121, January 2014.
- [165] Feng Jiao and Heinz Frei. Nanostructured Cobalt and Manganese Oxide Clusters as Efficient Water Oxidation Catalysts. *Energy & Environmental Science*, 3(8):1018, 2010.
- [166] Julius Scholz, Marcel Risch, Garlef Wartner, Christoph Luderer, Vladimir Roddatis, and Christian Jooss. Tailoring the Oxygen Evolution Activity and Stability Using Defect Chemistry. *Catalysts*, 7(5):139, May 2017.
- [167] Giuseppe Mattioli, Ivelina Zaharieva, Holger Dau, and Leonardo Guidoni. Atomistic Texture of Amorphous Manganese Oxides for Electrochemical Water Splitting Revealed by Ab Initio Calculations Combined with X-ray Spectroscopy. *Journal of the American Chemical Society*, 137(32):10254–10267, 2015.
- [168] Ivelina Zaharieva, M. Mahdi Najafpour, Mathias Wiechen, Michael Haumann, Philipp Kurz, and Holger Dau. Synthetic Manganese Calcium Oxides Mimic the Water-Oxidizing Complex of Photosynthesis Functionally and Structurally. *Energy & Environmental Science*, 4:2400–2408, 2011.
- [169] Denys Shevchenko, Magnus F. Anderlund, Stenbjörn Styring, Holger Dau, Ivelina Zaharieva, and Anders Thapper. Water Oxidation by Manganese Oxides Formed from Tetranuclear Precursor Complexes: the Influence of Phosphate on Structure and Activity. *Physical Chemistry Chemical Physics*, 16(24):11965, June 2014.
- [170] Diego González-Flores, Ivelina Zaharieva, Jonathan Heidkamp, Petko Chernev, Elías Martínez-Moreno, Chiara Pasquini, Mohammad Reza Mohammadi, Katharina Klingan, Ulrich Gernet, Anna Fischer, and Holger Dau. Electrosynthesis of Biomimetic Manganese-Calcium Oxides for Water Oxidation Catalysis-Atomic Structure and Functionality. *ChemSusChem*, 9(4):379–387, 2016.
- [171] Arindam Indra, Prashanth W. Menezes, Ivelina Zaharieva, Elham Baktash, Johannes Pfrommer, Michael Schwarze, Holger Dau, and Matthias Driess. Active Mixed-Valent MnO_x Water Oxidation Catalysts through Partial Oxidation (Corrosion) of Nanostructured MnO Particles. *Angewandte Chemie International Edition*, 52(50):13206–13210, 2013.
- [172] Monika Fekete, Rosalie K. Hocking, Shery L.Y. Chang, Cristina Italiano, Antonio F. Patti, Francesco Arena, and Leone Spiccia. Highly Active Screen-Printed Electrocatalysts for Water Oxidation Based on β -Manganese Oxide. *Energy and Environmental Science*, 6(7):2222–2232, July 2013.

- [173] M. M. Najafpour, Atefeh N. Moghaddam, Holger Dau, and Ivelina Zaharieva. Fragments of Layered Manganese Oxide are the Real Water Oxidation Catalyst After Transformation of Molecular Precursor on Clay. *Journal of the American Chemical Society*, 136(20):7245–7248, May 2014.
- [174] Mohammad Mahdi Najafpour, Foad Ebrahimi, Mahnaz Abasi, and Seyedeh Maedeh Hosseini. Manganese Oxides Supported on Nano-Sized Metal Oxides as Water-Oxidizing Catalysts for Water Splitting Systems: 2-Water-Oxidizing Activities. *International Journal of Hydrogen Energy*, 41(41):18472–18477, 2016.
- [175] D. C. Golden, J. B. Dixon, and C. C. Chen. Ion Exchange, Thermal Transformations, and Oxidizing Properties of Birnessite. *Clays & Clay Minerals*, 34(5):511–520, 1986.
- [176] Elizabeth A. Johnson and Jeffrey E. Post. Water in the Interlayer Region of Birnessite: Importance in Cation Exchange and Structural Stability. *American Mineralogist*, 91(4):609–618, April 2006.
- [177] Marcel Risch, Katharina Klingan, Franziska Ringleb, Petko Chernev, Ivelina Zaharieva, Anna Fischer, and Holger Dau. Water Oxidation by Electrodeposited Cobalt Oxides-Role of Anions and Redox-Inert Cations in Structure and Function of the Amorphous Catalyst. *ChemSusChem*, 5(3):542–549, 2012.
- [178] Marcel Risch, Franziska Ringleb, Mike Kohlhoff, Peter Bogdanoff, Petko Chernev, Ivelina Zaharieva, and Holger Dau. Water Oxidation by Amorphous Cobalt-Based Oxides: In situ Tracking of Redox Transitions and Mode of Catalysis. *Energy and Environmental Science*, 8(2):661–674, February 2015.
- [179] Linsey C. Seitz, Thomas J. P. Hersbach, Dennis Nordlund, and Thomas F. Jaramillo. Enhancement Effect of Noble Metals on Manganese Oxide for the Oxygen Evolution Reaction. *Journal of Physical Chemistry Letters*, 6(20):4178–4183, October 2015.
- [180] Mohammad Mahdi Najafpour, Gernot Renger, Małgorzata Hołyńska, Atefeh Nemati Moghaddam, Eva-Mari Aro, Robert Carpentier, Hiroshi Nishihara, Julian J. Eaton-Rye, Jian-Ren Shen, and Suleyman I. Allakhverdiev. Manganese Compounds as Water-Oxidizing Catalysts: From the Natural Water-Oxidizing Complex to Nanosized Manganese Oxide Structures. *Chemical Reviews*, 116(5):2886–2936, March 2016.
- [181] Mohammad Mahdi Najafpour, Davood Jafarian Sedigh, Babak Pashaei, and Sara Nayeri. Water Oxidation by Nano-Layered Manganese Oxides in the Presence of Cerium (IV) Ammonium Nitrate: Important Factors and a Proposed Self-Repair Mechanism. *New Journal of Chemistry*, 37(8):2448–2459, 2013.

- [182] Jacob S. Kanady, Emily Y. Tsui, Michael W. Day, and Theodor Agapie. A Synthetic Model of the Mn_3Ca Subsite of the Oxygen-Evolving Complex in Photosystem II. *Science*, 333(6043):733–736, August 2011.
- [183] Axel Knop-Gericke, Evgueni Kleimenov, Michael Hävecker, Raoul Blume, Detre Teschner, Spiros Zafeiratos, Robert Schlögl, Valerii I Bukhtiyarov, Vasily V. Kaichev, Igor P. Prosvirin, Alexander I. Nizovskii, Hendrik Bluhm, Alexei Barinov, Pavel Dudin, and Maya Kiskinova. Chapter 4 X-Ray Photoelectron Spectroscopy for Investigation of Heterogeneous Catalytic Processes. In *Advances in Catalysis*, pages 213–272. Elsevier, 2009.
- [184] S. Tanuma, C. J. Powell, and D. R. Penn. Calculations of Electron Inelastic Mean Free Paths (IMFPS). IV. Evaluation of Calculated IMFPs and of the Predictive IMFP Formula TPP-2 for Electron Energies Between 50 and 2000 eV. *Surface and Interface Analysis*, 20(1):77–89, 1993.
- [185] M. M. van Schooneveld and S. DeBeer. A Close Look at Dose: Toward L-edge XAS Spectral Uniformity, Dose Quantification and Prediction of Metal Ion Photoreduction. *Journal of Electron Spectroscopy and Related Phenomena*, 198:31–56, 2015.
- [186] B. Gilbert, B. H. Frazer, A. Belz, P. G. Conrad, K. H. Nealon, D. Haskel, J. C. Lang, G. Srajer, and G. De Stasio. Multiple Scattering Calculations of Bonding and X-Ray Absorption Spectroscopy of Manganese Oxides. *Journal of Physical Chemistry A*, 107(16):2839–2847, 2003.
- [187] Ruimin Qiao, Timothy Chin, Stephen J. Harris, Shishen Yan, and Wanli Yang. Spectroscopic Fingerprints of Valence and Spin States in Manganese Oxides and Fluorides. *Current Applied Physics*, 13(3):544–548, May 2013.
- [188] S. Voss, M. Fonin, U. Rüdiger, M. Burgert, U. Groth, and Yu. S. Dedkov. Electronic Structure of Mn_{12} Derivatives on the Clean and Functionalized Au Surface. *Physical Review B - Condensed Matter and Materials Physics*, 75(4):045102, January 2007.
- [189] Munirah Khan, Edlira Suljoti, Archana Singh, Shannon A. Bonke, Tim Brandenburg, Kaan Atak, Ronny Golnak, Leone Spiccia, and Emad F. Aziz. Electronic Structural Insights Into Efficient MnO_x Catalysts. *Journal of Materials Chemistry A*, 2(43):18199–18203, September 2014.
- [190] Wayne E. Morgan, John R. Van Wazer, and Wojciech J. Stec. Inner-Orbital Photoelectron Spectroscopy of the Alkali Metal Halides, Perchlorates, Phosphates, and Pyrophosphates. *Journal of the American Chemical Society*, 95(3):751–755, February 1973.

- [191] Ping-Ho Lo. The Electrochemical Behavior of Electroless Plated Ni-P Alloys in Concentrated NaOH Solution. *Journal of The Electrochemical Society*, 142(1):91, 1995.
- [192] Javier Fernández-Rodríguez, Brian Toby, and Michel Van Veenendaal. Xclaim: A Graphical Interface for the Calculation of Core-Hole Spectroscopies. *Journal of Electron Spectroscopy and Related Phenomena*, 202:81–88, July 2015.
- [193] F. Sulzmann, W. Jang, J. Melder, C. Rohner, F. Girgsdies, A. Knop-Gericke, R. Schlögl, T. Jones, P. Kurz, and K. Skorupska. No Title. *manuscript to be submitted*.
- [194] Marc F. Tesch, Shannon A. Bonke, Travis E. Jones, Maryam N. Shaker, Jie Xiao, Katarzyna Skorupska, Rik Mom, Jens Melder, Philipp Kurz, Axel Knop-Gericke, Robert Schlögl, Rosalie K. Hocking, and Alexandr N. Simonov. Evolution of Oxygen-Metal Electron Transfer and Metal Electronic States During Manganese Oxide Catalyzed Water Oxidation Revealed with In Situ Soft X-Ray Spectroscopy. *Angewandte Chemie*, 131(11):3464–3470, March 2019.
- [195] D. K. G. de Boer, C. Haas, and G. A. Sawatzky. Exciton Satellites in Photoelectron Spectra. *Physical Review B*, 29(8):4401–4419, 1984.
- [196] Sanjiv Kumar, V.S. Raju, Santanu Bera, K. Vijaynandhini, and T.R.N. Kutty. Studies on Surface Composition and Chemical States of Calcium Manganites. *Nuclear Instruments and Methods in Physics Research Section B: Beam Interactions with Materials and Atoms*, 237(3-4):623–630, August 2005.
- [197] A. E. Bocquet, T. Mizokawa, K. Morikawa, A. Fujimori, S. R. Barman, K. Maiti, D. D. Sarma, Y. Tokura, and M. Onoda. Electronic Structure of Early 3d-Transition-Metal Oxides by Analysis of the 2p Core-Level Photoemission Spectra. *Physical Review B*, 53(3):1161–1170, 1996.
- [198] G. van der Laan, C. Westra, C. Haas, and G. A. Sawatzky. Satellite Structure in Photoelectron and Auger Spectra of Copper Dihalides. *Physical Review B*, 23(9):4369–4380, 1981.
- [199] Blaise A. Pinaud, Zhebo Chen, David N. Abram, and Thomas F. Jaramillo. Thin Films of Sodium Birnessite-Type MnO_2 : Optical Properties, Electronic Band Structure, and Solar Photoelectrochemistry. *The Journal of Physical Chemistry C*, 115(23):11830–11838, June 2011.
- [200] Kevin P. Lucht and Jose L. Mendoza-Cortes. Birnessite: A Layered Manganese Oxide To Capture Sunlight for Water-Splitting Catalysis. *The Journal of Physical Chemistry C*, 119(40):22838–22846, 2015.
- [201] M. W. D. Mansfield. The Ca I Absorption Spectrum in the Extreme Ultraviolet: Excitation of the 2p Subshell. *Proceedings of the Royal Society A*:

- Mathematical, Physical and Engineering Sciences*, 348(1652):143–151, February 1976.
- [202] F. J. Himpsel, U. O. Karlsson, A. B. McLean, L. J. Terminello, F. M.F. De Groot, M. Abbate, J. C. Fuggle, J. A. Yarmoff, B. T. Thole, and G. A. Sawatzky. Fine Structure of the Ca 2p x-Ray-Absorption Edge for Bulk Compounds, Surfaces, and Interfaces. *Physical Review B*, 43(9):6899–6907, March 1991.
- [203] W. J. Landis and J. R. Martin. X-ray Photoelectron Spectroscopy Applied to Gold-Decorated Mineral Standards of Biological Interest. *Journal of Vacuum Science & Technology A*, 2(2):1108–1111, April 1984.
- [204] C. V. Krishnamohan Sharma, Charles C. Chusuei, Rodolphe Cl  rac, Teresia M  ller, Kim R. Dunbar, Abraham Clearfield, C. V. Krishnamohan Sharma, Charles C. Chusuei, Rodolphe Cl  rac, Teresia M  ller, Kim R. Dunbar, and Abraham Clearfield. Magnetic Property Studies of Manganese-Phosphate Complexes. *Inorganic Chemistry*, 42(25):8300–8308, December 2003.
- [205] Jonas Ohms. *Die elektrokatalytische Charakterisierung von Manganoxiden im Rahmen der heterogenen Wasseroxidationskatalyse*. PhD thesis, Albert-Ludwigs-Universit  t Freiburg im Breisgau, 2018.
- [206] P.J. Phillips, M. De Graef, L. Kovarik, A. Agrawal, W. Windl, and M.J. Mills. Atomic-Resolution Defect Contrast in Low Angle Annular Dark-Field STEM. *Ultramicroscopy*, 116:47–55, May 2012.
- [207] Blackmagic Design, DaVinci Resolve 16 free Version. <https://www.blackmagicdesign.com>, 2020.
- [208] Laurence A. J. Garvie, Alan J. Craven, and Rik Brydson. Use of electron-energy loss near-edge fine structure in the study of minerals. *American Mineralogist*, 79:411–425, 1994.
- [209] Haiyan Tan, Jo Verbeeck, Artem Abakumov, and Gustaaf Van Tendeloo. Oxidation State and Chemical Shift Investigation in Transition Metal Oxides by EELS. *Ultramicroscopy*, 116:24–33, May 2012.
- [210] T. Walther. Electron Microscopy of Quantum Dots. *Journal of Microscopy*, 257(3):171–178, March 2015.
- [211] Biaobiao Zhang, Hong Chen, Quentin Daniel, Bertrand Philippe, Fengshou Yu, Mario Valvo, Yuanyuan Li, Ram B. Ambre, Peili Zhang, Fei Li, H  kan Rensmo, and Licheng Sun. Defective and “c -Disordered” Hortensia-like Layered MnO_x as an Efficient Electrocatalyst for Water Oxidation at Neutral pH. *ACS Catalysis*, 7(9):6311–6322, September 2017.

- [212] T. Riedl, T. Gemming, and K. Wetzig. Extraction of EELS White-Line Intensities of Manganese Compounds: Methods, Accuracy, and Valence Sensitivity. *Ultramicroscopy*, 106(4-5):284–291, March 2006.
- [213] Diana B. Loomer, Tom A. Al, Louise Weaver, and Steven Cogswell. Manganese Valence Imaging in Mn Minerals at the Nanoscale Using STEM-EELS. *American Mineralogist*, 92(1):72–79, January 2007.
- [214] Kenneth J. T. Livi, Brandon Lafferty, Mengqiang Zhu, Shouliang Zhang, Anne-Claire Gaillot, and Donald L. Sparks. Electron Energy-Loss Safe-Dose Limits for Manganese Valence Measurements in Environmentally Relevant Manganese Oxides. *Environmental Science & Technology*, 46(2):970–976, January 2012.
- [215] Xiaoqi Sun, Victor Duffort, B. Layla Mehdi, Nigel D. Browning, and Linda F. Nazar. Investigation of the Mechanism of Mg Insertion in Birnessite in Non-aqueous and Aqueous Rechargeable Mg-Ion Batteries. *Chemistry of Materials*, 28(2):534–542, January 2016.
- [216] A. Azor, I. Gómez-Recio, L. Ruiz-González, M. Parras, and J. M. González-Calbet. Birnessite-Related Manganese Nano-Oxides: Dopant Location, a Key Factor to understand their Properties. *Journal of Chemical Science and Engineering*, 2(2):91–39, 2019.
- [217] R. F. Egerton, P. Li, and M. Malac. Radiation Damage in the TEM and SEM. *Micron*, 35(6):399–409, August 2004.
- [218] Roddatis, Lole, and Jooss. In Situ Preparation of $\text{Pr}_{1-x}\text{Ca}_x\text{MnO}_3$ and $\text{La}_{1-x}\text{Sr}_x\text{MnO}_3$ Catalysts Surface for High-Resolution Environmental Transmission Electron Microscopy. *Catalysts*, 9(9):751, September 2019.
- [219] R. F. Egerton. Radiation Damage to Organic and Inorganic Specimens in the TEM. *Micron*, 119:72–87, April 2019.
- [220] Nayda P. Arias, María E. Becerra, and Oscar Giraldo. Structural and Electrical Studies for Birnessite-Type Materials Synthesized by Solid-State Reactions. *Nanomaterials*, 9(8):1156, aug 2019.
- [221] D. S. Yang and M. K. Wang. Syntheses and Characterization of Well-Crystallized Birnessite. *Chemistry of materials*, 13(8):2589–2594, 2001.
- [222] M. Lainé, E. Balan, T. Allard, E. Paineau, P. Jeunesse, M. Mostafavi, J.-L. Robert, and S. Le Caër. Reaction Mechanisms in Swelling Clays Under Ionizing Radiation: Influence of the Water Amount and of the Nature of the Clay Mineral. *RSC Advances*, 7(1):526–534, January 2017.
- [223] Emiel J. M. Hensen and Berend Smit. Why Clays Swell. *The Journal of Physical Chemistry B*, 106(49):12664–12667, December 2002.

- [224] C. A. J. Appelo and D. Postma. Variable Dispersivity in a Column Experiment Containing MnO_2 and FeOOH -Coated Sand. *Journal of Contaminant Hydrology*, 40(2):95–106, December 1999.
- [225] R. F. Egerton. Beam-Induced Motion of Adatoms in the Transmission Electron Microscope. *Microscopy and Microanalysis*, 19(2):479–486, April 2013.
- [226] Binghong Han, Kelsey A. Stoerzinger, Vasiliki Tileli, Andrew D. Gamalski, Eric A. Stach, and Yang Shao-Horn. Nanoscale Structural Oscillations in Perovskite Oxides Induced by Oxygen Evolution. *Nature Materials*, 16(1):121–126, January 2017.
- [227] Marcel Risch, Alexis Grimaud, Kevin J. May, Kelsey A. Stoerzinger, Tina J. Chen, Azzam N. Mansour, and Yang Shao-Horn. Structural Changes of Cobalt-Based Perovskites upon Water Oxidation Investigated by EXAFS. *The Journal of Physical Chemistry C*, 117(17):8628–8635, May 2013.
- [228] Kevin J. May, Christopher E. Carlton, Kelsey A. Stoerzinger, Marcel Risch, Jin Suntivich, Yueh-Lin Lee, Alexis Grimaud, and Yang Shao-Horn. Influence of Oxygen Evolution during Water Oxidation on the Surface of Perovskite Oxide Catalysts. *The Journal of Physical Chemistry Letters*, 3(22):3264–3270, November 2012.
- [229] Holger Dau, Christian Limberg, Tobias Reier, Marcel Risch, Stefan Roggan, and Peter Strasser. The Mechanism of Water Oxidation: from Electrolysis via Homogeneous to Biological Catalysis. *ChemCatChem*, 2(7):724–761, 2010.
- [230] Lifei Xi, Christoph Schwanke, Jie Xiao, Fatwa F. Abdi, Ivelina Zaharieva, and Kathrin M. Lange. In Situ L-Edge XAS Study of a Manganese Oxide Water Oxidation Catalyst. *Journal of Physical Chemistry C*, 121(22):12003–12009, jun 2017.
- [231] Yelena Gorlin, Benedikt Lassalle-Kaiser, Jesse D. Benck, Sheraz Gul, Samuel M. Webb, Vittal K. Yachandra, Junko Yano, and Thomas F. Jaramillo. In Situ X-ray Absorption Spectroscopy Investigation of a Bifunctional Manganese Oxide Catalyst with High Activity for Electrochemical Water Oxidation and Oxygen Reduction. *Journal of the American Chemical Society*, 135(23):8525–8534, 2013.
- [232] C. Colliex, J. M. Cowley, S. L. Dudarev, M. Fink, J. Gjønnnes, R. Hilderbrandt, A. Howie, D. F. Lynch, L. M. Peng, G. Ren, A. W. Ross, V. H. Smith, J. C. H. Spence, J. W. Steeds, J. Wang, M. J. Whelan, and B. B. Zvyagin. Electron diffraction. In *International Tables for Crystallography*, pages 259–429. International Union of Crystallography, Chester, England, October 2006.
- [233] Justus Heese-Gärtlein. *Manganese Oxides as Electrocatalysts in Water Oxidation: Synthesis, Characterization and their Activity in the Oxygen Evolution*

- Reaction*. PhD thesis, Universität Duisburg-Essen, Duisburg-Essen, September 2018.
- [234] Jorge M. Lopez Fernandez and Omar A. Hernandez Rodriguez. Teaching the Fundamental Theorem of Calculus: A Historical Reflection. Technical report, Mathematical Association of America, 2012.
- [235] M. O. Krause and J. H. Oliver. Natural Widths of Atomic K and L levels, $K\alpha$ X-ray Lines and Several KLL Auger Lines. *Journal of Physical and Chemical Reference Data*, 8(2):329–338, 1979.
- [236] Rebecca A. Metzler, Il Won Kim, Katya Delak, John Spencer Evans, Dong Zhou, Elia Beniash, Fred Wilt, Mike Abrecht, Jau-Wern Chiou, Jinghua Guo, Susan N. Coppersmith, and P. U. P. A. Gilbert. Probing the Organic-Mineral Interface at the Molecular Level in Model Biominerals. *Langmuir*, 24(6):2680–2687, March 2008.
- [237] K. Kaznatcheyev, A. Osanna, C. Jacobsen, O. Plashkevych, O. Vahtras, Ågren, V. Carravetta, and A. P. Hitchcock. Innershell Absorption Spectroscopy of Amino Acids. *The Journal of Physical Chemistry A*, 106(13):3153–3168, April 2002.
- [238] Elena Macías-Sánchez, Marc G. Willinger, Carlos M. Pina, and Antonio G. Checa. Transformation of ACC Into Aragonite and the Origin of the Nanogranular Structure of Nacre. *Scientific Reports*, 7(1):12728, December 2017.

Supporting Information for Chapter 3

This chapter is a reproduction of the supporting information for the publication Ronge et al.^[27] represented in chapter 3.

Stability and Degradation Mechanism of Si-based Photocathodes for Water Splitting with Ultrathin TiO₂ Protection Layer

E. Ronge, T. Cottre, K. Welter, V. Smirnov, N. Ottinger, F. Finger, B. Kaiser, W. Jaegermann and C. Jooss

Republished with permission of de Gruyter, from “*Stability and Degradation Mechanism of Si-based Photocathodes for Water Splitting with Ultrathin TiO₂ Protection Layer*”, E. Ronge et al., *Zeitschrift für Physikalische Chemie* 234(6), 1171-1184, 2020;^[27] permission conveyed through Copyright Clearance Center, Inc. References, labels and arrangement of figures have been modified to suit this thesis.

***Corresponding author:** Christian Jooss, Institute of Materials Physics, University of Goettingen, 37077 Goettingen, Germany, e-mail: cjooss@gwdg.de
Emanuel Ronge and Natalie Jacqueline Ottinger: Institute of Materials Physics, University of Goettingen, 37077 Goettingen, Germany
Thorsten Cottre, Bernhard Kaiser and Wolfram Jaegermann: Institut für Materialwissenschaft, Technische Universität Darmstadt, 64287 Darmstadt, Germany
Katharina Welter, Vladimir Smirnov and Friedhelm Finger: Institut für Energie- und Klimaforschung (IEK-5), Forschungszentrum Jülich GmbH, 52425 Jülich, Germany

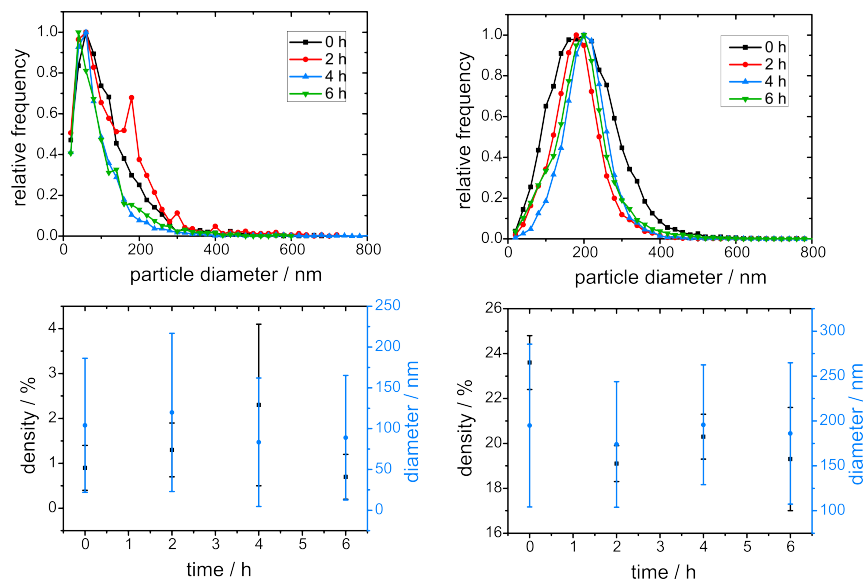


Figure A.1.: Platinum particle size and density from different areas of the a-Si:H/a-Si:H/100xTiO₂/Pt photocathode. left: low Pt density; right: high Pt density.

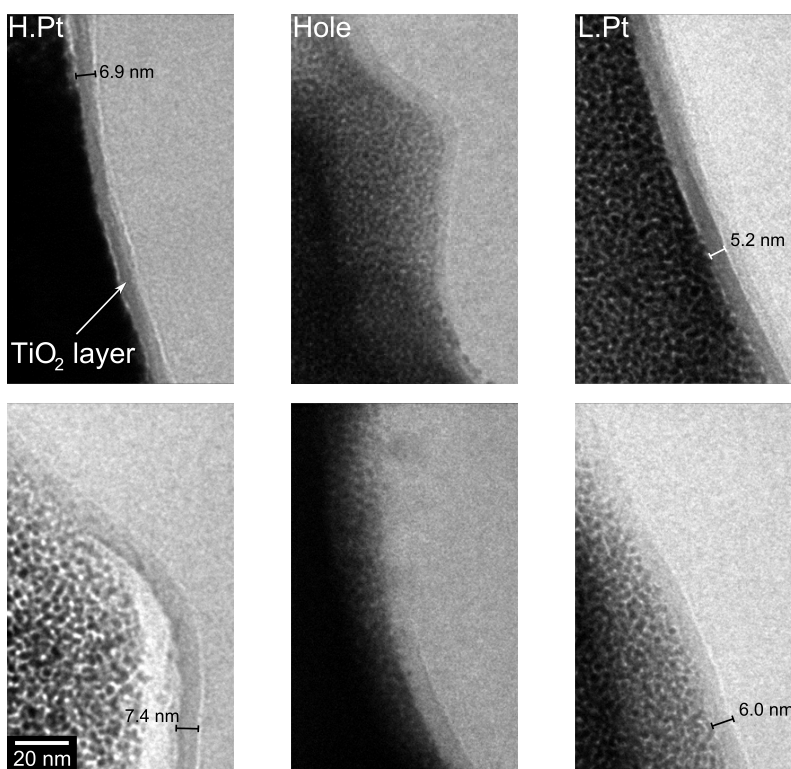


Figure A.2.: TEM bright field images of the TiO₂ layer from different areas of the a-Si:H/a-Si:H/100xTiO₂/Pt photocathode after 1 h of electrolysis. left: high Pt density; middle: hole; right: low Pt density.

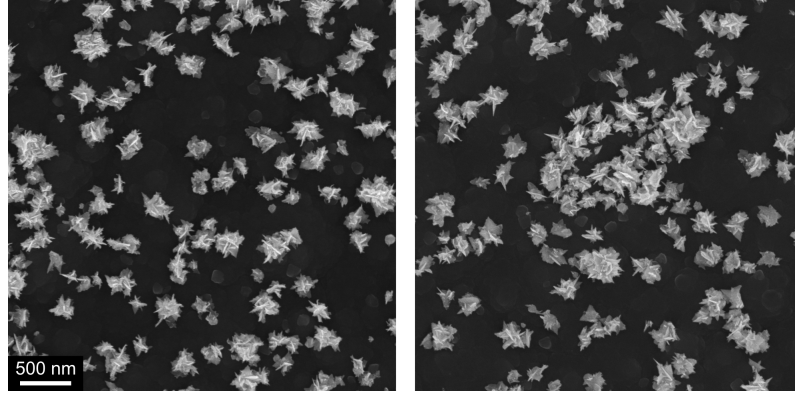


Figure A.3.: Surface with platinum particles of the pristine photocathode in the left image and after 6 h of electrolysis in KOH in the right image.

A SEM image of a triple cell based photocathode is shown in figure A.5. The typical two region of Pt rich and poor coverage can be distinguished. Table A.1 displays the similar Pt densities compared to the a-Si/a-Si/100xTiO₂/Pt sample. But in contrast to the a-Si/a-Si/100xTiO₂/Pt sample both areas are corroded. The reason is the thinner TiO₂ layer of the triple based cathode (table A.2). The smaller average hole diameter in Pt rich areas indicates additionally that a good Pt coverage slows down the dissolution of Si.

Table A.1.: Overview of the hole density, Pt density and the average hole diameter.

	Hole Density		Pt Density		Av. Hole diameter	
	[10 ⁻³ · 1/μm ²]		[%]		[nm]	
	H.Pt	L.Pt	H.Pt	L.Pt	H.Pt	L.Pt
a-Si/a-Si/ 100xTiO ₂ /Pt	-	36.8	54.3	0.9	-	3000 ± 1100
a-Si/a-Si/ μc-Si/100xTiO ₂ /Pt	4.0	4.8	59.1	0.1	3100 ± 2600	7800 ± 3400 ^{a)}

^{a)} Sample shows a scratch which results in an overestimation of the average hole diameter

Table A.2.: Overview of the average TiO₂ layer thickness of the triple and tandem cell device in the H.Pt and L.Pt areas.

d_{TiO_2}/nm	H.Pt	Hole	L.Pt
a-Si/a-Si/100xTiO ₂ /Pt	7.4 ± 1.2	4.8 ± 1.3	5.4 ± 0.8
a-Si/a-Si/μc-Si/100xTiO ₂ /Pt	3.2 ± 0.6	-	3.2 ± 0.9

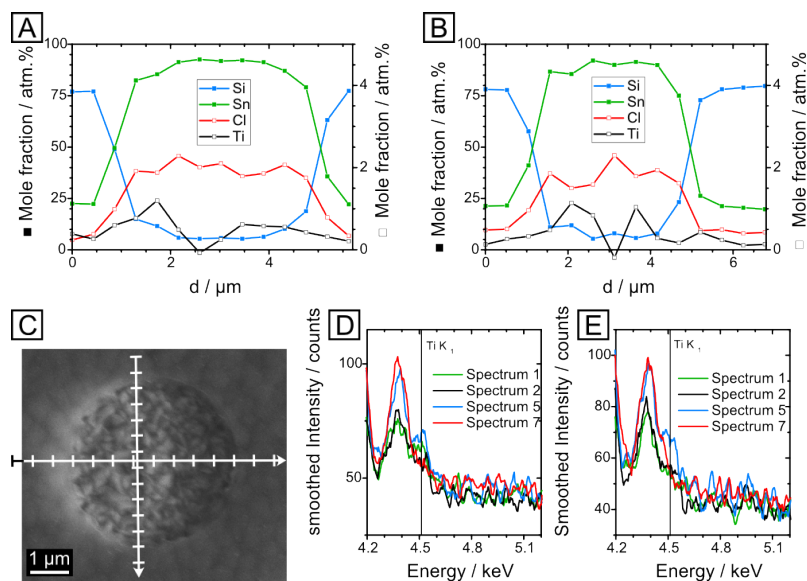


Figure A.4.: EDX analysis of a hole in a a-Si:H/100xTiO₂/Pt photocathode. A: vertical line scan; B: horizontal line scan; C: SEM image of the region of interest, the small ticks indicate the measurement points; D: spectra of the vertical line scan; E: spectra of the horizontal line scan.

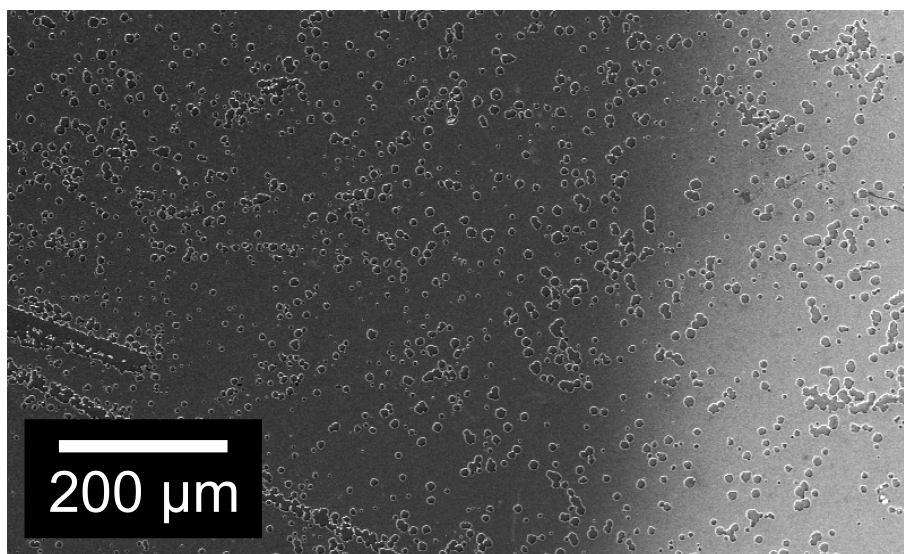


Figure A.5.: SEM image of a-Si/a-Si/ μ c-Si/100xTiO₂/Pt triple junction photocathode, showing degradation by hole formation in both areas (H.Pt at the right side of the image and L.Pt at the middle and left side of the images).

Supporting Information for Chapter 4

This chapter is a reproduction of the supporting information for the in chapter 4 presented publication^[28]

Structure of nanocrystalline, partially disordered MoS_{2+δ} derived from HRTEM - an abundant material for efficient HER catalysis

Emanuel Ronge, Sonja Hildebrandt, Marie-Luise Grutza, Helmut Klein, Philipp Kurz and Christian Jooss

originally published in *Catalysts* 2020, 10(8), 856^[28] under the terms and conditions of the CC BY license. doi:10.3390/catal10080856

References and labels of figures have been modified to suit this thesis.

¹ Institute of Materials Physics, University of Göttingen, Friedrich-Hund-Platz 1, 37077 Göttingen, Germany; emanuel.ronge@phys.uni-goettingen.de (E.R.); s.hildebrandt01@stud.uni-goettingen.de (S.H.)

² Institute for Inorganic and Analytical Chemistry and Freiburg Material Research Center (FMF), University of Freiburg, Albertstraße 21, 79104 Freiburg, Germany; marie-luise.grutza@ac.uni-freiburg.de

³ GZG Crystallography University of Göttingen, Goldschmidtstr. 1, 37077 Göttingen, Germany; hklein@uni-goettingen.de

⁴ International Center for Advanced Studies of Energy Conversion (ICASEC), University of Göttingen, D-37077 Göttingen, Germany

* Correspondence: philipp.kurz@ac.uni-freiburg.de (P.K.); cjooss@gwdg.de (C.J.); Tel.: +49-0761-203-6127 (P.K.); +49-551-39-25303 (C.J.)

B.1. XRD

XRD	SAD	XRD	SAD	Literature ^{a)}	
MoS _{2.6}	MoS _{2.6}	MoS _{3.4}	MoS _{3.4}	MoS ₂	(hkl)
Å	Å	Å	Å	Å	Å
7.37		8.19			
6.29					
6.08				6.15	002
	4.51			2.74	100
	3.18				
2.70		2.63		2.67	101
2.51				2.50	102
2.15	2.28	2.14	2.35	2.28	103
1.89		1.87	1.98	1.83	105
1.62	1.46	1.62	1.52	1.57	110
	1.04		1.09		

^{a)} Structure model of Wildervanck et al was used.^[47]

Table B.1.: Comparison of the experimental (XRD) d_{hkl} from figure 4.2 for the most intense XRD reflections of MoS₂^{a)} and selected area electron diffraction (SAD) pattern from Figure 4.3.

B.1.1. Rietveld refinement

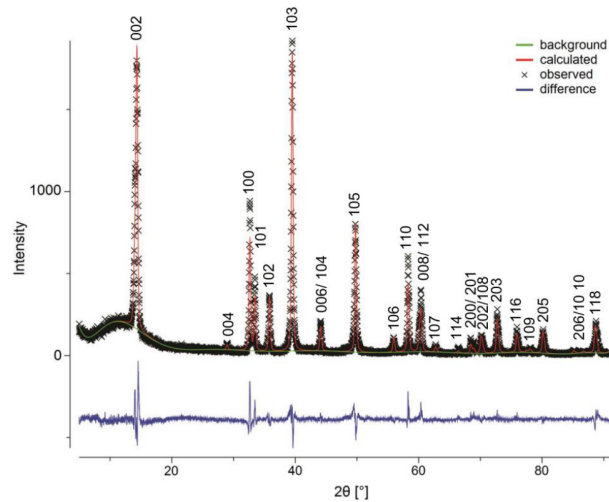


Figure B.1.: Plot of the Rietveld refinement of MoS₂.

χ^2	R_{wp}	G
2.857	0.1847	1.005 ± 0.003

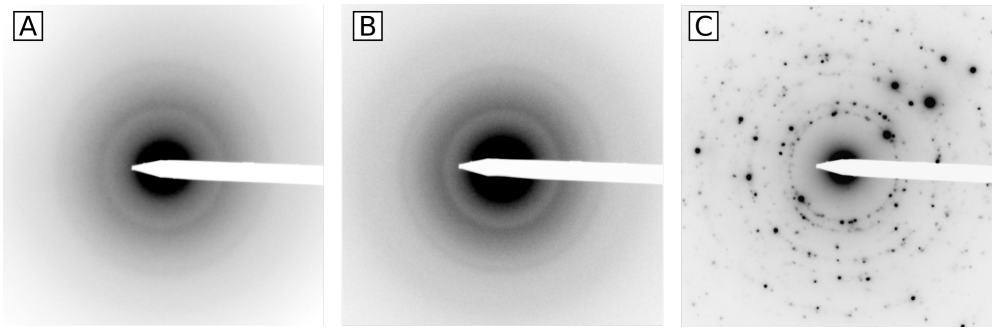
Table B.2.: Goodness parameters and correction factor for the texture.

a	b	c
Å	Å	Å
3.16354 ± 0.00014	3.16354 ± 0.00014	12.3086 ± 0.0008

Atom	a	b	c
Mo	0.3333	0.6667	0.2500
S	0.3333	0.6667	0.6225 ± 0.0003

Table B.3.: Refined lattice parameters and atom positions of MoS₂.

B.2. TEM

**Figure B.2.:** Selected areas electron diffraction (SAD) pattern of A: MoS_{2.6}; B: MoS_{3.4}; C: MoS₂.

In Table B.4 the most intense lattice reflections of MoS₂ from the structure of Wildervanck et al.^[47] are compared to experimental selected area electron diffraction (SAD) results of MoS₂, MoS_{2.6} and MoS_{3.4} after creating diffracted intensity profiles via circular integration as shown in Figure 4.3. There, the experimental numbers give the peak positions and the grey shadow represents the peak width. For MoS₂ every lattice reflection with $F2 > 106$ can be assigned. Some of the reflections are hidden in the flanks in the intensity profile (Figure 4.3) due to their lower intensity but are visible in the diffraction pattern in Figure B.3. The (004) reflection is probably missing due to its low structure factor and the (002) reflection is missing for all samples due to its overlap with the zero beam. The SAD intensity profiles of MoS_{2.6} and MoS_{3.4} is similar to the profile of MoS₂, but their shape is significantly broadened. Thus, most important MoS₂ reflexes can be assigned to the SAD data of the partially disordered systems. However, in the range of 1.29 Å and 1.15 Å no

broadened reflexes are visible for $\text{MoS}_{2.6}$ and $\text{MoS}_{3.4}$, in contrast to the expected diffraction maxima from the literature as well as the experimental MoS_2 data. This could indicate an increase of disorder for these lattice planes. In addition, the (004) reflection can be assigned to the $\text{MoS}_{2.6}$ data. The increased disorder in c direction could explain why these reflections are visible compared to MoS_2 . This is supported by XRD (main text Figure 4.2) which show in general a lower order compared to MoS_2 but a sharp c-direction compared to $\text{MoS}_{3.4}$.

Literature ^[47,232]					Experimental		
MoS ₂					MoS ₂	MoS _{2.6}	MoS _{3.4}
d [Å]	(h	k	l)	F ²	d [Å]	d [Å]	d [Å]
6.147	0	0	2	$4.61 \cdot 10^8$	Overlapp with zero beam		
3.074	0	0	4	$4.85 \cdot 10^6$		3.18	
2.737	$\bar{1}$	0	0	$1.40 \cdot 10^9$	Could be hidden in flank		
2.671	$\bar{1}$	0	$\bar{1}$	$6.98 \cdot 10^7$			
2.500	$\bar{1}$	0	$\bar{2}$	$7.01 \cdot 10^8$			
	$\bar{1}$	1	$\bar{2}$		2.52	2.31	2.35
2.276	$\bar{1}$	0	$\bar{3}$	$5.62 \cdot 10^9$			
2.049	0	0	$\bar{6}$	$2.86 \cdot 10^8$	2.13		
2.044	$\bar{1}$	0	4	$7.43 \cdot 10^6$			1.99
1.830	$\bar{1}$	0	5	$6.66 \cdot 10^9$	Hidden in flank		
1.640	$\bar{1}$	0	6	$4.36 \cdot 10^8$	1.72		
	$\bar{1}$	1	$\bar{6}$				
1.580	$\bar{2}$	1	0	$5.77 \cdot 10^9$	Hidden in flank		
	$\bar{1}$	$\bar{1}$	0				
1.537	0	0	8	$1.80 \cdot 10^9$			
1.530	$\bar{2}$	1	$\bar{2}$	$2.88 \cdot 10^9$			1.52
	$\bar{1}$	$\bar{1}$	$\bar{2}$				
1.478	$\bar{1}$	0	7	$2.47 \cdot 10^8$	1.47	1.45	
1.405	$\bar{2}$	1	4	$3.06 \cdot 10^7$	1.42		
1.368	$\bar{2}$	0	0	$1.46 \cdot 10^9$			
	$\bar{2}$	2	0				
1.360	$\bar{2}$	0	$\bar{1}$	$7.28 \cdot 10^7$	Hidden in flank		
1.340	$\bar{1}$	0	8	$2.75 \cdot 10^9$			
1.336	$\bar{2}$	0	$\bar{2}$	$7.29 \cdot 10^8$			
1.298	$\bar{2}$	0	$\bar{3}$	$5.84 \cdot 10^9$			
1.251	$\bar{2}$	1	$\bar{6}$	$1.79 \cdot 10^9$	1.27		
	$\bar{1}$	$\bar{1}$	$\bar{6}$				
1.250	$\bar{2}$	0	4	$7.71 \cdot 10^6$			
	$\bar{2}$	2	4				
1.222	$\bar{1}$	0	9	$5.87 \cdot 10^6$			
	$\bar{1}$	1	9				
1.196	$\bar{2}$	0	5	$6.93 \cdot 10^9$	1.20		
1.138	$\bar{2}$	0	6	$4.53 \cdot 10^8$	Hidden in flank		
1.102	$\bar{2}$	1	8	$1.13 \cdot 10^{10}$	1.11		
1.079	2	0	7	$2.57 \cdot 10^8$	1.06		
1.034	$\bar{3}$	1	0	$3.02 \cdot 10^9$		1.04	1.089
	2	$\bar{1}$	0				
1.031	$\bar{3}$	1	$\bar{1}$	$1.51 \cdot 10^8$			
	2	$\bar{1}$	$\bar{1}$				
1.022	$\bar{2}$	0	8	$2.86 \cdot 10^9$			
1.020	$\bar{3}$	1	$\bar{2}$	$1.51 \cdot 10^9$			
1.003	3	1	3	$1.21 \cdot 10^{10}$			

Table B.4.: Overview of the most intense lattice planes ($F^2 > 10^6$ and $d > 1 \text{ \AA}$) in electron diffraction of MoS_2 compared with experimental SAD data for MoS_2 , $\text{MoS}_{2.6}$ and $\text{MoS}_{3.4}$ from Figure B.3 and main text Figure 4.3. The structure model of Wildervanck et al.^[47] and the atomic scattering factor from Colliex et al.^[232] were used to calculate the structure factor F .

	d_{100} \AA	d_{001} \AA
$\text{MoS}_{2.6}$	2.70 ± 0.05	12.40 ± 0.09
	2.60 ± 0.05	12.57 ± 0.09
	2.66 ± 0.05	13.38 ± 0.10
	2.45 ± 0.05	14.05 ± 0.10
	2.56 ± 0.05	13.29 ± 0.10
	13.30 ± 0.10	
	11.15 ± 0.09	
$\text{MoS}_{3.4}$	2.75 ± 0.05	13.19 ± 0.08
	2.71 ± 0.05	15.93 ± 0.10
	2.61 ± 0.05	11.79 ± 0.07
	2.79 ± 0.05	14.28 ± 0.09
	2.73 ± 0.05	12.54 ± 0.08

Table B.5.: Result from the FFT analysis of HRTEM images of $\text{MoS}_{2+\delta}$ visible in Figure B.3

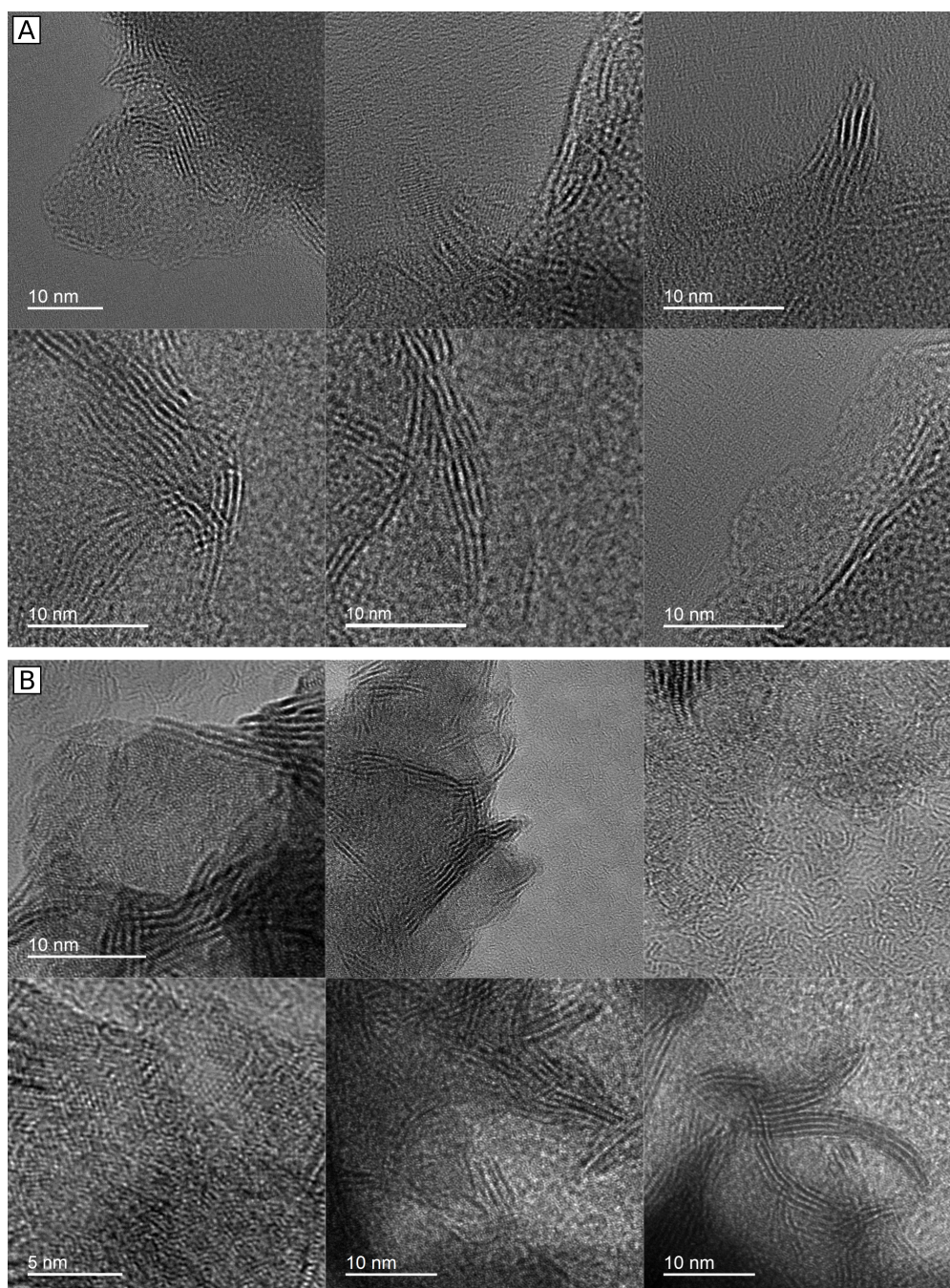


Figure B.3.: HRTEM images of A: MoS_{2.6} and B: MoS_{3.4} used for the lattice parameter analysis in Table B.5.

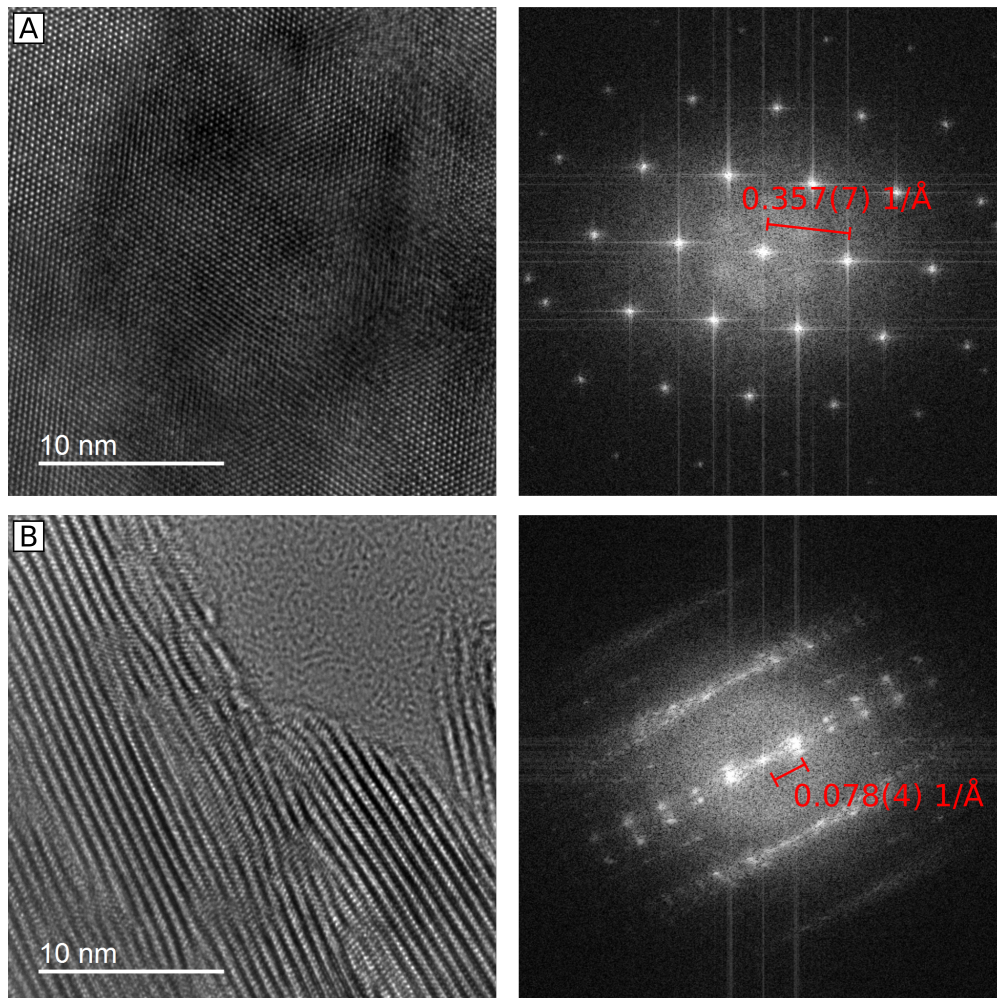


Figure B.4.: Representative HRTEM images of MoS₂ and their FFTs. A: in-plane ($1/d=(0.357\pm 0.007)1/\text{\AA} \rightarrow d=(2.80\pm 0.06) \text{\AA}$); B: out of plane ($1/d=(0.078\pm 0.004) 1/\text{\AA} \rightarrow d=(13.1\pm 0.7) \text{\AA}$).

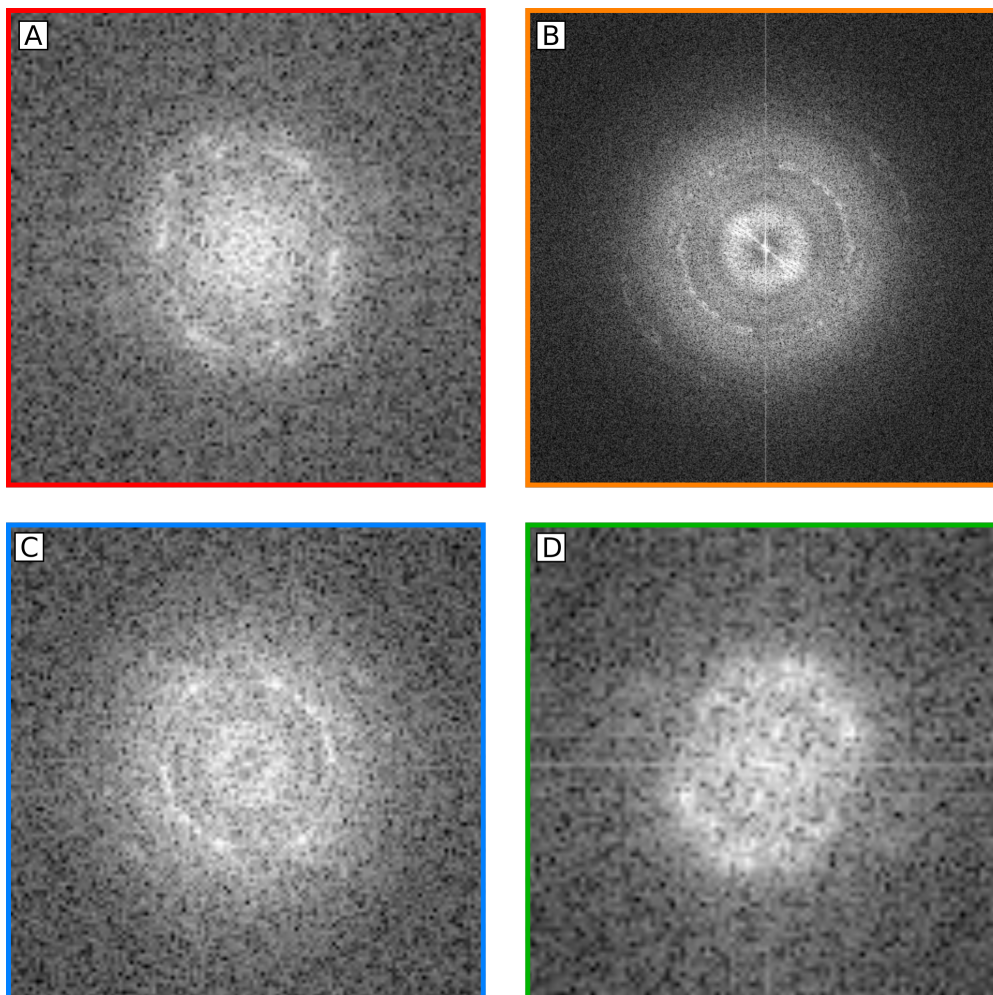


Figure B.5.: Reduced FFT of HRTEM image from figure 4.5 A & B which were used to create the intensity profiles in figure 4.5 C. A: FFT of small red area in figure 4.5 A left; B: FFT of figure 4.5 A right (entire image, orange); C: FFT of small blue area in figure 4.5 A right; D: FFT of small green area in figure 4.5 B left.

B.3. SEM

The geometric factor F_G is defined as the increase of the geometric surface area of the electrode after taking particle size and shape into consideration. Figure B.6 shows the shape of the particles of the commercial MoS_2 and the synthesized $\text{MoS}_{2.6}$ and $\text{MoS}_{3.4}$ powder. For the $\text{MoS}_{2+\delta}$ particles no difference between the two batches is visible and the shape is approximated with a sphere (r_S : radius) resulting in a surface area of

$$A_{O,S} = 4 \cdot \pi \cdot r_S^2.$$

The MoS_2 particles are approximated with a flattened rotational ellipsoid (r_E : in plane radius, h : height; $r_E > h$):

$$A_{O,E} = 2 \cdot \pi \cdot r_E \left(r_E + \frac{h^2}{\sqrt{r_E^2 - h^2}} \operatorname{arsinh} \left(\frac{\sqrt{r_E^2 - h^2}}{h} \right) \right)$$

Taking the different projected base areas $A_{C,E/S} = \pi \cdot r^2$ into account, the geometric factor can be described by:

$$F_{G,\text{MoS}_2} = \frac{A_{O,E}}{2 \cdot A_{C,E}}, \quad F_{G,\text{MoS}_{2+\delta}} = \frac{A_{O,S}}{2 \cdot A_{C,ES}}$$

With an average diameter of $2 \cdot r_S = (0.18 \pm 0.06) \mu\text{m}$ for $\text{MoS}_{2+\delta}$, $2 \cdot r_E = (0.8 \pm 0.9) \mu\text{m}$ and a height of $h = 0.04 \mu\text{m}$ for MoS_2 this results in a geometric factor of

$$F_{G,\text{MoS}_2} = 1.03 \quad \text{and} \quad F_{G,\text{MoS}_{2+\delta}} = 2. \quad (\text{B.1})$$

Thus, the surface of the $\text{MoS}_{2+\delta}$ electrode is by factor of ≈ 1.9 larger than the MoS_2 surface due to particle size and shape.

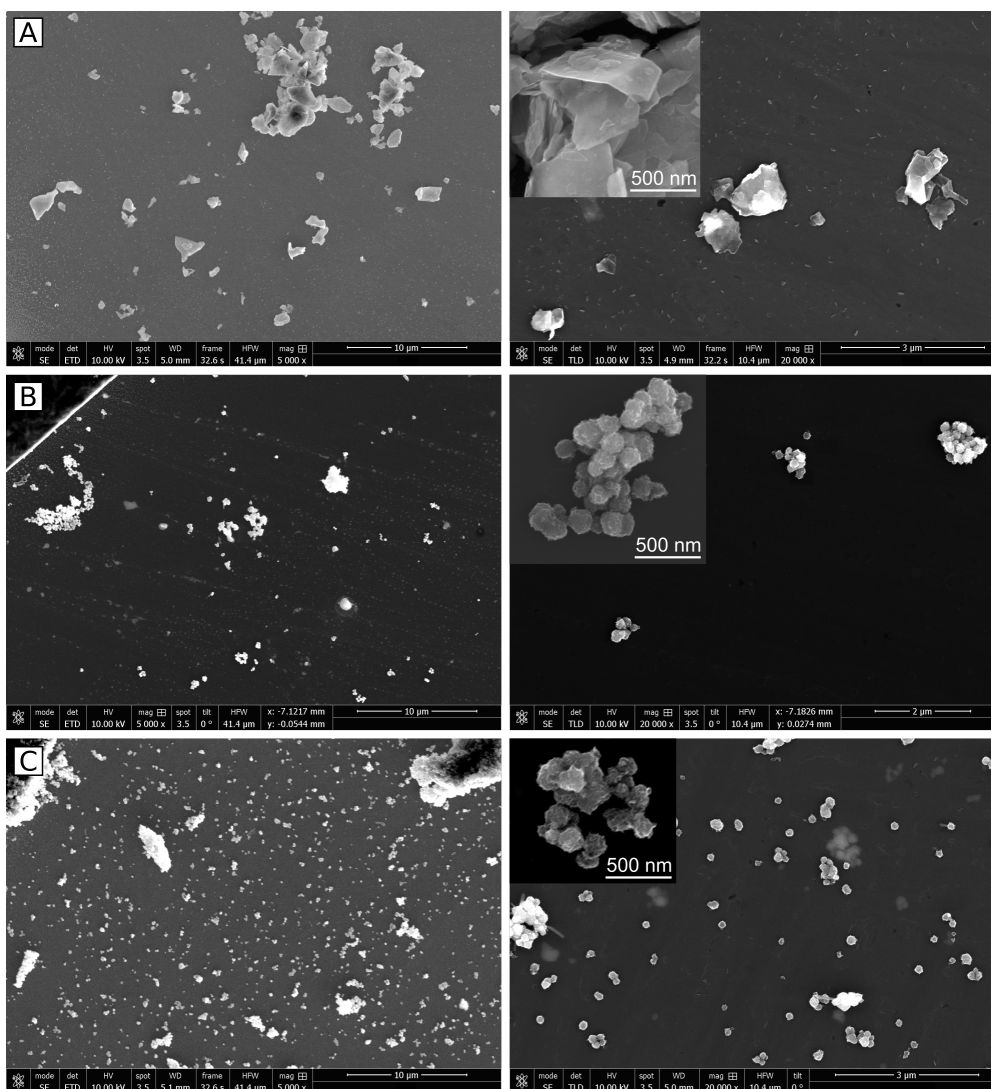


Figure B.6.: SEM images for particle size and shape analysis of A: MoS₂ powder; B: MoS_{2.6} powder and C: MoS_{3.4} powder representative for the MoS_{2+δ} sample in different magnifications. The powders are dispersed on a carbon membrane to separate the particles.

B.4. EC

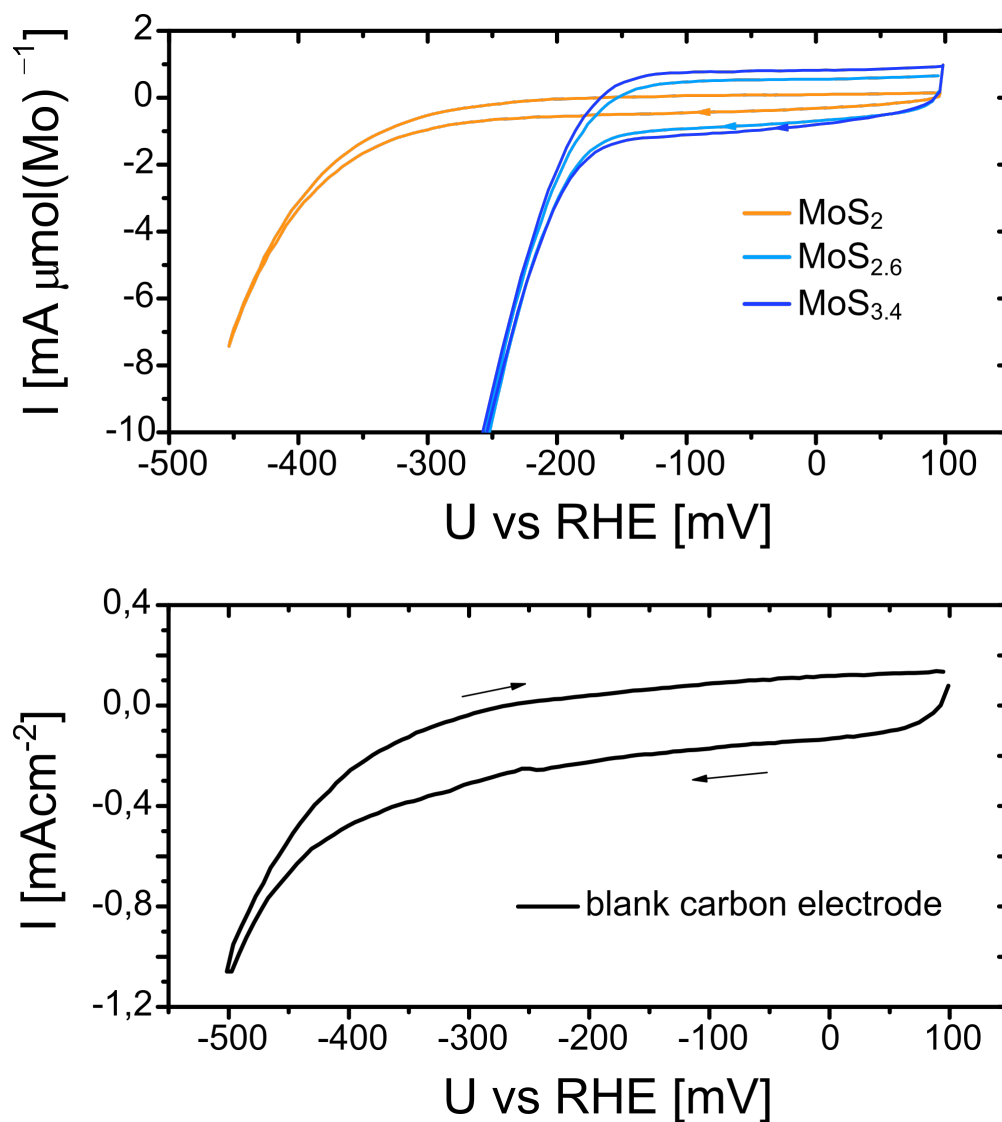


Figure B.7.: Cyclic voltammetry (cycle 6) in sulfuric acid (0.5 M, pH 0.3) of: *Top:* the two MoS_x samples and MoS₂ normalized to Mo content (scan rate 20 mVs⁻¹); *Bottom:* The blank carbon electrode.

Supporting Information for Chapter 5

This chapter is a reproduction of the supporting information for the in chapter 5 presented publication^[29]

Operation of Calcium-Birnessite Water-Oxidation Anodes: Interactions of the Catalyst with Phosphate Buffer Anions

Emanuel Ronge^a, Jonas Ohms^b, Vladimir Roddatis^a, Travis Jones^d, Frederic Sulzmann^d, Axel Knop-Gericke^d, Robert Schlögl^{d,e}, Christian Jooss^{,a,c}, Philipp Kurz^{*,b}, and Katarzyna Skorupska^{*,d,e}*

originally published as a preprint in *Chemrxiv* (2020)^[29] under the terms and conditions of the CC BY-NC-ND 4.0 license. doi:10.26434/chemrxiv.13153976.v1
References and labels have been modified to suit this thesis.

^a Institut für Materialphysik, Georg-August-Universität Göttingen, Friedrich-Hund-Platz 1, 37077 Göttingen, Germany.

^b Institut für Anorganische und Analytische Chemie and Freiburger Materialforschungszentrum (FMF), Albert-Ludwigs-Universität Freiburg, Albertstraße 21, 79104 Freiburg, Germany

^c International Center for Advanced Energy Studies, Georg-August-Universität Göttingen, Tammannstr. 4, 37077 Göttingen, Germany.

^d Max-Planck-Institut für Chemische Energiekonversion, Stiftstraße 34-36, 45470 Mülheim an der Ruhr, Germany.

^e Fritz-Haber-Institut der Max-Planck-Gesellschaft, Faradayweg 4-6, 14195 Berlin, Germany.

C.1. Experimental details

C.1.1. Materials

With the exception of the Ca-birnessite powder, all chemicals used in this study were purchased commercially and used as received. The electrolyte solutions were prepared using ultrapure water from an ELGA PURELAB flex 4 water-purification system (resistivity $> 18 \text{ M}\Omega \cdot \text{cm}$) and the following analytical grade chemicals (provider's name in brackets): KOH (Sigma Aldrich), KH_2PO_4 (VWR), K_2HPO_4 (Grüssing), imidazole (Chempur), H_2SO_4 (VWR) and K_2SO_4 (Roth). The OER catalyst material used for this study was a previously described, synthetic Ca-birnessite of the approximate stoichiometry $\text{Ca}_{0,2}\text{MnO}_{2,21} \cdot 1.4\text{H}_2\text{O}$ which was screen-printed onto FTO-coated glass slides (Sigma Aldrich, $7 \Omega \cdot \text{cm}^{-2}$) following a previously reported procedure.^[89]

C.1.2. Electrocatalysis

Electrochemical experiments were carried out using a Princeton Applied Research Versastat 4 potentiostat / galvanostat equipped with a FRA module for electrochemical impedance spectroscopy (EIS) measurements. All experiments were carried out in standard 100 mL electrochemical cells (Metrohm) in a three-electrode configuration consisting of a double junction Ag/AgCl reference electrode (Metrohm, inner electrolyte 3M KCl), a Pt rod counter electrode and the Ca-birnessite electrodes serving as working electrodes. An overview of the employed electrolyte solutions is given in Table C.1. All cyclic voltammograms were iR-compensated to 100 %. Prior to the experiments, the uncompensated resistance was determined by EIS. Please note that all experimental electrode potentials given in this report have been converted to the reversible hydrogen electrode (RHE) scale.

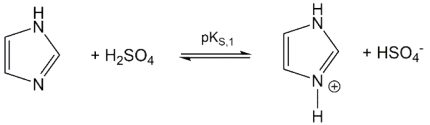
electrolyte	pH	$\kappa / \text{mScm}^{-1}$	buffering acid / base pair
$\text{H}_2\text{PO}_4^- / \text{HPO}_4^{2-}$	7,0	15,7	$\text{H}_2\text{PO}_4 + \text{H}_2\text{O} \xrightleftharpoons{\text{p}K_{\text{s},2}} \text{HPO}_4^{2-} + \text{H}_3\text{O}^+$
imidazole / H_2SO_4	7,0	15,4	 $\text{Imidazole} + \text{H}_2\text{SO}_4 \xrightleftharpoons{\text{p}K_{\text{s},1}} \text{Imidazolium}^+ + \text{HSO}_4^-$
K_2SO_4	7,0	20,3	-

Table C.1.: Compositions, basic properties and relevant buffering acid / base pairs of the three electrolyte systems used in this study. The total concentration of phosphate, imidazole or sulfate was 0.1 M in each case, respectively.

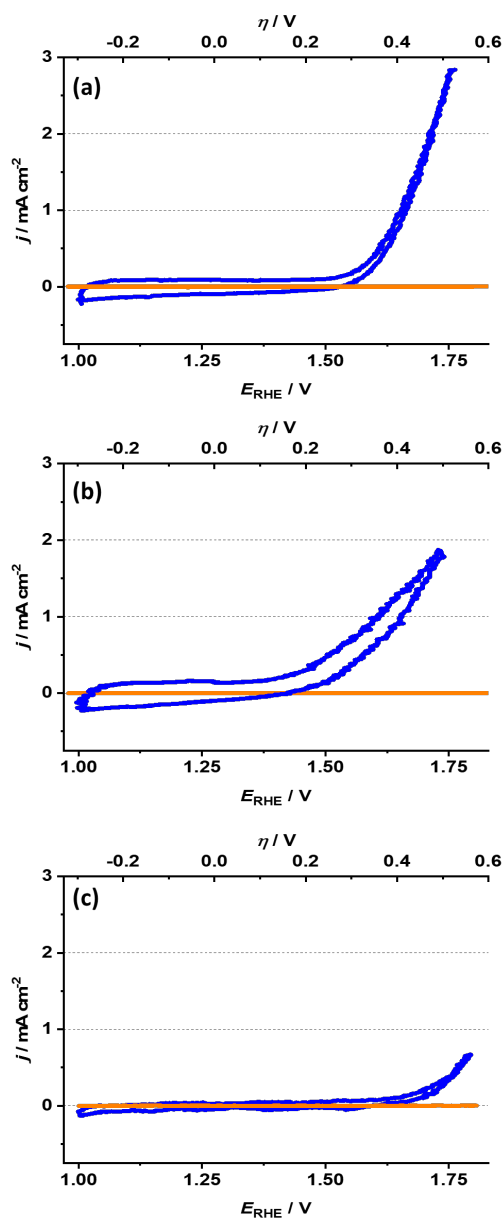


Figure C.1.: Cyclic voltammograms of Ca-birnessite-coated FTO-slides immersed in a) phosphate (pH 7), b) imidazolium (pH 7) and c) potassium sulphate solutions. In each case, the CVs for the fifth cycle are shown. Orange curves indicate data for bare FTO-coated glass slides immersed in the respective electrolytes. The concentrations of the respective buffer anions were carefully adjusted to: 0.1 M. The CV sweep rate was set to $20 \text{ mV} \cdot \text{s}^{-1}$ in all cases.

C.2. Electron Microscopy

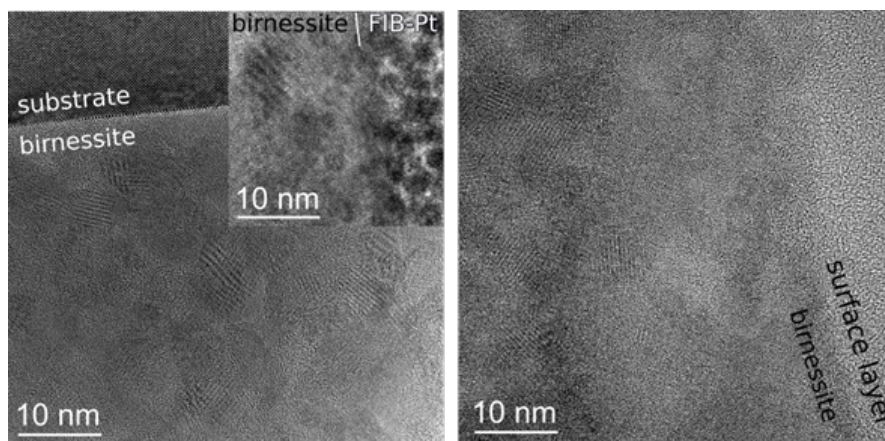


Figure C.2.: HRTEM-image of a Ca-birnessite electrode coated with a $0.2\ \mu\text{m}$ thick catalyst layer. Left: pristine sample with inset showing the pristine nanocrystalline surface; right: sample after 12 h of electrolysis in the phosphate buffer.

Figure C.2 shows two HRTEM-images of the $\approx 0.2\ \mu\text{m}$ thick virgin sample (left) and another sample after 12 hours electrolysis (right) in the phosphate buffer at an overpotential of 533 mV at pH 7. Nanocrystals with a diameter of a few nanometers can be observed in both samples and is not influenced by the choice of the substrate. The nanocrystalline structure is in good agreement with the electron diffraction patterns in Figure C.3, showing diffraction rings which are broadened due to the nm scale grain size. After electrolysis, the formed P-rich surface layer is visible. This surface layer is much less ordered than the primary birnessite and most probably is amorphous.

In Figure C.3, the selected area electron diffraction (SAED) pattern of two types of $\approx 4\ \mu\text{m}$ thick birnessite films on FTO substrates are shown. Figure S3 A shows the virgin sample and B another sample after 9 h electrolysis. Rings with diffraction spots are in both cases visible. The measured lattice plane spacing is noted in the diffraction pattern as well as in the radial intensity profiles of the diffraction pattern in figure S3 C and D. Note that the diffraction reflexes at $1.52\ \text{\AA}$ and $1.77\ \text{\AA}$ for the as prepared sample are only visible in the SAED pattern and not in the radial intensity profiles due to their sparse appearance. No significant changes in the lattice spacings can be observed after the electrolysis within the accuracy limit of 2%. In Table C.2, the measured lattice spacings are assigned to lattice planes of birnessite. The structure model from Lopano et al.^[81] and the electron atomic scattering factors from Colliex et al.^[232] was used to calculate the plane spacing d_{hkl} and the structure factor F . Note that only theoretical lattice spacings are given for those hkl with a large structure factor. In both HRTEM and SAED no (002) lattice plane is visible despite of its relative high structure factor ($F^2 = 6 \cdot 10^7$) indicating a poor c-axis

ordering. Consequently $\{001\}$ lattice planes are not included in Table C.2 and in addition less intense in-plane lattice planes like (200) with a $F^2 > 10^5$ are added.

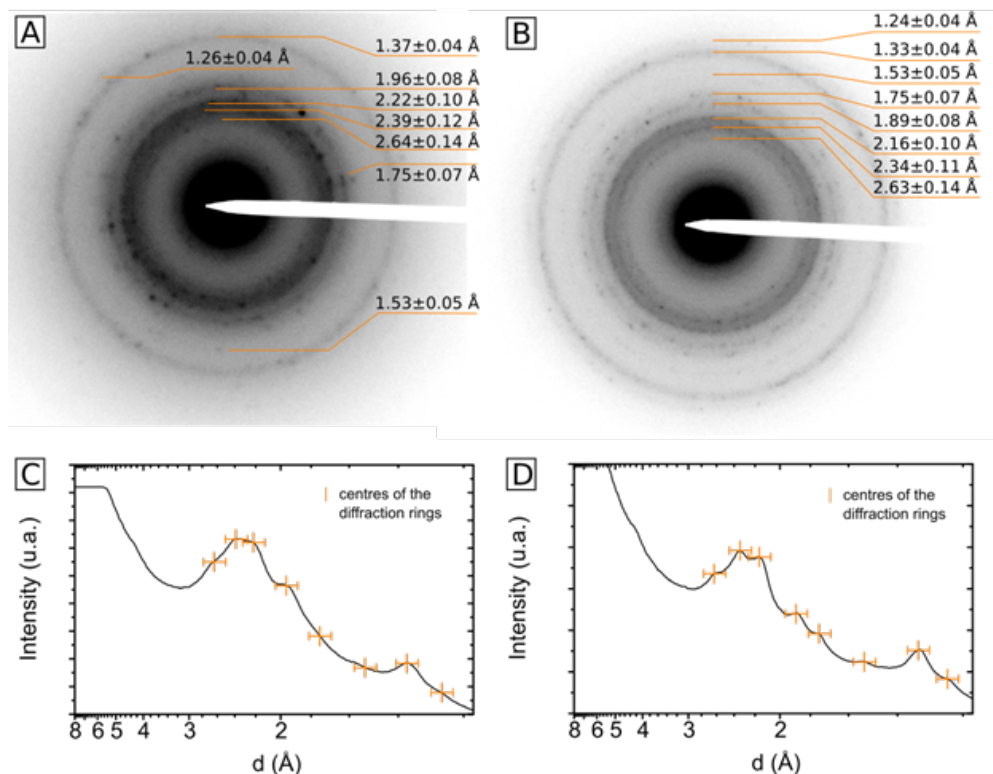


Figure C.3.: Electron diffraction pattern (top) and associated radial intensity profiles (bottom) of the Ca-birnessite layer. A and C: as prepared; B and D: after 9 h electrolysis in phosphate buffer.

The minor variation in intensity and broadness of the diffraction rings between the two samples are probably due to slight differences in the lamella thickness, grain size and number. Because of the relative breadth and partial overlap of diffraction rings, a distinct assignment of birnessite lattice planes to the diffraction rings is not possible. Instead Table C.2 show which theoretical birnessite lattice planes are consistent with the diffraction rings within the measurement accuracy of 2% which is represented by the grey shading. Overall, the birnessite structure is in accordance with the diffraction data with three noticeable deviations: 1) The $\{001\}$ lattice planes are missing probably due to a high c -axis disorder as mentioned earlier. 2) The (100) lattice plane at 5.05 Å overlaps with the zero beam and thus is not visible. 3) The diffraction ring at (1.53 ± 0.05) Å is very weak and broad. As a result, the calculated d_{hkl} reflexes in between 1.7 Å and 1.4 Å could be very well hidden in the flank, however, are not assigned to the data.

theoretical ^{3,4}			as prepared	after electrolysis
d Å	(hkl)	F ²	d Å	d Å
5.05	$\bar{1} 00$	$1.02 \cdot 10^6$		
2.67	$\bar{1} 0\bar{2}$	$2.46 \cdot 10^6$		
2.64	$0\bar{1} \bar{1}$	$1.56 \cdot 10^6$	2.64 ± 0.14	2.63 ± 0.14
2.53	$\bar{2} 01$	$5.88 \cdot 10^6$		
2.52	$\bar{2} 00$	$9.24 \cdot 10^5$		
2.49	110	$2.02 \cdot 10^7$		
2.47	$\bar{1}10$	$7.69 \cdot 10^6$		
2.42	$\bar{1}1 1$	$5.79 \cdot 10^7$	2.39 ± 0.12	2.34 ± 0.11
2.28	111	$3.27 \cdot 10^7$		
2.25	$\bar{2} 0\bar{1}$	$2.72 \cdot 10^7$	2.22 ± 0.10	
2.12	$\bar{1} 12$	$2.83 \cdot 10^7$		2.16 ± 0.10
1.95	112	$1.32 \cdot 10^7$	1.96 ± 0.08	
1.89	$\bar{2} \bar{1} 0$	$9.46 \cdot 10^6$		1.89 ± 0.08
1.80	$\bar{1}13$	$9.78 \cdot 10^7$		
1.77	211	$1.11 \cdot 10^7$	1.75 ± 0.07	1.75 ± 0.07
1.68	$\bar{3}00$	$2.73 \cdot 10^6$		
1.64	113	$5.80 \cdot 10^7$		
1.58	212	$1.27 \cdot 10^7$		
1.58	$\bar{2} 0\bar{3}$	$2.62 \cdot 10^7$		
1.51	$\bar{1}14$	$1.99 \cdot 10^7$	1.53 ± 0.05	1.53 ± 0.05
1.47	$\bar{3} \bar{1}1$	$1.37 \cdot 10^7$		
1.45	$\bar{3} 10$	$9.63 \cdot 10^7$		
1.45	$\bar{3}1 0$	$2.70 \cdot 10^7$		
1.43	$\bar{3}1 2$	$3.06 \cdot 10^7$		
1.42	$\bar{3} 12$	$8.31 \cdot 10^7$		
1.42	$0\bar{2}0$	$7.05 \cdot 10^6$		
1.40	$0\bar{2}1$	$4.44 \cdot 10^7$		
1.39	213	$1.43 \cdot 10^7$		
1.38	$\bar{2} 1\bar{3}$	$2.47 \cdot 10^7$		
1.37	$\bar{1}2 0$	$8.31 \cdot 10^6$	1.37 ± 0.04	
1.35	$\bar{2} 05$	$3.20 \cdot 10^7$		
1.33	$\bar{3} 13$	$1.43 \cdot 10^7$		1.33 ± 0.04
1.28	$\bar{1}1 5$	$6.67 \cdot 10^7$		
1.28	$\bar{4} 01$	$3.52 \cdot 10^7$		
1.27	$\bar{3} 1\bar{2}$	$4.76 \cdot 10^7$		
1.26	122	$1.11 \cdot 10^7$		
1.26	$\bar{4}00$	$1.19 \cdot 10^7$	1.26 ± 0.04	
1.24	$\bar{2} 20$	$1.40 \cdot 10^7$		1.24 ± 0.04
1.24	$\bar{2}21$	$3.55 \cdot 10^7$		
1.24	$\bar{2} \bar{2} 0$	$5.27 \cdot 10^7$		

1.22	$\bar{2}1\bar{5}$	$1.06 \cdot 10^7$	
1.22	$\bar{3}14$	$4.45 \cdot 10^7$	
1.21	$\bar{2}\bar{2}2$	$2.78 \cdot 10^7$	
1.21	$\bar{4}03$	$9.56 \cdot 10^7$	
1.21	214	$1.59 \cdot 10^7$	
1.20	$\bar{3}05$	$7.30 \cdot 10^7$	
1.20	$\bar{2}\bar{2}2$	$2.07 \cdot 10^7$	
1.20	$\bar{4}0\bar{1}$	$2.40 \cdot 10^7$	
1.19	115	$7.15 \cdot 10^7$	

Table C.2.: Assignment of the lattice spacing to calculated lattice planes of birnessite. The calculated lattice planes which are within the 2% measurement accuracy of the experimental diffraction ring centres are indicated with a grey shading. The structure model of Lopano et al.^[81] and the atomic scattering factor from Colliex et al.^[232] were used to calculate the structure factor F .

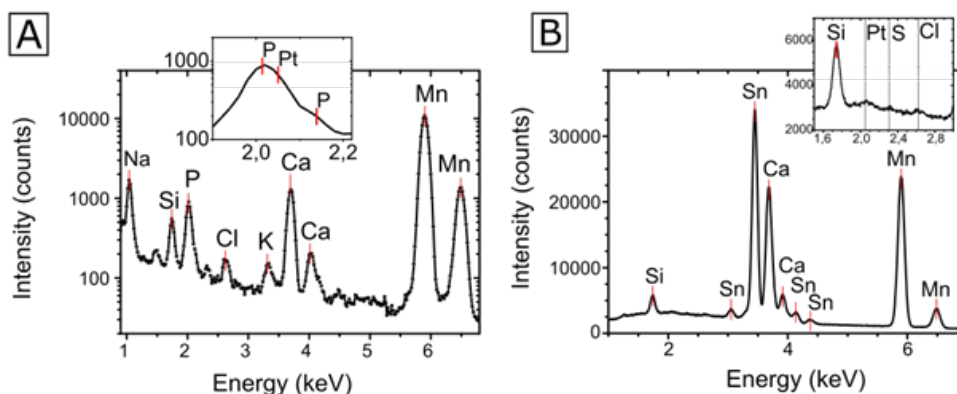


Figure C.4.: EDX element analysis of birnessite after electrolysis in different electrolytes. A: TEM EDX sum spectrum from the elemental mapping shown in Fig. 5.4 A right in the main text ($\sim 4\ \mu\text{m}$ thick birnessite electrode after 9 h of electrolysis in Na-phosphate buffer ($\eta = 530\ \text{mV}$)); B: SEM EDX 4x4 point grid of $4\ \mu\text{m}$ thick birnessite electrode after 9 h of electrolysis in H_2SO_4 adjusted with Imidazole to pH 7. The Si peak is a spurious signal from the detector and the small Sn signal originate from the substrate (FTO). The slight traces of Cl might stem from a tiny leak of the AgCl reference electrode.

Figure C.5 shows an EDX linescan of a $4\ \mu\text{m}$ thick sample after 9 h of electrolysis. The red arrow in the HAADF-image points the direction and position of the scan. In comparison to the linescan in Figure 5.5 C of the main text, the spatial resolution is much higher. The Mn-concentration roughly correlates to the thickness contrast of the HAADF-image and shows to separate particles. The highest P/Mn-ratio

can be found at the edge of the pore. This is in agreement with the linescan shown in Figure 5.4 C. Within the particle the P/Mn-ratio is not significant, however, the P/Mn-ratio increases close to the interface between the two particles. To strengthen the significance of the P/Mn ratio, the EDX spectra for selected points are also shown in Figure C.5. The EDX spectra clearly present a Phosphorous signal at the pore surface at spectrum #2, 7 and 8. Within the particle the P-signal is close to the noise level which is exemplified by spectra #3 and 6. The high P/Mn ratio for the first measuring point appears only because of the Manganese content is close to zero. Since the P signal is close to the noise level in spectrum 1, we cannot determine an accurate P/Mn ratio and thus no error bar is plotted for the P/Mn ratio. This indicates that in addition to the electrode surface and the surfaces of the pores, phosphorous is also located on the surfaces / interfaces of the birnessite nanoparticles and is below a level of one atomic percent in the nanoparticles volume.

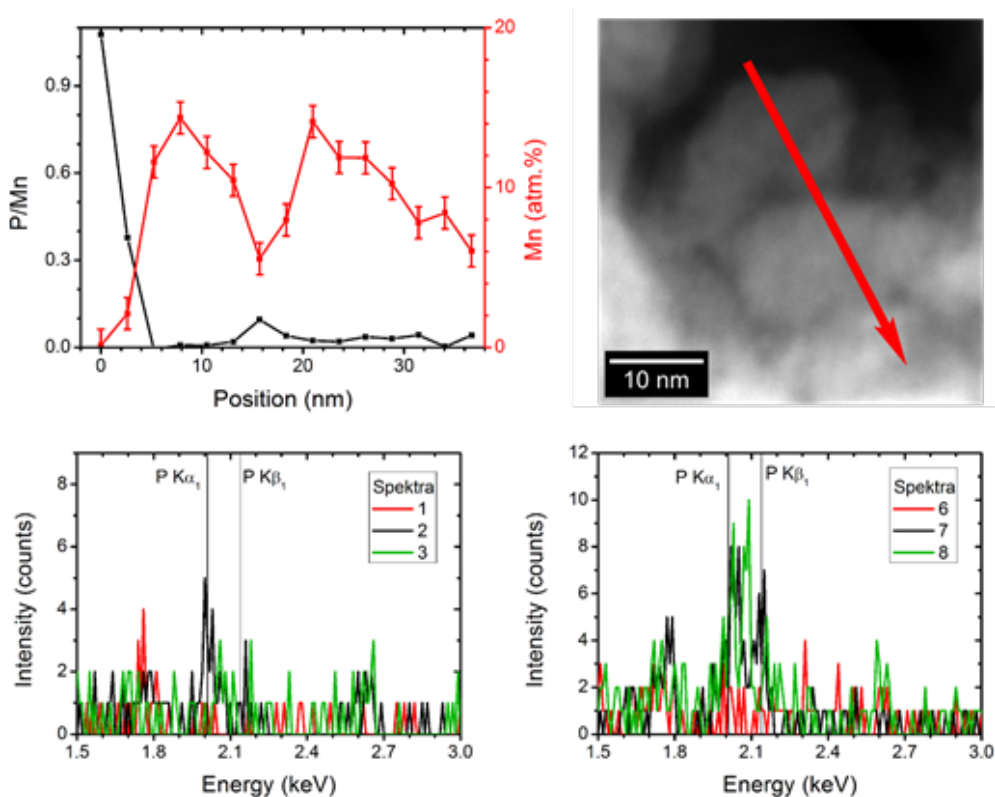


Figure C.5.: EDX linescan of a $4\ \mu\text{m}$ thick sample after 9 h of electrolysis in phosphate buffered electrolyte. The spectra #1-3 and #6-8 correspond to the first 3 and the grain boundary data points in the top left figure.

C.3. Spectroscopy

Interestingly, a Mn^{2+} signal (peak at 640.5 eV) is also present in all samples except the powder sample. It is especially pronounced for freshly prepared electrodes, where Mn-reduction most likely occurs by the carbon-containing ink. Furthermore, studies shown that Mn^{2+} ions can also be generated by X-ray irradiation of MnO_x , so it cannot be ruled out that the described increase of the Mn^{2+} concentration is merely an artefact (however, concerning the issue of beam damage).^[200]

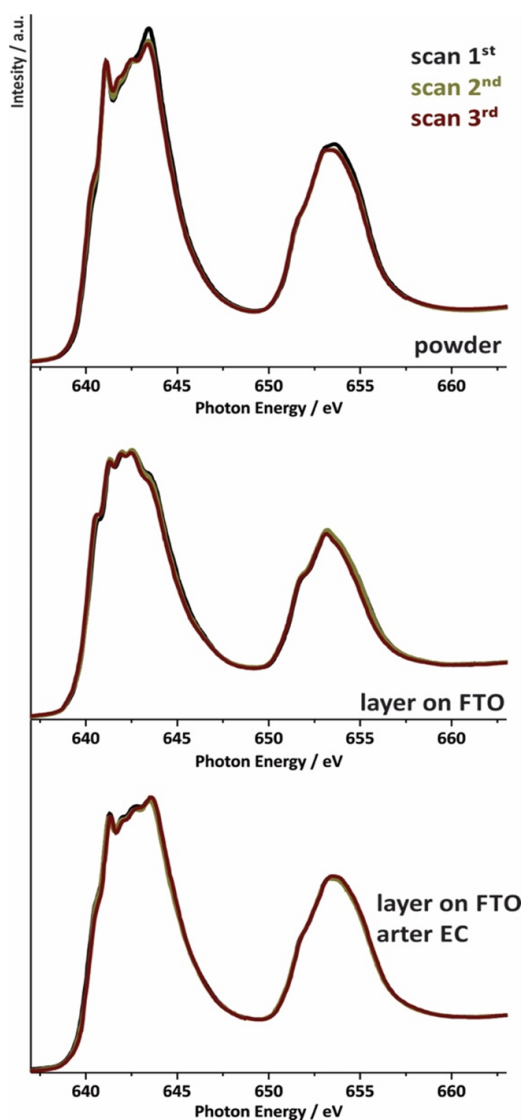


Figure C.6.: Stability studies for NEXAFS Mn L-edge measurements. For each sample, a new spot was chosen and three full scans (625-670 eV) were recorded on the same spot. color code: 1st spectrum - black, 2nd spectrum - dark yellow, 3rd spectrum - wine).

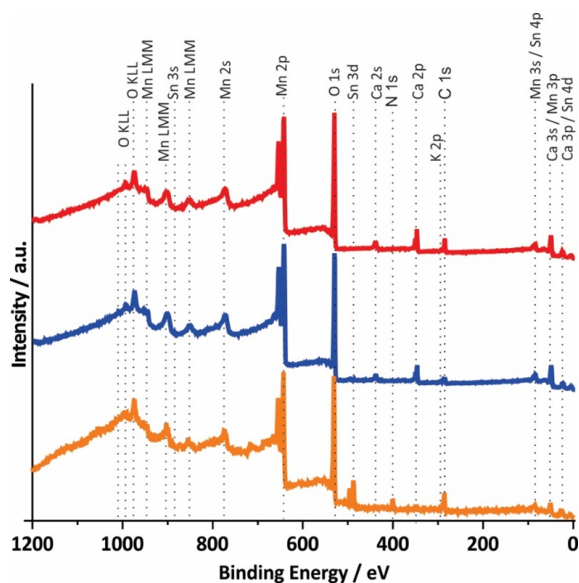


Figure C.7.: X-ray photoelectron survey spectra (XPS, $h\nu = 1486.7$ eV) of different Ca-birnessite samples. red: synthetic Ca-birnessite powder, blue: screen printed, $10\ \mu\text{m}$ thick Ca-birnessite layer on FTO substrate after annealing at 450°C and orange: XPS of an electrode after 16 h of OER electrocatalysis in $0.1\ \text{M}$ Imidazole - SO_4^{2-} buffer ($\eta = 540$ mV).

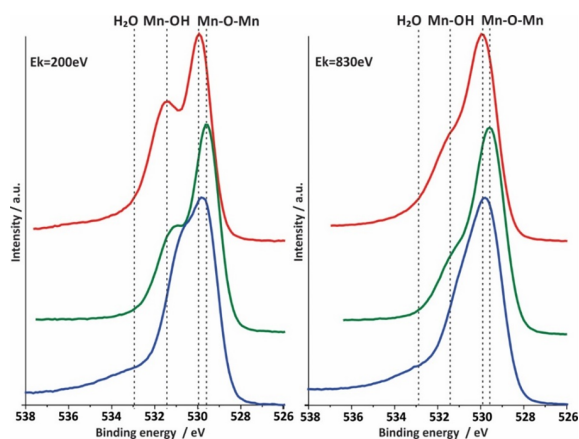


Figure C.8.: X-ray photoelectron spectra for the O 1s region for three Ca-birnessite samples: red: Ca-birnessite powder sample, green: screen printed, $10\ \mu\text{m}$ thick Ca-birnessite layer on FTO substrate after annealing at 450°C and blue: XPS of an electrode after 16 h in $0.1\ \text{M}$ phosphate buffer under OER conditions ($\eta = 540$ mV). The spectra on the left were recorded with a kinetic electron energy of $200\ \text{eV}$, those on the right for $830\ \text{eV}$.

Reference spectra and linear combination analysis (LCA)

- Reference spectra and difference spectra

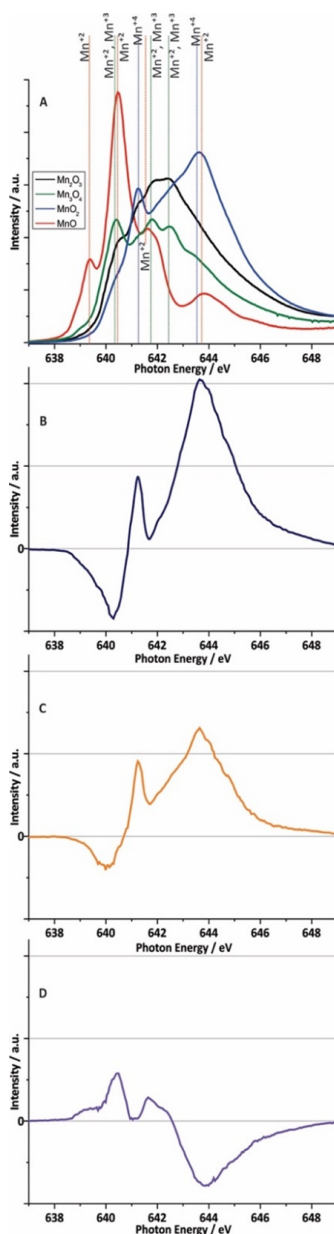


Figure C.9.: From the top: a) Mn L₃-edge reference spectra; c-d difference spectra of Mn L₃ edge; b) difference spectrum of the pristine electrode minus the powder Birnessite; c) difference spectrum of the pristine electrode minus the electrode after electrochemistry d) difference spectrum of the sample after electrochemistry minus the pristine electrode.

• Linear Combination Analysis (LCA)

Linear combination analysis (LCA) is performed by using a self-written python 3.7 script. MnO, Mn₃O₄, Mn₂O₃ and α -MnO₂ are used as components. A simple least square fit is applied to determine the composition of the of the investigated samples. A variety of 0.1 eV in excitation energy is allowed for the fitted data to account for uncertainty in energy calibration. Since the Mn L₃-edge is more sensitive to the local manganese environment, the fitted region is restricted between 638 and 648 eV excitation energy. Reference spectra and invested spectra are proceeded in the same way; photonflux normalization, linear background subtraction and normalization to the edge jump at 665 eV. The MnO, Mn₃O₄, Mn₂O₃ references (Fig. C.9) were synthesized by the group of Philipp Kurz, University Freiburg. The MnO powder was heated to 200°C in UHV prior the reference spectrum was taken. The α -MnO₂ reference powder was kindly provided by Justus Heese-Gärtlein (AG Behrens, Universität Duisburg Essen).^[233]

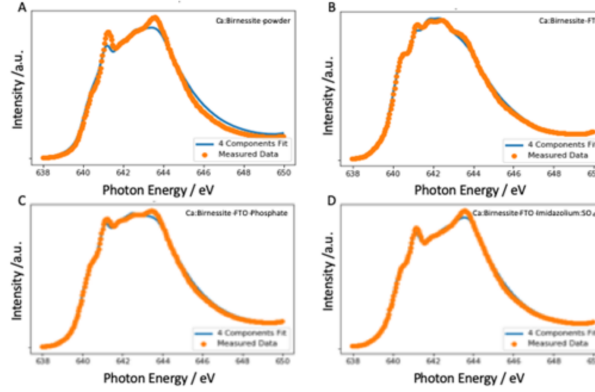


Figure C.10.: The four component fitting results for studied samples: a) powder Ca:Biressite; b) Ca:Biressite-FTO pristine electrode; c) Ca:Biressite-FTO-Phosphate the electrode after 16 h of OER electrocatalysis in 0.1 M phosphate buffer ($\eta = 540$ mV); d) Ca:Biressite-FTO-Imidazolium:SO₄²⁻ electrode after 16 h of OER electrocatalysis in 0.1 M Imidazole - SO₄²⁻ buffer. Orange line - measured data, blue line - LCA fit.

	MnO Mn _(oct) ²⁺	Mn ₃ O ₄ Mn ²⁺ , Mn ³⁺	Mn ₂ O ₃ Mn ³⁺	MnO ₂ Mn ⁴⁺
Ca:Biressite-powder	0	0	41%	59%
Ca:Biressite-FTO-pristine	7%	6%	65%	22%
Ca:Biressite-FTO-Phosphate	2%	5%	45%	48%
Ca:Biressite-FTO-Imidazolium: SO ₄ ²⁻	6%	7%	21%	66%

Table C.3.: Results of LCA for studied samples.

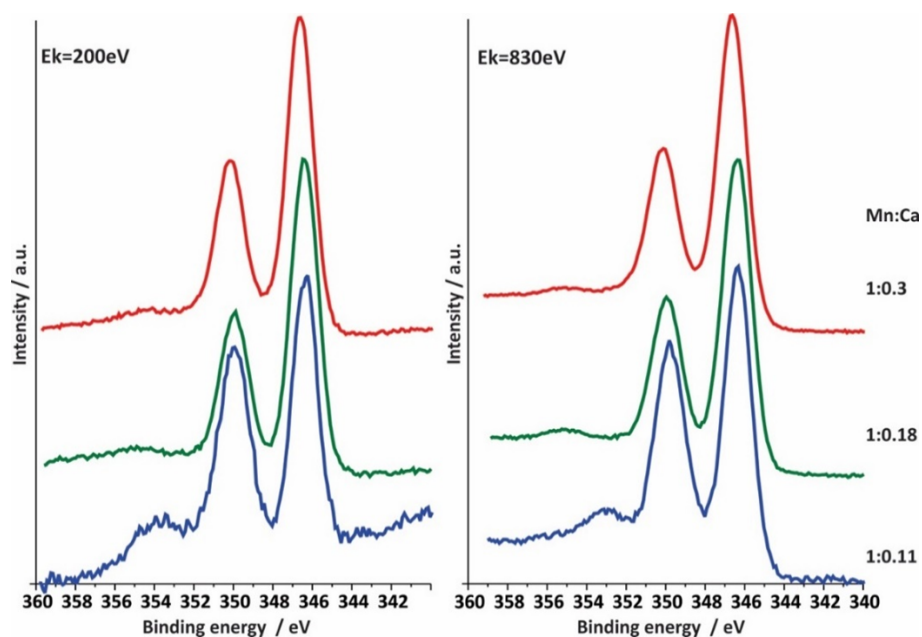


Figure C.11.: Ca 2p X-ray photoelectron spectra for three different Ca-Birnessite samples. The colour code is identical to the previous Figure C.8 with the respective kinetic electron energies stated at the top.

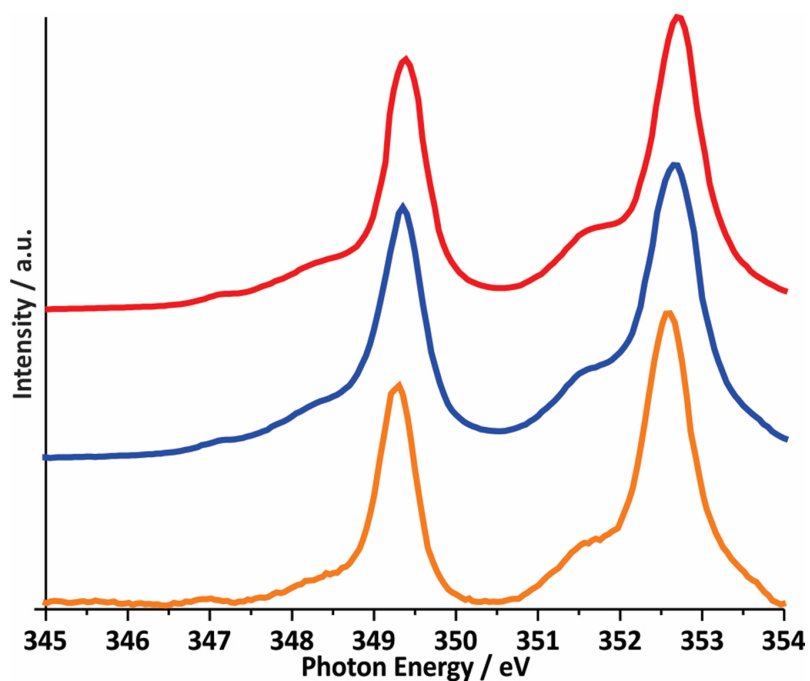


Figure C.12.: Ca L_3 -edge NEXAFS (TEY) spectra of the three different Ca-birnessite samples studied by XAS. Colour code and sample descriptions are identical to Figure C.7.

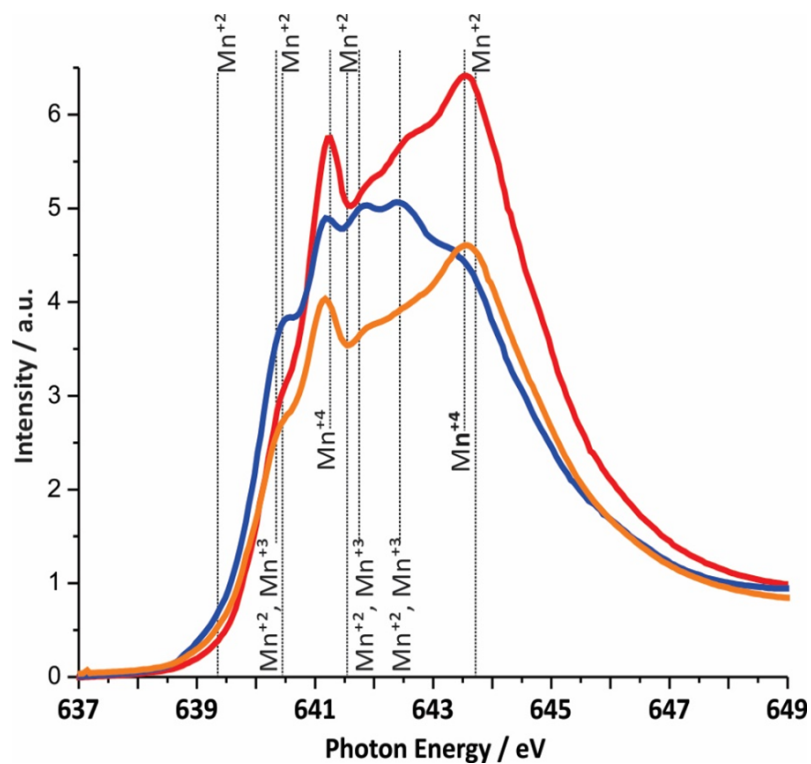


Figure C.13.: Mn L_3 -edge NEXAFS (TEY) spectra of the three different Ca-birnessite samples studied by XAS. Colour code and sample descriptions are identical to Figure C.7.

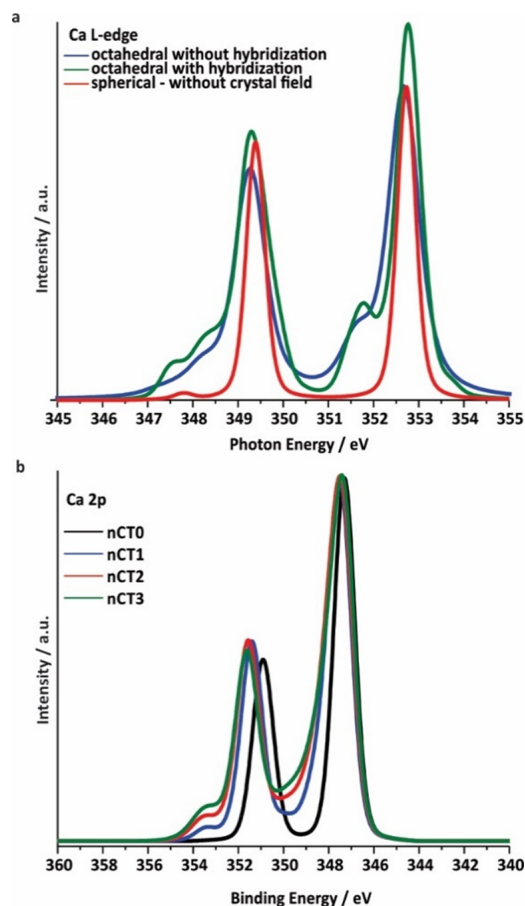


Figure C.14.: Computed Ca L-edges XA spectra and calculated Ca 2p XP spectra: (a) XAS calculations are shown for a spherical Ca^{2+} ion along with two results for a Ca^{2+} ion in an octahedral field with $10D_q = 0.75$ eV. The red line shows the result for spherical Ca^{2+} when hybridization between the Ca^{2+} ion and the ligand shell is ignored. The blue line shows the result for a Ca^{2+} ion in an octahedral field without hybridization. The green line shows the effect of including hybridization by allowing charge transfer from the ligand shell to the metal with a charge transfer parameter $\Delta = 0.75$ eV, i.e. a $|d^1\bar{L}\rangle$ configuration is included when describing the ground state. (b) The computed XPS spectra for a Ca^{2+} ion in an octahedral field with $10D_q = 0.75$ eV. The black line shows the result when there is no hybridization, which is simply the spin orbit split Ca 2p spectrum. The blue line shows the result when a $|d^1\bar{L}\rangle$ configuration is included, as with the XAS result. The ligand to metal charge transfer can be seen to give rise to a high binding energy satellite. The intensity of the satellite increases as higher $|d^n\bar{L}^n\rangle$ configurations are included, as shown by the red (green) line which includes configurations up to $|d^2\bar{L}^2\rangle$ ($|d^3\bar{L}^3\rangle$).

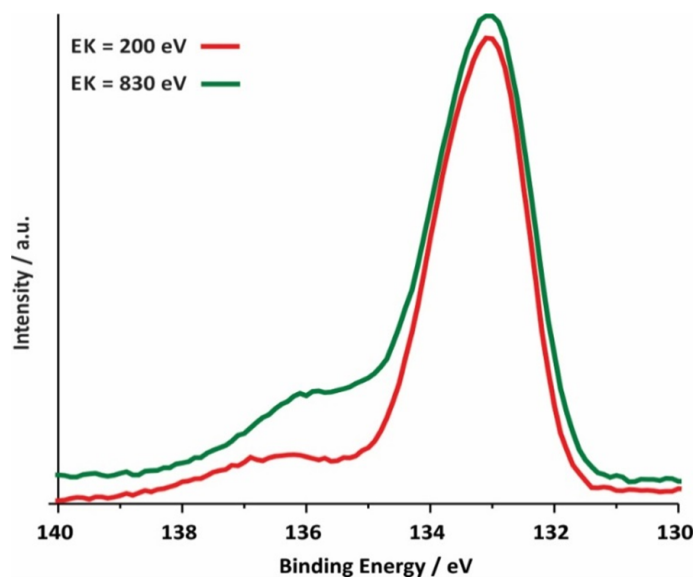


Figure C.15.: P 2p X-ray photoelectron spectra for Ca-birnessite electrode after electrolysis in phosphate buffer under OER conditions recorded at $h\nu = 960$ and 330 eV ($E_k = 830$ (green) and 200 eV (red)).

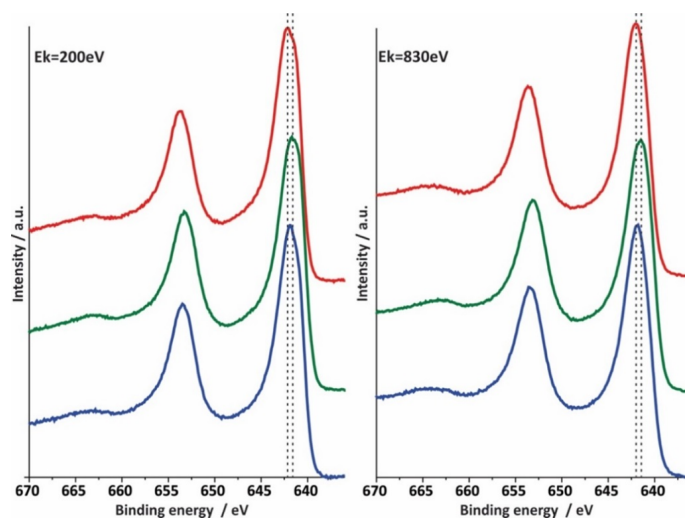


Figure C.16.: Mn 2p X-ray photoelectron spectra for three different Ca-Birnessite samples. The colour code is identical to the Figure C.8 with the respective kinetic electron energies stated at the top. Due to significant multiplet splitting of the three oxidation states of manganese (II, III, IV), and the overlapping binding energy for these multiplet splitting structures, the quantitative analysis of the Mn 2p spectra is not very reliable. For this reason, we based our analysis on NEXAFS Mn L-edges.

C.4. Theory: Hybridization and Calculation details

Hybridization between valence orbital of cation and anion is symbolized by the charge transfer satellite. The distance between the main line and the satellite, denoting the degree of hybridization, depends both on the Ca-ligand bond lengths and the charge transfer energy, the latter of which is likely proportional to the band gap of the material. If we consider only the monopole part of the Coulomb interactions, charge transfer will lower the energy of the final state in XPS by approximately $\Delta - Q$, where Δ is the charge transfer energy, e. g., the energy required to move an electron from the ligand to the metal, and Q is the core valence Coulomb attraction.^[197] To estimate Δ we note that the valence band of birnessite consists of O 2p-like orbitals.^[234] Thus, if the empty calcium s and d states are located at the bottom of the conduction band, Δ is approximately equal to the band gap, which has been measured to be $\sim 1.8 - 2.1$ eV for Na- birnessite.^[199] The core valence Coulomb attraction of Ca is 3.8 eV in the Hartree-Fock limit.^[234]

Using these estimates we expect the Ca 2p XPS spectrum of birnessite to have a main peak for the $|cd^1L\rangle$ configuration and a satellite at ~ 2 eV higher binding energy due to the $|cd^0\rangle$ configuration, where $|c\rangle$ indicates the Ca 2p core hole. In other words, the first doublet of the spectra corresponds to a p^5d^1 final state, where the additional d-electron more effectively screens the core hole, and the higher binding energy doublet a p^5d^0 final state.

We verified that hybridization can give the expected satellites by computing the XPS spectrum within a charge-transfer multiplet model (ESI Figure C.14b).^[234] We began by computing the Ca 2p spectrum for a Ca^{2+} ion in spherical symmetry using a core line width of 0.17 eV before introducing crystal field splitting and hybridization. As expected, including crystal field splitting, does not lead to the appearance of a satellite. We then introduced hybridization, with $\Delta=2$ eV, $U/Q=0.7$, $10D_q=0.75$, and an effective charge transfer integral, $T_{\text{eff}}=\sqrt{6T_{\pi}^2 + 4T_{\sigma}^2}$, of 3.43 eV. Doing so led to the expected charge transfer satellite (see ESI, Figure S13 for details) and a ground state, $\Psi = \alpha |d^0\rangle + \beta |d^1L\rangle + \gamma |d^2L^2\rangle$, with a high degree of covalence, where the weight of purely ionic configuration, α^2 , is approximately equal to that of the $|d^1L\rangle$ configuration.

With the applicability of our model ensured, we were able to interpret the measurements, beginning with the two spectra that show the charge transfer satellite (powder and after electrochemistry). Because Q should be nearly constant the increase in separation between the satellite and main line would imply an increase in covalency, either through a diminished Δ or an increased charge transfer integral, the latter of which could occur due to a reduction in Ca-ligand bond lengths. Lost of charge transfer satellite within our model would be expected if there were effectively no hybridization between Ca and its ligand shell due to either a decrease in T_{eff} or an increase in the charge transfer gap.^[197,199,234] The XAS and XPS spectra were computed using by way of multiplet ligand-field theory (MLFT) with the Xclaim package^[192] As is typical, the model Hamiltonian was treated as a sum of three terms: an atomic term describing the central atom, a crystal field term, and a

hybridization term. Of these terms the one describing hybridization deserves further discussion, which is written as:

$$H = \sum_{\Gamma_\gamma} T_{dL}(\Gamma)(d_\gamma^\dagger L_\gamma + L_\gamma^\dagger d_\gamma) + \sum_{\Gamma_\gamma} \epsilon_L(\Gamma) L_\gamma^\dagger L_\gamma \quad (\text{C.1})$$

, where Γ_γ is the irreducible representation to which the ligand orbital γ belongs. $\epsilon_L(\Gamma)$ is the on-site energy for the ligand electrons, which is the difference in energy between the d^n and $d^{(n+1)}$ ground states plus the charge transfer energy, symbolically:

$$\epsilon_L = E(d^n) - E(d^{(n+1)}) + \Delta \quad (\text{C.2})$$

d_γ^\dagger (d_γ) and L_γ^\dagger (L_γ) are the creation (annihilation) for electrons in the d and ligand shells, respectively. The transfer integrals are the $T_{dL}(\Gamma)$, which were written using the Slater-Koster parameters, $(pd\sigma)$ and $(pd\pi)$ with $\frac{(pd\sigma)}{(pd\pi)} = -2.2$, [2] as $T_\sigma = \sqrt{3}(pd\sigma)$ and $T_\pi = -2(pd\pi)$. The role of this hybridization term to include $|d^n \underline{L}^n\rangle$, with $n \geq 1$, configurations, which represent the transfer of n electrons from the ligand shell to the Ca d orbitals. Because $(pd4\sigma)$ controls the effective transfer integral, and therefore hybridization between the ligand shell and central ion, increasing $(pd\sigma)$ leads to an increase in covalency. Note that with this approach we do not need to know the exact atomic positions or nature of the atoms in the ligand shell to compute the XAS and XPS spectra. We can instead test how symmetry and hybridization change the spectra.

While in principle we could adjust parameters, such as $(pd\sigma)$, $(pd\pi)$, $10D_q$, broadening, and the charge transfer energy, to find those that agree best with experiment, we chose to select a set of parameters based on what is known about the system and those similar to it simply to show how crystal field splitting and hybridization are manifest in the spectra. Thus, for all calculations we used Lorentzian broadening with the natural width of the Ca LIII,II edges ($\Gamma = 0.17$ eV).^[235] For XAS (XPS) we also employed Gaussian broadening with a width of 0.5 eV (1.0 eV). The charge transfer energy was set to 2.0 eV, see main text. The core-valence valence monopole part of the Coulomb interaction, Q, was taken as 3.8 eV, see main text, and the valence-valence monopole part of the Coulomb interaction was taken as $0.7Q$, or 2.7 eV, due to the finding that $U/Q \sim 0.7$ for the 3d transition metals.^[195] The crystal field splitting was taken as 0.75 eV, between the 0.5 eV typical for early 3d transition metals and the 1.2 eV computed for CaO.^[202] $pd\sigma$ was taken to be 1.5 eV to reflect the expected large hybridization energy.^[197]

Supporting Information for Chapter 6

This chapter is a reproduction of the supporting information for the in chapter 6 presented publication^[30]

Atom Surface Dynamics of Manganese Oxide under Oxygen Evolution-Like Conditions Studied by In-Situ Environmental Transmission Electron Microscopy

Emanuel Ronge¹, Jonas Lindner¹, Jens Melder², Jonas Ohms², Vladimir Roddatis^{1,†}, Philipp Kurz², Christian Jooss^{1,}*

accepted by *The Journal of Physical Chemistry C* (2020)

References, labels and arrangement of figures have been modified to suit this thesis.

¹ Institut für Materialphysik, Georg-August-Universität Göttingen, Friedrich-Hund-Platz 1, 37077 Göttingen, Germany.

² Institut für Anorganische und Analytische Chemie and Freiburger Materialforschungszentrum (FMF), Albert-Ludwigs-Universität Freiburg, Albertstraße 21, 79104 Freiburg, Germany

Movie	Electrode	Environment	Dose rate $e^-/(\text{\AA}^2 \text{s})$	Speed
S1	Pressed	1 hPa O_2	22600	8.6x
S2	Pressed	1 hPa H_2O	60000	6.2x
S3	Pressed	1 hPa H_2O	7100	4.1x
S4	Pressed	1 hPa O_2	7500	8.6x
S5	Printed	1 hPa O_2	7400	4.1x
S6	Printed	0.1 hPa H_2O	5000	22.3x
S7	Printed	1 hPa H_2O	7700	11.2x
S8	Pressed	HV no cold trap	42000	6.2x

Table D.1.: Overview of the movies and used parameters: electrode type, environment, dose rate and speed.

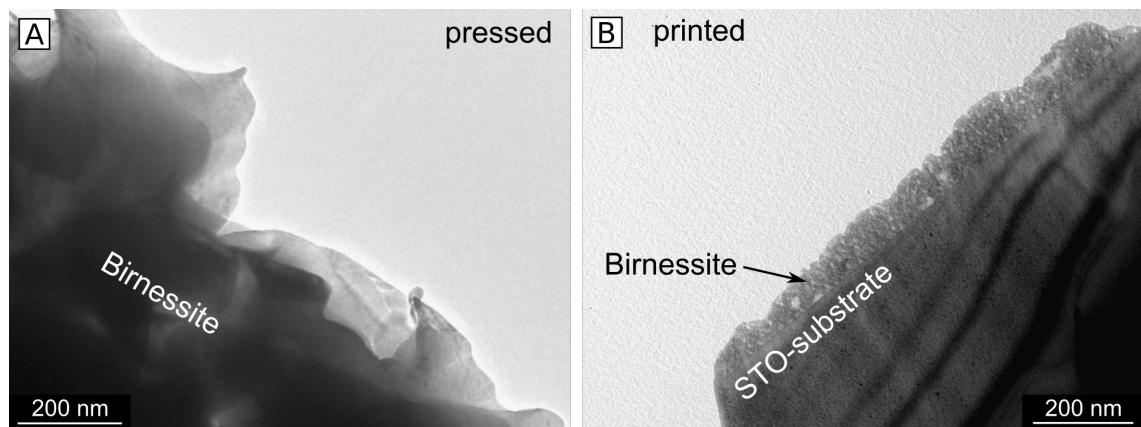


Figure D.1.: Overview TEM images of pressed (A) and printed (B) birnessite electrodes.

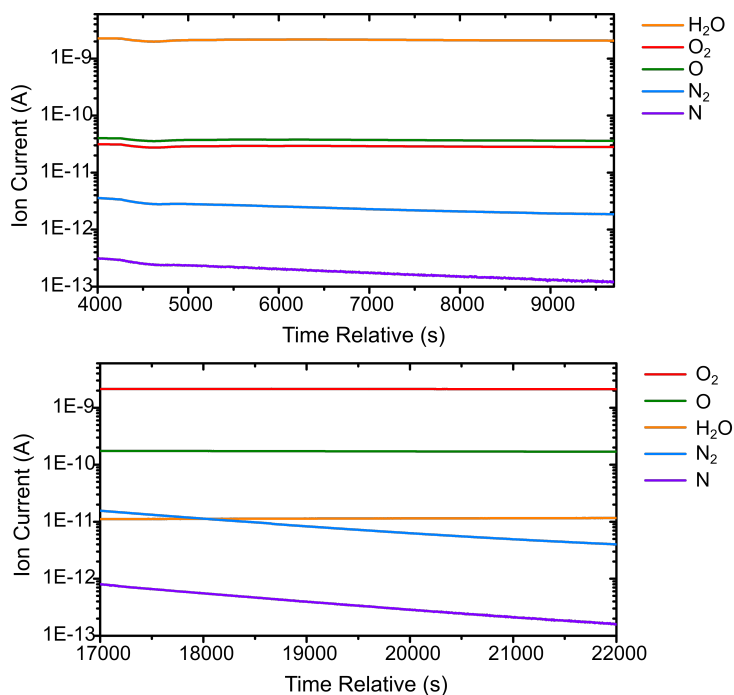


Figure D.2.: Relative gas composition in ETEM experiment in H₂O (top) and O₂ (bottom) determined with a residual gas analyser (RGA). The total gas pressure is 1 mbar.

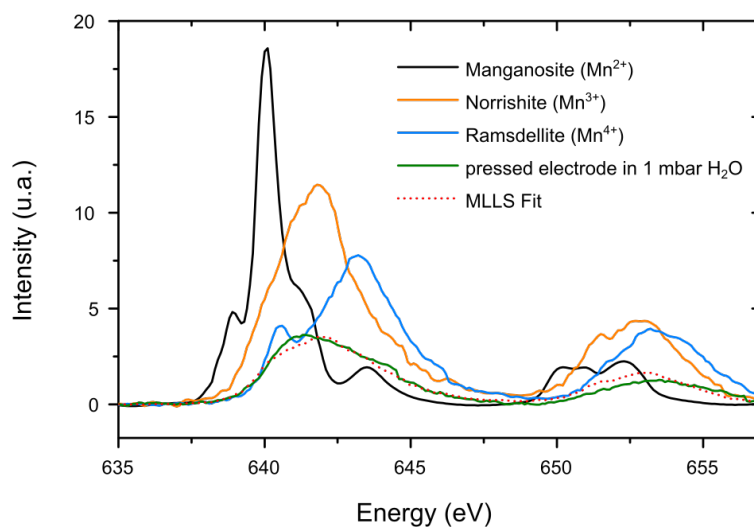


Figure D.3.: MLLS Fitting of the Mn L-Edge of the pressed electrode in 1 hPa H₂O (R^2 /coefficient of determination=0.96). Reference spectra taken from Garvie et al.^[208].

STEM EELS mapping of the printed electrode

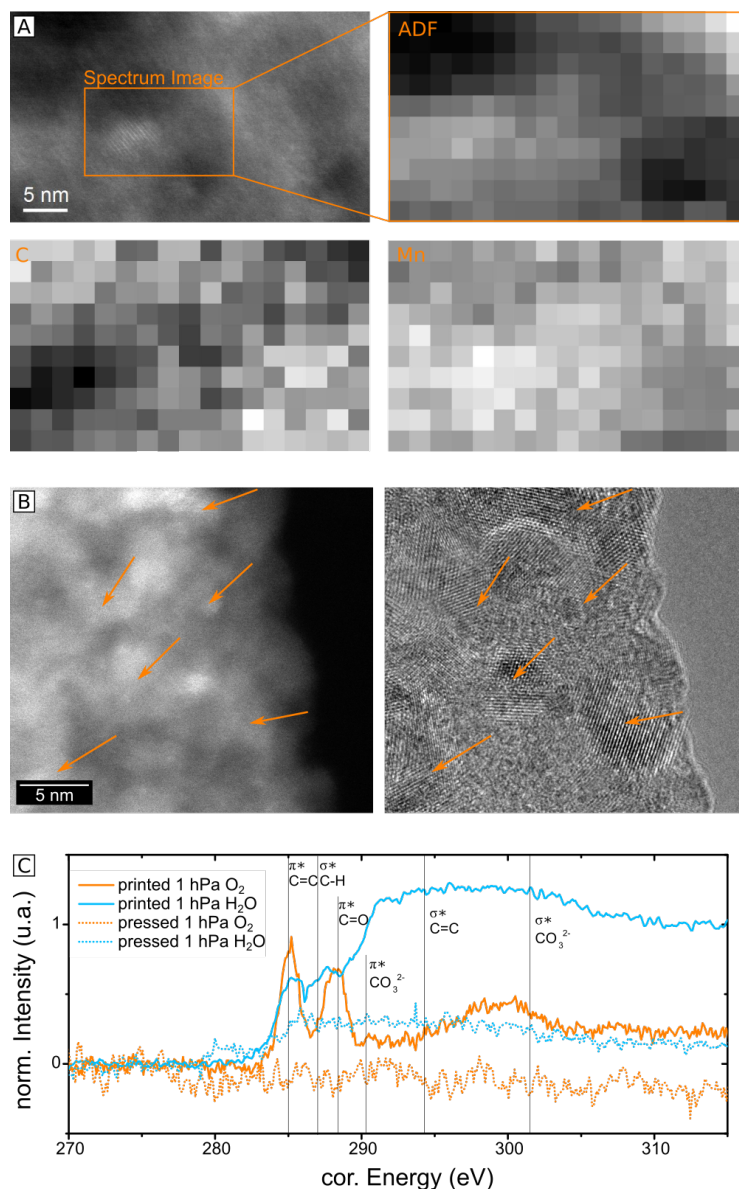


Figure D.4.: STEM-EELS, ADF mapping and HRTEM imaging of the printed electrode in 1 hPa O₂. A: Carbon and manganese EELS-map. B: HRTEM image of printed electrode with arrows indicating birnessite nanocrystals. C: EELS carbon K-edge spectra of the printed and pressed electrode in 1 hPa O₂ and H₂O.

Figure D.4 shows the STEM and EELS mapping of the printed electrode. The measurements were carried out in 1 hPa of O₂ in order to avoid additional beam induced carbon contamination in STEM mode. Here, the measured carbon stems from the electrode and not from surface contamination. The spectral image of the

Mn L edge in Figure D.4 A shows a high Mn concentration on the lower left side, indicating a birnessite nanocrystal. This contrast correlates to a bright contrast in the ADF detector. Areas with high Mn contrast show lower carbon contrast in the mapping of the C K edge in Figure D.4 A, supporting the presence of the expected heterogeneous nanostructure with birnessite particles and carbon binder. In conjunction with thickness variations, this is the origin of the inhomogeneous STEM ADF contrast in Figure D.4 A.

Figure D.4 B correlates the STEM ADF image with an HRTEM image taken at the same area. The bright areas in ADF contrast are crystals that correspond to a darker contrast in HRTEM. The darker carbon rich areas in ADF correlates in HRTEM to a brighter contrast in areas which appear to be less ordered. However, in many places an overlap of carbon rich areas and birnessite crystals leads to inconclusive contrasts in the TEM. As mentioned above, the appearance of disordered areas in HRTEM can be either due to an orientation of a crystal far from a low index zone axis or due to amorphous carbon. The correlation of less ordered areas with higher carbon content confirms again the heterogeneity of the printed electrode consisting of birnessite nanocrystals embedded in a disordered, carbon rich matrix.

Figure D.4 C displays the carbon K-edge EELS spectra of printed and pressed electrodes in 1 hPa O₂ and confirms the absence of carbon in the pressed sample within the detection limit. The position and shape of carbon edge of the printed electrode gives information about nature of the carbon. In O₂ and H₂O the carbon K-edge consists of two sharp peaks at 285 eV and 288.2 eV and a less intense broad peak at about 300 eV. While in H₂O the spectrum is dominated by the very broad peak between 290 eV and 305 eV (see Figure D.4 C). The first sharp peak can be assigned to the C1s → π* transition ($E_{lit}=285\text{ eV}$) of C=C typical for amorphous carbon. In addition, the σ* transition results in a broad peak at 294.3 eV. At 288.4 eV the C1s → π* transition of C=O is located which can be assigned to the second sharp peak. CO₃²⁻ has transitions at $E_{\pi^*}=290.3\text{ eV}$ and $E_{\sigma^*}=301.5\text{ eV}$ and could be hidden in the broad peak between 290 eV and 305 eV^[236–238], presumably due to carbon related contamination of the printed lamella.

The oxygen atmosphere prevents a surface contamination by carbon species for both types of electrodes in STEM mode. These usually originate from electron-beam induced cracking of hydrocarbons in the vacuum system. However, in H₂O, depending on the cleanness of the lamella and electron dose rate, a surface contamination by carbon in STEM mode is observed. This explains the difference in the EELS spectra for H₂O and O₂. Carbon contamination for the printed electrode, can additionally stem from the carbon containing protection layer used in FIB lamella fabrication.

In summary, printed electrodes consist of birnessite nanocrystals in an amorphous, carbon containing matrix.

Pristine state of the electrode - lattice distances and stability

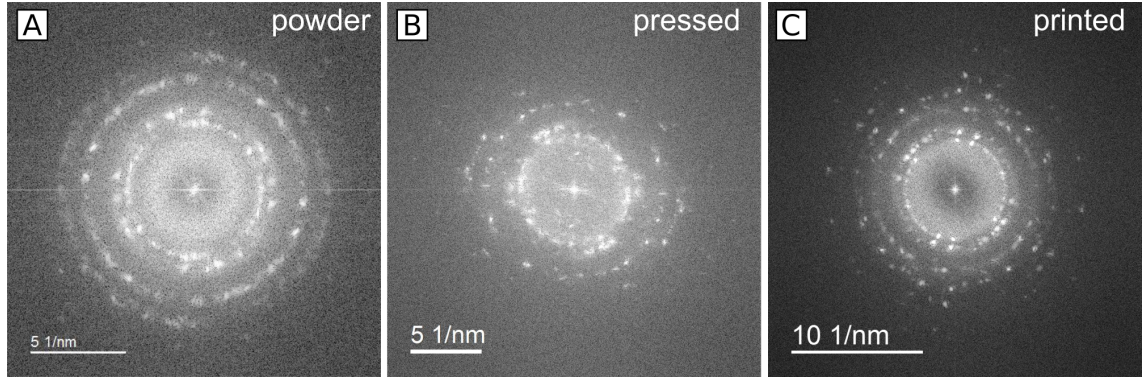


Figure D.5.: FFTs of HRTEM images of the birnessite A: powder, B: pressed and C: printed electrode in Figure 6.2 (main text).

\bar{d} Å	d Å	(h k l)	F^2	\bar{F}^2	d_{Exp} Å	Lit/Exp	Abs. dev.
5.05	5.05	-1 0 0	$1.02 \cdot 10^6$	$1.02 \cdot 10^6$	-	-	-
2.85	2.85	0 -1 0	$9.56 \cdot 10^5$	$9.56 \cdot 10^5$	2.68	1.06	0.17
2.52	2.52	-2 0 0	$9.24 \cdot 10^5$	$9.24 \cdot 10^5$	2.29	1.10	0.23
2.48	2.49	-1 -1 0	$2.02 \cdot 10^7$	$2.78 \cdot 10^7$	2.29	1.08	0.19
	2.47	-1 1 0	$7.69 \cdot 10^6$				
1.80	1.89	-2 -1 0	$9.46 \cdot 10^6$	$9.75 \cdot 10^6$	-	-	-
	1.88	-2 1 0	$2.87 \cdot 10^5$				
1.68	1.68	-3 0 0	$2.73 \cdot 10^6$	$2.73 \cdot 10^6$	1.6	1.05	0.08
	1.45	-3 -1 0	$2.70 \cdot 10^7$				
1.44	1.44	-3 1 0	$9.63 \cdot 10^7$	$1.30 \cdot 10^8$	1.4	1.03	0.04
	1.42	0 -2 0	$7.05 \cdot 10^6$				
1.37	1.37	-1 -2 0	$8.31 \cdot 10^6$	$8.56 \cdot 10^6$	1.33	1.03	0.04
	1.37	-1 2 0	$2.47 \cdot 10^5$				

Table D.2.: Comparison of the lattice distance for Birnessite with the experimental values d_{Exp} . Structure factor F is calculated for electron diffraction with structure model of Lopano et al.^[81] and the atomic scattering factor from Colliex et al.^[232]. Similar lattice distances are combined in \bar{d} and \bar{F}^2 .

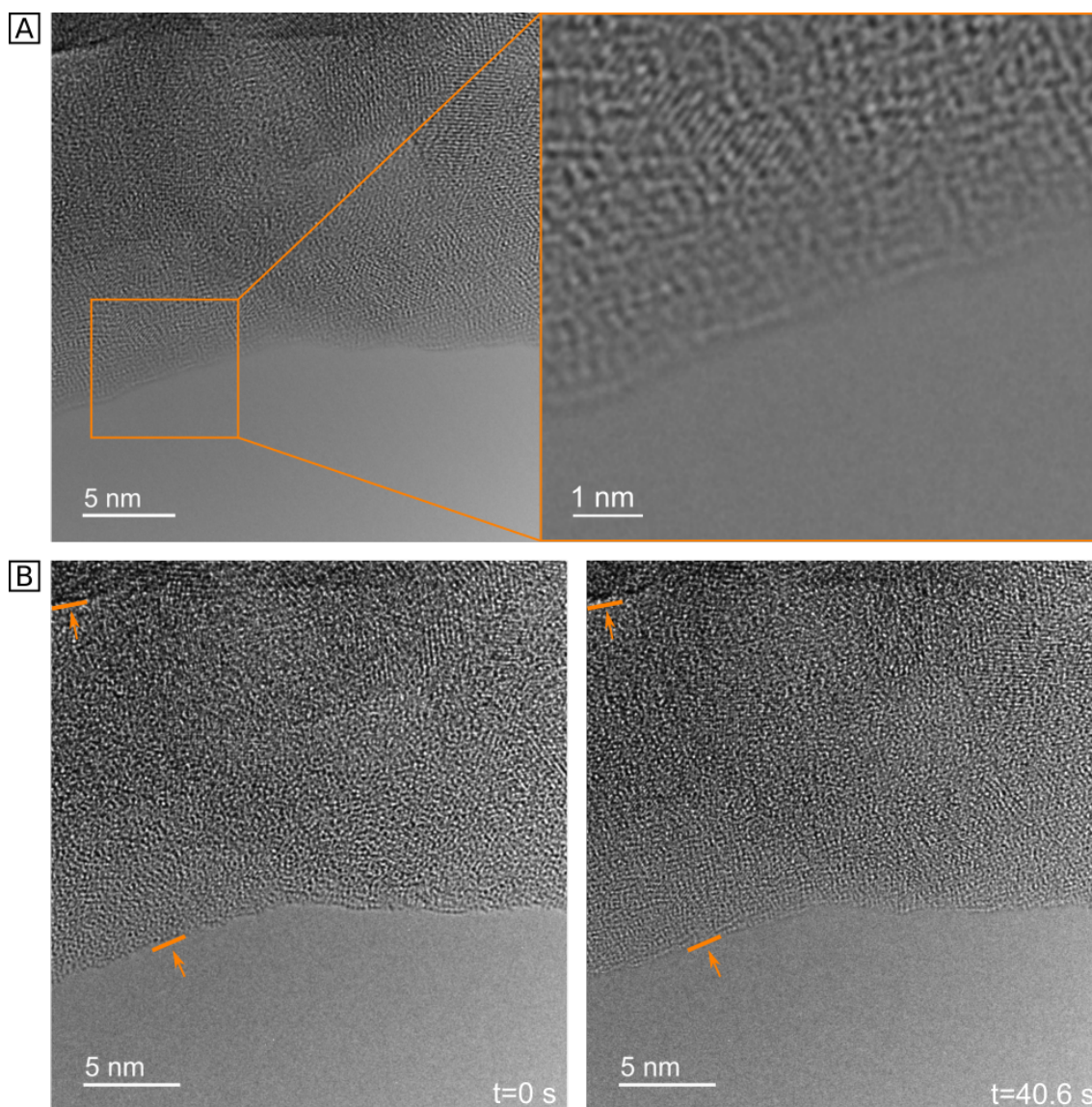


Figure D.6.: Time dependent HRTEM Analysis of the pressed electrode in HV with no cold trap from movie M8. A: Averaged image ($\bar{N}=219$, $T=53$ s, $D=42,000$ $e^-/(\text{\AA}^2\text{s})$) with overview on the left and zoom-in on the right side; B: left side single after 0 s and right side single frame after 40.6 s. The upper orange markers indicate a grain boundary and the lower marker the birnessite surface. In both images the markers are in the same position relative to the frame a indicate no removal of the surface.

Bubble formation in pressed and printed electrodes

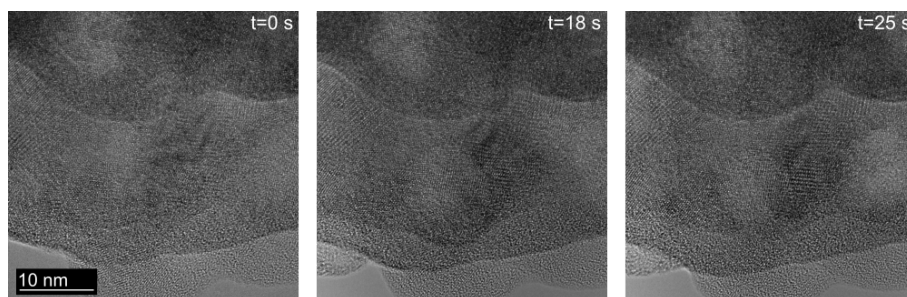


Figure D.7.: Bubble formation in a pressed electrode in $60,000 e^-/(\text{\AA}^2\text{s})$ in 1 hPa H_2O . Frames taken from Movie M2.

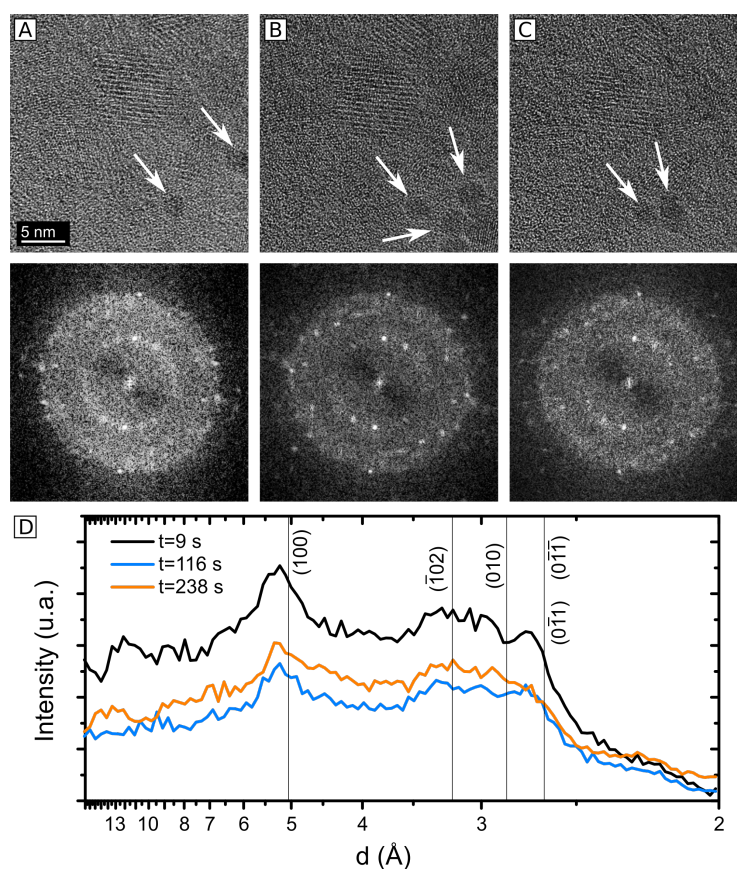


Figure D.8.: HRTEM analysis of the moving bubbles (printed electrode) in $5000 e^-/(\text{\AA}^2\text{s})$ and $100 \mu\text{bar}$ water. HRTEM image and corresponding FFT after: A: 9 s; B: 116 s and B: 238 s. D: Intensity profile of the FFT shown in A-C. Frames taken from Movie M6.

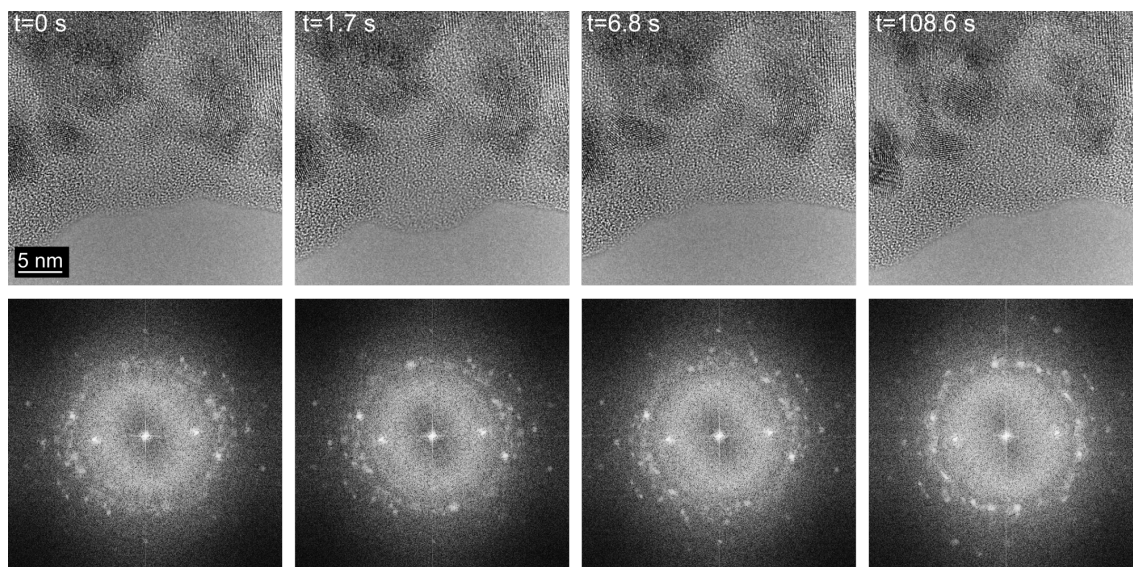


Figure D.9.: Time resolved surface dynamics of the printed electrode 1 hPa H₂O ($\bar{N}=516$, $T=88$ s, $D=22,200$ e⁻/(Å²s), for the average frame see Figure 6.5 B main text.

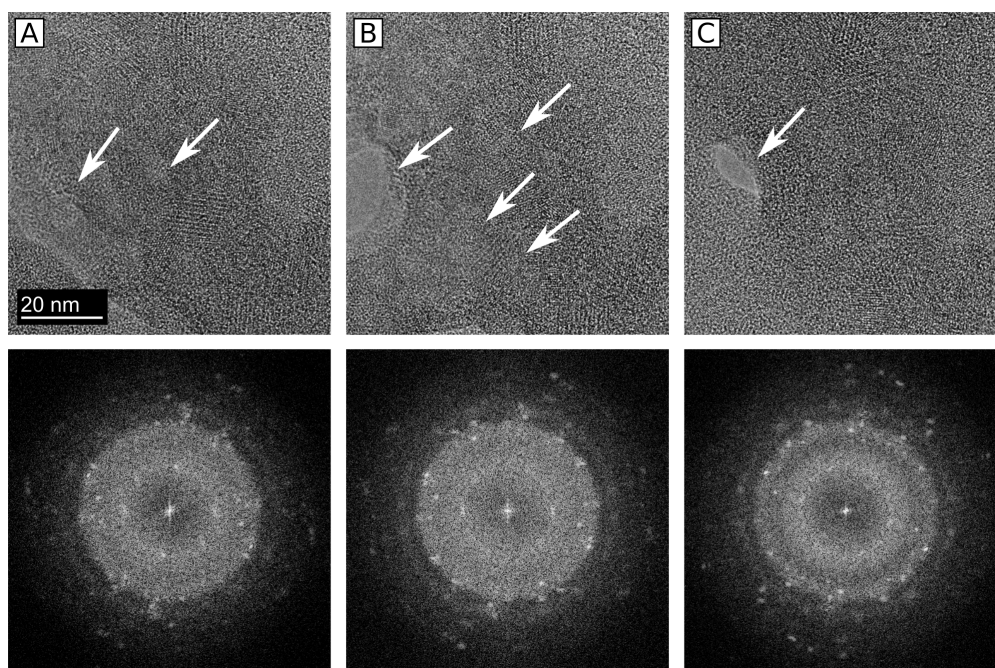


Figure D.10.: Strong bubble formation and cracking in the printed electrode at 7700 e⁻/(Å²s) in 1 hPa H₂O. Frames taken from Movie M7.

Electron energy loss spectroscopy data in high vacuum, O₂ and H₂O

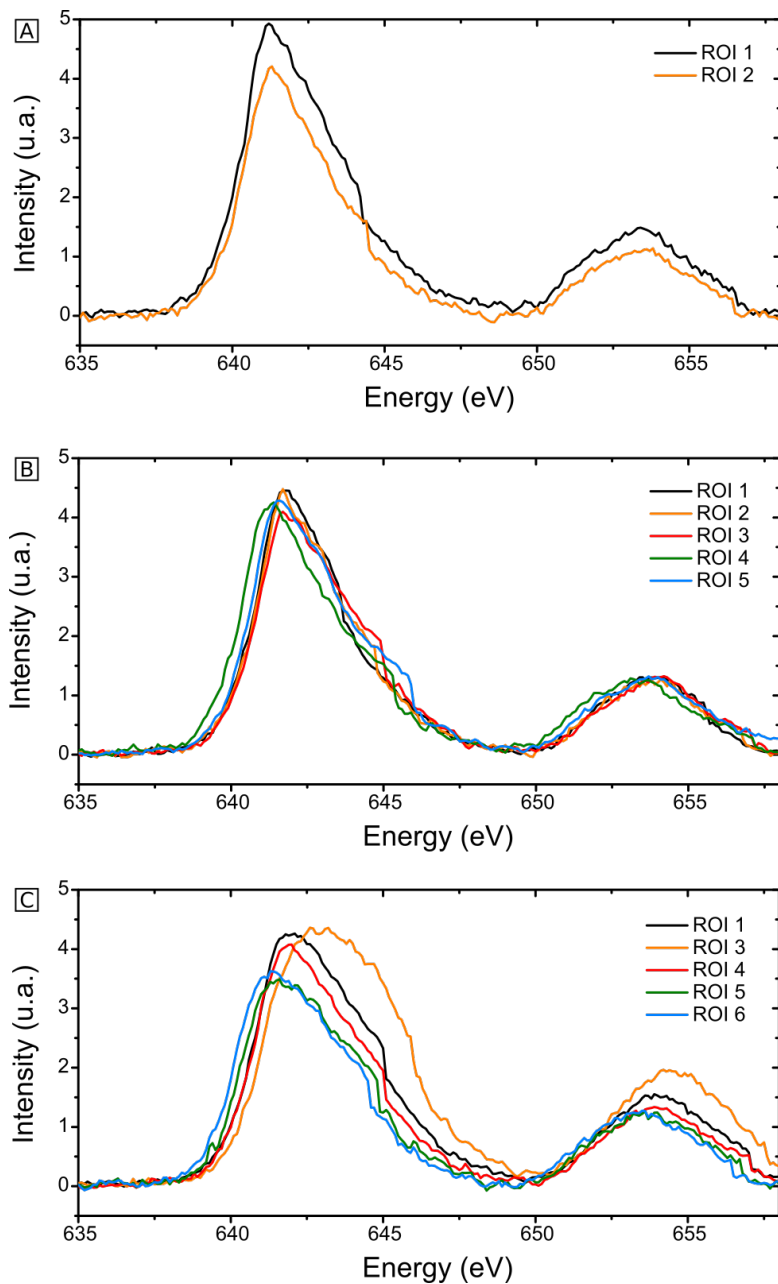


Figure D.11.: All Mn-L spectra from different region of interest (ROI) of pressed electrode which are used in the EELS analysis. A) HV B: 1 hPa O₂ C: 1 hPa H₂O.

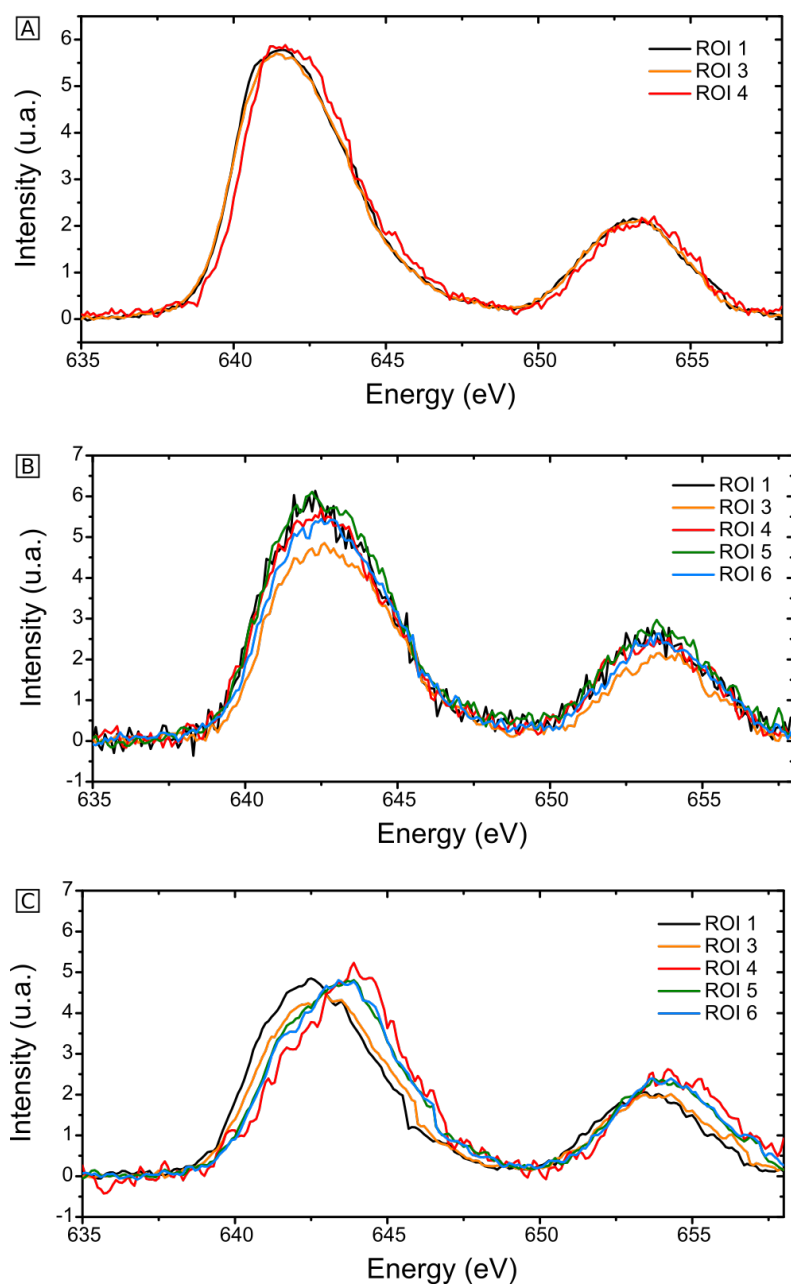


Figure D.12.: All Mn-L spectra from different region of interest (ROI) of printed electrode which are used in the EELS analysis. A) HV B: 1 hPa O₂ C: 1 hPa H₂O.

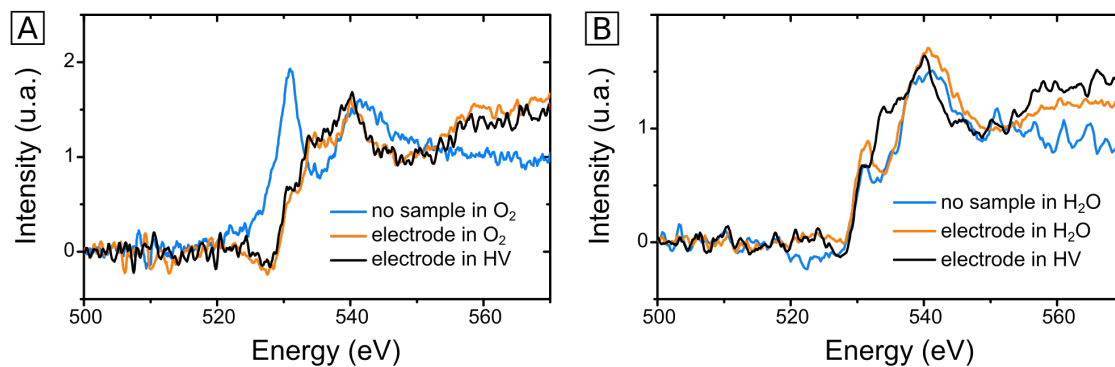


Figure D.13.: EELS O-K edge of the pressed electrode in A: HV and 1 hPa O₂ B: HV and 1 hPa H₂O, compared to the spectra without a sample.

Determination of the electric resistance of the TEM lamella

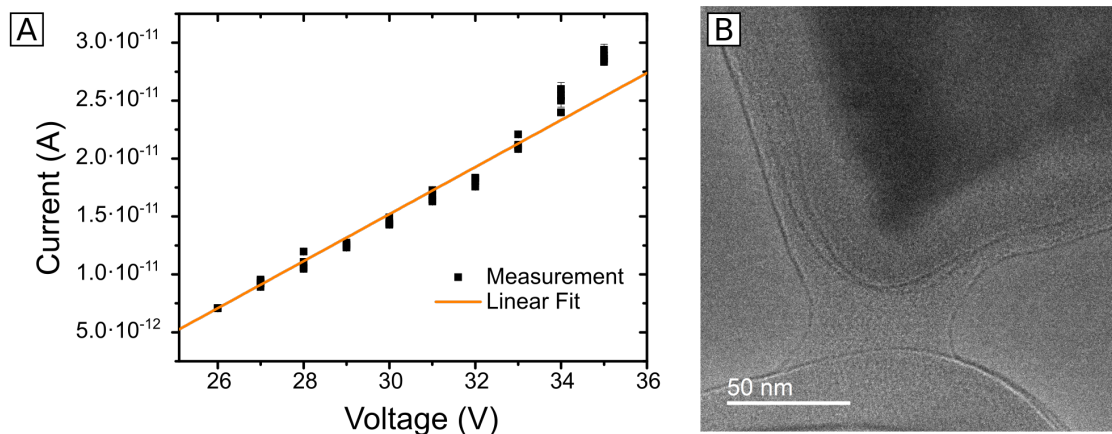


Figure D.14.: A: IV curve with linear fit to determine the resistivity of the printed electrode lamella ($R \approx 5 \cdot 10^{11} \Omega$). B: TEM image of STM tip which is connected to the lamella via a carbon bridge.

Dose rate dependent surface dynamics

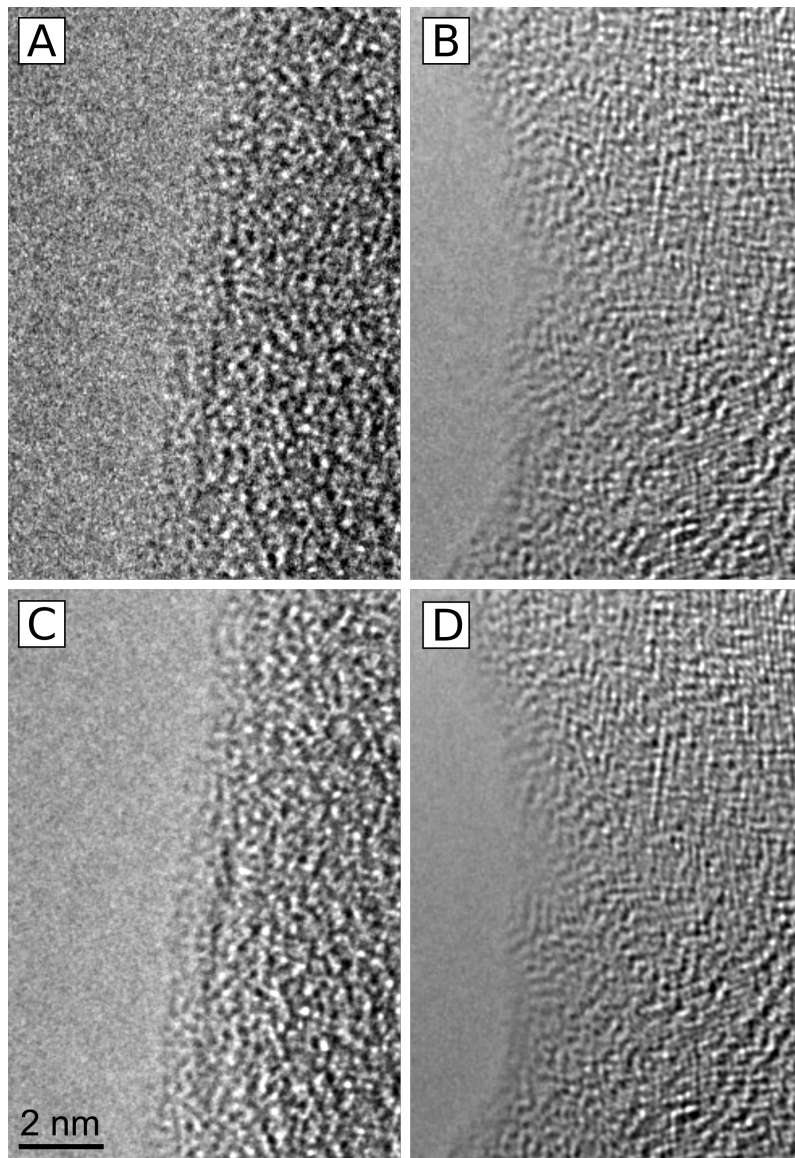


Figure D.15.: Comparison of speed / intensity of the dynamics of the pressed electrode in dependence of the beam induces potential by averaging the frames over a short time ($T = 1$ s). Left column: $5900 \text{ e}^- / (\text{\AA}^2 \text{ s})$; right column: $D = 55,000 \text{ e}^- / (\text{\AA}^2 \text{ s})$; A: single frame with an acquisition time of 0.2 s; B: single frame with an acquisition time of 0.1 s C: averaged image with $\bar{N} = 6$ and $T = 1$ s, no significant blurring visible; D: averaged image with $\bar{N} = 4$ and $T = 1$ s, slight blurring at the surface visible.

Stationary state of the pressed electrode in H₂O - absence of surface sputtering

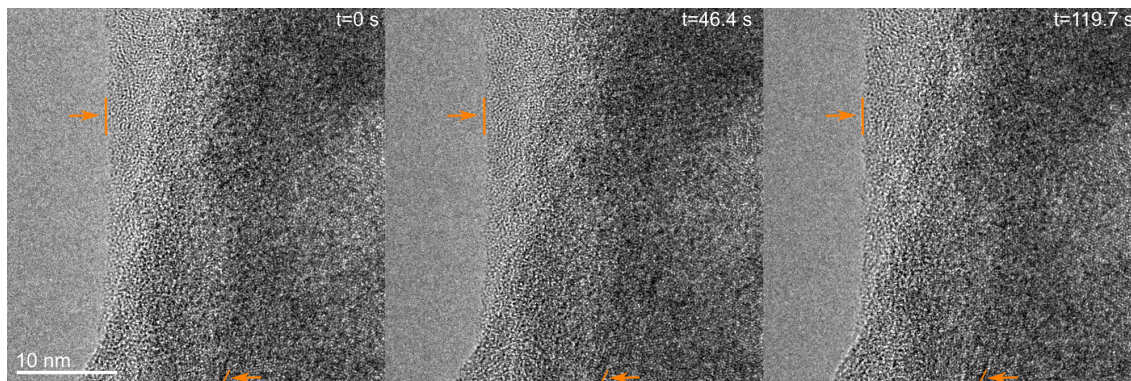


Figure D.16.: Single frames from movie M3 (pressed electrode in 1 hPa H₂O, $D=7100 e^-/(\text{\AA}^2\text{s})$). The orange markers are positioned relative to the frame in the same way and indicate the electrode surface and a dark contrast which is correlated to the crystal structure.

Author Contributions

This thesis includes four articles which present original research by the author and have been published or submitted for publication:

- Chapter 3** Emanuel Ronge, Thorsten Cottre, Katharina Welter, Vladimir Smirnov, Natalie Jacqueline Ottinger, Friedhelm Finger, Bernhard Kaiser, Wolfram Jaegermann, and Christian Jooss. Stability and Degradation Mechanism of Si-based Photocathodes for Water Splitting with Ultrathin TiO₂ Protection Layer. *Zeitschrift für Physikalische Chemie*, 234(6):1171–1184, June 2020
- Chapter 4** Emanuel Ronge, Sonja Hildebrandt, Marie-Luise Grutza, Helmut Klein, Philipp Kurz, and Christian Jooss. Structure of Nanocrystalline, Partially Disordered MoS_{2+δ} Derived from HRTEM-An Abundant Material for Efficient HER Catalysis. *Catalysts*, 10(8):856, August 2020
- Chapter 5** Emanuel Ronge, Jonas Ohms, Vladimir Roddatis, Travis Jones, Frederic Sulzmann, Axel Knop-Gericke, Robert Schlögl, Philipp Kurz, Christian Jooss, and Katarzyna Skorupska. Operation of Calcium-Birnessite Water-Oxidation Anodes: Interactions of the Catalyst with Phosphate Buffer Anions. *Chemrxiv.13153976.V1*, <https://doi.org/10.26434/chemrxiv.13153976.v1>, October 2020
Preprint on Chemrxiv
- Chapter 6** Emanuel Ronge, Jonas Lindner, Jens Melder, Jonas Ohms, Vladimir Roddatis, Philipp Kurz, and Christian Jooss. Atom Surface Dynamics of Manganese Oxide in OER like Conditions revealed by in-situ Environmental TEM. *The Journal of Physical Chemistry C (accepted)*, 2021

In the following the author contributions to the respective article will be stated:

Chapter 3 - Stability and Degradation Mechanism of Si-based Photocathodes for Water Splitting with Ultrathin TiO₂ Protection Layer

The Si-based photocathodes solar cells were prepared by Katharina Welter and Vladimir Smirnov under the supervision of Friedhelm Finger. Thorsten Cottre conducted the device integration, deposition of the TiO₂ layer and Pt catalyst, and photoelectrochemical characterization under supervision of Bernhard Kaiser and Wolfram Jaegermann. The SEM and EDX measurements and analysis were carried out by the author and Natalie Ottinger under supervision of Christian Jooss. TEM lamella preparation and TEM analysis were conducted by the author. Christian Jooss and the author prepared the manuscript with contributions by Thorsten Cottre, Vladimir Smirnov, Bernhard Kaiser and Wolfram Jaegermann.

Chapter 4 - Structure of nanocrystalline, partially disordered MoS_{2+δ} derived from HRTEM - an abundant material for efficient HER catalysis

The MoS_x electrodes were prepared and electrochemically measured by Marie Grutza under supervision of Philipp Kurz in Freiburg. The XRD experiments were conducted and analyzed by Sonja Hildebrandt under supervision of Helmut Klein. Christian Jooss and the author also contributed to the evaluation of the XRD results for MoS_x. The SAED measurements were carried out by the author and analyzed with help from Sonja Hildebrandt. Lamella preparation, TEM and HRTEM work as well as the analysis were carried out by the author. The interpretation and writing of the manuscript was mainly performed by the author with support by Christian Jooss and Philipp Kurz, and contributions by Marie Grutza and Sonja Hildebrandt.

Chapter 5 - Operation of Calcium-Birnessite Water-Oxidation Anodes: Interactions of the Catalyst with Phosphate Buffer Anions

The birnessite electrodes were prepared and electrochemically measured by Jonas Ohms under supervision of Philipp Kurz in Freiburg. SEM, EDX and cross-section imaging were carried out and analyzed by the author. The TEM lamella preparation and (S)TEM analysis were conducted by the author with the help of Vladimir Roddatis. The X-ray spectroscopy experiments were carried out, analyzed and interpreted by Katarzyna Skorupska, Travis Jones, Frederic Sulzmann, Axel Knop-Gericke and Robert Schlögl. The writing of the manuscript was performed by Katarzyna Skorupska, Philipp Kurz, Christian Jooss, the author and Jonas Ohms, while the TEM section was mainly written by the author.

Chapter 6 - Atom Surface Dynamics of Manganese Oxide in OER like Conditions Revealed by in-situ Environmental TEM

The birnessite samples were prepared by Jens Melder and Jonas Ohms under supervision of Philipp Kurz in Freiburg. Lamella preparation and the TEM analysis were conducted by the author. The in-situ TEM experiments were carried out by the author with the help of Jonas Lindner and Ulrich Ross under supervision of Vladimir Roddatis and Christian Jooss. The analysis of the in-situ data were performed by the author. The manuscript has been mainly prepared by the author with some help from Christian Jooss.

Acknowledgment

During my time at Institute for Materials Physics, several colleagues, friends and relatives supported my research and contributed to the success of this thesis in various ways. This is the time to express my gratitude.

First of all, I want to thank my supervisor Prof. Christian Jooss for his guidance, support, motivation and the freedom to follow my ideas along with the inspirational discussions. Furthermore, my thanks go to Prof. Michael Seibt who kindly agreed to be the co-referee of this thesis.

I greatly benefited from the collaboration with Prof. Philipp Kurz, Jonas Ohms and Marie Grutza from Freiburg and Prof. Wolfram Jaegermann, PD Dr. Bernhard Kaiser and Thorsten Cottre from Darmstadt, and I would like to thank them for the successful cooperation, sample preparation, electrochemical measurements as well as the interesting and fruitful discussions. I am also very thankful to Dr. Vladimir Roddatis for his support at the ETEM and sample preparation as well as the critical discussions.

As this thesis was financed by the Deutsche Forschungsgemeinschaft (DFG) as part of the priority program (SPP) 1613 and the collaborative research center (CRC) 1073, I would like to express my gratitude for the funding.

In the last years I had the fortune to share the office with Jonas Lindner and I'm really thankful for the great atmosphere, the numerous discussions and the joint ETEM experiments which not only tremendously improved my scientific work but also reinforced my curiosity and enjoyment of fundamental research. I am also grateful to Stephanie Mildner and Ulrich Ross for their support with the ETEM experiments, not only for the scientific part, but also for the company which helped in complex experiments and situations.

Besides them I would like to thank my former Bachelor students Natalie Ottinger and Sonja Hildebrandt who helped to push this thesis forward. I greatly appreciate the training and help of Mathias Hahn, Volker Radisch and Tobias Schulz concerning the TEMs and FIB. My gratitude naturally also extends to several not specifically mentioned (current and former) PhD, Master and Bachelor students as well as technicians at the Institute for Materials Physics.

Last but not least my parents deserve my greatest gratitude for the generous support throughout the years.